

Yao Ma

**Vapor-Facet-Solid (VFS)
mechanism: A new route for
catalytic CVD growth of one-
dimensional nanostructures**

**Schriftenreihe der Arbeitsgruppe
des Lehrstuhls für Oberflächen- und Werkstofftechnologie
im Institut für Werkstofftechnik**

Herausgeber: Prof. Dr. rer. nat. habil. Xin Jiang

Band 4

Yao Ma

Vapor-Facet-Solid (VFS) mechanism: A new route for catalytic CVD growth of one-dimensional nanostructures at low temperature

Schriftenreihe der Arbeitsgruppe des Lehrstuhl für Oberflächen-und
Werkstofftechnologie im Institut für Werkstofftechnik

Impressum

Prof. Dr. rer. nat. habil. Xin Jiang
Lehrstuhl für Oberflächen- und Werkstofftechnologie
Institut für Werkstofftechnik
Universität Siegen
57068 Siegen
ISSN: 2194-0096
Zugl.: Siegen, Univ., Diss., 2015

Vapor-Facet-Solid (VFS) mechanism: A new route for
catalytic CVD growth of one-dimensional nanostructures
at low temperature

Vom Department Maschinenbau
der Universität Siegen

zur Erlangung des akademischen Grades
Doktor-Ingenieur
genehmigte

Dissertation

von:	M. Sc., Yao Ma
aus:	Shaanxi, China
eingereicht am:	10. September 2014
Mündliche Prüfung am:	2. Dezember 2014
Referent:	Prof. Dr. rer. nat. habil. Xin Jiang
Korreferent:	Prof. Dr. rer. nat. Holger Schönherr

Zusammenfassung

Die einzigartige Morphologie wie auch die neuartigen Eigenschaften eindimensionaler Kohlenstoff-Nanostrukturen zogen in den vergangenen Jahren viel Aufmerksamkeit auf sich. Typischerweise werden diese Strukturen, zu denen unter anderem Nano-Röhrchen, -Fasern, -Kegel, -Bänder, -Spiralen und –Helix-Strukturen zählen, mittels eines katalytischen *chemical vapor deposition* (CVD) Prozesses erzeugt. Letzterer nutzt Übergangsmetalle (Fe, Co, Ni sowie ihre Legierungen) als Katalysatoren. Diese Prozesse werden dann üblicherweise mit Hilfe des allgemein anerkannten *vapor-liquid-solid* (VLS) Mechanismus interpretiert. Dieser Mechanismus beinhaltet zunächst die Löslichkeit wie auch die Diffusion des Kohlenstoffes in dem entsprechenden Katalysator. Im Weiteren bilden sich die Kohlenstoffnanostrukturen durch ein Ausscheiden überschüssigen Kohlenstoffes auf bzw. direkt unterhalb der Oberfläche des metallischen Katalysatorpartikels aus. Wenn der CVD Prozess jedoch bei deutlich niedrigeren Temperaturen als für einen VLS Prozess üblich (hier sind Temperaturen von $\geq 600^\circ\text{C}$ typisch) ausgeführt wird, lassen sich widersprüchliche experimentelle Ergebnisse beobachten. In diesem Zusammenhang konnten beispielsweise im Rahmen eines CVD Prozesses, welcher bei einer Temperatur von 250°C mit C_2H_2 als Prozessgas und Cu-Nanopartikeln als Katalysatoren durchgeführt wurde, neue polymerartige Nanostrukturen, die einen bemerkenswert hohen Anteil an Wasserstoffatomen aufweisen, gefunden werden. Der VLS Mechanismus kann hierbei das Wachstum dieser Strukturen nicht erklären, da weder Kohlenstoff noch Kohlenwasserstoff in Cu löslich sind oder aber diffundieren können. Konsequenterweise bedarf es daher eines alternativen Modelles, welches dieses Cu-basierte CVD-Wachstum bzw. andere Prozesse bei niedrigen Temperaturen, deren Kohlenstofflöslichkeit wie auch –Diffusion deutlich mit sinkender Temperatur abfallen, zu beschreiben vermag. Dies gilt hierbei sogar für Prozesse, die Fe-, Co- oder Ni-Katalysatoren nutzen.

Diese Arbeit widmet sich daher der Entwicklung eines einfachen Wachstumskonzeptes, welches sich deutlich vom konventionellen VLS Mechanismus absetzt. Das neue Konzept ist in der Lage Phänomene, die bei der Synthese von Wasserstoff-reichen Polymer/Kohlenstoff-Nanostrukturen bei niedrigen Temperaturen auftreten, zu erklären. Das Cu- C_2H_2 Reaktionssystem wird hierbei als typisches Beispiel eines katalytischen CVD Prozesses bei niedriger Temperatur herausgegriffen und eingehend untersucht. Das Verhalten des Wachstumsprozesses wird sowohl unter thermodynamischen als auch kinetischen Aspekten untersucht, um so ganz grundlegenden Fragestellungen wie den katalytischen Reaktionen, Diffusions-Pfaden und auch der treibenden Kraft nachgehen zu können. Basierend auf diesen

Studien wird dann ein *vapor* (Adsorption) – *facet* (Diffusion) – *solid* (Ausscheidung) Prozess eingeführt, der im Folgenden als VFS Mechanismus bezeichnet wird. Dieser neue Mechanismus basiert auf dem Konzept der Formation und anschließenden Diffusion von Kohlenwasserstoff-Bindungen auf der Oberfläche der Katalysatorpartikel anstelle einer direkten Löslichkeit und des Transportes von Kohlenstoff-Atomen. Er beinhaltet die Vorstellung eines drei-stufigen Wachstumsmodells: 1) Das kohlenwasserstoffhaltige Prozessgas bildet auf der Katalysator-Oberfläche Oligomere aus 2) Die Oligomere diffundieren entlang der Katalysator-Oberfläche 3) Die Oligomere polymerisieren weiter und sorgen schließlich für den Aufbau von Nanofasern. Eine sorgfältige Analyse zeigt hierbei, dass die dritte Stufe für die Rate des gesamten Wachstumsprozesses bestimmend ist. Schließlich werden die Untersuchungen auf weitere typische Übergangsmetalle ausgedehnt. Hierbei kommen Fe- und Ni-Katalysatoren verschiedener Gestalt bei niedrigen Prozesstemperaturen zum Einsatz. Ein erfolgreiches Nanostruktur-Wachstum zeigt die breite Anwendbarkeit des neuen Konzeptes. Zudem können durch Vergleiche mit dem Cu-basierten Wachstum Gemeinsamkeiten in den Wachstumsprozessen identifiziert werden, die ihrerseits zu einer Vertiefung des Verständnisses eines allgemein gültigen Modells führen.

Zusätzlich wurde die Korrelation zwischen der sich ausbildenden Mikrostruktur der Nanostrukturen und den Details der Geometrie (Form, Größe, Oberflächen-Indizierung) der entsprechenden Katalysatorpartikel eingehend erkundet. In diesem Zusammenhang wird auch die Evolution des Katalysatorpartikels während des Prozesses verfolgt, um so Einflussfaktoren identifizieren zu können. Basierend auf dem eingehenden Verständnis der Zusammenhänge zwischen sich ausbildender Nanostruktur und Geometrie der Katalysatorpartikel, wird schließlich eine allgemeine Facetten-selektive katalytische CVD-Wachstums-Methode entwickelt, die es erlaubt gezielt Nanostrukturen mit gewünschter Morphologie zu erzeugen. Es gelingt so, kontrolliert 2-, 3-, 6- und 8-zweigige Kohlenstoff-Nanostrukturen zu synthetisieren. Hierbei fungieren Cu-Nanopartikel als Katalysatoren, die ein Wachstum von Nano-Fasern nur auf bestimmten kristallinen Facetten zulassen.

Abschließen werden die physikalische und chemische Eigenschaften der hergestellten Nanostrukturen bestimmt, um so ihr Potential für entsprechende Anwendungen zu evaluieren.

Acknowledgements

I would like to express my sincere appreciation, first and foremost, to my thesis advisor Prof. X. Jiang. He guided me patiently to accomplish this thesis with his broad knowledge, acute scientific insight, and dedication towards research. It's a great honor to work under his guidance. What I learned from him is valuable asset in my whole life.

I would like to express my special thanks of gratitude to Prof. H. Schönherr for readily providing instrument for my research and agreeing to be a co-referee for my thesis. I'm also extremely grateful to Prof. H. -J. Christ and Prof. R. Brandt for readily accepting to be my examiner.

It is with immense gratitude that I acknowledge the support and help of Dr. X. Sun. He is not only an excellent collaborator but also a sincere friend.

This thesis would not have been possible without the help of my colleagues at LOT, University of Siegen. Dr. H. Zhuang always offers me wonderful guidance, support and friendship in past five years. The microscopic work with the aid of Mr. L. Zhang and Dr. J. H. Xia is an important part of this thesis. Dr. T. Staedler helped me in preparing German version abstract of this thesis as well as my manuscript for publication. Dr. N. J. Yang also gave me help in preparing manuscript and inspired me via brilliant discussion. Collaborative work with Mr. C. Weimer boosted my thesis greatly. Dr. C. Q. Zhuang and Mr. X. B. Yan gave me support in handling the ECR and MWCVD devices. I learned a lot about instruments from Mr. M. Vogel. I also got technique support from Ms. R. Fuchs, Mr. T. Degen, Mr. J. Meyer, and Ms. Petra. Ms. A. Brombach engaged patiently in administrative work to solve my problems. I am indebted to all my colleagues who supported me.

Great thanks are given to Dr. R. Bornemann for his help in optical measurement. He also saved our Raman instrument from collapse. It's an interesting and pleasing experience to share his knowledge. Special thanks to Mr. L. Wang for his help, both in work and life. Thanks also to Dr. Q. H. Su, Mr. K. Chen, Ms. Y.Y. Du, Prof. R. Z. Hu, Prof. M. Zhu and Dr. T. Kowald for their support in experiments. I render my appreciation to Dr. S. Ma and Ms. Gumira for providing experimental materials.

I dedicate this thesis to my lovely wife H. Y. Zhang, adorable daughter L. X. Ma, and my dear parents. They grant me power with encouraging words. They drive away my fatigue via smiling face.

Contents

Symbol List	III
Abstract.....	VII
1 Introduction	1
2 Research background	4
2.1 one-dimensional (1D) Carbon nanostructures (CNs)	4
2.2 Polymer-like nanostructures (PNs) prepared at low temperature	6
2.3 Goals of this thesis	11
3 Experimental Methods.....	12
3.1 Catalyst preparation	13
3.1.1 <i>Sol-gel route</i>	13
3.1.2 <i>Precipitation-decomposition route</i>	14
3.1.3 <i>Bulky metal route</i>	14
3.1.4 <i>Other routes</i>	15
3.2 Nanostructures synthesis.....	16
3.3 Characterization	18
3.3.1 <i>Morphology characterization</i>	18
3.3.2 <i>Structure characterization</i>	18
3.3.3 <i>Property evaluation</i>	19
4 Fundamental investigations of catalytic CVD growth of polymer nanostructure at low temperature.....	21
4.1 Structural characterization and growth mechanism	21
4.2 Kinetics process of the growth.....	27
4.3 Catalyst evolution	33
4.4 Size effect.....	39
5 Morphology control of multi-branched carbon nanostructures via facet-selective catalytic growth	45
5.1 Basic idea	45
5.2 Realization	47
5.3 Characterization	49

5.4 Modeling	52
5.5 Summary	56
6 VFS growth with aid of other transition metal catalysts	58
6.1 Fe catalyzed nanostructure-growth at low temperature	58
6.1.1 <i>Experimental facts</i>	58
6.1.2 <i>Discussion</i>	63
6.1.3 <i>Summary</i>	68
6.2 Ni catalyzed nanostructure-growth at low temperature	69
6.2.1 <i>Bulky Ni catalyzed growth</i>	69
6.2.2 <i>Growth catalyzed by individual Ni nanoparticle (Sol-Gel route)</i>	75
6.2.3 <i>Growth catalyzed by individual Ni nanoparticle (Nanopowder route)</i>	78
6.3 The adoptability of VFS mechanism	98
7 Applications and prospects	100
7.1 Applications as optical absorber	102
7.2 Applications as energy materials	107
7.3 In-situ doped CNs	110
7.4 Two-dimensional (2D) nanostructures	112
8 Conclusions	115
9 References	119

Symbol List

Abbreviations

1D	one-dimensional
2D	two-dimensional
3D	three-dimensional
AFM	atomic force microscopy
BCC	body centered cubic
BET	Brunauer-Emmet-Teller
CNs	carbon nanostructures
CNFs	carbon nanofibers
CNTs	carbon nanotubes
COT	cyclooctatetraene
CVD	chemical vapor deposition
DEC	diethyl carbonate
DSSC	dye-sensitized solar cells
EC	ethylene carbonate
ECR	electron cyclotron resonance
EDS	energy-dispersive X-ray spectroscopy
EEW	electric explosion of wires
EMC	ethyl methyl carbonate
ESB	energy selective back scattering
ESI-MS	electrospray ionization - mass spectrometry
FCC	face centered cubic
FESEM	field emission scanning electron microscopy
FIB	focused ion beam
FTIR	fourier transform infrared spectroscopy
FWHM	full width at half maximum
HRTEM	high resolution transmission electron microscopy
MOCVD	metal organic chemical vapor deposition
MWCVD	microwave assisted chemical vapor deposition
NFs	Nanofibers
PEG	polyethylene glycol
PNs	polymer nanostructures

PVD	physical vapor deposition
RDS	rate-determining step
SAED	selected area electron diffraction
STEM	scanning transmission electron microscopy
TD-GC/MS	thermal desorption - gas chromatography/mass spectrometry
TDS	temperature-programmed thermal desorption spectroscopy
TEM	transmission electron microscopy
TG-DSC	thermogravimetry-differential scanning calorimetry
TG-DTA	thermogravimetry-differential thermal analysis
UHV	ultra-high vacuum
VFS	vapor-facet-solid
VLS	vapor-liquid-solid
VSS	vapor-solid-solid
XPS	X-ray photoelectron spectroscopy

Symbols

Å	angstrom
°	degree
°C	degree Celsius
~	approximate
>	greater than
%	percentage
<	less than
β	the line broadening at half of the maximum intensity (FWHM)
θ	Bragg angle
λ	X-ray wavelength
μ	micron
μm	micrometer
Ø	diameter
A/mm ²	ampere/square millimeter
at. %	atomic percent
C	atomic carbon
C ₂	molecule containing two carbon atoms
C ₂ H ₂	acetylene

C_2H_4	ethylene
C_3	molecule containing three carbon atoms
C_5	molecule containing five carbon atoms
C_8H_8	cyclooctatetraene
CH_4	methane
cm^{-1}	wave number per centimeter
Co	cobalt
CO	carbon monoxide
Cu	copper
Cu_2O	cuprous oxide
CuO	cupric oxide
D	mean grain size
D_p	size of catalyst particle
D_v	difference of growth velocity between side A and B
eV	electron volt
Fe	iron
g	gram
h	hour
H	atomic hydrogen
H_2	molecular hydrogen
H_2O	water
H_2O_2	hydrogen peroxide
HCl	hydrogen chloride
in-lens	immersion Lens
I(D)	intensity of D band
I(G)	intensity of G band
k	shape factor
K	Kelvin
L_a	size of graphite cluster or sheet
Li	lithium
Li^+	lithium ion
M	mol per liter
m^2/s	square meter per gram
m^2/s	square meter per second

mA	milliampere
mAh/g	milliampere-hour per gram
mbar	millibar
mg	milligram
min	minute
mm	millimeter
m/z	mass-to-charge ratio
NH ₃	ammonia
Ni	nickel
nm	nanometer
O	atomic oxygen
Pd	palladium
Pt	platinum
R_f	curvature radius of as-grown nanofiber
R_{pi}	the i^{th} highest peak over the entire sampling length
R_{vi}	the i^{th} lowest valley over the entire sampling length
R_z	surface roughness: an average height difference between peak and valley based on the five highest peaks and lowest valleys over the entire sampling length
S	solubility
sccm	standard cubic centimeters per minute
SE2	secondary electrons induced by the backscattered electrons
Si	silicon
SiC	silicon carbide
T	temperature
V	volt
V_a	growth velocities on side A of catalyst particle
V_b	growth velocities on side B of catalyst particle
wt. %	weight percent

Abstract

The unique morphologies as well as novel properties of one-dimensional (1D) carbon nanostructures (CNs) attracted a lot of attentions over recent years. Typically these structures, including nanotubes, nanofibers, nanocones, nanobelts, nanocoils and nanohelices, etc. are synthesized via catalytic chemical vapor deposition (CVD) processes, which employ transition metals (Fe, Co, Ni and their alloys) as catalysts. The processes are usually interoperated by a commonly accepted vapor-liquid-solid (VLS) mechanism which assumes carbon dissolves, diffuses in the catalyst and CNs grow due to the precipitation of excess carbon on the surface of the metal catalyst particles. However, conflicting experimental evidence was observed when the CVD process was carried out at a much lower temperature compared to a typical VLS process (temperature $\geq 600^{\circ}\text{C}$). For instance, at 250°C new types of polymer-like nanostructures that featured a remarkable amount of hydrogen atoms were synthesized utilizing catalytic Cu nanoparticles and C_2H_2 source gas. It is not possible to apply the VLS mechanism to the growth of these structures as neither carbon nor hydrocarbon molecule can dissolve (diffuse) in copper. Therefore an alternative model is required for these Cu catalyzed CVD processes and for other low temperature processes in which the carbon solubility and diffusion coefficient decreases significantly with decreasing temperature, even with Fe, Co, Ni catalysts.

This thesis is dedicated to derive a simple growth scheme contrasting the conventional VLS mechanism. The novel scheme is able to explain phenomena in synthesizing hydrogen-rich polymer/carbon nanostructures at a relative low temperature. The Cu- C_2H_2 reaction system which is the most typical case of the low temperature catalytic CVD growth is systematically investigated. The behavior in the growth process is studied both in terms of thermodynamics and kinetics to clarify elementary issues, such as fundamental catalytic reactions, diffusion route and driving force. Based on these works we propose a basic scheme to describe the growth as a Vapor (adsorption) - Facet (diffusion) – Solid (precipitation) process and we call it VFS mechanism. This new mechanism is based on the concept of the formation and subsequent diffusion of hydrocarbon molecules on the surface of the catalyst particles instead of direct solution and transportation of carbon atoms. It corresponds to a 3-step growth model: 1) hydrocarbon source gas coupling on catalyst surface to form oligomers, 2) oligomers diffusion through the catalyst surface, 3) oligomers further polymerization and nanofiber formation. Carefully analysis proves the third step rate-limits the whole process. Then the investigation extends further to the other commonly used transition metal systems.

Fe and Ni catalysts with different appearance are used in the low temperature growth. Positive growth results reveal the extensive adaptability of the new model. Meanwhile, by comparing with the Cu catalyzed process, common features are extracted to enrich the understanding of the general mechanism.

In addition, we studied the interrelation of the microstructures of the novel nanostructures and the detailed geometry (shape, size and surface index) of their corresponding catalysts particles. The history of catalyst evolution is also traced to find out the influential factors. Relying on the in-depth understanding of the intrinsic symmetry and corresponding geometry feature of the metal catalyst, a universal facet-selective-catalytic CVD growth method is developed for controllable growth, which creates nanostructures with desired morphology. Well controlled 2-, 3-, 6-, and 8-branched carbon nanostructures are synthesized, where Cu nanocrystal works as the node and carbon nanofibers grow selectively on certain crystalline facets.

At the end, physical and chemical properties of synthesized nanostructures are evaluated for potential applications.

1. Introduction

The unique morphologies as well as novel properties of one-dimensional (1D) carbon nanostructures (CNs) attracted many attentions over recent years. Their atomic architecture does not only give rise to their outstanding potential in structure reinforce¹⁻⁴, electronic transport^{5, 6}, thermal conduct^{7, 8}, fluorescence^{9, 10}, field emission^{11, 12}, energy storage^{13, 14}, etc., but also makes them the ideal candidates for synthesizing 1D or 2D nanostructures using template approaches^{15, 16}. The interests in CNs initially were focused on carbon nanofibers (CNFs)¹⁷ and carbon nanotubes (CNTs)¹⁸ but nowadays extends to other structures such as nanocones¹⁹, nanobelts²⁰, nanocoils²¹, nanohelices²², etc. Typically these structures are synthesized by catalytic chemical vapor deposition (CVD) techniques, which employ transition metals (Fe, Co, Ni and their alloys) as catalysts. This strategy features the inherent advantage of a cost efficient large-scale production.

The boom of the CNs synthesizing research was naturally accompanied by dedicated efforts to study the corresponding growth mechanisms. Only a thorough understanding of these mechanisms enables an efficient process design, which, in turn, is required by nanotechnology-based industry to obtain structures in sufficient quality and/or quantity^{23, 24}. Growth mechanisms have been investigated with both theoretical^{25, 26} and experimental methods²⁷⁻²⁹; even in-situ transmission electron microscopy (TEM) observations were employed to achieve direct access to the growth process³⁰. The commonly accepted growth mechanism assumes carbon dissolves, diffuses in the catalyst and CNs grow due to the precipitation of excess carbon on the metal surface of the catalyst particle. This idea is based on the vapor-liquid-solid (VLS) mechanism suggested by Wagner et al., who proposed it in order to explain the growth of single crystal Si wire^{31, 32}. In particular, it is currently used to interpret the catalytic growth of 1D carbon nanostructures in CVD based processes. However, numerous dedicated studies revealed various inconsistencies concerning details of this model. Among those inconsistencies are issues such as: (i) does a catalyst particle really feature its liquid state during the growth process³³; (ii) which is the dominating diffusion route, within or from the surface of catalyst^{30, 34}; (iii) what is the role of any potential metal carbide forming and what is the real driving force for the diffusion^{35, 36}. However, despite any doubts concerning some of details of the model, one crucial prerequisite was seldom challenged, namely the growth is initiated by carbon containing gas being dissociated on a catalysts surface, and subsequently controlled by a carbon atoms dissolving-precipitation process, until

conflicting experimental evidence was observed in a low-temperature CVD growth based on Cu-C₂H₂ reaction³⁷⁻³⁹.

In the aforementioned 250°C process, new types of polymer-like nanostructures with a remarkable amount of hydrogen atoms were synthesized utilizing catalytic Cu nanoparticles and C₂H₂ source gas³⁸. Among those growth products, multiform polymer nanostructures (PNs) were observed^{37, 40, 41}. Nevertheless, it is not possible to apply the VLS mechanism to the growth of these structures as neither carbon nor hydrocarbon molecule can dissolve / diffuse in copper⁴². On the contrary, strong experimental evidence that indicates their growth is based on a surface diffusion process exists. The latter is based on the concept of the formation and subsequent diffusion of hydrocarbon oligomers on the surface of the catalyst particles instead of any direct solution and transportation of carbon atoms. However, the surface diffusion based growths model certainly requires dedicated refinement.

On the other hand, the fact that the PNs were synthesized at a much lower temperature comparing with a typical VLS process (temperature $\geq 600^\circ\text{C}$) is intriguing as there is no immediate reason why the new growths mode should not be applicable to other transition metals such as Fe, Co, Ni. In all of these systems surface diffusion is a feasible and likely path at low process temperatures because even for Fe, Co, Ni catalyst the carbon solubility and diffusion coefficient decreases significantly with decreasing temperature⁴³⁻⁴⁵. Fortunately, research concerning the interaction of acetylene with low-index metal single-crystal surfaces under ultra-high vacuum (UHV) condition has been an extraordinarily active field for a long time. In that field, various hydrocarbon molecules have been identified⁴⁶, which represent potentially crucial intermediates for the synthesis of PNs at low temperature. Additionally, the surface reactions being responsible for the formation of such hydrocarbon molecules may also play an important role, which can be a counterpart step of the dissociation of carbon containing gas during the VLS process.

Based on the considerations presented above, in present thesis, systematic investigations initiate from the most typical case of the low temperature catalytic CVD growth: the Cu-C₂H₂ reaction system. The behavior in growth process is interpreted in terms of both thermodynamics and kinetics to clarify elementary issues in the growth, such as fundamental surface reaction, diffusion route and driving force, rate-determining-step (RDS), etc. Based on these works a basic growth model can be proposed. Then the investigation extends to other commonly used transition metals. Fe and Ni catalysts with different appearance are used in the growth. Positive growth result reveals the extensive adaptability of proposed model.

Meanwhile, by comparing with the Cu catalyzed process, common features are extracted for establishing a general mechanism. In addition, in the investigations, correlation between the microstructures of the resultant novel nanostructures and the geometry (shape, size and surface index) of the responsible catalysts is studied in detail. The history of catalyst evolution is also traced to find out influential factors. In-depth understanding of the geometry characteristic of catalyst pioneers the approach to controllable growth, which creates nanostructures with desired morphology. At the end, physical and chemical properties of synthesized nanostructure are evaluated for potential applications.

2. Research background

2.1 One-dimensional (1D) Carbon nanostructures (CNs)

1D carbon nanostructures usually refer to the structures, which feature a large aspect ratio and small diameter (<100nm). The typical 1D CNs, carbon nanofibers (CNFs) entered people's consciousness initially as a harmful byproduct in metallic catalyst synthesis processes, and the early researches aimed to inhibit the formation of CNFs. An interesting turning occurred in 1991 due to a special CNF was discovered by Iijima⁴⁷, which is constructed by cylindrical graphitic sheets and named as carbon nanotube (CNT). People are attracted by distinct properties of the CNTs such as extremely high strength, aspect ratio, specific surface area, as well as unique optical and electrical properties⁴⁸⁻⁵⁰. Since then many researchers worldwide have focused their work on exploring new techniques for synthesizing CNTs, because of their extensive application potential.

Three main preparation techniques have been developed namely catalytic CVD, arc-discharge^{51, 52}, and laser-ablation techniques^{53, 54}. Among them the catalytic CVD strategy has the distinct advantages in its large-scale production ability of the CNTs at relative low temperatures and a low cost hence is most popular. In a catalytic CVD growth process, the small sized metal catalyst particles are heated up in a reaction chamber, then carbon containing source gas is introduced in, a series of chemical and physical processes lead to carbon deposition on catalyst particle and finally construction of CNTs.

In the research of catalytic CVD growth, a lot of other types of carbon nanostructures besides cylindrical CNTs were also synthesized. In term of morphology, they can be sorted to straight nanofiber⁵⁵, nanohelix²², nanocoil⁵⁶, nanocone¹⁹, nanobelt²⁰, etc. According to structural characteristic (the size and orientation of graphitic sheets constructing the CNs), they feature tubular^{57, 58}, herringbone-like⁵⁹⁻⁶¹, bamboo-like⁶²⁻⁶⁵ and amorphous nature⁶⁶. The morphology, microstructure and property of CNs prepared in CVD process are determined by both the catalysts preparation and subsequent growth. In this context, it has been found that transition metals, such as Fe, Co, Ni and their alloys are the effective catalysts for the growth of CNs, and the transition metals with different compositions and morphologies can lead to CNs with different morphologies. As a result, preparation of effective catalysts has become a significant step for synthesis of CNs. According to the vast literatures, different methods, including sol-gel method^{67, 68}, co-reduction of precursors^{69, 70}, impregnation and incubation^{71, 72}, ion-exchange-precipitation⁷³, reverse micelle method⁷⁴, thermal decomposition of carbonyl complexes^{75, 76}, and metal organic chemical vapor deposition (MOCVD)⁷², have been

employed to prepare the catalysts. For the growth process, different gases, including CH₄, CO, C₂H₂, C₂H₄, benzene were used as carbon source. The effects of flow rate, temperature, and additional ingredient such as oxygen and sulfur in reaction atmosphere have been investigated. Special configuration of the synthesis equipment was also explored. By using microwave assisted chemical vapor deposition (MWCVD) technique, iron catalysts were used to catalytically synthesize the carbon nanocone¹⁹, carbon nanohelix⁴⁰, carbon nanotip^{77, 78}, and Carbon nanobelt⁷⁹. Aligned CNs arrays were often synthesized in electric field induced by bias in system^{80, 81}. Nowadays, the research of CNs is keeping in development towards more precise morphology control and extensive applications.

To date, the upsurge of the research about CNF, CNT and other CNs has lasted for two decades. During this period the investigations were not only focused on the synthesis methods and applications, attention was also devoted to the essence of the CVD growth. In the commonly accepted growth mechanism, carbon dissolves into the catalyst and CNs grow due to the precipitation of excess carbon on the metal surface of the catalyst particle. This idea originates from the vapor-liquid-solid (VLS) mechanism suggested by Wagner et al. to explain the growth of single crystal Si wire^{31, 32}. In particular, it is now usually used to interpret the catalytic CVD growth of one-dimensional carbon nanostructures. The basic concept is as follows: (i) adsorption and dissociation of hydrocarbon gas on the surface of the catalyst, (ii) diffusion of carbon atoms through the catalyst, and (iii) precipitation of carbon from saturated catalyst particles to form 1D carbon nanostructures, see Figure 2.1(a). In this model, the catalyst forms a liquid droplet and preferentially adsorbs the growth species from the surrounding vapor, and the solid carbon wire grows from this supersaturated eutectic liquid.

In the VLS model, catalyst particle is the core of whole reaction system because all the important processes progress on or within the catalyst. Any change of the catalyst will be finally reflected on the grown nanostructure. The size of the catalytic nanoparticle is treated as the determining factor for the diameter of the CNs grown on it; whilst the crystalline orientation plays a critical role in the determination of CNTs chirality^{26, 82}. As for the preparation methods of the catalyst nanoparticles, they influence the catalysts' size and their dispersion on the support surface and thereby their catalytic properties^{83, 84}. The interactions between metal and support surface were found to determine the growth mode^{27, 57, 85}, where weak interactions yield tip-growth whereas strong interactions lead to base-growth. Moreover, distinct activity for hydrocarbon molecule dissociation or carbon atom extrusion on different catalyst surfaces^{86, 87} is believed to be responsible for symmetrical-growth, see Figure 2.1(b).

These experimental facts suggest the geometry feature of catalyst plays important role in the growth. However, in previous researches the geometry shape of catalyst particle did not attract enough attention because this concept is beyond the basic framework of VLS mechanism, certain shaped catalyst particle is not necessary in the VLS process.

On the other hand, according to the VLS mechanism, we understand the peculiar ability of transition metals (Fe, Co and Ni) to catalyze CNs' formation is greatly linked to their catalytic activity in the decomposition of hydrocarbon and their allowance of extremely rapid carbon atomic diffusion (both through and over their surfaces). This ability depends strongly on temperature, because at a lower temperature the catalytic reactions on metal surface are quite different, and the carbon solubility and diffusion coefficient decrease significantly. Therefore, in practical most of the CVD growth processes were carried out at a temperature higher than 600°C. However, the attempt to synthesize nanostructures through CVD growth at a low temperature should not be given up. On the contrary, it's a valuable topic because lower synthesis temperature is of great importance for industrial production. It remarkably simplifies the equipment and reduces the costs.

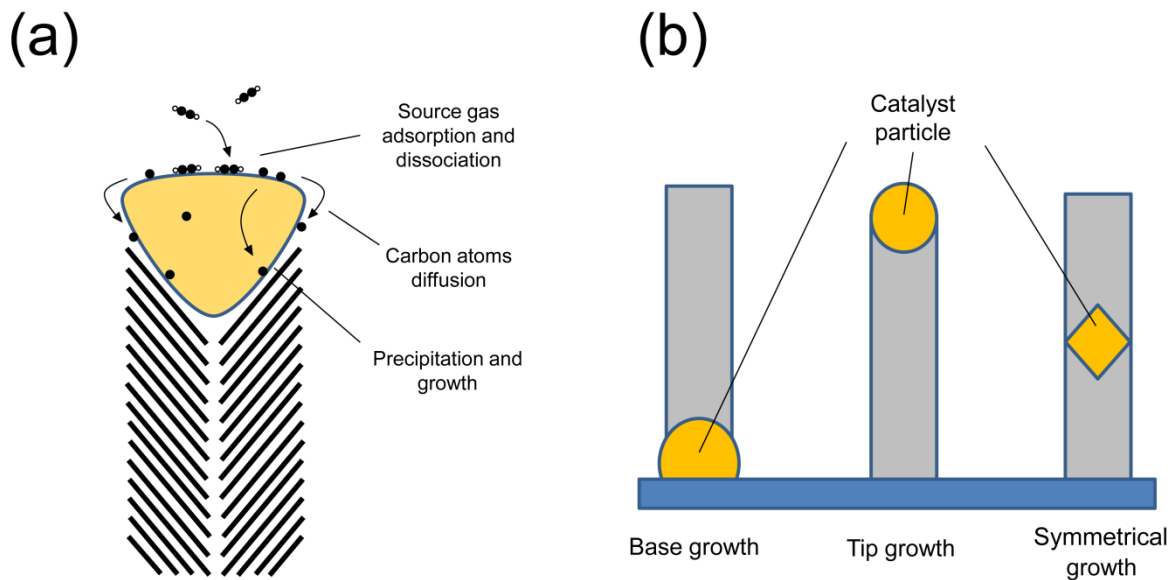


Figure 2.1. Sketch of the nanofiber growth: (a) VLS mechanism (b) three different growth modes.

2.2 Polymer-like nanostructures (PNs) prepared at low temperature

In fact the low-temperature-CVD-growth of nanostructure has already been achieved and it was found the geometry shape of catalyst particle is a key factor in the process. As an

example, recently a new type of novel 1D nanostructures were synthesized at a low temperature of 468 K by using copper nanocrystals as catalysts and acetylene as gas source under atmospheric pressure³⁸. The synthesized nanostructures contain large amount of hydrogen and show polymer nature. A subsequent heat-treatment carbonizes the hydrocarbon polymer nanofibers into carbon nanofibers without changing the original morphology. Typically the synthesized nanostructures have highly symmetric straight or helical morphologies: in a straight nanofiber two branches stretch from opposite sides of catalyst particle; and the helical nanofibers are regularly coiled in the form of a single-helix and exhibit a mirror symmetric growth mode featuring two twin helices. The two nanocoils have identical coil diameter, coil pitch, fiber diameter and cross section. However, their helical senses or coiling directions are absolutely opposite, as shown in Figure 2.2.

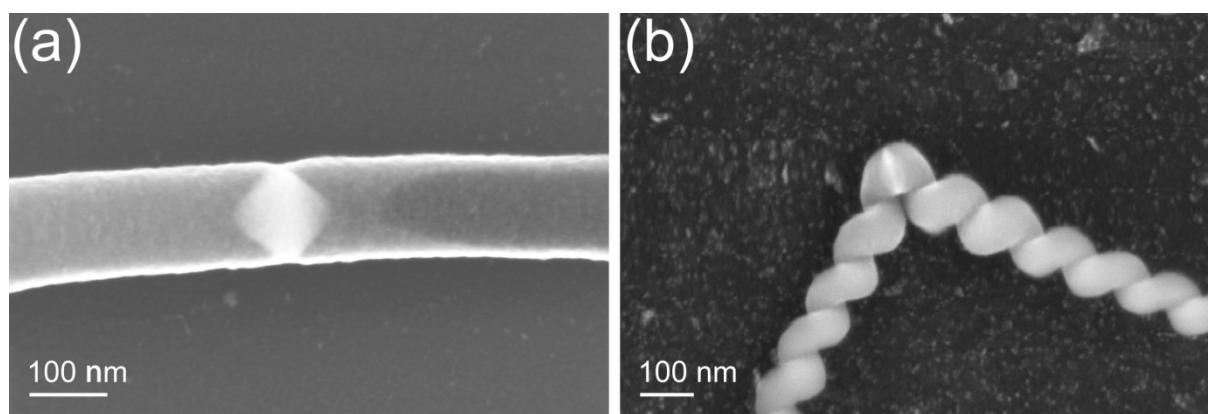


Figure 2.2. Nanostructures synthesized at a low temperature of 468 K: (a) straight nanofiber. (b) nanohelix.

Unfortunately, conventional VLS mechanism cannot be used to interpret and explain the growth of hydrocarbon polymer nanofibers on copper nanocrystals, because neither carbon nor oligomers (responsible for hydrocarbon polymers growth) can dissolve (diffuse) in copper⁴². Qin et al. suggest the growth is based on surface reactions such as C_2H_2 coupling and oligomers formation on low index Cu surface³⁸. Careful literature survey in this context shows that certain surface diffusion mechanisms based on carbon diffusion on catalyst surfaces have been proposed for CVD growth of one-dimensional carbon nanostructures⁸⁸⁻⁹⁴, especially for low temperature growth as in plasma-enhanced CVD, which is a low energy path for the growth of carbon nanotubes⁹⁵. For some special CVD process where unusual carbon source such as C_6Cl_6 is used for the low temperature synthesis, the core process is also supposed to progress on the surface of catalyst⁹⁶. However, till date, effort has been seldom made on exploring the mechanism via which hydrocarbon building blocks diffuse on the

surface of copper catalysts. Therefore, a thorough exploration and explanation of the growth of polymer nanofibers on copper catalysts via the surface diffusion mechanism is needed.

For this purpose the geometry feature of Cu catalyst particle must be taken into consideration, because it is directly correlative to the exposing surface. Interestingly, the copper particles are always faceted with regular shapes after fiber growth, the majority of which have a rhombic projection. Detailed investigations indicate that they undergo a shape change from an irregular to a regular faceted form during nanofiber growth, and that their shapes have considerable effects on the final fiber cross-sections. Based on systemic TEM observations as well as accompanying selected area electron diffraction (SAED) index work by Xia et al., the Cu catalyst particles in as-grown nanostructures can be sorted to three kinds of basic highly symmetric polyhedrons, namely octahedron, triangular prism and tetrahedron. They are all encompassed by low index faces and the grown nanofiber always attaches on $\{111\}$ faces, see Figure 2.3⁹⁷. It indicates the surface reaction occurring on certain indexed Cu catalyst surface, especially $\{111\}$ face, plays important role in the growth. Further high resolution TEM (HRTEM) investigation observed discontinue sheet-like growth product stacking in a partially ordered way, and the sheets almost parallel to the low index surface of catalyst, see Figure 2.4⁹⁷. Such a structural characteristic is distinct from the conventional carbon nanofiber, which is constructed by large graphitic sheets or amorphous carbon.

Meanwhile, the interaction of hydrocarbon such as acetylene with low-index metal single-crystal surfaces under UHV conditions has been investigated for a long time. These efforts can very well contribute to a fundamental understanding of important catalytic surface processes, unravel fundamental mechanisms in heterogeneous catalysis, and identify important surface intermediates in practical reactions. The adsorption and surface reactions of acetylene on copper low-index surfaces ($\{110\}$, $\{001\}$, and $\{111\}$) under UHV conditions have been widely investigated by both theoretical and experimental methods^{30, 98-101}. It is worth to notice that acetylene coupling reactions (in which cyclobutadiene (C_4H_4), benzene (C_6H_6) and cyclooctatetraene (C_8H_8) are formed) easily occur on copper low-index surfaces and no coverage threshold is observed for the onset of the coupling reactions on $\{110\}$, $\{001\}$, and $\{111\}$ Cu surfaces, which implies high adsorbate mobility. Another aspect that should be taken into consideration is the fact that a graphene sheet matches a copper $\{111\}$ facet very well (both are in D_{6h} symmetry and the mismatch of lattice parameter is about 2%), which can dramatically increase the interactions between a copper $\{111\}$ facet and a graphene sheet as well as its derivatives.

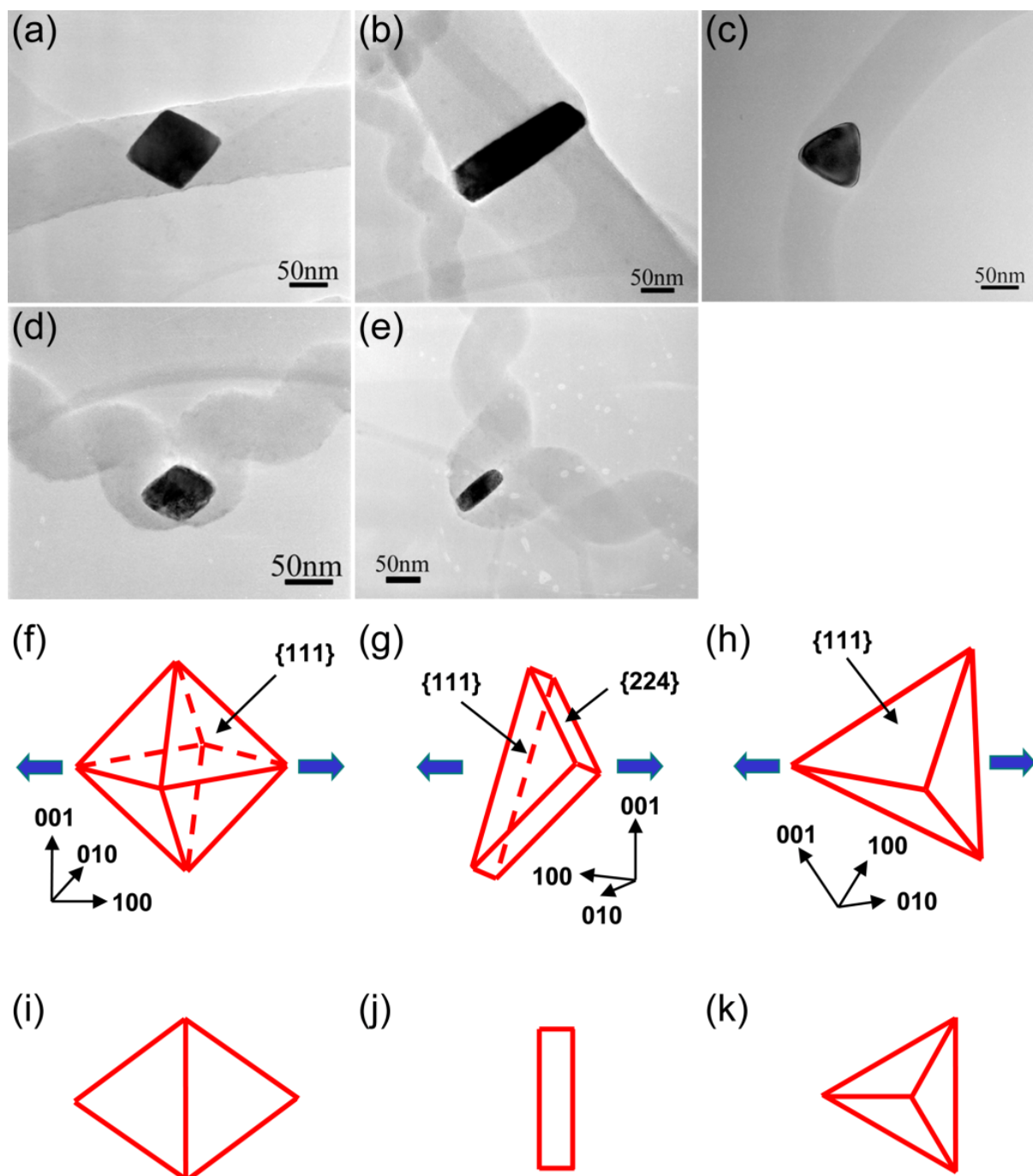


Figure 2.3. (a-e) TEM images of different morphologies of nanostructures obtained along Cu $\langle 110 \rangle$ zone axis. (f-h) Three kinds of catalyst polyhedrons: octahedron, triangular prism and tetrahedron, respectively. (i-k) The respective projections of the polyhedrons (f-h) obtained along Cu $\langle 110 \rangle$ zone axis.

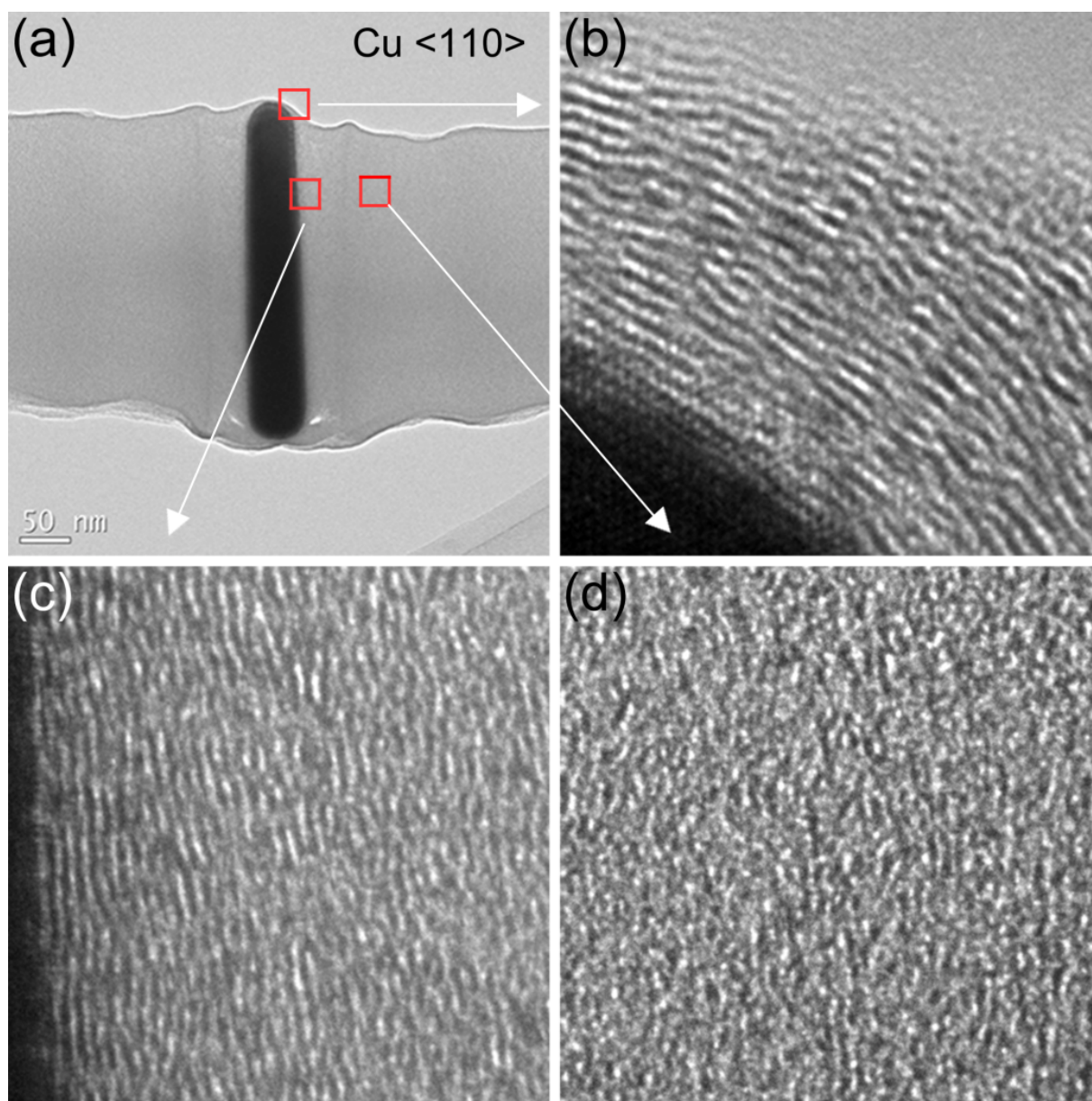


Figure 2.4. HRTEM images for a two-branched CNF with triangular prism catalyst after heat treatment. (a) TEM image on Cu $\langle 110 \rangle$ zone axis. The fiber is grown on the catalyst along Cu $\langle 111 \rangle$ direction. (b), (c) and (d) HRTEM images of the domains indicated with three red squares in (a). Partially ordered periodic fringes of $\sim 4.00 \text{ \AA}$ are shown in (b) and (c), but the structure in (d) shows nearly an amorphous structure.

In summary, the previous researches about the Cu catalyzed nanostructure growth under low temperature condition exhibited crucial features, which is inconsistent with the conventional VLS mechanism. It was also suggested the low temperature growth tightly links to the geometry shape of catalyst particle, which is often ignored in VLS process. An alternative model however is still missing. The patches obtained from previous researches are not sufficient to derive a convictive new model, because some fundamental issues, for example, the role of different indexed crystalline face of the catalyst, the detailed route and

driving force for diffusion, the rate-determining-step, etc. are still unclear. These issues will be clarified in this thesis.

2.3 Goals of this thesis

Main goal of the thesis is to derive a simple growth scheme for the carbon nanostructures that the conventional VLS mechanism cannot explain. The novel scheme should be able to explain phenomena encountered in synthesis of carbon nanostructures (e.g. carbon nanocoils and other special CNFs) by coupling acetylene on the surfaces of copper nanoparticles at relative low temperatures, but will not necessarily be limited to this materials system.

By preparing systematic experiments, a number of valuable information can be gathered while progressing on the path to the main goal. Among those intermediate goals are:

- Information about the reaction rates on various catalysts and reaction environment.
- Revealing the rate-determining step for growth of amorphous carbon nanofibers by evaluating individual steps involved in the growth process.
- Tracing the nucleation/evolution of the catalyst particle, from original irregular precursor to final regular nanocrystal.
- Deducing a trend in the reactivity of nanostructures growth with respect to size of catalyst.

Based on the understanding of the growth scheme as well as evolution of catalyst, novel nanostructures with various morphologies can be designed and realized by controllable growth.

Finally, in order to investigate the application potential, the physical and chemical properties, such as optical, electrochemical features of the synthesized carbon nanofibers will be investigated.

3. Experimental methods

A general surface diffusion mechanism fitting the low-temperature-growth of PNs must be put forward based on systematic and careful analysis of experimental facts. In this context, the first goal of this study is to investigate the relationships among morphologies, microstructures of as-prepared PNs and geometries of the corresponding catalysts. Accordingly, the as-prepared PNs as well as their corresponding catalysts namely Cu, Fe and Ni nanoparticles, should be characterized in detail. The influence of synthesis condition on final nanostructures also has to be taken into consideration. Therefore, the research tasks were performed in a strategy that firstly prepare catalysts with different composition, size and shape; then use such catalysts to synthesize a variety of novel PNs/CNs by thermal CVD technique under different reaction conditions; characterize the structures of the as-prepared PNs/CNs and their corresponding catalysts; finally study the growth mechanism of the PNs and trying to generalize the growth modes of different structures. It can be illustrated as a brief flowchart in Figure 3.1.

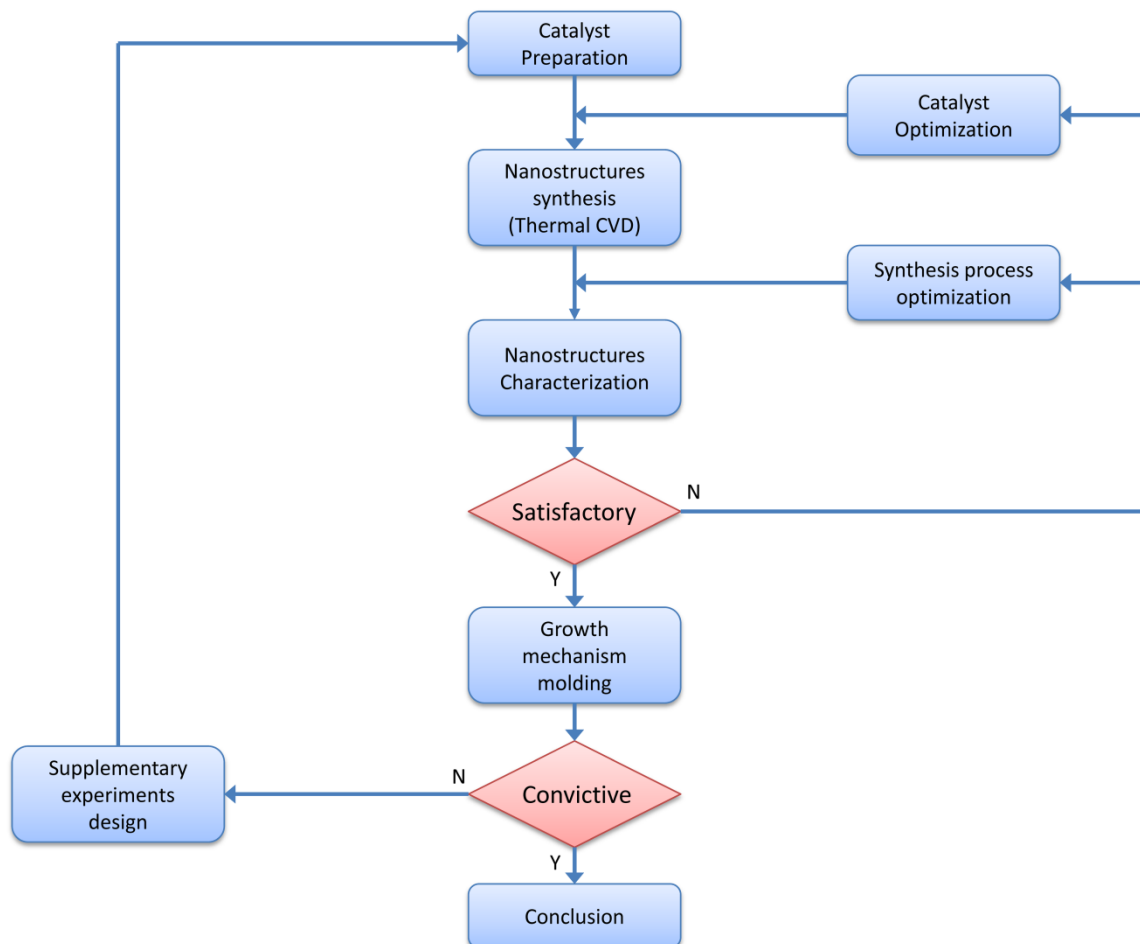


Figure 3.1. Flowchart of the research route.

3.1 Catalyst preparation

Since the dissociation, diffusion, and precipitation of carbon/hydrocarbon basic unit are supposed to take place on the surface of the metal catalyst, any features of the catalyst are of great importance. The relationship between the size of metal catalyst particles and their activity of catalyzing can only be deduced when initial catalysts with different features are available. This strategy also allows determining the critical size above or below which catalyst particles are not active for nanofiber growth any more. With this concern the metal catalysts were prepared in following routes.

3.1.1 Sol-gel route

A simple and very effective sol-gel method was utilized to prepare several kinds of uniform metal or metal oxide particles with a wide range in size. Firstly, metal containing sol (water/ethanol solution of metal nitrite, citric acid and polyethylene glycol (PEG)) was dip-coated onto the silicon wafer to form a thin film, which subsequently broke into separate islands in a drying process at 100°C, see Figure 3.2(a). In the following step, a 500°C calcination in air was employed to eliminate organic component in the gel, after that combining metal oxide nanoparticles generated and attached on Si wafer, featuring a network appearance (Figure 3.2(b)). Metal nanoparticles with better dispersion were prepared using an electron cyclotron resonance (ECR) or microwave plasma treatment to replace the calcination. In plasma environment the gel decomposed into individual metal nanoparticles (Figure 3.2(c)). The size, size distribution and shape of metal catalyst nanoparticles were controlled by the optimized experimental conditions, including concentration and viscosity of the sol, gas compositions, power and duration of plasma treatment.

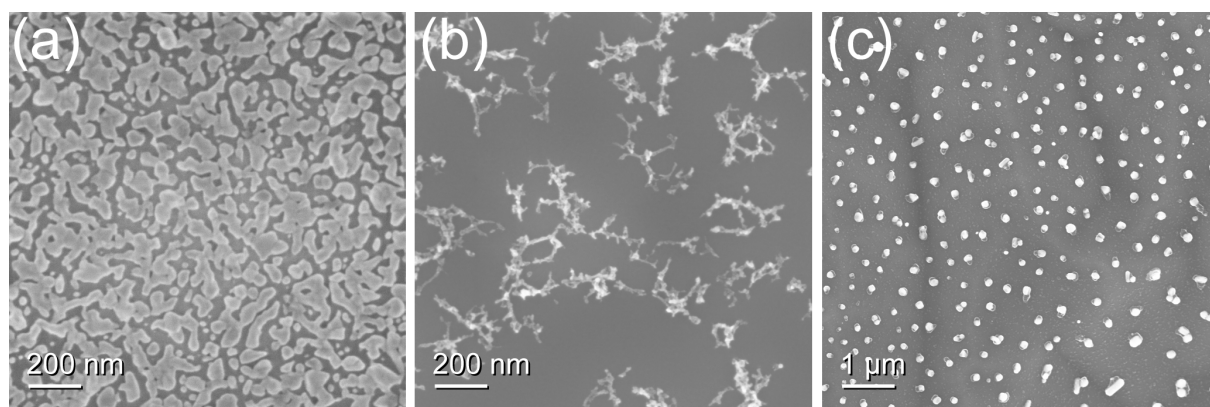


Figure 3.2. SEM images of metal catalyst prepared using sol-gel route: (a) islands of Cu gel on Si wafer (b) Ni network. (c) individual Cu nanoparticles.

3.1.2 Precipitation-decomposition route

Although the sol-gel method shows ideal controllability, the productivity is too low to support kinetic research in the following growth as well as application of as-grown nanostructures. Therefore a precipitation-decomposition method, which is suitable for large amount of metal catalyst production, was employed. Here nanoparticles were prepared as follows: 1) metal tartrate was formed in the co-precipitation reactions between corresponding metal nitrate and potassium sodium tartrate; 2) Metal or metal oxide catalyst nanoparticles were achieved via thermal decomposition of corresponding metal tartrates. In the case of metal oxide, it was reduced into metal during the growth stage, which was under acetylene atmosphere, and the latter one acted as the true catalyst. In this part, several parameters of co-precipitation reaction were tuned to control composition, size and shape of the catalyst nanoparticles; parameters such as the concentration of both metal nitrates and potassium sodium tartrate solutions, heating temperature during thermal decomposition were tuned.

3.1.3 Bulky metal route

As a compare with those catalysts which had nanoparticle appearance, metal (Cu, Ni, Fe) slugs and plates were also used as catalyst directly. To obtain adjustable catalytic activity, the surfaces of metals were pretreated to have different roughness. Relatively rough surfaces were prepared by polish using sandpapers from 500 to 4000 mesh, and adopting diamond and SiC slurry with the particle size of 3μ , 1μ and 40 nm respectively induced smoother one. At last, an electrolytic polish process to produce extremely smooth surface was applied, as shown in Figure 3.3. Aside from the roughness, effect of chemical state of surface on catalytic activity was also a concern in investigation, for this purpose the polish process was followed by a H_2 reduction treatment in some cases.

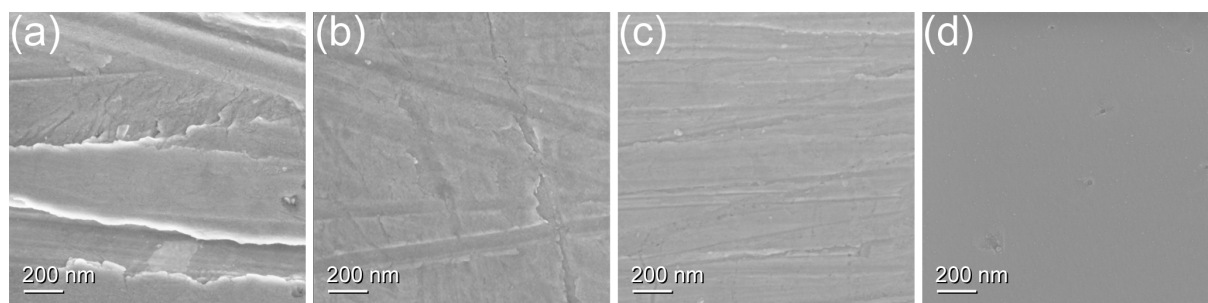


Figure 3.3. SEM images of Cu slugs polished using (a) 4000 mesh sandpaper, (b) 3μ Diamond slurry, (c) 1μ Diamond slurry, (d) electrolytic polish.

3.1.4 Other routes

Cooperating with other institutes, we prepared large amount of Fe, Ni nanopowder with spherical shape. With the assistance of the Institute of Metal Research (IMR), Chinese Academy of Sciences (CAS), Fe nanopowder catalyst was prepared using vacuum arc plasma jet evaporation method. The sketch of preparation device is shown in Figure 3.4(a). During the powder preparation, the working chamber was firstly evacuated and then filled by working gas. In the next step, direct-current-arc-discharge-plasma generating in working atmosphere heated, melted and evaporated the Fe target on the anode. Fe vapor cooled down rapidly during the spread. As a result Fe formed and subsequently deposited on the inner wall of the working chamber. SEM image of collected nanopowder is shown in Figure 3.4(b). The nanoparticles have approximately spherical shape with inequality size from 30 to 300 nm, most of the particles connect together to form chains of beads.

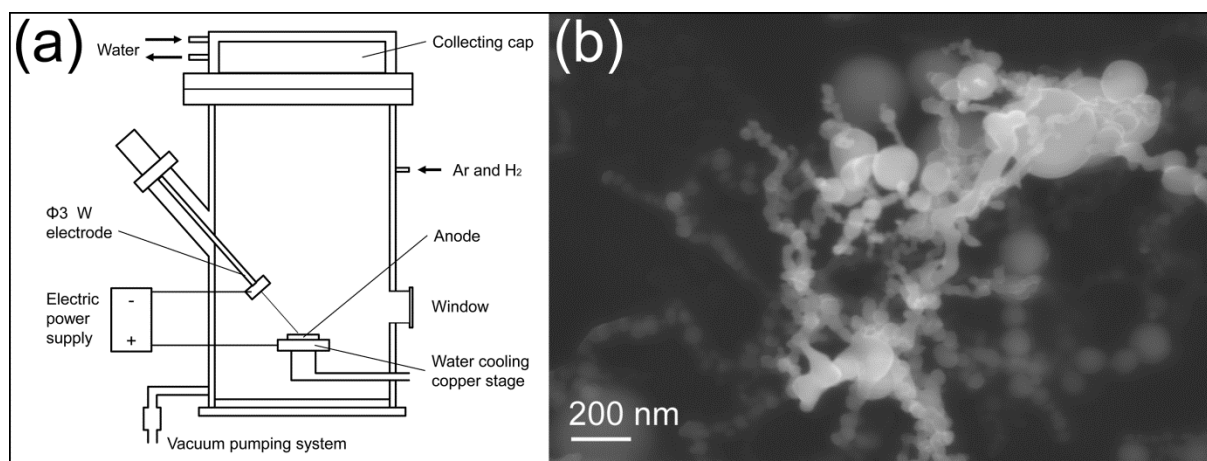


Figure 3.4. (a) Configuration of vacuum arc plasma jet evaporation equipment. (b) SEM image of the prepared Fe nanopowder.

Ni nanopowder provided by Al-Farabi Kazakh National University was prepared using electric-explosion-of-wires (EEW) technique¹⁰². The configuration of EEW device is shown in Figure 3.5(a). In an EEW nanopowder preparation process, capacitor bank 2 was charged by high voltage power source 1, and wire supply unit 3 fed Ni wire into explosion chamber 7. When the wire reached high voltage electrode 5, commutator 6 acted and the discharge of the capacitor bank produced a high-density current pulse (10^4 – 10^6 A/mm²), which passed through the Ni wire. The density of the energy in the wire may considerably exceed the binding energy¹⁰², inducing the wire explosion and generating small droplets of Ni. As a result, Ni nanopowder can be collected from the liquid filled explosion chamber. SEM image of as prepared Ni nanopowder is shown in Figure 3.5(b). The powders have spherical shape and a

size distribution between 10 to 100 nm. Very few particles have anomalous size as large as 1 μm .

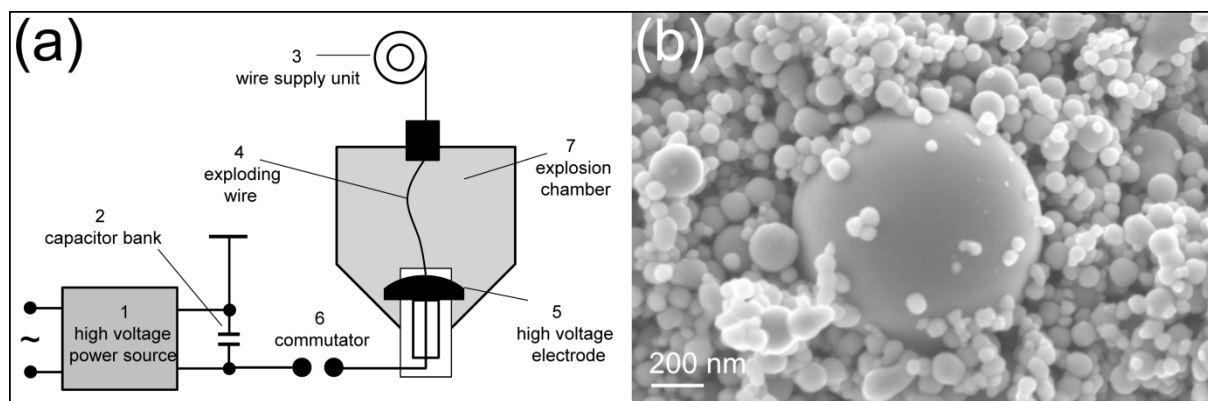


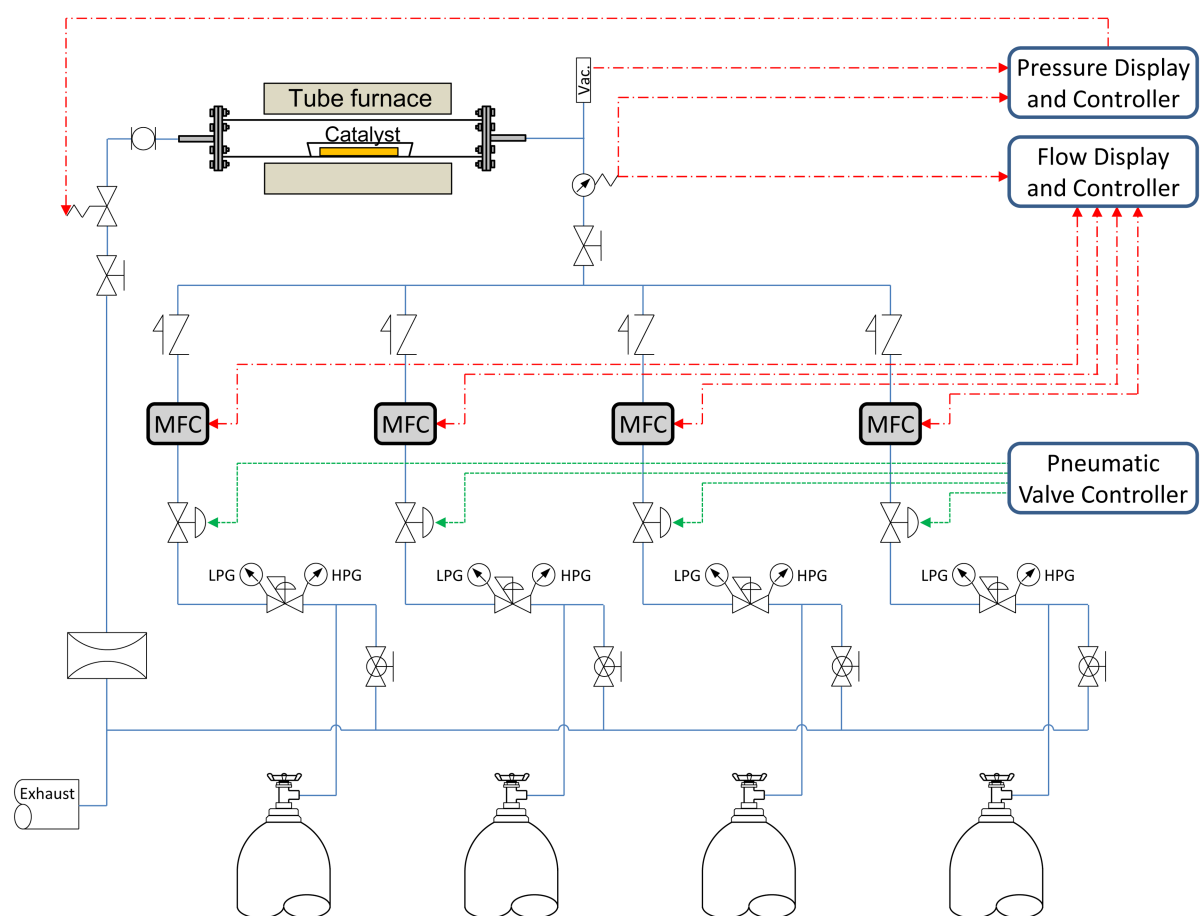
Figure 3.5. (a) Configuration of EEW equipment. (b) SEM image of the prepared Ni nanopowder.

3.2 Nanostructures synthesis

All the PNs syntheses were achieved in a Thermal CVD device. The configuration of the Thermal CVD system is shown in Figure 3.6. The core of this device is a tube oven equipping a quartz tube as reaction chamber, which connects to gas supplying system at the upstream end and to the pump at the downstream end. The four-channels gas supply system allows processes to progress in pure or mixture gas environments as well as in vacuum. During the reaction, a digital pressure gauge measured the gas pressure in the reaction chamber continuously and delivered the data to a computer. The acquired data was used to evaluate the reaction progressing.

In a standard synthesis process, in order to initiate the growth of the corresponding nanostructures the catalyst specimens were pre-set in the reaction chamber. After heating the samples to a given process temperature in vacuum below 0.1 mbar, the chamber was filled with pure C_2H_2 up to a set point pressure. Sequentially, the system was kept at set temperature for various process times allowing for the growth. Finally, the process chamber was quickly evacuated and cooled down to room temperature. The growth products were collected for the following characterizations after weighing.

Pre-treatment to metal catalyst, e.g. reduction in H_2 , and post heat-treatments to the synthesized PNs at different temperature were also carried out in the same device. In latter case the as-grown PNs in the reaction chamber were heated up to desired temperature rapidly in vacuum and kept for certain time. The pump at downstream end kept running in the whole process to exhaust the volatile substance releasing from PNs. The heat treatment converted the as-grown PNs into CNs in certain degree, depending on process temperature and time.



Illustration

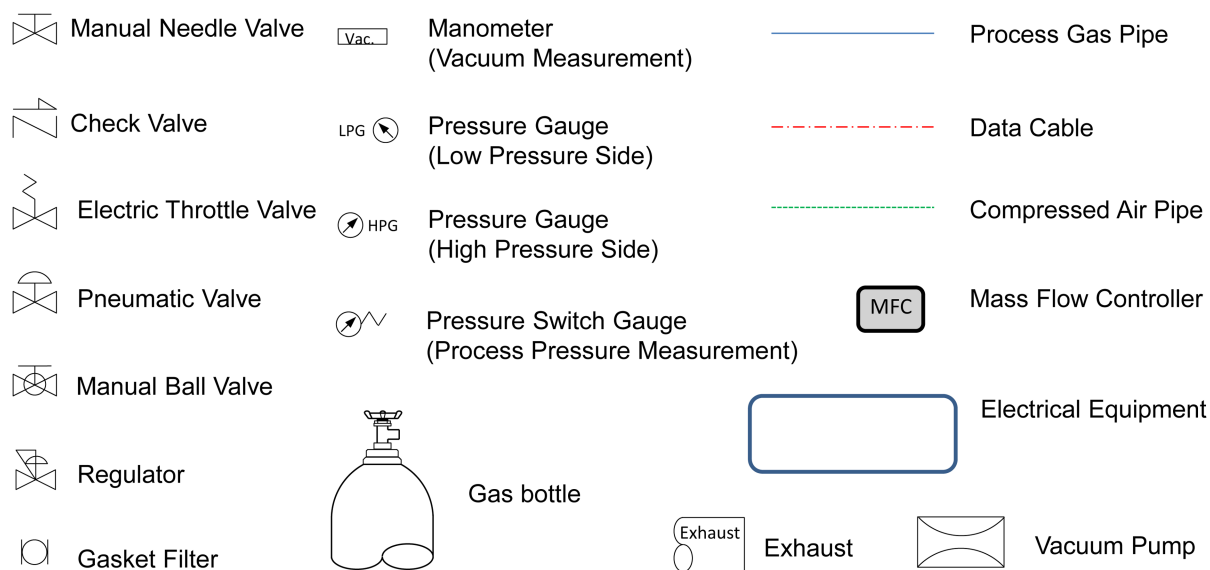


Figure 3.6. Configuration of the Thermal CVD system.

3.3 Characterization

General speaking, the features of growth process must be reflected in the reaction products. Therefore the obtained nanostructures and catalyst particle were characterized by various characterization methods for a better understanding of the growth mechanism.

3.3.1 Morphology characterization

For nanomaterials, morphology is the primary concern in investigation. Employing a powerful field emission scanning electron microscopy (FESEM) with a variety of operating modes, high-resolution image of as-grown nanostructures and corresponding catalyst were recorded. To investigate the relationship between as-grown nanostructures and catalyst, e.g. whether the catalyst particle is embedded in the tip or centre part of as-grown nanofiber, the sample was also dispersed in ethanol and then supported by carbon film covered copper grids to facilitate the observation in scanning transmission electron microscope (STEM), wherein high-atomic-number metal appeared as dark spots and polymer/carbon fiber was semitransparent. Accompanying the STEM measurement, images in in-lens mode, which was surface sensitive, were recorded synchronously to reveal both the inside and surface features of the nanostructure at the same position. Meanwhile, we noticed all the important processes of nanostructure growth occurred on the surface of catalyst, and a lot of valuable information can be obtained from the interface between nanostructure and catalyst particle. Practically, as-grown sample was cut by focused ion beam (FIB) to expose the cross section of the interface for following SEM observation.

Besides the SEM, the morphology of bulky metal catalyst namely slugs and plates were also measured by atomic force microscopy (AFM) before growth to evaluate the surface roughness quantitatively. For those surfaces which were too rough that beyond the ability of AFM, 3D measuring laser microscope was employed as a substitution.

3.3.2 Structure characterization

Since the nanostructure growth did not follow the classical VLS mechanism, hydrocarbon dissociation was not the dominating even necessary surface reaction. The as-grown sample consisted of extensive elements beyond carbon, i.e. hydrogen and oxygen. Elemental analysis provided basic information for structural analysis. It was performed based on combustion and chromatographic separation. A Euro EA-CHNS elemental analyzer was utilized to get carbon and hydrogen proportion; and a Leco TCH600 N/O/H Determinator was applied for oxygen content. Following the elemental analysis, fourier transform infrared spectroscopy (FTIR) and

X-ray photoelectron spectroscopy (XPS) spectra delivered important information about the bounding state between different elements. Then combining a result of electrospray ionization - mass spectrometry (ESI-MS) measurement, which reflected mass distribution of molecules constructing the nanostructures, we can speculate the molecular structure. Furthermore, valuable clues about reaction route were carried by low molecular weight intermediate products, which were generated during the growth and finally embedded into the as-grown nanostructures. By employing thermal desorption - gas chromatography/mass spectrometry (TD-GC/MS) technique we separated and then identified these intermediate products/fragments, subsequently bridging the fundamental surface reactions and finally growth products.

Besides above works, Raman spectroscopy was used to evaluate the nanostructures, especially after the post heat-treatment at high temperature, in respects of defect density, degree of order, and dimension of structural unit. Thermogravimetry - differential scanning calorimetry (TG-DSC) analysis was also carried out to observe the behavior of as-grown sample during thermal evolution.

Furthermore, during the growth the catalyst particle experienced a geometrical and crystalline transformation. X-ray diffraction (XRD) measurements performing on the catalyst both before and after growth are helpful for tracing that. After a surface diffusion growth metal catalyst particles always exhibit regular shape with low index faces exposing out. TEM plus SAED can index these outer surfaces of catalyst, which are of great importance for growth mechanism modeling, because catalytic activity of metal surface depends significantly on crystalline orientation, and it subsequently decides the result of surface reactions as well as growth. Using this strategy the orientation relationship between metal catalyst and carbon/polymer part in an as-grown nanostructure also can be confirmed. When further enlarge the image of interface between metal and carbon/polymer by HRTEM, the diffusion path, diffusion direction and some other features of the growth process can be presented clearly.

3.3.3 Property evaluation

For the potential applications, also as a supplement of morphology and structural characterizations to support the growth mechanism analysis, physical and chemical properties of prepared nanostructures were evaluated. Since the applications of nanostructures often rely on their high specific surface area, nitrogen adsorption-desorption isotherm analysis was carried out in present study to get fundamental data about specific surface area. Considering

the potential optical and photoelectric applications, optical absorbance of prepared nanostructures was measured at different wavelength by spectrophotometer.

In addition, carbon nanostructures are promising energy material for applications in Lithium-ion polymer batteries, supper capacitor and dye-sensitized solar cell. In present study after heat treatment the as-grown nanostructures were converted into carbon nanostructures, which have unique structure distinguishing from the traditional CNT and CNF hence their electrochemical performance was evaluated by voltammetry analysis.

4. Fundamental investigations of catalytic CVD growth of polymer nanostructure at low temperature

As the typical case of the low temperature nanostructure catalytic CVD growth, Cu catalyzed reaction excludes the possibility of VLS approach. Therefore it's most suitable for the fundamental modeling research. Here the investigation was initiated by the growth with Cu catalyst in C_2H_2 source atmosphere. Based on the model extracted from Cu/ C_2H_2 reaction system, the research can then be extended to other transition metal catalysts.

4.1 Structural characteristics and growth mechanism

A growth process always leaves traces in its product. Systematical characterization on as-grown sample is critical for mechanism modeling. So a growth and following characterizations were carried out as the description in chapter 3.1.2, 3.2 and 3.3.2. Copper (II) tartrate hydrate was used as catalyst precursor in the growth which progressed at 250°C for 1h. Various nanostructures can be observed in the as-grown sample, including straight nanofiber, nanocoil and nanohelix, see Figure 4.1(a). Despite the morphology, the catalyst particles which are embedded in nanostructures always feature regular shaped projections, see the bright spots in Figure 4.1(b) and (c). It indicates after growth the Cu catalyst particles have highly symmetrical shapes.

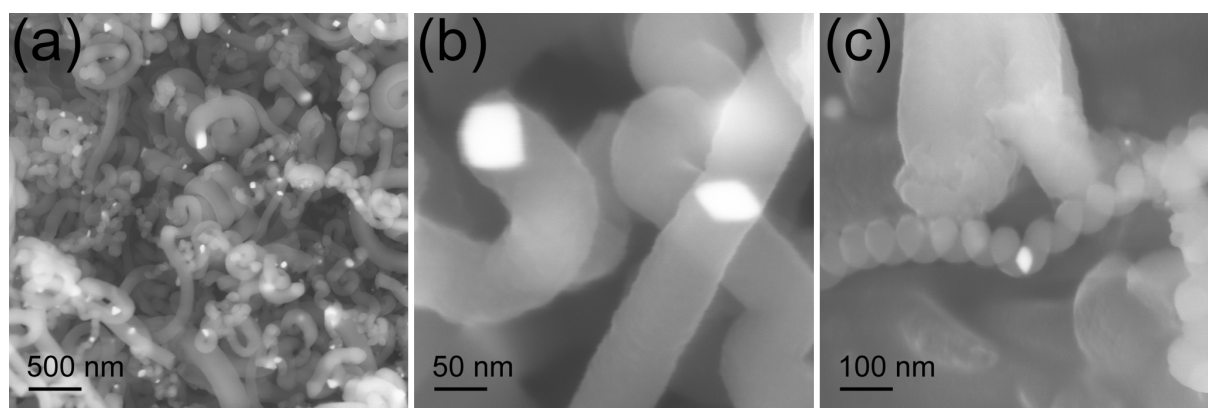


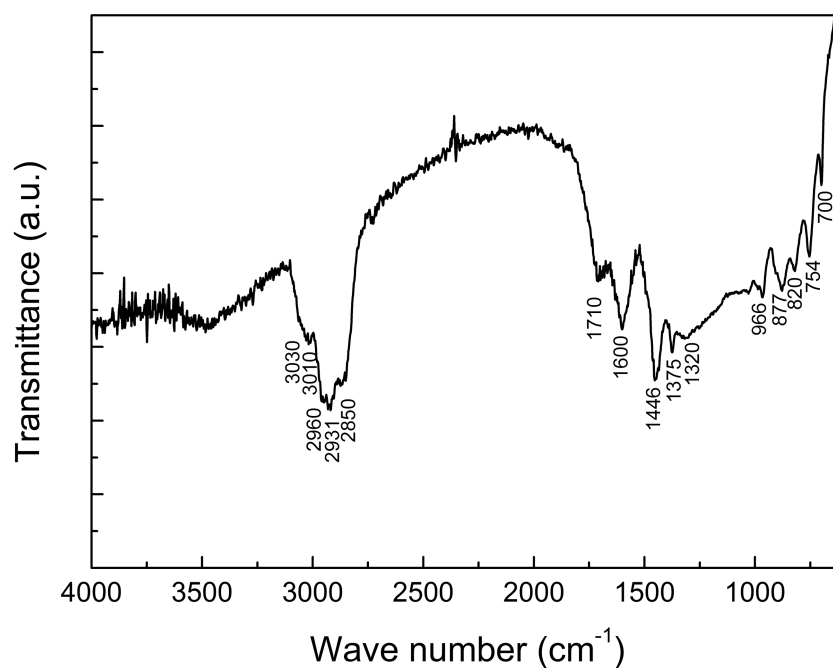
Figure 4.1. SEM images of (a) Nanostructures prepared via CVD growth process. (b) Straight nanofiber. (c) Nanohelix.

The as-grown nanostructures are brown powder. Elemental analysis (see chapter 3.3.2) reveals large amount hydrogen is contained in the as-grown samples, as shown in Table 4.1. Therefore the nanostructures have a polymer-like essence rather than pure carbon. Meanwhile, considerable amount of oxygen is also detected.

Table 4.1. The composition of as-grown nanostructures.

	C	H	O	Cu
wt. %	71.6	5.4	3.9	19.1
at. %	50.3	45.2	2.1	2.5

To get in-depth understanding of the molecular structure, IR spectroscopy analysis was carried out on the as-grown nanostructures. Figure 4.2 shows the IR spectrum. The peaks at 1375 cm^{-1} and 1446 cm^{-1} can be ascribed to the C–H deformation in $-\text{CH}_3$ and $-\text{CH}_2$. The peaks at 2850 cm^{-1} and 2960 cm^{-1} are assigned to the C–H stretch vibration in $-\text{CH}_3$ while the one at 2931 cm^{-1} is induced by the C–H stretch in $-\text{CH}_2$. The absorption peaks at 700 cm^{-1} , 754 cm^{-1} and 966 cm^{-1} are assigned to the wagging of disubstituted olefins ($-\text{RHC}=\text{CRH}-$)¹⁰³. The peaks at 3010 cm^{-1} and 3030 cm^{-1} are ascribed to C–H stretch in aromatic ring, and the stretch of unsaturated C=C induces the peak at 1600 cm^{-1} . No peak related to $\text{C}\equiv\text{C}$ can be seen. The IR spectrum also reveals the existence of oxygen in the growth product by showing the peak at 1710 cm^{-1} . The IR results further confirm the polymer-like nature of growth product. In particular, the simultaneously appearing strong peaks at 1600 cm^{-1} and 1446 cm^{-1} indicate the as-grown nanostructure is based on aromatic ring structure.

**Figure 4.2.** IR spectrum of the as-grown nanostructures.

TD-GC/MS measurement directly identified a series of planar benzene derivatives, such as diphenyl, phenanthrene, anthracene, benz(a)azulene, 9-Methylene-fluorene, etc. Some of them contain oxygen in molecule, e.g. (6-Hydroxymethyl-2,3-dimethylphenyl)methanol. They are believed to be the intermediate products or fragments of the nanostructure.

The role of oxygen in as-grown nanostructures is clarified by XPS measurement. It shows high intensity C 1s peak at 285.2 eV and O 1s peak at 533.0 eV (Figure 4.3(a)). These binding energies agree with the value of C-H/C-H-O polymer, but are different from the typical graphite or CNTs, which should have a C 1s peak at 284.6 eV. Cu 2p 3/2 peak at 941.9 eV indicates the existence of CuO (Figure 4.3(b)). However the XRD measurement only detected Cu peaks instead of CuO (Figure 4.3(c)). If we notice a fact that the XPS measurement delivers superficial composition but XRD spectrum corresponds to the lattice of whole catalyst particle, we can suppose the Cu catalyst is only oxidized superficially. The oxygen in as-grown sample is mainly bonding in the polymer-like growth product.

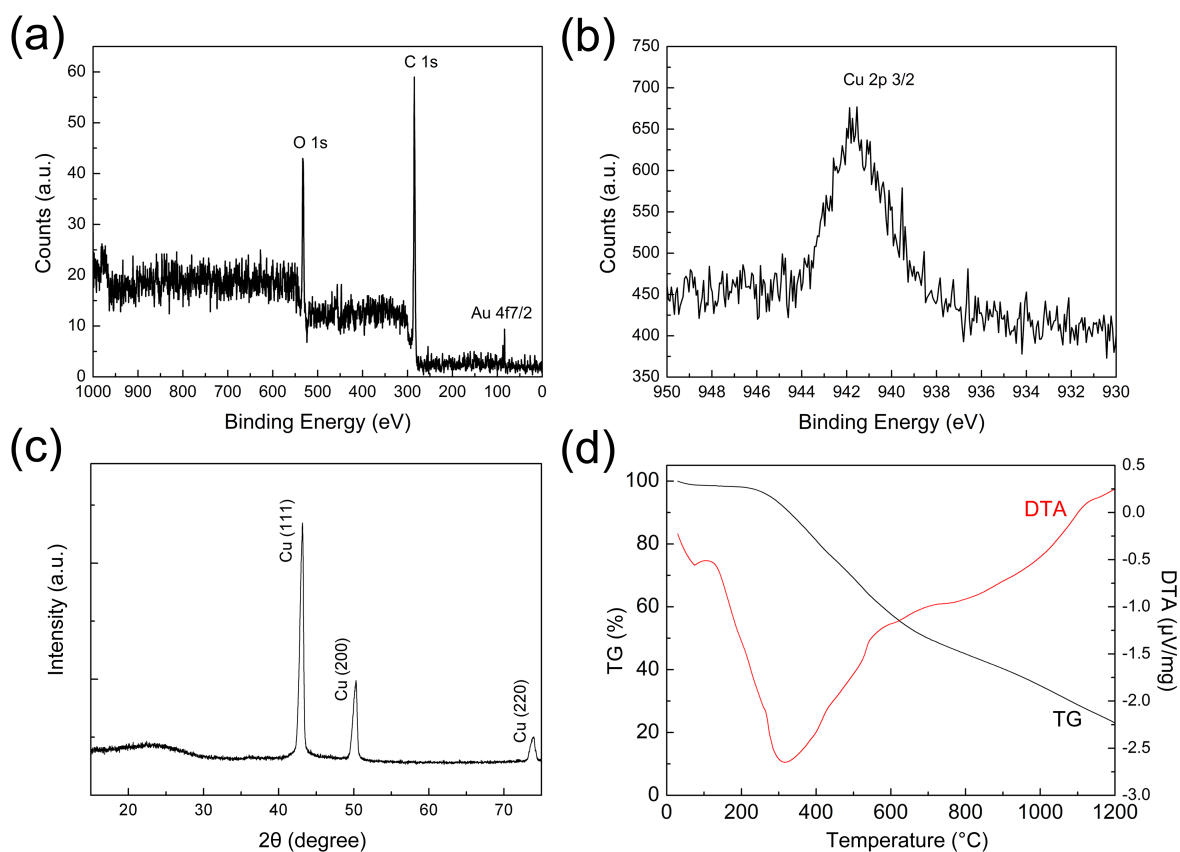


Figure 4.3. (a) XPS spectrum, survey; (b) XPS spectrum of Cu 2p region; (c) XRD spectrum; (d) TG-DTA analysis of the as-grown nanostructures.

The behavior of as-grown nanostructures at high temperature was evaluated via TG-DTA analyses. In Figure 4.3(d), an endothermic peak appears at 315 °C on the DTA curve, accompanying by the beginning of weight loss which is shown on TG curve. It indicates the

thermal decomposition of sample started at this temperature. When the sample was heated, it underwent a dehydrogenization as well as partial disassembly, which released a serial of hydrocarbon species depending on temperature. Such a carbonization process converted the polymer like nanostructure into carbon nanostructure. The Steady downward TG curve and the DTA curve which lacks peak in the broad temperature range (400-1200°C) reveal the mixture essence of the nanofiber, which consists of a serial of molecules with continuously changing mass. These molecules were confirmed by ESI-MS measurement, see Figure 4.4 (also shown in Figure 4.8(a)). The measured m/z values appear interesting periodicity. It suggests the molecules with different masses have essentially similar structure by means of assembling different number of basic structural units.

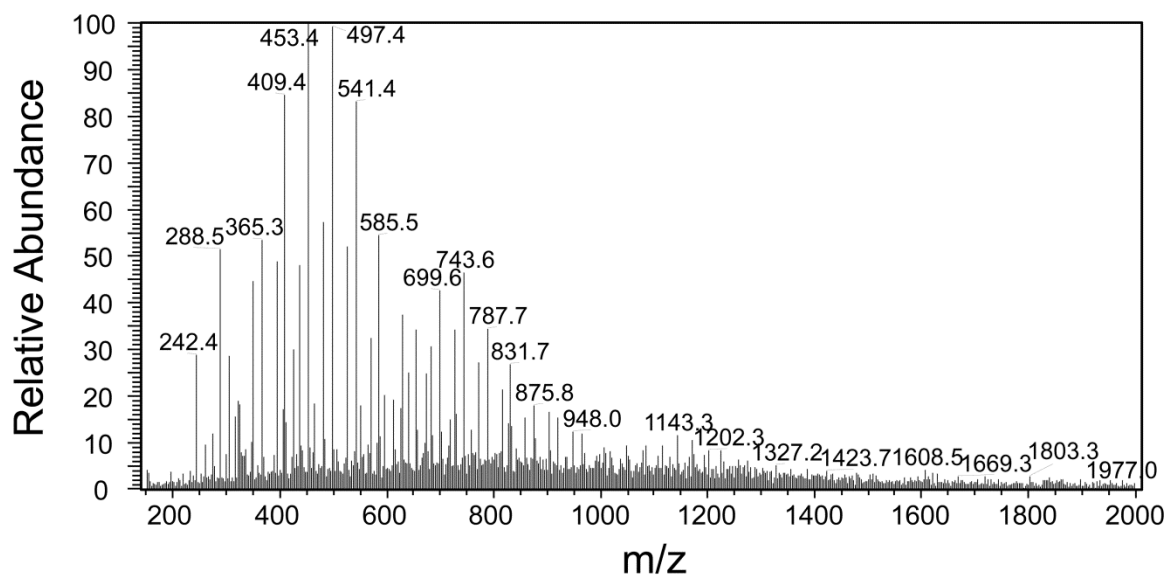


Figure 4.4. ESI-MS result of the as-grown nanostructures.

Referring the HRTEM image in Figure 2.4, it can be deduced that planner polymer sheets construct the nanostructures. Here the structural characterizations reveal the essential of the polymer sheets are a serial of molecules with broad mass distribution but similar molecular structure, which includes aromatic bone. In addition, since the Cu catalyst particle in as-grown nanostructures always appears highly symmetrical shape with low index faces, see TEM images in Figure 2.3, obviously the growth is based on surface process on Cu catalyst. Surface reactions, which produce polymer molecules and the role of certain indexed Cu faces are the crucial issues during the growth mechanism modeling.

Previous researches about the adsorption and surface reactions of acetylene on copper low-index facets under UHV conditions exposed the strong interaction between copper surface and acetylene molecular, as well as the polymerization tendency of the latter one. The

coupling of acetylene on copper surface has been demonstrated, which forms benzene (C_6H_6) on $\{001\}$ ¹⁰⁴, $\{110\}$ ¹⁰⁵, $\{111\}$ facets¹⁰⁶ and cyclooctatetraene (COT, C_8H_8) on $\{111\}$ facet¹⁰⁶. In these investigations, no coverage threshold for the onset of the cyclization reactions was observed on any copper facets, implying high adsorbate mobility¹⁰⁴⁻¹⁰⁶. It was also confirmed that the reaction pathway of copper catalytic reaction in atmospheric pressure of acetylene were in good agreement with the model under UHV conditions^{38, 106}. Thus a new mechanism based on the coupling of acetylene on copper surface and subsequent surface diffusion of oligomers and further products should be proposed.

Here, we describe a 3-step mechanism to interpret the polymer/carbon nanofibers growth process. At the pretreatment stage, copper oxide/copper particles derived from decomposition of copper (II) tartrate are reduced to metallic copper right after acetylene gas is introduced into reaction chamber. In a first step, at a growth temperature of 250 °C which is much lower than the melting point, copper particles remain in solid phase. They initiate from irregular shapes. Along with the reduction process of copper, the acetylene molecules adsorb on the copper surface and start to couple and polymerize each other as well as induce copper surface to reconstruct.

The interaction and reaction route of acetylene molecular with copper facets differ according to the index of facets. On $\{001\}$ and $\{110\}$ facets, the coupling reaction products, oligomers such as benzene and its derivatives, have high mobility; while on $\{111\}$ facet, in addition to benzene formation, small amount of COT forms and then it is immobilized at a temperature lower than approximately 300°C¹⁰⁶. Therefore, at a relatively low reaction temperature like 250°C, eventually the $\{111\}$ facet was blocked by COT and its derivatives because of the strong interaction between the copper surface and the compound. It leads to two consequences, a terminated coupling reaction and stabilized $\{111\}$ facets, respectively. The reaction activity of the blocked facets dramatically drops, so that the coupling reaction is terminated. As a result, a concentration gradient of movable oligomers and the further derivatives between $\{001\}$, $\{110\}$ facets and $\{111\}$ facets establishes since reaction products accumulated unceasingly on $\{001\}$ and $\{110\}$ facets whereas the surface reaction terminates on $\{111\}$ facets. In the second step, the concentration gradient drives the movable oligomers and derivatives to diffuse from $\{001\}$ and $\{110\}$ facets to $\{111\}$ facets through the surface of copper particles, thus excess oligomers and derivatives precipitate on $\{111\}$ facets to build up nanofibers in the third step. This process can be depicted as Figure 4.5.

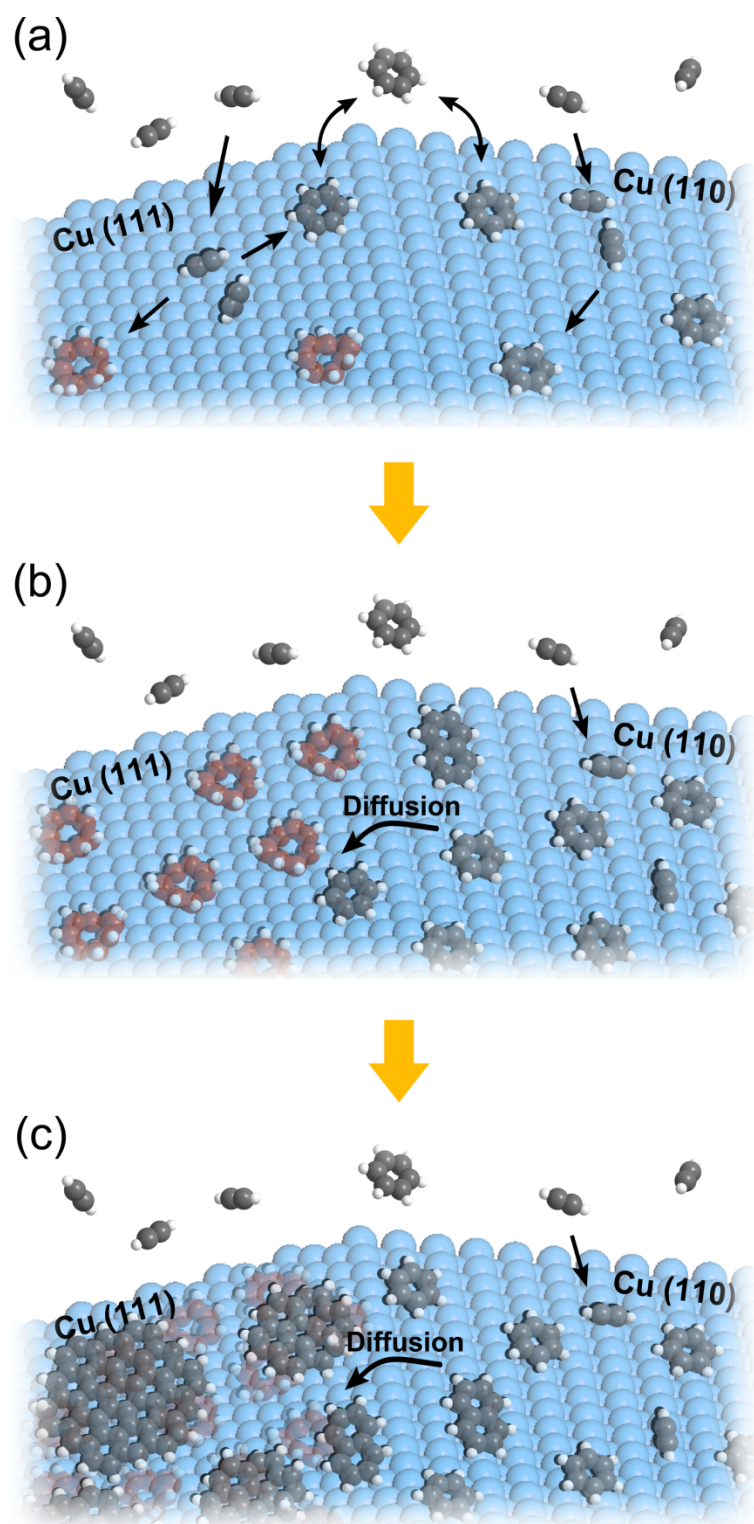


Figure 4.5. Sketch of the growth mechanism: (a) C_2H_2 adsorbs on Cu surface, coupling to form different oligomers, movable ones on (110) facet and immobilized ones on (111) facet. (b) The immobilized oligomers block the (111) facet, and the movable oligomers diffuse from (110) to (111) facet. (c) Movable oligomers and further derivatives creep to overlay those immobilized oligomers and form nano-sheets during the diffusion.

4.2 Kinetics process of the growth

In the above discussions, the growth was interpreted mainly with respect to thermodynamic issues. We have answered some of the fundamental questions related to the growth of nanofibers, such as how hydrocarbon molecules in gas phase convert to solid phase nanofibers, and what is the driving force as well as where is the route of the diffusion. However, for achieving a more complete understanding of the kinetics to support the proposed mechanism, a critical question must be answered: which step is the rate-determining step (RDS)? For example, in the VLS mechanism, the growth was summarized in three steps namely 1) carbon containing source gas decomposes on catalyst surface, 2) carbon atoms dissolve and diffuse in catalyst, and 3) carbon atoms precipitate and nanofibers form. It was supposed that depending on the reaction conditions such as catalyst composition, carbon source and growth temperature, the first or second step rate-limits the whole process^{91, 107-110}. Hereby, in the new proposed mechanism coincidentally three corresponding stages are included: 1) coupling of hydrocarbon molecules on catalyst surface, 2) oligomers diffuse through the catalyst surface, 3) oligomers further polymerize and nanofibers form. To answer which step is the rate-determining step), a serial of systematic kinetics research have been carried out.

During growth process, the source gas C_2H_2 keeps being consumed. If the reaction chamber is sealed to cut off C_2H_2 supplement, the chamber pressure drops naturally, and the pressure-drop-rate can act as a probe for evaluating the reaction rate, which means the growth rate at each moment. With this concern, a serial of experiments in sealed reaction chamber have been completed. The precursor containing 1g copper (II) tartrate hydrate was put into a quartz tube (5.4 liter), acting as the catalyst precursor. The quartz tube was carefully evacuated (<0.1 mbar) and then sealed. The system was subsequently heated up to the desired temperature of 250°C . First, catalyst precursor decomposed to form CuO nanoparticles and released gases which induced pressure increase in the sealed chamber. The pressure finally came to a stable level at the end of decomposition (in present system the pressure kept at ~ 70 mbar). Then C_2H_2 was introduced into the quartz tube to allow a growth. With different initial pressure (different amount of C_2H_2 was filled in the chamber for each process), the pressure dropping behavior in a serial of growth processes was recorded continuously.

The results are shown in Figure 4.6. Interestingly, it can be seen that when the growth process starts at a higher initial pressure of 900 mbar (blue line), the pressure-drop is slower than the one starting at a lower pressure of 500 mbar (black line). This experimental fact

strongly conflicts with any order reaction kinetics in which the reaction rate correlates the reactant concentration in system. An explanation is that the C_2H_2 is not involved in the rate-determine process hence irrelative to the growth rate. Then more factors in the system should be considered. Noticing the as-grown nanostructure contains 3.9 wt.% of oxygen, see Table 4.1. The presence of oxygen which comes from the decomposition of catalyst precursor (in forms of CO and H_2O) attract our attention. To prove the influence of oxygen-containing-molecules, a contrastive experiment was carried out by evacuating the reaction chamber to eliminate released gas during precursor decomposition. After the precursor decomposition, the reaction chamber was sealed again. Then the C_2H_2 was introduced in to the reaction chamber to start the growth process under very low concentration of oxygen-containing-molecules. As expected, the pressure drops extremely slowly, see the red line in Figure 4.6. The result showed that the presence of oxygen-containing-molecule in gas phase is indispensable to the reaction so as to the growth of nanostructure.

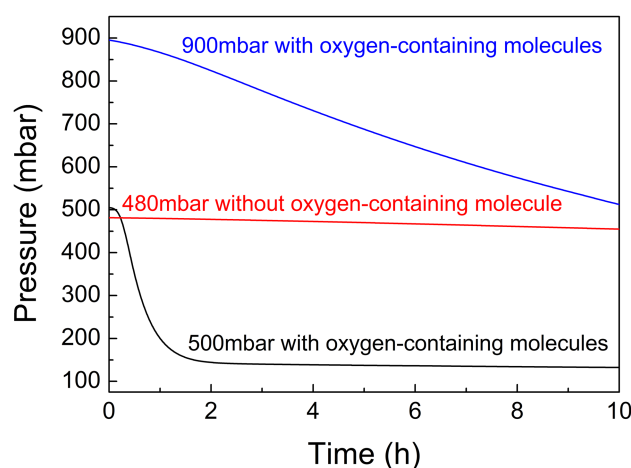


Figure 4.6. The pressure-drop during different growth processes.

Notably, the black curve in Figure 4.6 turns to be nearly flat after 2h reaction, which indicates the termination of growth (or an extremely slow growth). We suppose it is a result of reactant exhaustion. In present process only three possible reactants are involved, namely C_2H_2 , CO and H_2O . Here we investigate the whole growth process in integration but ignore the detailed reaction steps. Then based on the composition of as-grown nanofiber (Table 4.1), it can be deduced that the C_2H_2 and oxygen-containing-reactant were consumed nearly in a molar ratio of 12.5:1 for growth. According to this ratio, oxygen-containing-reactant would be excess in present process which started with a C_2H_2/O molar ratio of 6:1. However, it's unconvincing to own the termination of growth to C_2H_2 exhaustion, if we notice a fact that large amount of gas (~135 mbar) remained in system when growth terminated. A reasonable

assumption is that only partial of the oxygen-containing-molecule in gas phase is reactive hence C_2H_2 is actually excess, for example, only oxidative H_2O participates in the reaction while CO is inactive. Then the partial pressure of effective oxygen-containing-molecule in initial atmosphere is ~ 30 mbar. Accordingly ~ 375 mbar of C_2H_2 is consumed till the H_2O exhaustion. This calculation result agrees with the remnant gas pressure in system when growth terminated. Therefore the growth rate is actually associated to the oxygen-containing-molecule (H_2O in present case) in gas phase.

To further confirm the accelerative effect of H_2O on growth, we intentionally introduce H_2O into the reaction system. Firstly, the reaction chamber was evacuated to eliminate any released gas during precursor decomposition. After that the reaction chamber was sealed again. Then C_2H_2 plus 30 mbar H_2O (same amount as the H_2O released during the precursor decomposition) was introduced into the reaction chamber to start the growth. In this way CO was excluded from the process and the effect of H_2O can be investigated solely. It clearly shows the accelerative effect of H_2O on growth, see the blue line in Figure 4.7. With H_2O presence, the system-pressure-drop (growth) is much faster than the process without oxygen-containing-molecule in gas phase (red line). Interestingly, when H_2O was added into reaction atmosphere solely, the growth progressed faster than the case wherein H_2O and CO were introduced into the process together (black line). It proves our aforementioned assumption that H_2O instead of CO accelerates the growth.

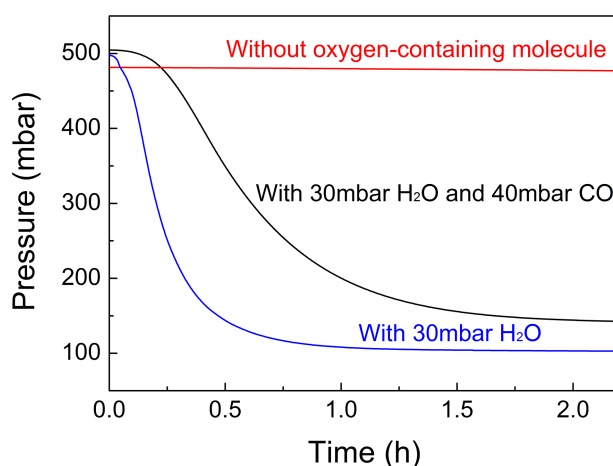


Figure 4.7. The pressure-drop in process with H_2O presence.

The H_2O not only accelerates growth, but also influences the microstructure of as-grown nanofibers. Figure 4.8 shows ESI-MS spectra of as-grown nanofibers which were synthesized in processes with and without H_2O , respectively, corresponding to the black and red line in Figure 4.6. Comparing the two spectra, we can see in the upper spectrum (for nanofiber

synthesized with H₂O presence in process) the high intensity peaks move relatively to high m/z side. Because the electrospray ionization (ESI) is a ‘soft’ ionization method, which overcomes the propensity of molecules fragmentation when ionized, the measured m/z value in ESI-MS spectra can correspond to the real mass of integrated molecule in nanofibers. Therefore the results reveal more H₂O in reaction atmosphere leads to larger polymer sheets in as-grown nanofibers.

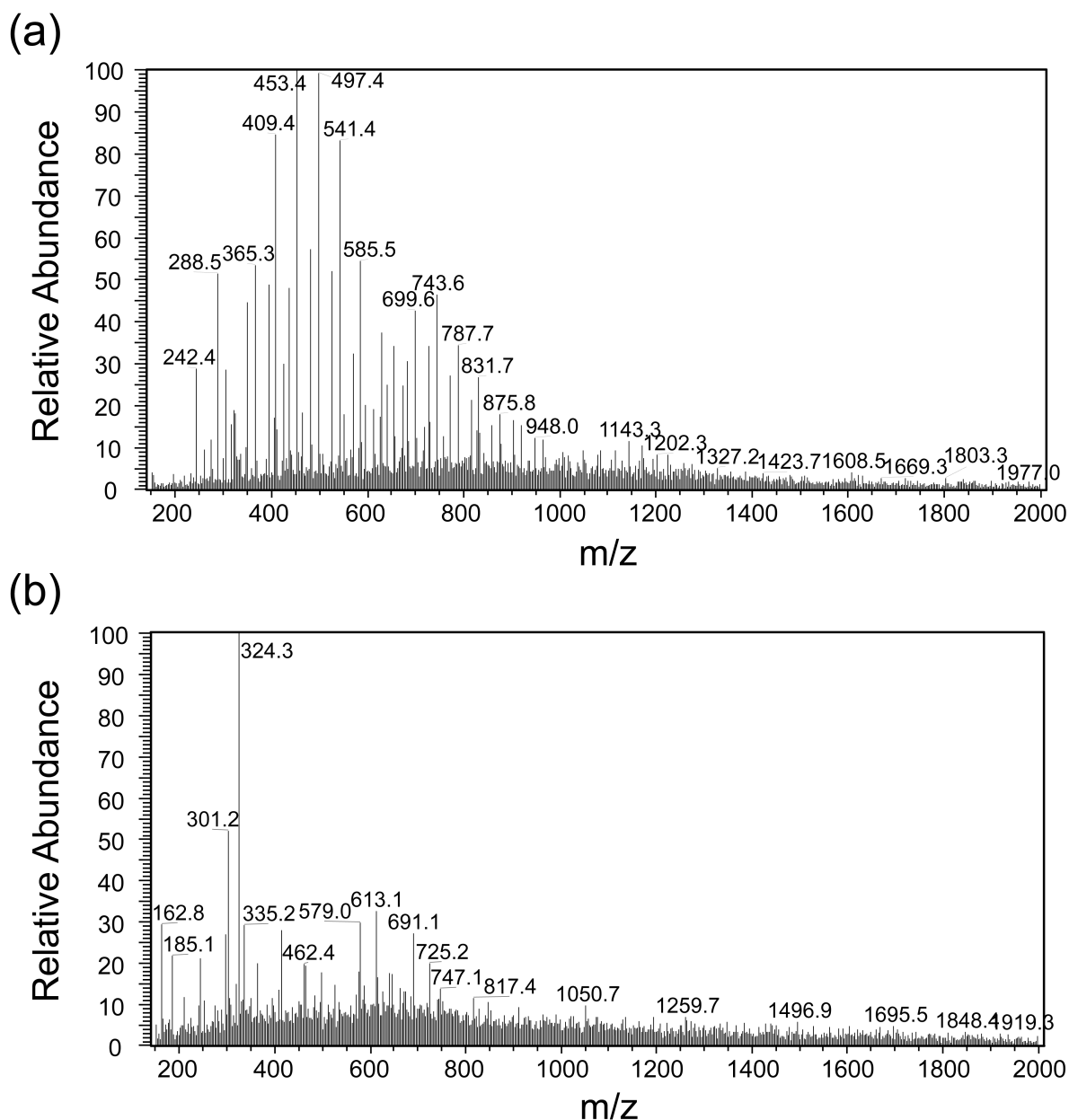


Figure 4.8. ESI-MS spectra of the as-grown nanofibers which were synthesized using the initial pressure of ~500 mbar with different atmosphere compositions: (a) with H₂O, (b) without H₂O.

Now we come back to the original issue: what is the rate-determining-step of the growth. To answer this question some experimental facts are notable: 1) the growth rate is associated to the gas pressure, namely reactant concentration; 2) oxygen-containing-reactant (e.g. H₂O)

affects the growth rate significantly; 3) oxygen-containing-reactant also influences the microstructure of growth product as enlarging the polymer sheets in as-grown nanofiber. Keeping these points in mind the growth can be then analyzed step by step. According to our 3-step-growth model, for the initial step, the coupling of C_2H_2 and oligomers formation (e.g. the benzene formation through trimerization) must progress on Cu catalyst surface. Normally a surface-catalyzed reaction is related to reactant gas pressure only under ultra high vacuum (UHV) condition, appearing as a reactant molecule coverage dependency^{104, 105, 111}. For present process which occurs in atmospheric pressure, the gas pressure hardly influences the rate because the catalyst surface is always saturated to adsorb reactant gas. If the C_2H_2 coupling is the rate-determining step, the whole growth would feature nearly a constant growth rate, in other words independent to gas pressure. It strongly conflicts with the observed gas-pressure-dependency in experiment. Meanwhile, in previous literatures it was illustrated C_2H_2 coupling on catalyst surface is sufficient fast that the reaction is rate-limited by desorption of the product^{112, 113}. As counterpart of desorption, in present process the diffusion of coupling product has more chance to limit the process rather than coupling. On the other hand, the coupling of C_2H_2 on Cu does not require oxygen or oxygen-containing-molecule participation, the oxygen covering on catalyst even hinders the coupling^{113, 114}. Therefore the clear accelerative effect of H_2O in present experiment also indicates the C_2H_2 coupling isn't the rate-determining-step. For the second step of growth, the diffusion cannot be associated to H_2O as well. Then we should think about the third step that the oligomers further coupling to form polymer sheets, namely polymerization. No doubt, along with polymerization the size of molecules increases and their mobility decreases significantly. If the polymerization progresses faster than C_2H_2 coupling or oligomers diffusion, the formed oligomers would polymerize locally and stay there. Only a slow polymerization step allows oligomers diffuse under the driving of concentration gradient. Combing the experimental facts and these discussions, it can be deduced the growth is rate-limited by polymerization.

Because polymerization can be promoted by oxygen-containing-group in a lot of cases¹¹⁵⁻¹¹⁷, the accelerative effect of H_2O in present experiment is logical. Larger polymer sheets generation in reaction system with H_2O presence is also reasonable. We can understand it in this way, in the situation without oxygen-containing-molecule, the oligomers hardly connect each other, therefore the polymerization as well as the whole growth progress slowly. If certain oxygen-containing reactant (e.g. H_2O) presents in gas phase, the oxygen can connect to the oligomers to form functional group on them. Actually in the TD-GC/MS measurement, during a 250°C thermal desorption of the as-grown nanofibers, we had identified molecule

which had oxygen-based functional group, e.g. (6-Hydroxymethyl-2,3-dimethylphenyl) methanol. The oxygen-based functional group is a bridge which facilitates the connection between oligomers. Therefore the polymerization is promoted. With more H_2O presence in reaction atmosphere, it has more chance to form oxygen-based functional group, the growth is consequently faster.

At the end, we give an explanation for the experimental fact observed at the beginning, which looks like a paradox: when a growth starts with higher initial pressure (more C_2H_2 is introduced into system), it progresses slower, see the blue and black curves in Figure 4.6. We differentiate the pressure-drop curves in Figure 4.6 with respect to time, and then numerical pressure-drop-rate at each moment is plotted in Figure 4.9. Regardless of initial pressure, the

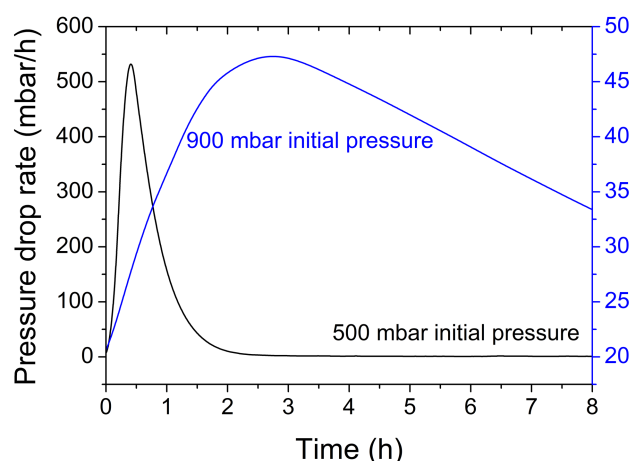


Figure 4.9. The pressure-drop-rate of processes with different initial pressures.

pressure-drop-rate (growth rate) increases to achieve a maximum value and then declines. We suppose this trend is associated to catalyst evolution. Because the growth is based on processes occurring on low-index Cu surface, to establish a stable growth, Cu particles have to evolve from irregular shape to highly symmetrical appearance in advance. Along with this evolution more Cu surface emerges and enlarges in appropriate orientation hence truly catalyzes the process. The enlarging catalytic surface leads to the increase of overall-growth-rate. When catalyst evolution finishes, the growth rate turns to decrease due to other controlling factors, e.g. reactant consumption. Therefore the summit on curves can be approximately a sign of evolution-accomplishment. Obviously, the curves in Figure 4.9 reveal that catalyst evolution takes more time in the process with higher initial pressure (900 mbar process), because more C_2H_2 in system dilutes the constant amount of H_2O (released during catalyst precursor decomposition) which is necessary for catalyst evolution. In the stable

growth stage following the long-time catalyst evolution, the growth is also slow for 900 mbar process because of low concentration of H_2O .

4.3 Catalyst evolution

The kinetics research reveals a fact that upon the three basic steps of a stable growth, a crucial process namely catalyst evolution must progress in advance. In former discussion we already discovered the tight connection between as-grown nanostructures and geometry of corresponding catalyst. An in-depth investigation on catalyst evolution is helpful for comprehensively understanding the growth process and consequently brings the research forward to advanced level: controllable synthesis.

In our large number of synthesis experiments, despite the catalyst preparation methods and synthesis parameters as well as nanostructures finally obtained, it is found original shape of Cu catalyst is unimportant for the growth. The Cu catalyst always shows powerful capability to ‘self-organize’ the surface during the growth. It evolves to have a highly symmetrical nanoparticle appearance to meet the requirement at the end. Therefore, here Cu slug which differs greatly from the final regular nanoparticle is used as catalyst precursor in process to trace the catalyst evolution.

Cu slugs (Alfa Aesar, 99.99%, \varnothing 6.35 \times 3 mm) were firstly polished by 800 mesh sandpaper to create a rough surface. Then these slugs was utilized as catalyst precursor in standard CVD growths progressed at 250°C with 500 mbar C_2H_2 , for detailed operations see chapter 3.1.3 and 3.2. The growths lasted for 5 min and 1h respectively and then were terminated by evacuating the reactant gas rapidly. After growth the Cu slug is covered mainly by two kinds of nanofiber-clusters, namely flower-like (Figure 4.10(a)) and comb-like morphologies (Figure 4.10(d)). In both kinds of morphologies the nanoparticle Cu catalysts locate in the middle of nanofibers, hence they feature symmetrical-growth. For the flower-like morphology the nanofibers converge to a point at the end. In the comb-like morphology the parallel aligning nanofibers also combine together at the end, but they converge to a line. Tracing the early stage of growth (Figure 4.10(b) and (e)) it can be found the two kinds of unique morphologies are ascribed to the topography feature of original Cu slug. Large numbers of Cu catalyst nanoparticles in a nanofibers-cluster actually originate from the same matrix by splitting the protruding portion of Cu slug. The overhanging particles (Figure 4.10(c)) and the edges of grooves (Figure 4.10(f)) on the initial rough Cu surface cause flower- and comb-like morphologies, respectively. The result reveals in present growth the catalytic activity of a Cu particle isn’t confined by its initial size. The interaction with reactant

gas can reconstruct the Cu surface and subsequently split the particle into a size suitable for nanofibers growth. This is quite different from the VLS growth wherein careful catalyst preparation is usually necessary.

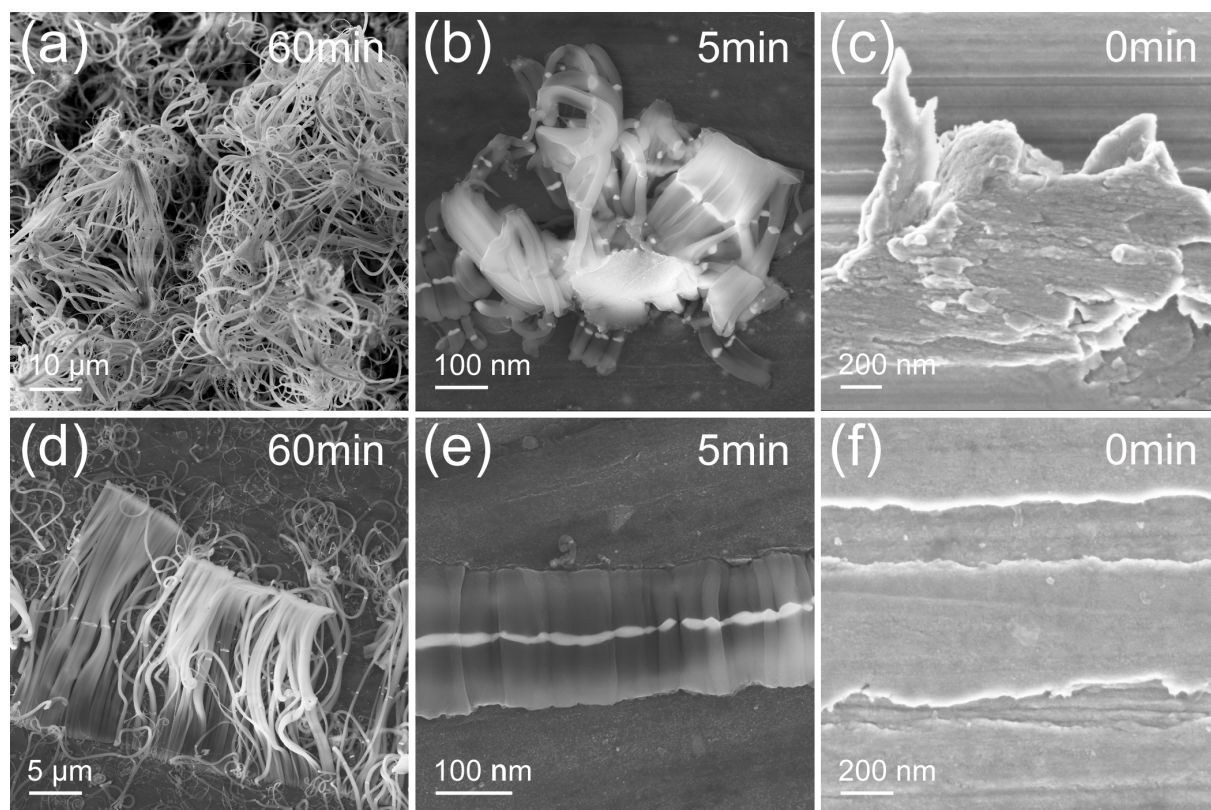


Figure 4.10. SEM images of different morphologies of nanofiber-clusters: (a) flower-like morphology; (b) early stage of the growth of flower-like morphology; (c) overhanging particle on initial Cu slug; (d) comb-like morphology (e) early stage of the growth of comb-like morphology; (f) groove on initial Cu slug.

In above growth experiments the small Cu catalyst particles originate always at the uneven part of the slug surface, in other words, catalyst evolution is associated to the curvature of precursor. We therefore predict when the Cu slug is well polished to eliminate any unevenness on surface, effective catalyst particle cannot form via shape evolution any more. To prove this, Cu slug was pretreated by electrolytic polish, and then a standard CVD growth was performed for 1h on this slug. After process the surface of sample is quite smooth without any nanofiber attaching on it, see the upper part of Figure 4.11(a). To expose the cross section, the as-grown sample was cut by FIB, see the lower part of Figure 4.11(a). It clearly shows the Cu substrate is covered by a thick layer of polymer. Further enlarging the image of the cross section (Figure 4.11(b)), it can be seen Cu fragments (bright) has been peeled from the substrate layer by layer and embedded in the polymer (grey). This is a result of interaction between hydrocarbon species and Cu slug, which reconstructed the surface of

Cu substrate. However, the peeled Cu fragments have random sheet-like shape and none of

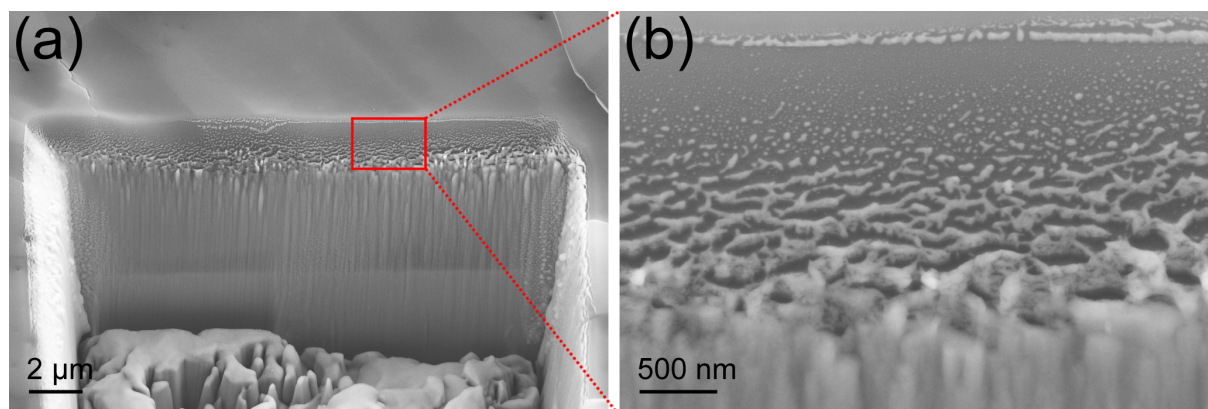


Figure 4.11. SEM images of: (a) an incision on polymer coated Cu surface, cut by FIB; (b) the cross section of the polymer/copper interface.

them shows a tendency of regularization. This experimental fact suggests although the Cu catalyst shows an impressive capability of ‘self-organizing’ during growth, to form effective catalyst particle for nanofiber growth, sufficient initial curvature on precursor is required. The curved precursor surface benefits a shape evolution remarkably, because with initial curvature a local adjustment is enough to create couples of low-index-faces for catalyzing surface processes. In contrast, on extremely smooth Cu surface, to form a highly symmetrical Cu particle too many atoms have to be rearranged. It is beyond the capability of evolution. In latter case the C_2H_2 coupling and oligomers polymerization however still progress on Cu surface. At last the reaction products precipitate slowly and homogeneously to cover the whole Cu slug. But rapid nanofiber growth is impossible due to absence of collaboration between different low-index facets, which is the base of nanofiber growth (see the 3-step-growth model in Figure 4.5).

An interesting phenomenon is the polymer layer on the Cu substrate can be very thick (more than 1μ in present experiment). It indicates the polymer coverage doesn’t block the catalytic surface. Therefore the polymer layer can keep growing to be very thick via catalytic process. On the contrary, in a high temperature VLS growth once the whole catalyst particle is covered by carbon, the growth will terminate. The key point of above difference is that in present process the incompact stacking structure of polymer allows reactant gas to contact the Cu surface beneath. This unique feature is of great importance to the catalyst evolution as well as growth. In fact, even with enough initial curvature presence, the catalyst evolution is still time-consuming, because the low-index facets have to enlarge gradually. Before a Cu nanoparticle separates from host substrate and evolves into a suitable shape to support rapid nanofiber growth, it has already been buried by homogeneously growing polymer layer. It

looks like a seed underground, see the bright spot in the center of Figure 4.12(a), it corresponds to a Cu particle in evolution underground. Attribute to the ability to pass the covering polymer layer, reactant gas can approach the Cu surface to support the interaction and evolution. Progressively the reaction-products-precipitation on Cu nanoparticle is faster than around flat area because the collaboration between enlarging low-index facets. Rapidly growing nanofiber finally breaks the covering polymer layer, like a plant emerging from soil, as shown in Figure 4.12(b). However, if the catalyst evolution progresses too slowly for some reason, for example lack of initial curvature, the Cu fragment which separates from host substrate has no chance to break the covering polymer layer, just like the Cu sheets in Figure 4.11(b).

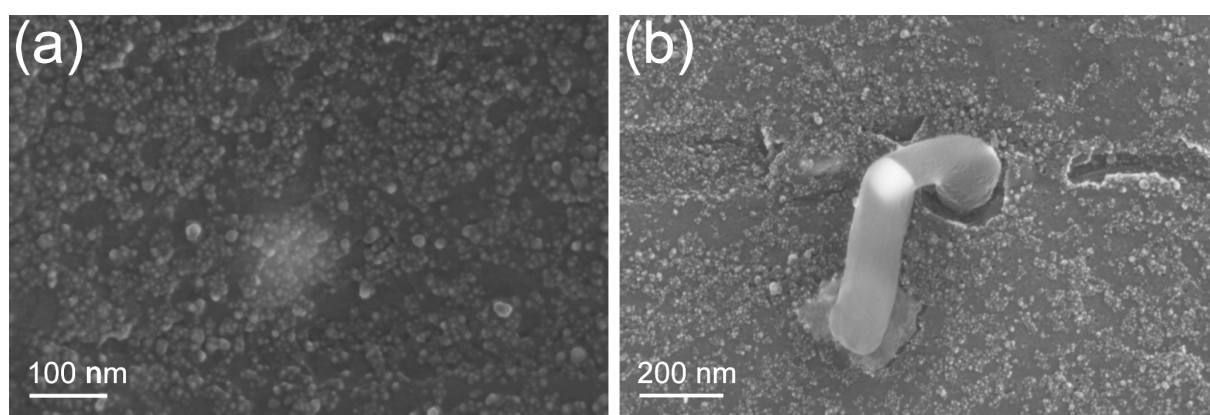


Figure 4.12. SEM images of the Cu surface at early stage of growth.

Aside from initial curvature of precursor, catalyst evolution is also associated to composition of reaction atmosphere. In our discussion about kinetics, we have found signs which suggest H_2O presence in gas phase can accelerate catalyst evolution. Here the effect of H_2O /oxygen is further confirmed by controlled experiment which introduces H_2 reduction as a pre-treatment of precursor. Cu slug with rough surface was firstly reduced in 100sccm H_2 flow at 250°C for 1h to eliminate oxygen in system, and then C_2H_2 was introduced into the reaction chamber to start a standard growth (see chapter 3.2). After 1h growth the morphology of as-grown sample, see Figure 4.13(a), is completely different from those processes without H_2 reduction step, see Figure 4.10(a). For present sample, only a small proportion is covered by nanostructure. Meanwhile, in these as-grown nanostructures the Cu catalysts still combine together and the polymer nanofibers are quite short (Figure 4.13(b)). The result reveals without oxygen presence in reaction system the catalyst evolution is weakened seriously. For a detailed explanation we can analyze the reaction occurring in a normal growth process: at the beginning the oxidized Cu slug surface is firstly reduced by C_2H_2 and consequently resultant H_2O absorbs on Cu. The adsorbed H_2O remarkably reduces the surface free energy of Cu^{118} .

It facilitates catalyst evolution which splits the original Cu into smaller nanoparticles and generates more free-surface. Interestingly, H_2O cannot induce the catalyst evolution alone, so does the C_2H_2 . Only when H_2O and C_2H_2 exist together in the atmosphere and induce a growth, the catalyst evolution can progress rapidly. We can understand this as collaboration between thermodynamic and kinetic factors. The H_2O reduces the surface free energy to make Cu splitting be possible in thermodynamic. Meanwhile, the kinetic processes make the evolution realizable, which are correlated to C_2H_2 and progress on Cu surface, including coupling, diffusion, and polymerization.

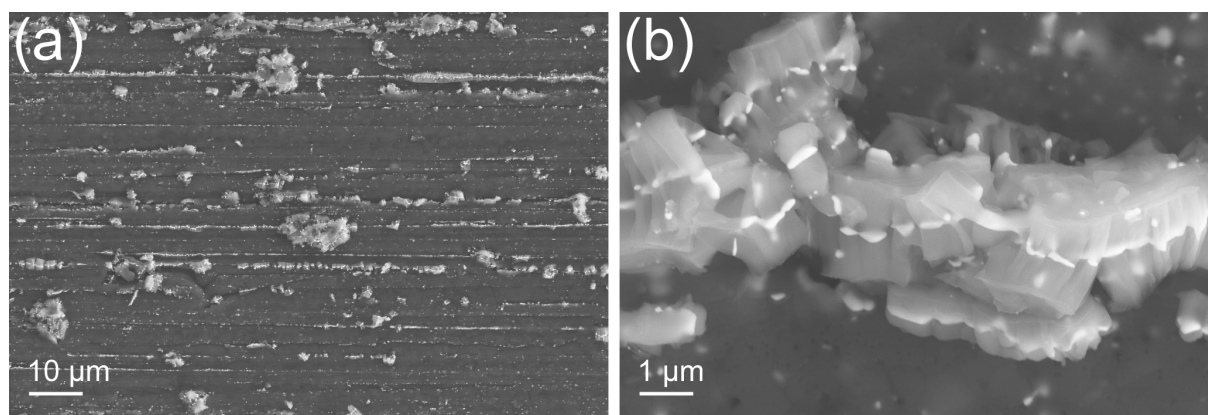


Figure 4.13. SEM images of the nanostructures grew on the Cu slug which was pretreated by H_2 reduction before the growth process.

Besides the initial curvature and composition of reaction atmosphere, the catalyst evolution is also restricted by initial crystal structure of the Cu precursor. Since a stable growth needs large area low-index catalytic surfaces, after evolution the Cu catalyst should be a regular single crystal particle. If the lattice of precursor is distorted, the evolution will be difficult because more adjustment of atoms is required. Figure 4.14 shows Cu nanopowder with abnormal crystal structure. Distorted lattice can be observed in HRTEM image of Figure 4.14(b). In XRD spectrum (Figure 4.14(d)) the (111) and (200) peaks feature obvious splitting. Meanwhile, it shows abnormal (100) peak. This peak should not appear in XRD spectrum of normal Cu sample (fcc lattice), because it corresponding to a phase with primitive cubic lattice. In addition, according to the TEM image, see Figure 4.14(a), the particles have small size therefore their surface is curved enough. Oxygen homogenously distributes in particles, see the distribution map of Cu and O in Figure 4.14(c). Therefore this Cu nanopowder agrees with our previous description about effective catalyst precursor, except absence of normally ordered crystal structure. When this nanopowder was used as catalyst in a standard growth at 250°C for 2h, after the process no fiber can be observed in specimen. The particles almost keep their original morphology, as shown in Figure 4.15. This result reveals in catalyst

evolution the adjustment of atoms is restricted on the surface area of precursor. It's impossible to reconstruct the whole Cu particle in present reaction condition.

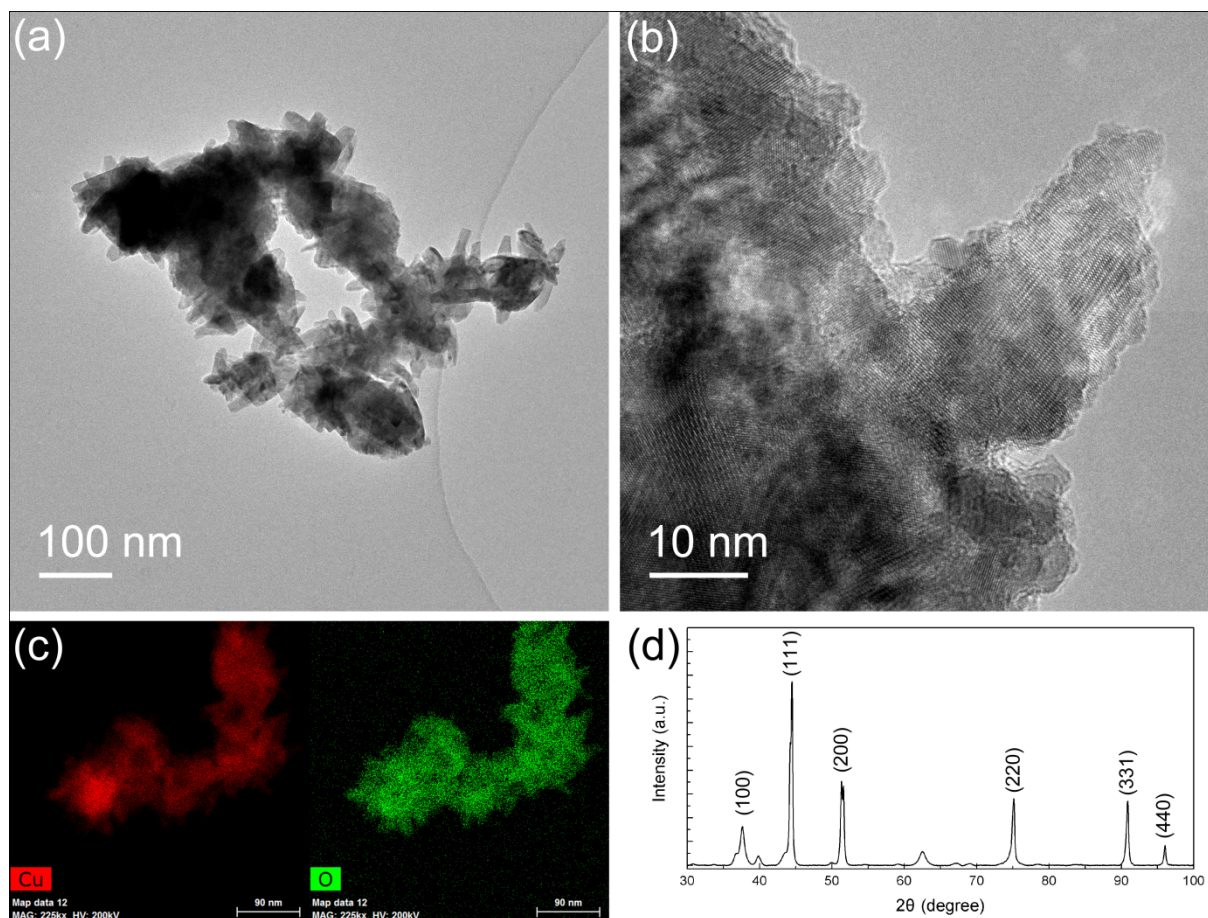


Figure 4.14. (a) TEM image (b) HRTEM image (c) Mapping mode of elemental analysis (d) XRD spectrum of the Cu nanopowder with abnormal crystal structure.

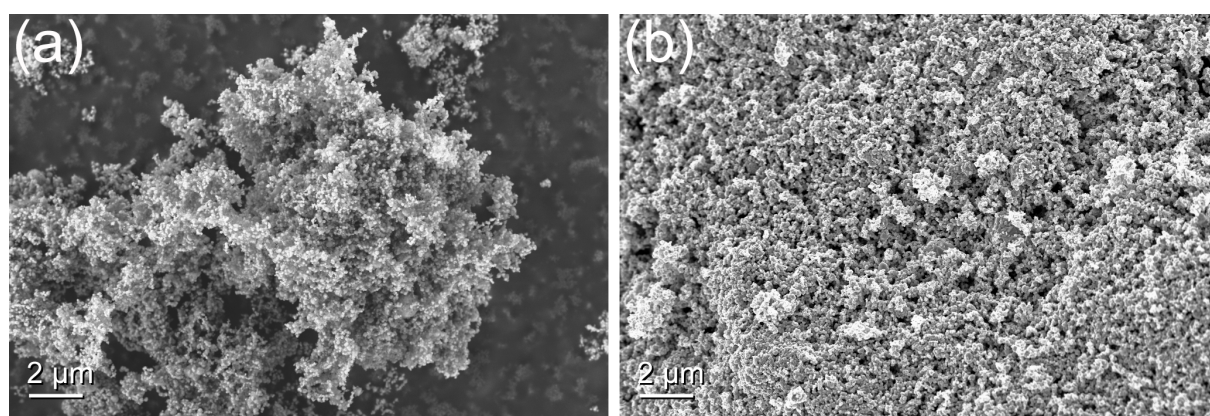


Figure 4.15. SEM images of the Cu nanopowder which has abnormal crystal structure: (a) before growth; (b) after CVD process.

In summary, catalyst evolution allows the growth to initial with a catalyst precursor featuring random size and shape. However, some preconditions are crucial. Certain molecules, such as H_2O , in reaction system reduce the surface free energy; curved surface and well

ordered crystal structure of the catalyst precursor facilitate the evolution by reducing the number of atoms which need to be reorganized. Then the evolution is able to progress under the acceleration of the kinetic processes progressing on Cu surface.

4.4 Size effect

In above discussions, we pointed out Cu slug was able to catalyze nanofiber growth only when it had a rough surface to provide required curvature for catalyst evolution. Actually, the effect of surface roughness of Cu slug on growth is far more complex and interesting, beyond to benefit catalyst evolution. In our study, nanostructures with entirely different morphologies were synthesized depending on the surface roughness of the Cu slugs (catalyst precursors). To investigate the correlation between the surface roughness of Cu precursor and morphology of as-grown nanofiber, here we introduce surface roughness R_z for quantitatively evaluation. The R_z is defined as average height difference between peak and valley based on the five highest peaks and lowest valleys over the entire sampling length. It can be expressed in equation:

$$R_z = \frac{1}{5} \sum_{i=1}^5 (R_{pi} - R_{vi}) \quad (4.1)$$

where R_{pi} and R_{vi} are the i^{th} highest peak and lowest valley respectively. R_z reflects the size or curvature radius of the protrusion on Cu slug if we approximate the protrusion to be hemisphere. The Cu slug precursor which corresponds to the as-grown sample shown in Figure 4.16(a) was polished by 800 mesh sandpaper and featured a R_z of 2.88 μm . The as-grown sample is covered by dense nanofibers, which show normal symmetrical-growth nature. When a smoother Cu surface was applied, which was polished by 4000 mesh sandpaper and had a R_z of 184 nm. The surface of as-grown sample is also covered by similar nanofiber but the density is quite low, see Figure 4.16(b). The R_z can be further reduced to 36 nm by using 3 μ diamond slurry for polish, then after growth the whole Cu substrate is mainly covered by nanohelices, see Figure 4.16(c). Besides nanohelices only a small amount of straight nanofibers can be observed but their diameters are much lower than the nanofibers in former two samples. Pure nanohelices can be synthesized on the Cu slug polished by 1 μ diamond slurry. In this case the R_z reduced to 23 nm (Figure 4.16(d)). In all the cases the nanohelices still feature symmetrical-growth mode. If the Cu slug was polished by 40 nm SiC slurry, the surface roughness can be reduced to a R_z of 17nm. Then the growth followed different mode, namely tip-growth. Here very small Cu catalyst particles locate in the tips of straight thin nanofibers, see Figure 4.16(e). At last, when the Cu slug was pre-treated by electrolytic polish,

the extremely smooth surface which had a R_z of 9nm loosed the ability to catalyze any nanofiber growth, just like Figure 4.16(f). The as-grown Cu slug shows a smooth surface without fiber-like structure.

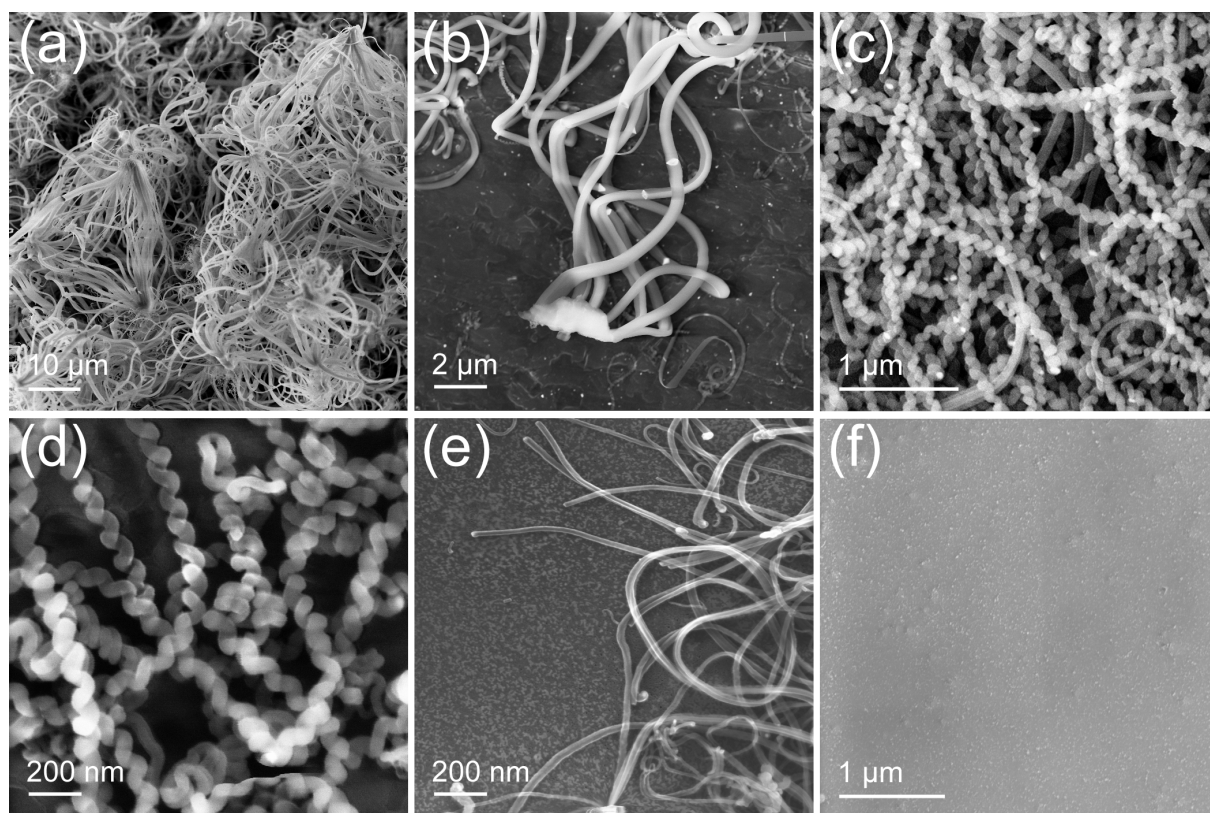


Figure 4.16. SEM images of nanostructures prepared on Cu slugs (catalyst precursors) with different surface roughness. The Cu slugs were pre-polished by: (a) 800 mesh sandpaper; (b) 4000 mesh sandpaper; (c) 3 μ diamond slurry; (d) 1 μ diamond slurry; (e) 40 nm SiC slurry; (f) electrolytic polish.

The various morphologies of as-grown nanostructures are actually ascribed to the different sized Cu catalyst particles as well as their evolution process associating to surface roughness of Cu slug precursor. When the surface of Cu slug is quite rough, the large sized protrusion splits into a lot of effective catalyst particles in evolution and consequently catalyzes dense nanofiber-cluster growth. Accordingly, relative small protrusion on smoother Cu surface can only split into fewer catalyst particles and induce sparse nanofibers on the as-grown substrate, as we can see in Figure 4.16(b), a nanofiber-cluster originated from a Cu protrusion includes only 7 fibers, in contrast a cluster in Figure 4.16(a) consists of tens of members. Further reduced surface roughness corresponds to smaller protrusion, which is not inclined to split any more. In this case the final effective Cu catalyst nanoparticle has a size comparable to the original protrusion. Practically, the size of nanoparticle in as-grown nanostructure is approximately double of the measured R_z of Cu slug precursor. Depending on whether the particle size is larger or smaller than a critical size, as-grown nanofiber tends to

be straight or helical, here the observed critical size is about 70 nm, same as the description in Xia's report⁴¹.

Interestingly, altering Cu nanoparticle size induces changes not only on morphology but also on growth mode as well as microstructure of as-grown nanostructures. This influence has not been reported before. Here we give an explanation based on symmetry of catalyst particle. Firstly, for both straight and helical nanofibers, which are catalyzed by relatively large Cu particles, symmetrical-growth dominates the process. It is reasonable because the evolution tends to generate highly symmetrical catalyst particle, which is encompassed by low-index faces to reduce the surface energy (see Figure 2.3). These faces feature large orientation difference. If the reaction product precipitating on different low-index faces converges to form a nanofiber in tip-growth mode, it will induce strong bending strength, and the reaction products must overcome a difficult long-distanced-diffusion. Therefore nanofiber tends to grow in a more realizable way: to symmetrically spread toward two opposite sides of catalyst particle, namely symmetrical-growth.

In contrast, for those extremely small Cu particle catalysts, they show relatively lower symmetry even after evolution, see Figure 4.17. Figure 4.17(d) shows a HRTEM image of an extremely small Cu catalyst nanoparticle. It has a size of 35nm, which is double of the R_z of the corresponding Cu slug precursor. The electron beam is parallel to [111] direction. It can be seen although the Cu particle features partial flat surface in {110} orientation, it shows low symmetry in overall. Accordingly, unsymmetrically precipitating growth product tends to converge to a preferential direction through the short diffusion route, hence the whole structure appearing a tip-growth feature.

In addition, the size of catalyst particle also influences microstructure of as-grown nanostructure. For the growth catalyzed by large symmetric catalyst particle, the large flat Cu faces play a role of template for growth product precipitation. As a result in the as-grown nanostructure planner polymer sheets can stack in a partial ordered way (see Figure 2.4). In contrast, on the small Cu catalyst there isn't enough space for polymer molecules stretching. The molecules squeeze each other and finally stack in a disorder way. At last the as-grown nanofiber exhibits amorphous feature, whatever at the portion far away (Figure 4.17(c)) or close to the catalyst surface (Figure 4.17(d)).

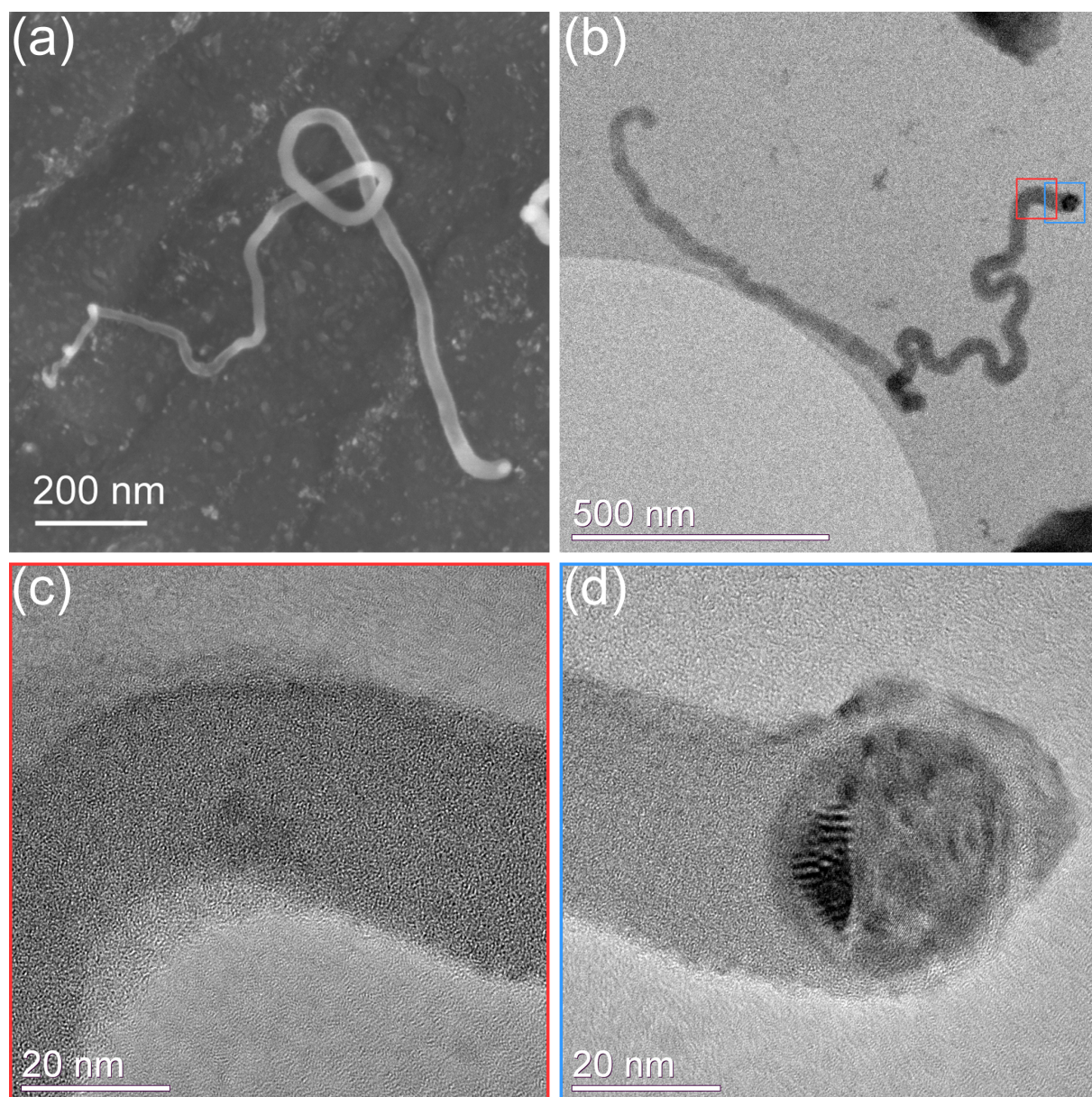


Figure 4.17. (a) SEM images of a tip-growth nanofiber. (b) TEM image of a tip-growth nanofiber. (c) and (d): HRTEM images of the stem and tip part of the nanofiber in (b).

Furthermore, Figure 4.17(a) shows the diameter of nanofiber is changing from the tip to the tail. It indicates the Cu facet for growth product precipitation is enlarging during the growth. Meanwhile, the length of this nanofiber is relatively shorter comparing with the nanofiber in Figure 4.16(a)-(d). Therefore we can defer the catalyst evolution for small Cu particle is slower. In the extreme case the collaboration between low-index faces as well as diffusion path cannot be established, then no fiber-like product forms, see Figure 4.16(f).

The substance of the size effect is the unsymmetrical growth. We consider a catalyst-nanofiber system which features different growth velocities at each side of catalyst particle, see Figure 4.18(a). Unsymmetrical growth induces the bending of the as-grown nanofiber. If

to note the growth velocities on each side as V_a , V_b , and the size of catalyst particle as D_p , then the curvature radius of as-grown nanofiber, R_f , can be calculated in equation:

$$R_f = \frac{V_a}{V_a - V_b} D_p = \frac{V_a}{Dv} D_p \quad (4.2)$$

where Dv represents the difference of growth velocity between side A and B. From this equation we can see the curvature radius of as-grown nanofiber reduces, while the velocity difference of growth increases. When Dv has a value close to V_a , the R_f is comparable to the size of catalyst particle. In this case the two nanofiber branches fuse to appear a tip-growth, see Figure 4.18(b). When Dv has a relative lower value, although the fiber bends severely, the R_f is not small enough for the nanofiber branches fusing, so nanohelix forms as a result. If the velocity difference is quite small, the R_f has a high value and consequently the as-grown nanofiber looks straight.

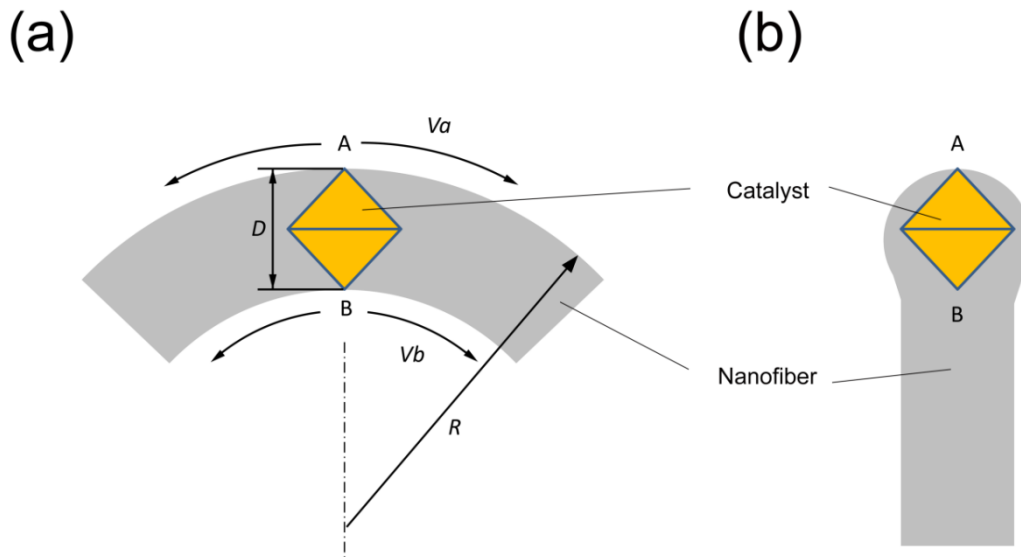


Figure 4.18. (a) Sketch of an unsymmetrical growth (b) Sketch of a tip-growth fiber.

Therefore the core factor to determine the morphology and growth mode is the growth-velocity-difference on different part of catalyst particle. According to the proposed growth mechanism, all important processes occur on low-index catalyst surface, whatever initial C_2H_2 coupling or final polymerization. Then the growth velocity depends on the area of effective catalytic surface. Comparing the TEM image of Figure 2.3 and Figure 4.17(d), we know the smaller catalyst particle has lower symmetry. That means the areas of effective catalytic surface on each side of small Cu particle are quite different, it leads to a high Dv . In addition, from the equation (4.2) we know also the R_f is proportional to D_p , it indicates for the

small sized catalyst particle, the effect of velocity-difference is magnified in the growth. The observed low symmetry of small sized Cu nanoparticle is probably due to unstable nature of system. A little disturbance caused by kinetic process, for example adsorption of gases or diffusion of reaction products, can induce partial Cu atoms reorganizing on catalyst surface. For an extremely small Cu particle which consists of a small number of Cu atoms, above reorganization is sufficient to lead to deviations from symmetric shape.

General speaking, the morphology, growth mode and microstructure of the nanofiber are associated to the size of corresponding Cu catalyst particles, which can be controlled by altering the surface roughness of Cu slug precursor. Two critical sizes are extracted by SEM observation. Nanofiber and nanohelix tend to form on the catalyst particles which are larger and smaller than 70nm, respectively. They all feature symmetrical-growth. When the Cu particle size is smaller than 35nm, amorphous nanofiber tends to form in the tip-growth mode.

5. Morphology control of multi-branched carbon nanostructures via facet-selective catalytic growth

In last chapter the copper-catalyzed CVD growth was investigated with respect to thermodynamics and kinetics, respectively. The proposed growth mechanism reveals that the low index facets of Cu catalyst particle play a decisive role in the growth. However, special attention was not paid to the geometry of catalyst particle, although it directly determines the orientation of the exposing outer facets. In all the experiments discussed above, the symmetric catalyst particle was formed via spontaneous evolutions instead of purposive design. In this chapter we focus on the geometry of Cu catalyst particle as well as corresponding nanostructures, and intended morphology control is executed. The results pioneer a new approach toward the shape-controlled synthesis of carbon nanostructures.

5.1 Basic idea

Various nanostructures have attracted tremendous attention due to their electronic, electrochemical, optical, magnetic, and catalytic features as well as their applications¹¹⁹⁻¹²⁴. These features are known to be affected sensitively by the surface states, sizes, and shapes of nanostructures. To get deep insight into those properties, considerable effort has been devoted especially to the synthesis of shape-controlled nanostructures¹²⁵⁻¹²⁷. Take the carbon nanostructures, one of the most studied nanomaterials, as an example, chemical vapour deposition (CVD) at high temperatures (>500 °C) has been frequently used to synthesize carbon nanotubes²⁸, fullerenes¹²⁸, nanocones¹⁹, Y-junctions^{129, 130}, nanohelices²². Another example, the elaborate synthesis method allows not only controlling the aspect ratio of different shapes^{131, 132}, but also tailoring the detailed geometry features to form cube, octahedron, tetrahedron nanoparticles, and their truncated counterparts^{126, 133}. More complex structures (e.g. icosahedra¹³⁴, hourglass¹³⁵ and star shape¹³⁶) are also possible to be produced. Unfortunately these precise shape-controls are only workable on metal nanocrystal^{120, 122, 124}, metal oxide, and/or semiconductor^{119, 125}. Actually most available shape-control methods are not applicable over carbon. This is ascribed to the nature that carbon takes highly ordered crystalline lattice. Therefore up-to-now, few reports deal with the precise shape-control of carbon nanostructures, especially at low temperatures³⁷.

In a CVD process, the morphology of grown carbon nanostructures correlates tightly to the metal catalyst^{20, 137, 138}. The metallic catalysts are intrinsically symmetric and always tend to expose favourable low index facets in thermodynamic equilibrium status¹¹⁸. For instance, Cu

nanoparticle has a combination of {001}, {110} and {111} facets¹¹⁸, which have different catalytic activities. When reactive species (e.g. acetylene, C_2H_2) is introduced at a relatively low temperature ($<300\text{ }^{\circ}C$), free and movable oligomers like benzene (C_6H_6) are formed on {001}¹⁰⁴, {110}¹⁰⁵, and {111} facets¹⁰⁶. Meanwhile, cyclooctatetraene (C_8H_8) is formed and adsorbed tightly only on the {111} facet¹⁰⁶, leading to the loss of the catalytic reactivity of the {111} facet. In this context the growth of a precisely shape-controlled carbon nanostructure can be achieved via a facet-selective-catalytic process, namely growing carbon nanobranched on the certain facets of a metal catalyst nanocrystal. The number of carbon nanobranched can be designed by intentionally exposing specific facets of the nanocrystal via altering reaction temperature and atmosphere. In this way the stretching directions of carbon nanostructure will follow the symmetry of nanocrystal. The length of carbon nanostructures can be tailored by growth duration. By means of patenting the catalyst, the precise control of the size and the location of carbon nanostructures are also possible.

In this chapter, we describe the formation of several novel star-shaped carbon nanostructures with 2-, 3-, 6- and 8- branches, respectively. They are all synthesized by a universal copper-catalyzed CVD reaction of acetylene. The morphology of nanostructure is mainly controlled by reaction temperature and gaseous environment. An interesting feature of these carbon nanostructures is that all the branches selectively grow on certain facets of a single nanocrystal catalyst, the 'node'. This discovery shows a typical case of facet-selective catalytic growth which not only offers a universal process for synthesis of various branched carbon nanostructure but also enriches the knowledge of its growth mechanism.

5.2 Realization

For branched nanostructures preparation the catalysts, copper nanoparticles were needed. They were prepared by using dip-coating method. A piece of silicon wafer was dipped into the solution of water/ethanol 1:7 with copper (II) nitrate, citric acid and polyethylene glycol (PEG), and subsequently dried at $100^{\circ}C$ to form a thin film. After that, electron cyclotron resonance (ECR) nitrogen plasma bombing was used to decompose the film into separate copper nanoparticles in the range of 100-300 nm in diameter. Then the silicon wafer with copper catalyst was sent into a sealed quartz tube reactor and acted as the substrate for the growth of carbon nanostructures. The substrate was heated up with a heating rate of $6\text{ }^{\circ}C/\text{min}$ under vacuum. Right after reaching $200^{\circ}C$, acetylene was introduced into quartz tube rapidly while the temperature continuously elevated till the set point (from $250^{\circ}C$ to $350^{\circ}C$, depending on the target nanostructure). The pressure was kept stably at 500 mbar for 60

minutes to grow polymer nanofibers on silicon wafer substrate. Then the quartz tube was evacuated again to stop the reaction. Subsequently a heat treatment at 900°C under vacuum was applied to carbonize the as-prepared polymer nanofibers into carbon if necessary. The products before and after heat treatment were collected and examined with SEM, HRTEM, Raman, IR, and Mass spectroscopy, respectively.

Figure 5.1(a) shows SEM image of the sample prepared at 350°C. A 6-branched structure which is named as nano-hexapus can be seen in the image. Such nanostructure consists of two parts: the copper nanocrystal in the center and six branches around. The copper node is a single nanocrystal proved by electron diffraction with a size of 300 nm, approximately. It is accordant with the size of copper nanoparticles in the catalyst synthesized by electron

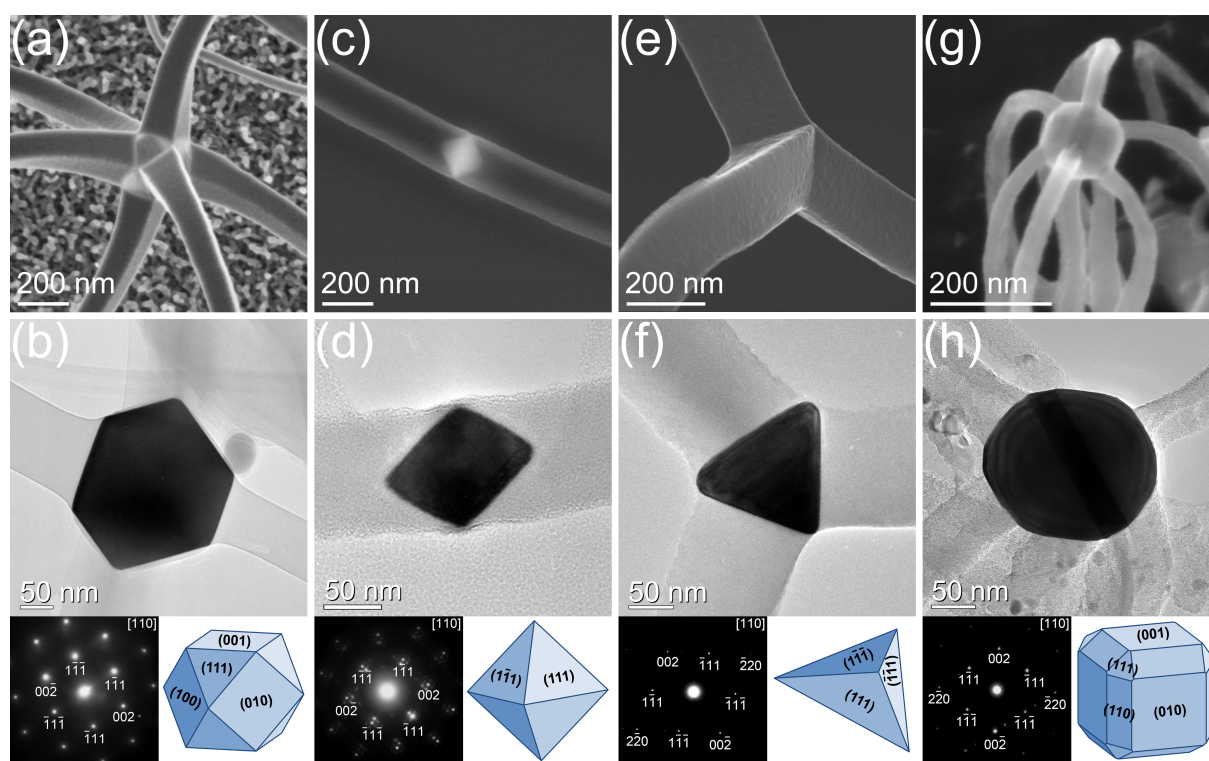


Figure 5.1. (a) SEM image and (b) TEM image, electron diffraction pattern, catalyst particle sketch of 6-branched nanostructure prepared at 350°C. (c) SEM image and (d) TEM image, electron diffraction pattern, catalyst particle sketch of 2-branched nanostructure prepared at 250°C. (e) SEM image and (f) TEM image, electron diffraction pattern, catalyst particle sketch of 3-branched nanostructure prepared at 275°C. (g) SEM image and (h) TEM image, electron diffraction pattern, catalyst particle sketch of 8-branched nanostructure prepared at 250°C with additional HCl in the reaction atmosphere.*

* SEM image in (a) was photographed by Xiao Sun. TEM and SAED images in (b) and (d) were photographed by Junhai Xia

cyclotron resonance (ECR) nitrogen plasma bombing process. The SEM image remarkably shows a regular shape of truncated cube (or cubo-octahedron) with six square facets and eight smooth triangular facets, which are confirmed to be $\{001\}$ and $\{111\}$ facets of the copper nanocrystal respectively by TEM image and the corresponding electron diffraction (Figure 5.1(b)). The sketch map of copper catalyst particle is also shown in Figure 5.1(b). All of the six branches of carbon nanofibers grew merely on square $\{001\}$ facets while triangular $\{111\}$ facets were clean without any growth. The branches of carbon nanostructure are tens of microns in length and 110-160 nm in diameter, which are a little thinner than the size of central copper nanocrystal. The cross-section of carbon nanofibers is in square shape, which corresponds the shape of $\{001\}$ facets of copper catalyst particle. It is interesting to notice that each fiber (each branch) shows inhomogeneity in diameter along their longitudinal direction, the closer to the node, the wider. It implies that surface reconstruction of copper catalyst might have taken place, enlarging $\{001\}$ facets during the fiber growth.

During experiments we noticed that the growth of nanostructures is sensitive to temperature. When a reaction process was carried out at a relatively lower temperature at 250°C with other parameters unchanged, straight nanofibers instead of nano-hexapus were obtained. Figure 5.1(c) shows the SEM image. It is seen that centre located catalyst has a quadrangle-shaped projection and nanofibers grow symmetrically on the two opposite sides of catalyst particle. Hence this morphology is defined as the 2-branched nanostructure. According to TEM image and corresponding electron diffraction pattern (Figure 5.1(d)), octahedron-shaped crystalline copper nanoparticle seems partially oxidized (the brightest set of diffraction pattern shows a crystalline nature of copper, and others are probably from Cu_2O) and encapsulated by eight facets indexed as $\{111\}$ facets, and the corresponding sketch map is also figured out in the Figure 5.1(d).

Coincidentally, 3-branched nanostructures were obtained at a medium reaction temperature at 275°C. Figure 5.1(e) shows their SEM image. In this case, the catalyst node has a regular tetrahedron appearance which is encompassed by four $\{111\}$ facets. Branches of carbon nanofibers grew merely on three $\{111\}$ facets while the last one was left clean. All the fibers have equilateral triangle cross section which coincides with the geometry of $\{111\}$ facet of catalyst node. Similar to others two cases, TEM image and corresponding electron diffraction (Figure 5.1(f)) show its single nanocrystalline nature and support the deduction above. The sketch map of catalyst node is given in the Figure 5.1(f) as well.

Further investigation revealed that the morphology of obtained nanostructures was not only influenced by reaction temperature, but also related to the gaseous environment. In another experiment at 250°C, a little amount of additional hydrogen chloride (HCl, 2.5 mbar partial pressure) was introduced into the reaction atmosphere. Instead of 2-branched straight fiber, 8-branched nanostructure (or named as nano-octopus) was obtained. Figure 5.1(g) shows its SEM image. TEM image and corresponding electron diffraction pattern are shown in Figure 5.1(h) as well as the sketch map of catalyst particle. From SEM and TEM images, it is clearly seen that a catalyst nanocrystal in the shape of beveled cube locates at the node of this nanostructure. Each of eight truncated vertexes connects a nanofiber. All of the eight branches grew merely on truncated triangular {111} facets while truncated square {001} facets and rectangular {110} facets remained clean. The {110} facets of copper catalyst were remarkably enlarged comparing to those samples prepared with pure C₂H₂.

5.3 Characterization

Micro-Raman spectroscopy measurement is applied to analyze the composition and the degree of graphitization of the as-grown and post heat-treated products. The aforementioned four kinds of nanostructure have almost the same feature of Raman spectra after the 900°C heat treatment, but before heat treatment only the sample grown at 350°C appears weak signal while the other samples grown at lower temperature are undetectable. Typical spectra corresponding to the 6-branched nano-hexapus are revealed in Figure 5.2. In both spectra, before and after heat treatment, respectively, two major Raman bands are revealed, D band at ~1350 cm⁻¹ and G band at ~1600 cm⁻¹. The D band corresponds to the defect types in the graphitic layers, while the G band corresponds to the crystalline graphitic sheets¹³⁹. The intensity ratio between the D and G peaks is inversely proportional to the degree of graphitization of carbon materials. The low ratio of I(G)/I(D) of heat treated sample, which is 0.35, reflects relatively large amount of amorphous phase from a little part crystalline phase. Furthermore, according to the I(G)/I(D) ratio, based on the T-K (Tuinstra and Koenig) relationship^{139, 140}

$$\frac{I(D)}{I(G)} = \frac{C(\lambda)}{L_a} \quad (5.1)$$

where $C(\lambda)$ is ~44 Å, L_a is the size of graphite cluster or sheet, it can be estimated that the crystallites size in nanofibers is about 1.5 nm. The Raman signal from the as-grown sample without heat treatment shows poor signal-to-noise ratio and the elementary analysis reveals a

C/H ratio close to 1:1, which implies it is more like polymer nanostructures than carbon ones. Both results reflect the amorphous nature of the as-grown sample rather than graphite. This fact accords with one of Qin's result about amorphous carbon nanocoils³⁸.

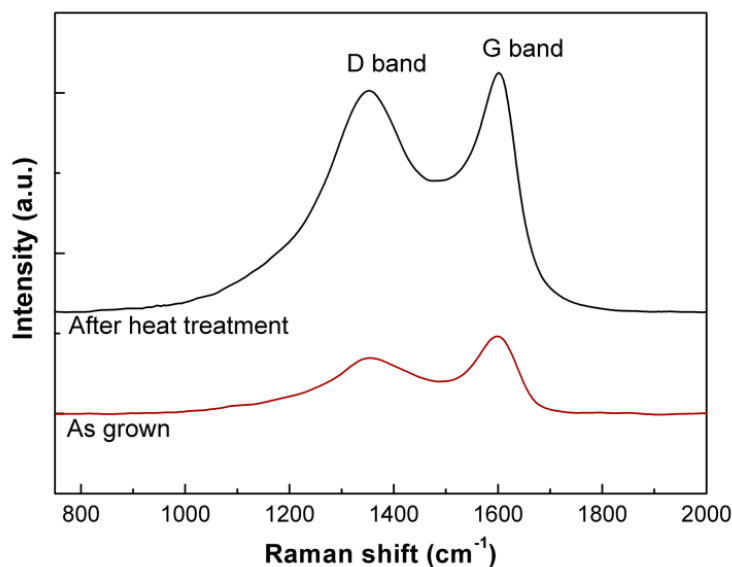


Figure 5.2. Raman spectra taken from the 6-branched nanostructure prepared at 350 °C, before and after heat treatment, respectively.

To obtain more microstructure information, high resolution transmission electron microscope (HRTEM) images of the as-grown polymer sample were recorded⁹⁷. Figure 5.3(a) shows the image of a 6-branched nano-hexapus structure in which the copper particle oriented with the [110] zone axes parallel to the electron beam. The copper particle looks in hexagonal shape, corresponding to the projection of a cubo-octahedron along [110] direction. In Figure 5.3(a), the two clear branches, which are inside the image plane and in opposite directions (left and right) are grown on {001} facets of the copper nanocrystal. And other four branches cannot be clearly seen, since they are in upper or beneath positions of image plane and are not focused. In addition, the magnified HRTEM image (Figure 5.3(b)) reveals that the branch consists of numerous small polymer sheets stacking parallel to the catalyst surface. Each polymer sheet is independent and has a diameter of 1-2 nm with a thickness of 3.8-4.0 Å. Such dimensional feature is coincident with the calculation result derived from Raman spectra. Further observation at {111} facets (Figure 5.3(c)), from where no polymer nanofiber grew up, reveals that they are actually not 'clean'. The magnified image reveals that the {111} facets are fully covered by 4-5 layers of polymer sheets. The thickness of each polymer layer is about 4 Å. It is the same as the polymer sheets which build up those branches.

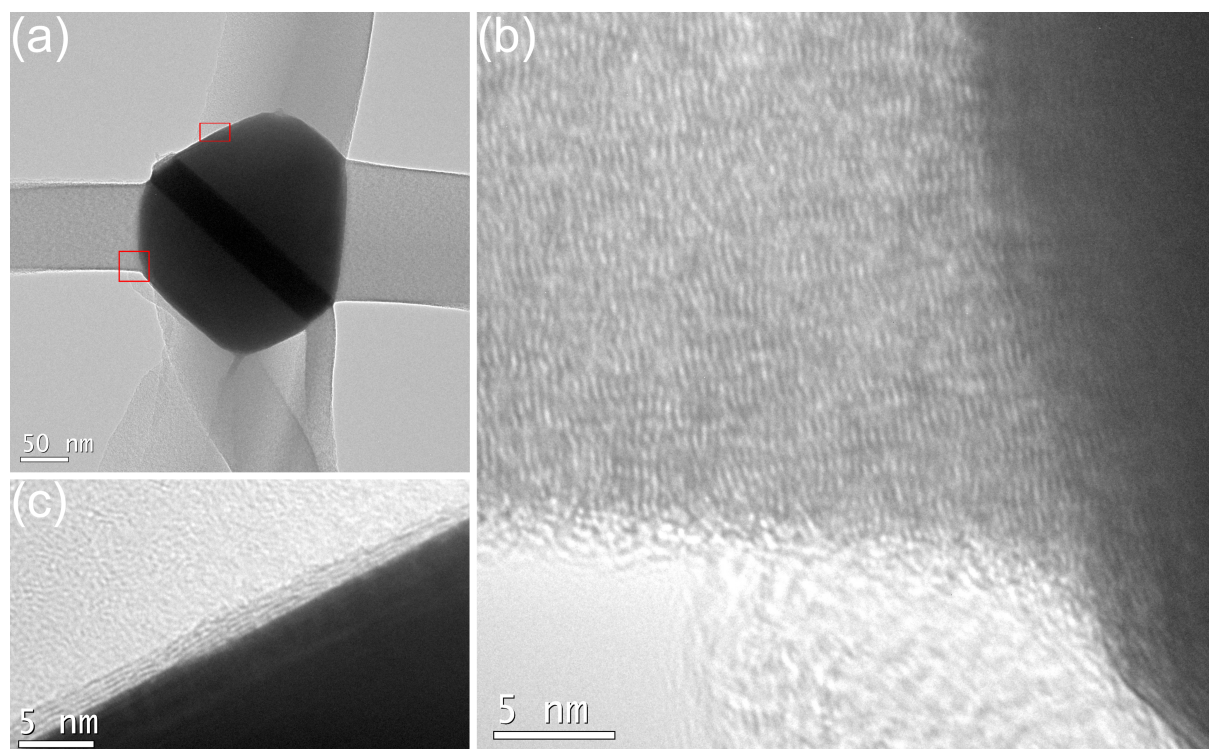


Figure 5.3. (a) TEM image of 6 branched nano-hexapus. (b) The HRTEM image of the interface of (200) plane. (c) The HRTEM image of the interface of (111) plane.[†]

To confirm the molecular structure, supplementary infrared (IR) and Mass spectroscopy analyses were carried out on the 2-branched nanostructure prepared at 250°C. Figure 5.4 shows the IR spectrum. To compare with the nanostructures synthesized in chapter 4.1, each peak in present spectrum can find its counterpart in Figure 4.2. It indicates although different

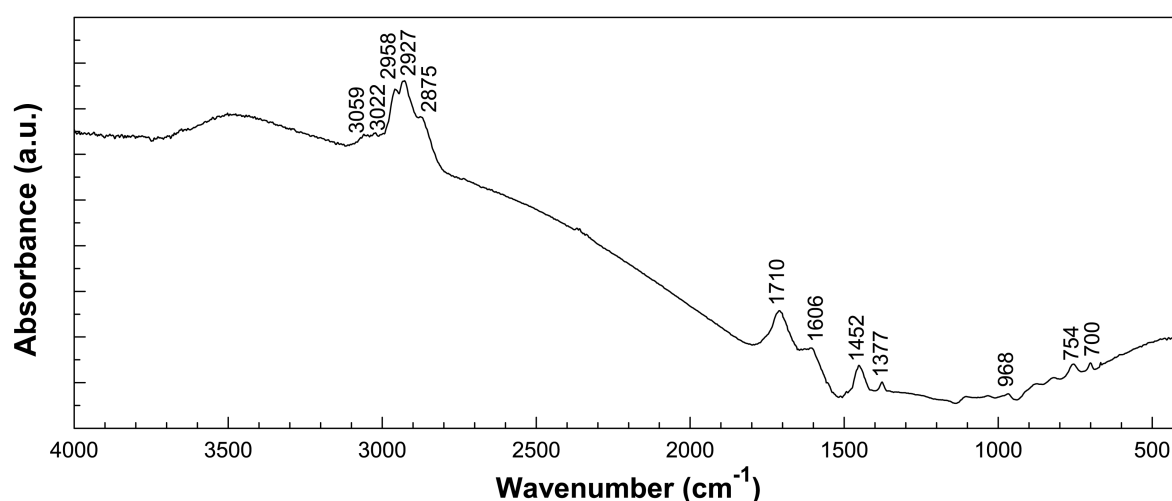


Figure 5.4. IR spectrum of the 2-branched nanostructure prepared at 250°C.

[†] This HRTEM image was photographed by Junhai Xia

catalyst precursors, namely sol-gelled and thermal decomposed CuO, respectively, were used in the growths, the as-grown nanostructures have similar molecular structure. However, the peak at 1710 cm^{-1} in present spectrum, which is assigned to the stretch of C=O, has much higher intensity than the one in Figure 4.2. Accordingly, the mass spectrum for present sample features a distribution moving towards higher m/z region, see Figure 5.5. The results are coincident with the claim in chapter 4.2, that the oxygen leads to polymer molecule enlarging in the growth. The molecular masses appear periodicity, implying a series of molecules consisting of different number of uniform structural unit. We performed a calculation with an assumption that these molecules have graphene like planar structure and mainly consist of carbon and hydrogen atoms. Then according to the mass spectrum data, these molecules have the diameter between 1.2 and 1.7 nm, which is agreed with the HRTEM image very well.

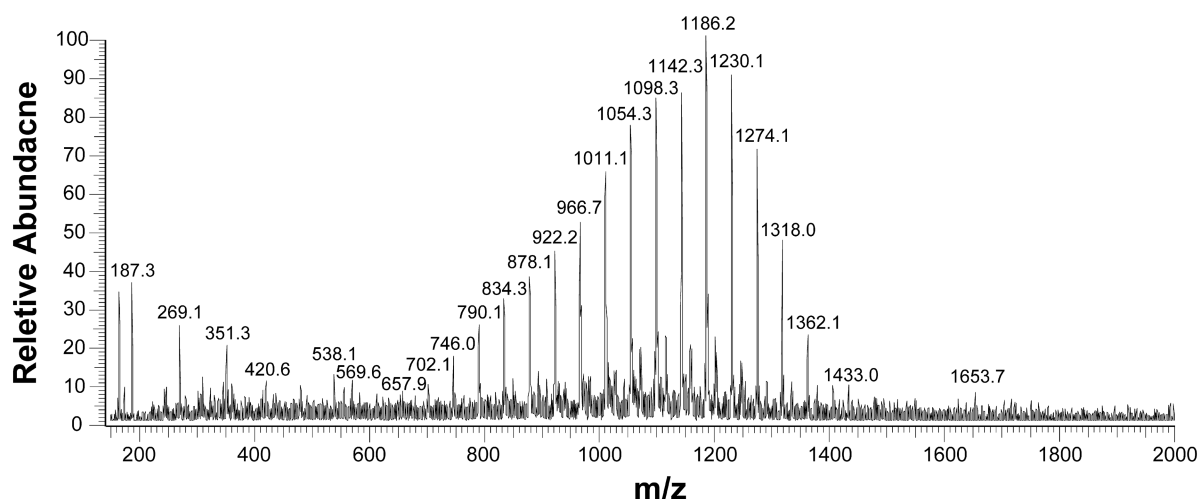


Figure 5.5. Mass spectrum of the 2-branched nanostructure prepared at 250°C .

5.4 Modeling

The 3-step mechanism proposed in chapter 4.1 is also applicable for interpreting the growth of multi-branched nanostructure, see Figure 4.5. But the role of each low index Cu facets changes depending on the reaction condition. For the 2-branched nanostructure which is synthesized at a relatively low reaction temperature of 250°C , the growth progresses in a same way as the description in chapter 4.1. The coupling of acetylene on copper surface induces benzene (C_6H_6) forming on $\{001\}^{104}$, $\{110\}^{105}$, $\{111\}$ facets¹⁰⁶, but cyclooctatetraene (COT, C_8H_8) only generates on $\{111\}$ facet¹⁰⁶. Immobilized COT and its derivatives block the $\{111\}$ facet and stop the C_2H_2 further coupling on that. As a result, a concentration gradient of movable oligomers and the further derivatives between $\{001\}$, $\{110\}$ facets and $\{111\}$ facets

drives the diffusion from $\{001\}$ and $\{110\}$ facets to $\{111\}$ facets through the surface of copper particles, thus excess oligomers and derivatives precipitate on $\{111\}$ facets to build up nanofibers. During this process, the interaction between copper surface and hydrocarbon compounds reconstructs and smoothes the copper surface, especially enlarges $\{111\}$ facets to form a more regular octahedron appearance, which is fully encompassed by eight $\{111\}$ facets. The $\{110\}$ facets actually appear as edges of the octahedron (Figure 5.1(d)), and the $\{001\}$ facets locate at the vertexes position if they exist. The polymer sheets derived from each four adjacent $\{111\}$ facets converge into one polymer fiber. The whole nanostructure appears as a symmetrical straight fiber with the copper catalyst located in the center.

To our understanding, the key factor of the formation of octahedron-shaped copper particles and consequent growth of polymer nanofiber is the combination of the surface energy of catalyst particles and the dynamic process of oligomers diffusion. The adsorbate-induced changes in surface energy resulting in the morphology evolution of copper nanocrystals had been observed before^{118, 141, 142}. For example, in former work, hydrogen chloride (HCl) is proved to have strong interaction with copper $\{110\}$ facet and induces surface reconstruction^{141, 142}. Based on this, we utilized HCl gas to change the surface energy of different facets of copper nanocrystals and were about to observe how it would affect the formation of polymer nanofibers. With a little amount of HCl gas mixed to the atmosphere at 250°C, as we were expecting, it lead to the formation of copper nanocrystals with enlarged $\{110\}$ facets (Figure 5.1(g),(h)) comparing to the sample prepared in pure C₂H₂. In this case all the three facets, $\{110\}$, $\{111\}$ and $\{001\}$, expose out remarkably and collaborate together to grow an 8-branched nano-octopus structure, because each $\{111\}$ facet is separated by other facets and does not adjoin each other anymore (Figure 5.1(h)). However, in present study it is more complicated than a surface-energy–dominating-nanocrystal-evolution, because kinetic process such like surface diffusion of hydrocarbon species is also involved to assist forming regular shape of copper catalyst particles. Nevertheless, introducing HCl into the reaction offers an opportunity to observe the morphology evolution of nanocrystal as well as helps us understand the diffusion route by enlarging Cu $\{110\}$ facets clearly. The geometry of catalyst particle implies the diffusion might be from $\{110\}$ to $\{111\}$ facets rather than from $\{001\}$ facets, because the $\{110\}$ facets adjoin $\{111\}$ facets by a long edge, as a contrast, the $\{001\}$ facets adjoin $\{111\}$ facets by a very short edge or even by a vertex, which is probably too narrow to establish effective diffusion channel.

Not only gaseous environment but also reaction temperature has strong effect on the surface energy of copper nanocrystals. A series of experiments were progressed at a relatively

higher temperature of 350°C, beyond the temperature that the COT starts to be moveable on the Cu{111} facet¹⁰⁶, and finally resulted in the formation of polymer nano-hexapus. At this temperature, the adsorption and coupling reactions of acetylene is supposed to occur on all {110}, {111} and {001} facets and a new concentration gradient different from that at 250°C established. According to the literatures, the {110} and {111} surfaces convert ~75% and ~60% of the originally adsorbed acetylene to benzene, respectively, while that on {001} facet is only ~30%¹⁰⁴⁻¹⁰⁶. It means that in new concentration gradient, {110} and {111} facets probably have advantages over {001} facets. Combining the present experimental results, it's reasonable to propose that the diffusion underwent in the direction from {111} to {001} facets. However, another diffusion channel from {110} to {001} could not be excluded, although the {110} facets only appeared as edges on the catalyst particle. Briefly, comparing with the growth progressing at the lower temperature, the diffusion route reversed at 350°C, in which {111} facets (and probably {110} facets as well) acted as donors of build up materials of nanofiber. Similar to the process at 250°C, the interaction between copper surface and coupled oligomer molecular reconstructed the copper nanocrystals into truncated octahedron appearance. The excess oligomers precipitated and polymerized on six {001} facets of a copper nanocrystal and then formed six polymer fibers, constructing the 6-branched structure (Figure 5.1(a)). At the end of reaction, when the C₂H₂ was pumped out of the reaction chamber, coupling reaction and diffusion process terminated and the remnant oligomers which had not diffused to {001} facets yet remained on {111} facet. Therefore, few layers of polymer sheets can be observed on {111} facet, even there is no fiber attaching on them (Figure 5.3(c)).

At last, when the reaction was carried out at the moderate temperature of 275°C, the temperature was still too low to activate the COT molecular on {111} facet; therefore the diffusion route might be the same as that at 250°C, from {110} to {111} facets. However, the equilibrium shape of catalyst particle was different, it had the regular tetrahedron appearance (Figure 5.1(f)), instead of the octahedron at 250°C (Figure 5.1(d)). Interestingly, although the catalyst nanocrystal was encompassed by four equivalent {111} facets, only three of them were attached by nanofibers but the last one was missing (Figure 5.1(e)). The reason is still unclear, perhaps relates to the evolution of catalyst shape. We notice that the lengths of three branches of nanostructure are not identical (Figure 5.6(a)), and it implies those branches did not generate simultaneously. At the early stage of reaction, because copper catalyst was in irregular shape, nanofibers initialized only to stretch towards two main directions and the diameters of the two branches were different. The thicker branch congregated more building

up materials from other copper facets (Figure 5.6(b)). During the reaction, the copper catalyst evolved into more symmetrical shape and exposed new growing facets because of the surface reconstruction, but nanofiber stretching out from new facet still merged to the thicker branch by curving itself. The stress became larger along with the new facet growing. When the stress was high enough, the new branch would eventually generate and stretch out in its intrinsic direction. Once the third branch generated, the stress was released and the nanostructure became stable again. There was probably not enough ‘driving force’ to trigger further generation of the fourth branch. Therefore, the reaction only synthesized 3-branched nanostructure instead of 4-branched. Furthermore, it’s reasonable to predict that 4-branched nanostructure could be obtained by optimizing reaction parameter or changing catalyst system, but 5- or 7- branched nanostructures are impossible because they conflict the fundamental symmetry of crystal.

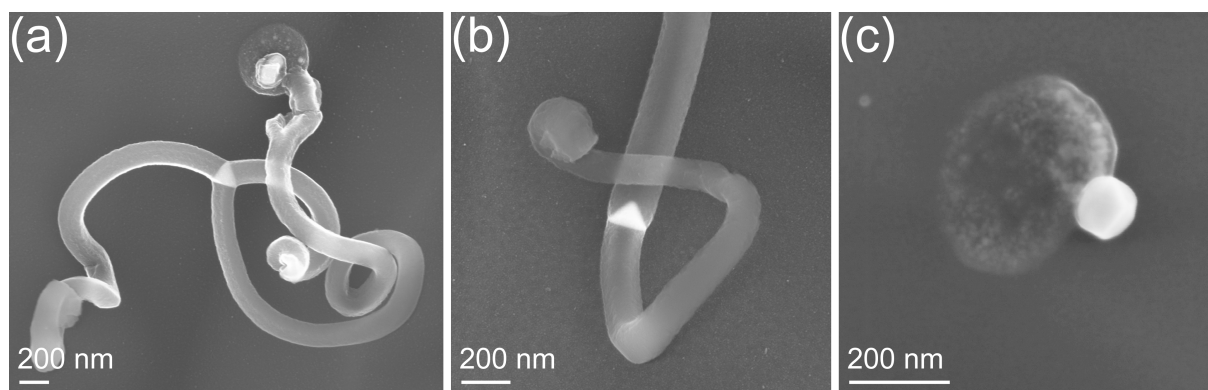


Figure 5.6. SEM images of: (a) A 3-branched nanostructure with one branch sticking on Si wafer. (b) An asymmetrical 2-branched nanostructure synthesized at 275°C. (c) A copper nanoparticle attaches on a carbon island on Si wafer.

All above mentioned carbon nanostructures which progressed at different temperatures and gaseous environments could be described as an adsorption (Vapor) - diffusion (Facet) - precipitation (Solid) process and we name it as VFS mechanism to distinguish from the classical VLS mechanism and vapor-solid-solid (VSS) mechanism¹⁴³, since a surface diffusion process of hydrocarbon dominates the whole process instead of bulk/surface diffusion of carbon atoms. This mechanism features: i) Competition among different catalyst facets is the core factor (See Figure 4.5). The facets on which C_2H_2 molecular is absorbed and couples are defined as adsorbent facets, while the facets receiving coupling products and finally building up the polymer nanofibers are defined as growth facets. The adsorbent facets and the growth facets may reverse, depending on surface reactions and surface energy of catalyst nanocrystal, which are actually influenced by reaction temperature and gaseous environment; ii) The loose stacking nanostructure of polymer sheets allows the new build-up

units to insert themselves into gaps between existing nanofibers and the copper facets, and consequently to lift the old nanofibers up a bit to become a new part of it. It presents that the existing nanofibers do not act a barrier blocking further growth of themselves. iii) Catalyst nanocrystals have undergone a surface reconstruction process, and turned into regular appearance with certain low index and smooth facets, which correspond to its intrinsic symmetry.

In addition, an important feature of synthesized polymer nanostructures is surface-bound, in which they always had one branch sticking on the substrate after growth. It is due to the unique preparation process of catalyst nanocrystals. Figure 5.6(c) shows an SEM image of the Si wafer which was coated by copper containing gel and then underwent ECR plasma bombing. Energy-dispersive X-ray spectroscopy (EDS) analysis confirms the bright particle is composed of copper and the main composition of the large gray island under copper particle is carbon. During the catalyst preparation process, the copper containing gel shrank into islands on the Si wafer in plasma environment and then the copper further enriched to form several nanoparticles on each island, separated from carbon-containing matrix. In next growth process, once C_2H_2 was introduced into the system at reaction temperature, the polymer fibers started to grow from the bottom side of copper nanoparticles, connecting the residual carbon islands on Si wafer and copper catalyst nanocrystals together, lifting the copper nanoparticles up when the branch stretched longer. Therefore, after growth, the branch was always bound to the substrate, just like the longest branch in Figure 5.6(a). This feature grants us the possibility to obtain nanostructures at desired positions by pre patterning of catalysts or copper containing gel selectively. No doubt, the as-synthesized nanostructures can be further tailored such as removing or cutting several branches by post micromanipulation to assemble certain nanocircuits.

5.5 Summary

2-, 3-, 6-, 8-branched carbon nanostructures were synthesized by using a universal facet-selective-catalytic growth method in thermal CVD device, and the intrinsic symmetry of nanocrystal catalysts is the key factor of the morphology tailoring of polymer/carbon nanostructures. The number and length of branches can be controlled by changing reaction temperature, atmosphere and duration. The diameter of branches and the location of whole nanostructures are also controllable by means of proper catalyst preparation and pre patterning. In the growing process, coupling reaction of hydrocarbons species (C_2H_2 in this case) takes place on the surface of catalyst nanoparticles, subsequently a surface diffusion

process between different catalyst facets induces the growth of nanofibers. It exhibits different features than the well-known VLS and any other growth mechanism based on diffusion of dissolved carbon atoms⁹⁵, hence we proposed hereby a new one named VFS (vapor-facet-solid) mechanism. The catalyst-facet selectivity is derived from different facet specific adsorption energies of C_2H_2 and its coupling reaction products on copper surface. During the growth, the interaction between copper surface and hydrocarbon molecular always reconstructs the copper catalyst nanoparticles into regular appearance with certain low index facets exposing out.

6. VFS growth with aid of other transition metal catalysts

Aforementioned Cu catalyzed low-temperature CVD process is a typical case of VFS growth. Two primary factors determine that VFS mechanism dominates the process rather than VLS. Firstly, carbon has extremely low solubility in Cu catalyst so that the VLS approach which relies on carbon solution and diffusion is unrealistic. On the other hand, intense surface reactions on Cu low-index faces create various hydrocarbon molecules as building block for PNs construction. It thus makes the VFS process be possible. Accordingly, we have no reason to exclude the possibility of VFS mode from processes with aid of other transition metal catalysts, such as Fe, Co, and Ni, especially when a growth progresses at a much lower temperature comparing with a typical VLS process. In that case, the carbon solubility as well as diffusion coefficient decline significantly with decreased temperature, even for Fe, Co, Ni catalysts⁴³⁻⁴⁵. Meanwhile, the study about the interaction of acetylene with low-index Fe, Co, Ni single-crystalline surfaces under UHV conditions has identified various hydrocarbon molecules^{46, 111, 144-149}, which represent potentially crucial intermediates for the synthesis of PNs in a low-temperature VFS process.

With above concern, in this chapter we prepare Fe, Ni catalyst with different appearance to synthesize PNs by using thermal CVD as the growth technique. The correlation between the microstructures of the resultant novel PNs and the geometry features (shape, size and facet index) of the corresponding catalysts is researched in detail. The results not only reveal the universality of VFS model, but also help for establishing an in-depth understanding of this mechanism.

6.1 Fe catalyzed nanostructure-growth of at low temperature

6.1.1 Experimental facts

Large amount of Fe nanopowder with approximately spherical shape was prepared using vacuum arc plasma jet evaporation method, see chapter 3.1.4, and then this catalyst was employed in CVD growth processes for 2h at different temperatures, see chapter 3.2.

In correspondence with respect to the process temperature different phenomena were observed. At process temperatures beyond 300 °C an onset of a roughening effect of the catalyst particle surfaces was observed. At process temperatures of 350 °C the surface roughness was sufficient to facilitate nanofiber growth, see Figure 6.1.

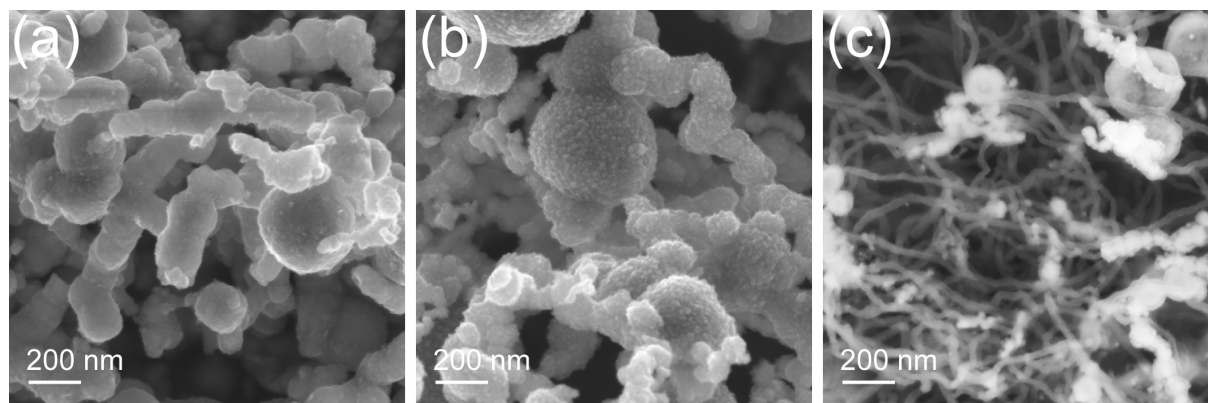


Figure 6.1. SEM images of samples prepared via Fe nanopowder catalyzed CVD processes at: (a) 250 °C, (b) 300 °C, (c) 350 °C.

The nanofibers featured a uniform diameter of about 30 nm and all structures solely showed a tip growth mode. In this context it was found that smaller Fe catalysts particles detach from their roughened host particle and, subsequently, are responsible for the growth of the nanostructures, see Figure 6.2.

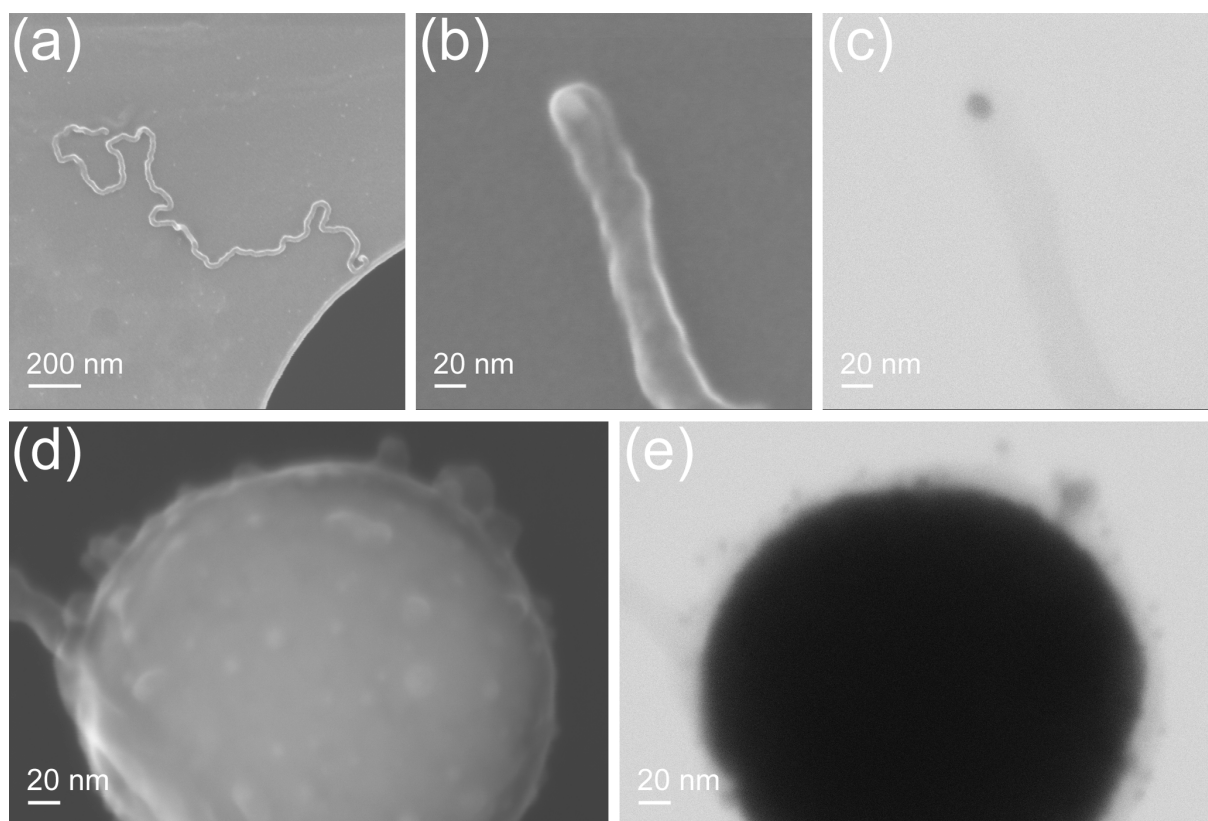


Figure 6.2. SEM images of nanofiber prepared via Fe nanopowder catalyzed CVD process at 350 °C: (a) an individual nanofiber; (b) tip of the nanofiber. (c) STEM images of a catalyst particle embedded in the tip of the nanofiber. (d) Early stage of the growth: SEM image of Fe particle covered by growth product. (e) STEM image taken from the same position as Figure 6.2(d) indicating the detachment of small Fe particles from the surface of the host particle

Elemental analysis, which showed a composition with high hydrogen content (Table 6.1), strongly suggested a polymer-like structure of the as-grown fibers. This polymer-like structure was also reflected by XPS measurements. Here, a very intense C 1s peak appears at a binding energy of 285.4 eV and a weak O 1s peak appears at 533.7 eV, respectively (Figure 6.3). These values agree with that of C-H/C-H-O polymer rather than typical pure-carbon based material, such as graphite and CNT which should show a C 1s peak at 284.6 eV.

Table 6.1. The composition of as-grown sample.

	C	H	O	Fe
wt. %	57.5	1.6	1.0	39.9
at. %	66.9	22.2	0.9	10.0

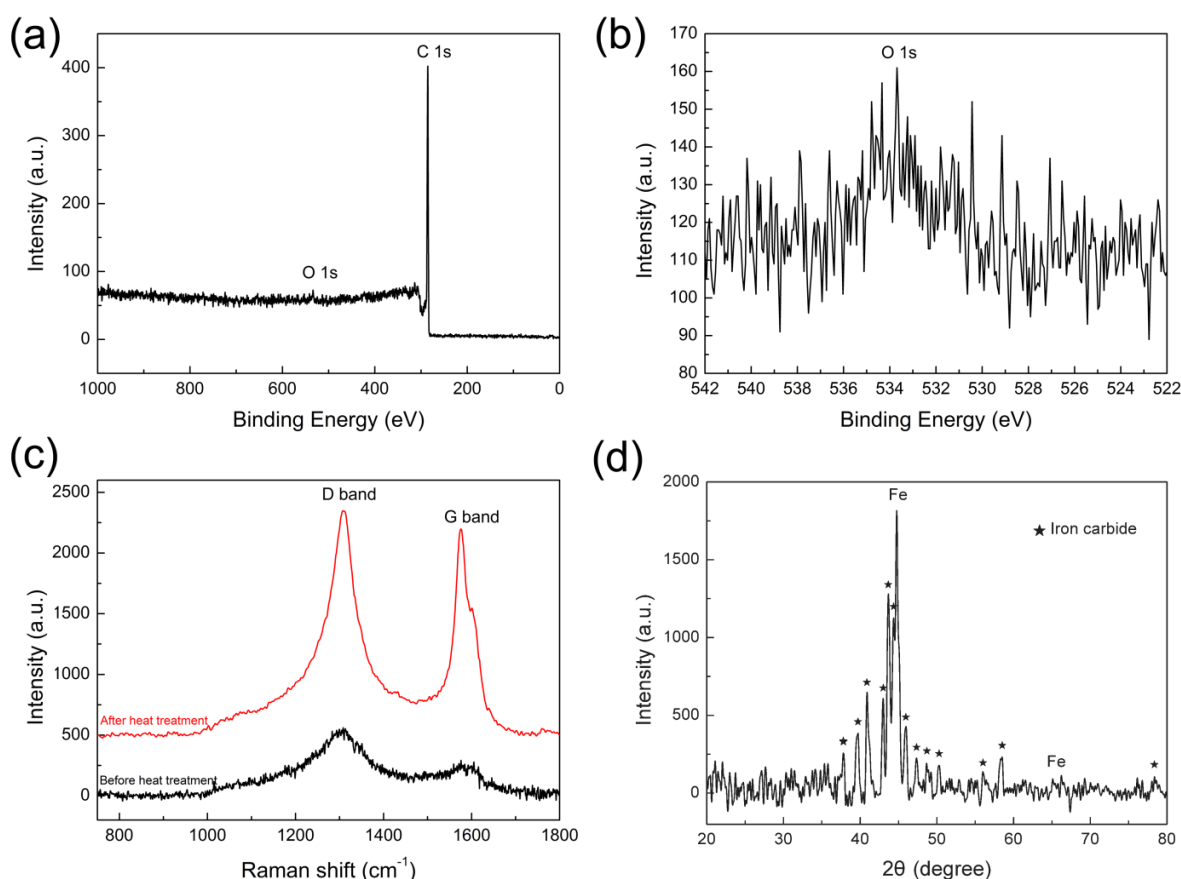


Figure 6.3. XPS spectra (a) survey of as-grown nanofiber; (b) O 1s peak. (c) Raman spectra of as-grown nanofiber before and after an 800 °C heat treatment. (d) XRD spectra of an as-grown sample.

The organic fragments released by the as-grown nanofibers during a 300°C thermal desorption were analyzed by TD-GC/MS. Statistical results are presented in Table 6.2. The

complete list of TD-GC/MS results is given in the Appendix A. In principle all detected molecules feature a planar cyclic structure and contain one or more aromatic rings. Larger and thus thermally more stable hydrocarbon molecules, which represent the building blocks of the nanofibers, were observed by ESI-MS, see Figure 6.4.

Table 6.2. Molecules detected in GC/MS measurement.

Substance	Peak Area (a.u.)	Area Percentage (%)	Toluol-equivalent (mg/kg)
Indene and derivative	42094224	7.2	6836
Naphthalene and derivative	76410839	13.0	12409
Biphenyl and derivative	57143090	9.7	9280
Fluorene and derivative	192087175	32.8	31194
Phenanthren and derivative	74134538	12.6	12039
Anthracene and derivative	48020722	8.2	7798
Pyrene and derivative	14000608	2.4	2274
Other aromatic hydrocarbons	82596082	14.1	13413
Sum	586487278	100	95243

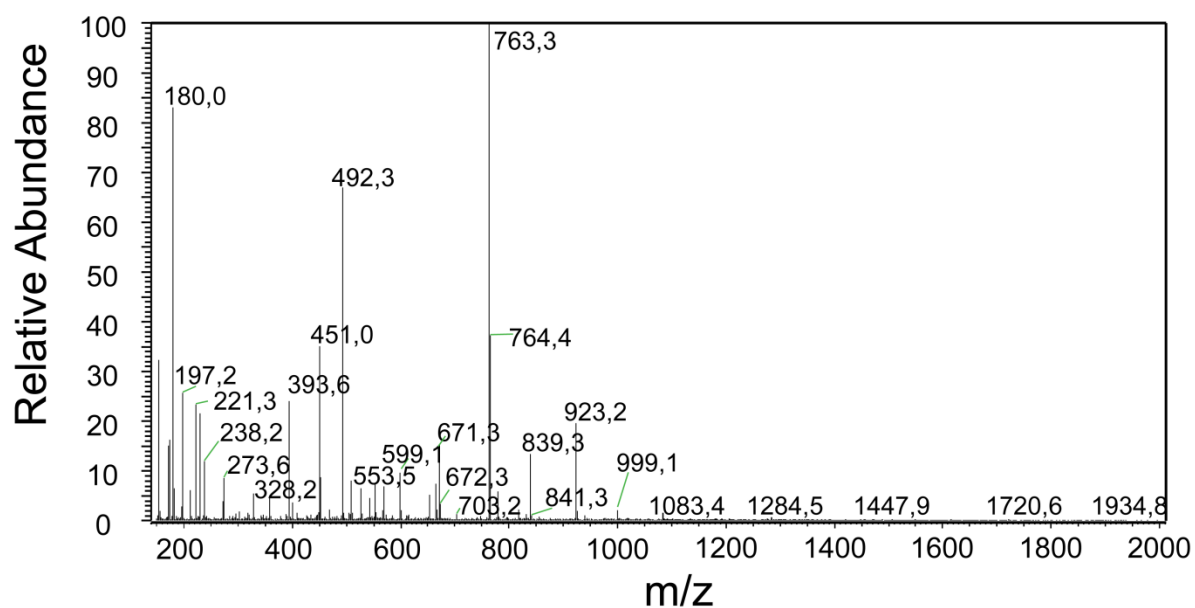


Figure 6.4. ESI-MS spectrum of the as-grown nanofibers.

Furthermore, micro-Raman spectroscopy was utilized to evaluate the microstructure of the as-grown nanofibers. Unfortunately, the spectrum shown in Figure 6.3(c) features a low signal-noise ratio. Nevertheless, the characteristic carbon D and G band at $\sim 1308\text{ cm}^{-1}$ and $\sim 1575\text{ cm}^{-1}$, respectively, can still be observed. The peaks appear relative broad, which indicates a poor ordering of the sample. According to the $I(D)/I(G)$ ratio found in the spectrum, a cluster size L_a of 0.82 nm can be calculated^{139, 140}. A heat treatment of the polymer nanofibers at 800 °C for one hour causes a substantial carbonization of the structures and hence increases the Raman signal significantly, as also illustrated in Figure 6.3(c).

Supplementary TEM analysis of the nanofibers revealed interesting structural details, see

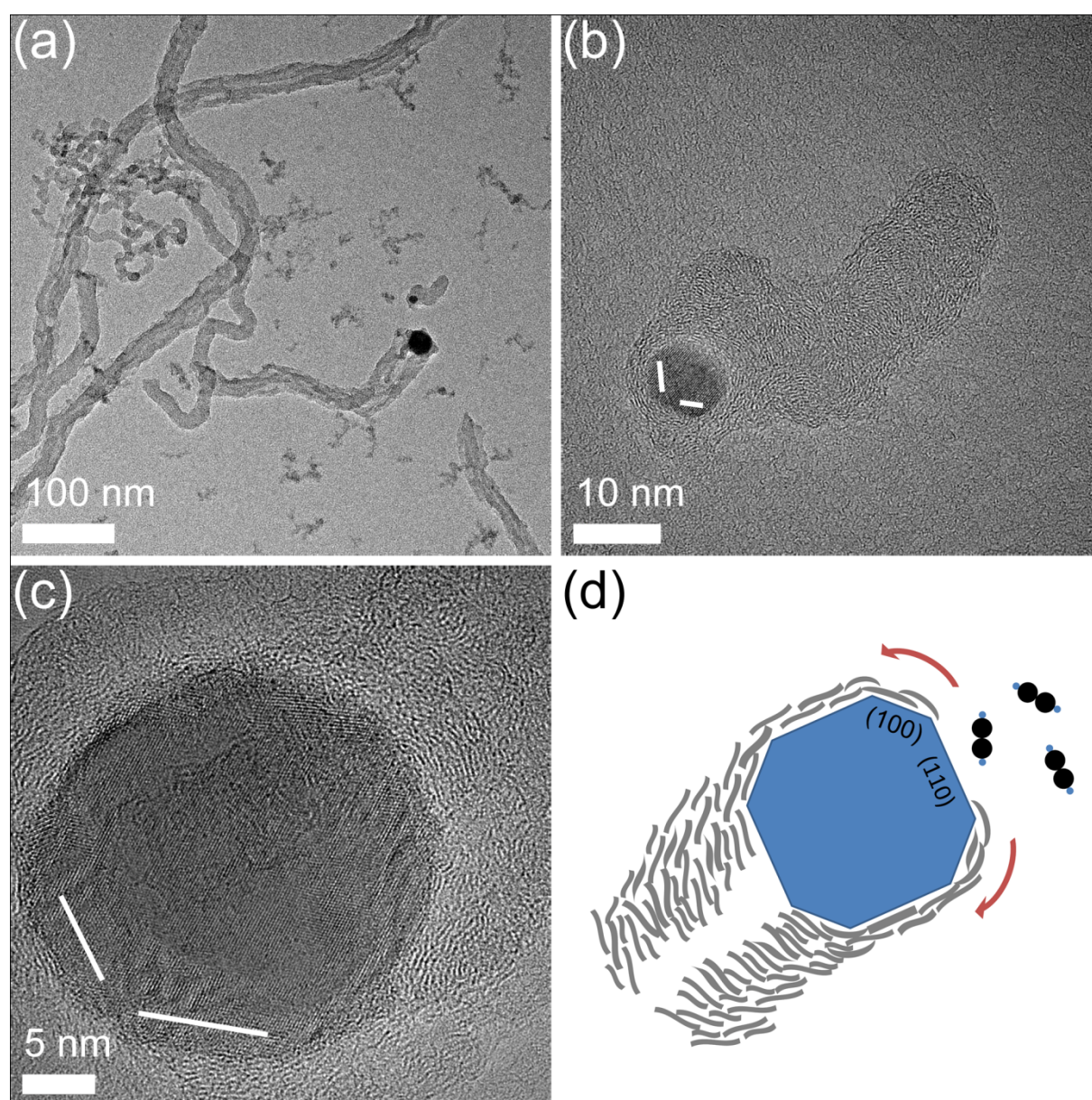


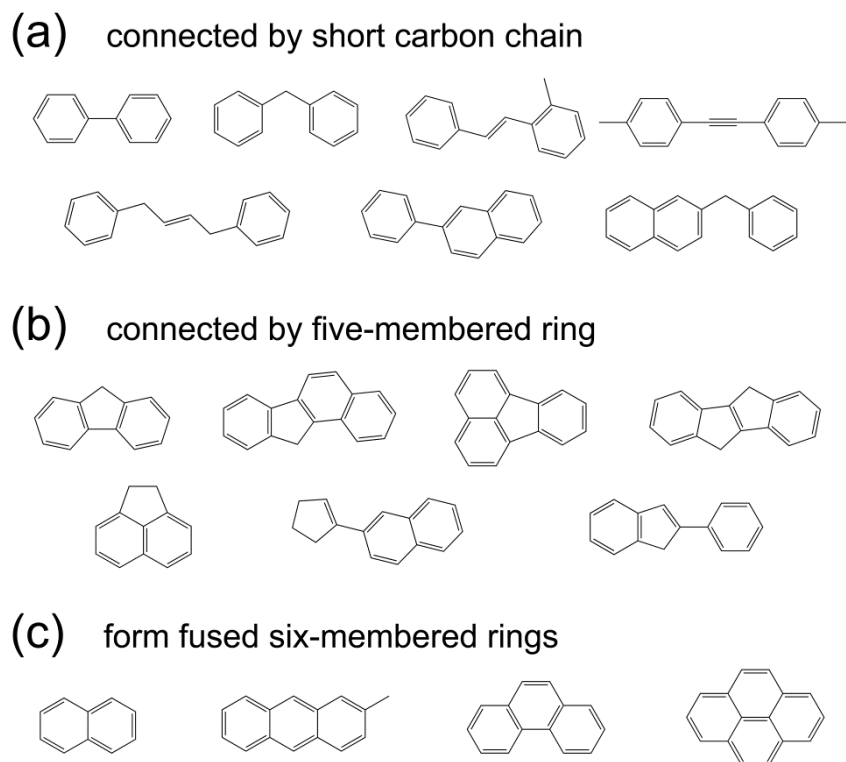
Figure 6.5. (a) TEM image of the nanofibers, (b) HRTEM image of a short solid nanofiber, (c) HRTEM images of Fe catalyst particle in a tubular-like nanofiber, (d) sketch of the growth process.

Figure 6.5. The structures show either tube-like or solid geometry depending on the size of their corresponding catalyst particle. The fibers consist of small discontinuous, stacked carbon sheets showing a limited order. Consequently the fibers feature a structure between the characteristics of graphite and amorphous carbon, which is reflected in the Raman spectrum. Furthermore, the dimensional features of carbon sheets observed in TEM, showing diameters between 0.5 and 1.5 nm, also agree well with the Raman results. The Fe catalyst particle at the tip of the structure features a polygonal projection, revealing a regular shape of the catalyst particle. This finding combined with the inside offered by corresponding HRTEM images (Figure 6.5(b) and (c)), which provide information about the crystalline lattice, allows for the indexing of the facets of the catalyst.

6.1.2 Discussion

Combining the review on existing literature provided above and our own experimental findings, we are in a position to can propose the growth mechanism. As previous research carried out at ultra-high vacuum (UHV) condition was able to show that the adsorption of C_2H_2 on a Fe surface induces the formation of various hydrocarbon species such as methane, ethane, butane and benzene, but never found any evidence of C3 and C5 products, it was always assumed that the former were created via hydrogen abstraction, C-C bond breaking, dimerization, and trimerization of C2 entities⁴⁶. In the present study, however, TD-GC/MS was able to detect and identified more than 50 kinds of hydrocarbon molecules present in our as-grown nanofibers. All of them feature a planar structure and contain at least one benzene ring, hence can be considered as benzene derivative. Consequently it can be concluded that a trimerization reaction, which occurs on the Fe surface and couples C_2H_2 to form six-membered rings, is the basis of the nanofibers growth studied here. Subsequently, these benzene rings act as fundamental structural units and are able to form other planar molecules. Among the paths to construct other molecules are a connection by short carbon chains, one that includes five-membered rings as well as a third that results in the formation of fused six-membered rings, see Scheme 6.1.

Scheme 6.1. Molecules identified by TD-GC/MS present in as-grown nanofibers utilizing benzene rings as fundamental building blocks

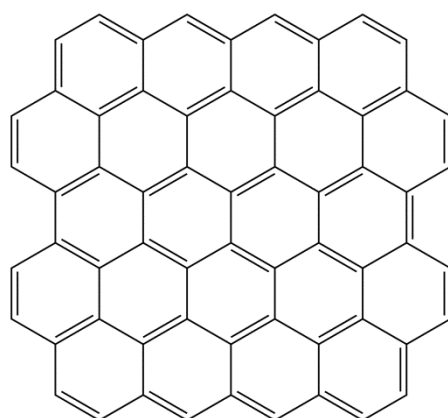


Due to the limited operating temperature of thermal desorption, TD-GC/MS only detected small volatile hydrocarbon molecules, but it's reasonable to assume that larger, thermally stable integrate polymer sheets, which contain more aromatic rings, exist in the as-grown nanofibers. Finally, we were able to observe such sheets directly by HRTEM (Figure 6.5(b)) as well as by ESI-MS measurements (Figure 6.4). Additionally, their existence is confirmed by calculations based on the corresponding Raman spectra (Figure 6.3(c)).

Elemental analysis also delivers important structural information. For any planar molecule based on benzene rings the C/H ratio increases with increasing number of rings involved (in particular, an individual benzene molecule that contains only one ring features the lowest C/H ratio of 1.0). Here we consider a planar molecule constructed of pure fused six-membered rings, similar to the structure in scheme 6.1(c) but with more benzene units, see scheme 6.2. A simple calculation is able to show that a molecule consisting of 22 rings will feature a C/H ratio of 3.1, a size of 1.2 nm, and a m/z value of 764, respectively. These parameters are in precise agreement with the results provided by elemental analysis, HRTEM image as well as the first high intensity peak observed in the ESI-MS spectrum. Aside from carbon and hydrogen, the role of oxygen is also not insignificant. Elemental analysis confirmed small amounts of oxygen in the as-grown nanofibers. Furthermore, TD-GC/MS

was able to identify the presence of an oxygen containing molecule (9H-Fluoren-9-one). In the XPS spectrum the binding energy of carbon and oxygen peak locate in the region corresponding to C-H-O polymer. In addition, oxygen was found to accelerate the growth of the nanofibers. A likely explanation for this finding might is that a small amount of oxygen acts as free radical and promotes the construction of polymer sheets.

Scheme 6.2. *An imaginary Molecule.*



Chemical Formula: $C_{62}H_{20}$

Exact Mass: 764.16

Molecular: 764.82

m/z: 764.16(100%), 765.16(67.3),
766.16(22.1%), 767.17(4.8%)

Elemental Analysis: C, 97.36; H, 2.64

However, the existence of a mechanism that allows for the formation of polymer sheets does not necessarily imply that a fiber like structure will grow. The latter only happens if a stable transportation path between products' generation and precipitation/extrusion is established on the catalyst. Otherwise the polymer formed will simply accumulate on the surface until the whole catalyst particle is covered. This will prevent any further surface reaction and consequently any growth as well. In order to understand such a growth process in more detail, it is therefore necessary to consider its two key factors, i.e. diffusion route and driving force. In the classical VLS mechanism, it is assumed that a carbon containing source gas initially absorbs on the catalyst surface, followed by a thermal dissociation process leaving carbon behind. These carbon atoms will, subsequently, diffuse through the catalyst particle and extrude on the opposite side. Carbon dissolving-precipitation is involved in this process and the carbon concentration gradient in the catalyst particle is the most popular interpretation basis of the driving force required for the diffusion process. However, in the present study hydrocarbon molecules instead of carbon atoms act as structural units to construct the nanofibers. Large sized hydrocarbon molecules hardly dissolve in Fe particles, let alone pass through them. Therefore, the surface of a Fe particle is the only feasible diffusion route. In all HRTEM images taken in the framework of this study the Fe catalyst particles always showed a polygonal projection and always featured the (110) face as growth

front. This observation strongly suggests that surface diffusion takes place from Fe(110) to other low index faces. For emphasis, the (110) faces are marked by white lines in the corresponding HRTEM images (Figure 6.5(b) and (c)).

The diffusion is ascribed to the different catalytic activities of the various crystalline faces of Fe. Although C_2H_2 trimerization represents the key process responsible for the formation of nanofibers, it isn't the sole reaction occurring on Fe surface. The C_2H_2 dissociation also contributes to the diffusion process by generating a carbon layer to selectively shield certain crystalline face of the Fe catalyst. Theoretically^{144, 145} as well as experimentally^{146, 147, 150-152}, there is evidence for the Fe(100) face to be more active with respect to C_2H_2 than Fe(110) or (111). In temperature-programmed thermal desorption spectroscopy (TDS) investigations carried out under UHV condition, after a pre-adsorption of C_2H_2 , desorption was found on the Fe(110) and (111) faces. In contrast, all chemically absorbed C_2H_2 on the Fe(100) faces dissociated during the thermal evolution, leaving carbon on the corresponding catalyst surface¹⁴⁶. The TDS research proved also sensitive to the situation where the Fe(100) face was pre-covered by carbon and subsequently exposed to C_2H_2 . In such a situation a desorption process is only able to detect a significantly decreased amount of H_2 . The latter corresponds to a significantly decreased surface activity with respect to the formation of various hydrocarbon species¹⁴⁶. Therefore, it can be deduced that carbon layer already accumulated on a Fe(100) surface prevents further surface reaction which potentially lead to the formation of hydrocarbon species.

In summary, combining all of the arguments provided above, the actual growth process can be schematically presented by Figure 6.5(d). Initially, C_2H_2 is absorbed on the Fe (100) face followed by a thermal dissociation process leaving carbon on the surface. At a relative low reaction temperature of about 350°C, however, carbon atoms hardly pass through the Fe catalyst particle thus accumulate in the surface region and result in superficial carburization to form iron carbide, see the XRD data shown in Figure 6.3(d). The carbon atoms incorporated in this region also tend to induce local lattice distortion in the Fe catalyst, which can be observed in HRTEM images, refer to Figure 6.5(c). In this particular image it is quite obvious that the Fe particle features larger lattice distances on the side compared to the ones found at the growth front. This carbon layer locally prevents further surface reactions. On the Fe(110) face, however, the surface reactions stay active because of its weaker dissociation reaction and lower carbon atoms generation compared to the (100) face. Low molecular weight hydrocarbon species form here and, driven by a concentration gradient, diffuse towards the blocked Fe(100) face. Parallel to the pure diffusion process small hydrocarbon molecules

connect or fuse to form larger polymer sheets. The reaction products accumulate on the (100) face and finally start to extrude from the particle initiating the formation of the nanofiber.

The key aspect of the growth mechanism proposed here is the competition as well as cooperation between different crystalline faces of the catalyst. As mentioned above, it was observed that small Fe catalyst detach from large spherical host particles prior to the onset of any growth of nanofibers. This can be interpreted in such a way that the interaction between C_2H_2 and Fe has to reform the Fe surface by stabilizing and enlarging the low index crystalline faces in order to finally meet the requirements for growth. However, such a ‘surface reconstruction’ is limited and strongly depends on temperature. In case of a process temperatures of 300 °C or lower, although the surface reactions lead to the generation of a polymer layer and a corresponding surface roughening, no independent small Fe catalyst formed and consequently no synthesis of nanofibers was found (Figure 6.1(a) and (b)). Additionally, we prepared different catalyst types to be studied with respect to their behavior in identical growth processes. In particular, bulky Fe slugs featuring rough surfaces as well as Fe nanoparticles featuring sizes on the order of 30 to 100nm, synthesized by a sol-gel process, on Si wafer surfaces were prepared. After the corresponding growth process all of the surfaces were covered by polymer but none of them showed any fiber like structures, see Figure 6.6 and Figure 6.7. These finding imply that even though carbon containing material was created on the surface, no stable diffusion path between an absorption site and a potential precipitation site could be established.

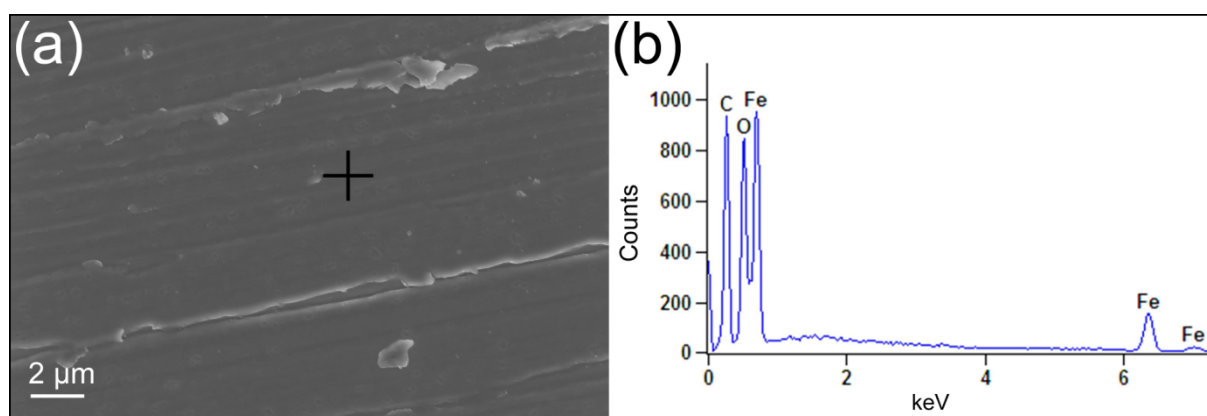


Figure 6.6. (a) SEM images and (b) EDS spectra of the Fe slugs after the growth at 350°C for 2 hours.

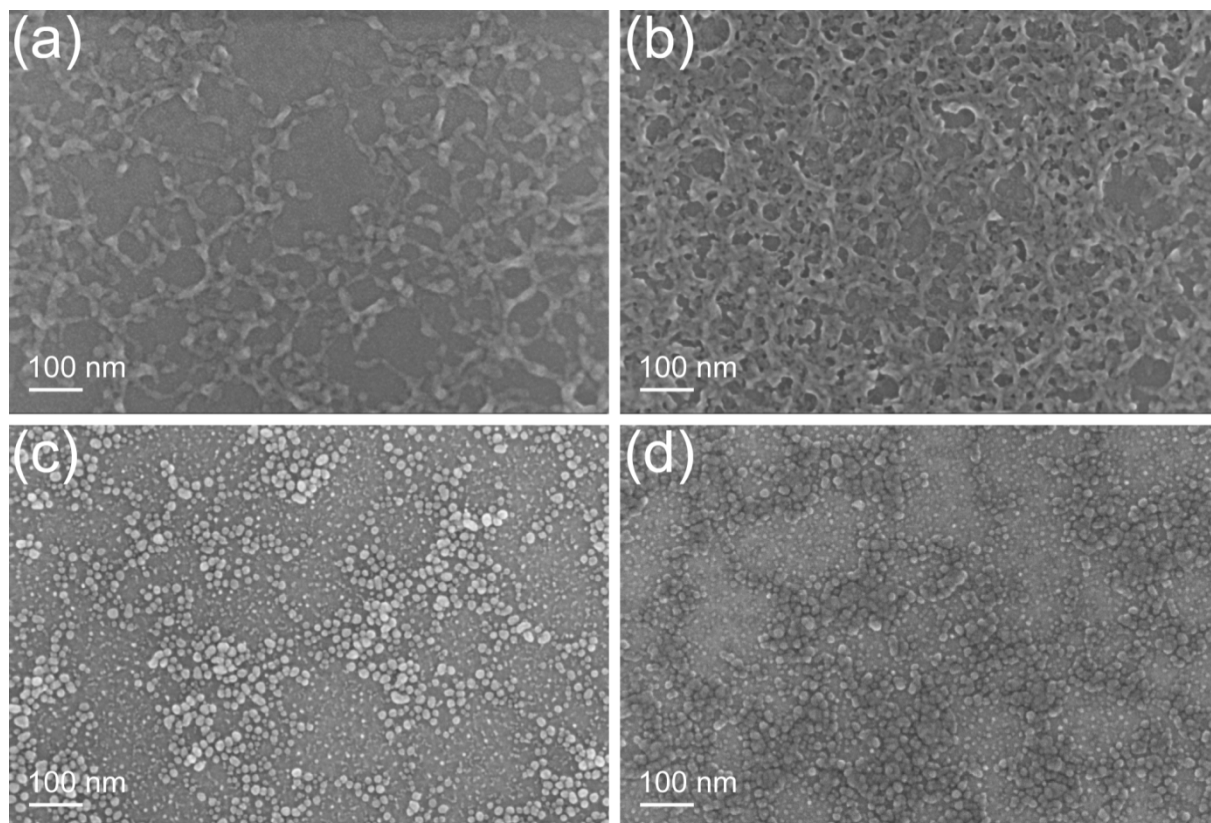


Figure 6.7. SEM images of: (a) Fe network on Si wafer; (b) Fe network wrapped by carbon layer after growth; (c) dispersed Fe nanoparticle on Si wafer; (d) dispersed Fe nanoparticle wrapped by carbon layer after growth.

6.1.3 Summary

Nanofibers were successfully prepared by means of a thermal CVD process at temperatures as low as 350°C. The growth process featured three distinct characteristics: i) surface reactions based on the coupling of C_2H_2 provided the basic building blocks required for the formation of polymer like nanofibers. In this context C_2H_2 initially formed six-membered rings via a trimerization reaction occurring on the Fe surface. Subsequently, these units coupled to construct larger planar molecules. This coupling potentially followed three paths, here a connection by short carbon chains or five-membered rings or even a fusion of multiple six-membered rings was found. ii) The competition and cooperation between different crystalline faces of the Fe catalyst induced a stable diffusion. Due to the different catalytic activities of the various Fe crystalline faces, carbon atoms which are generated in a C_2H_2 dissociation block the Fe(100) face but not the Fe(110) face leaving the latter free to continuously participate in the coupling reaction. Furthermore, this phenomena induces a concentration gradient which drives the diffusion of reaction products from the Fe(110) to the (100) faces along the surface of catalyst particle. These hydrogen rich coupling products accumulated on the Fe(100) faces in form of polymer sheets and finally extruded to initiate

the growth of a nanofiber. iii) the interaction between C_2H_2 and the Fe surface reshapes the topology of the Fe catalyst during the process. It is not only responsible for the detachment of small Fe particles from the surface of the original spherical host particle, but also reconstructs the surface of these small Fe particles by stabilizing and enlarging low index faces. As a result small Fe particles featuring a regular shape act as the true catalysts inducing a tip growth mode of nanofibers which feature a uniform diameter.

The growth process observed during this study is completely different from the classical VLS mechanism but agrees well with the Vapor-Facet-Solid (VFS) growth model, which we firstly proposed to explain Cu catalyzed nanostructure growth at low temperatures. Therefore, the proposed VFS mechanism appears to be not limited to the special case of the C_2H_2 -Cu system but rather applicable to the general case of nanostructure growth at low temperatures.

6.2 Ni catalyzed nanostructure-growth at low temperature

The results of the Fe catalyzed low temperature CVD growth reveal the extensive applicability of VFS mechanism. However, the Fe catalyst exhibits obviously different behavior from Cu during the growth. The Fe catalyzed process follows solely the tip-growth mode. Multiform symmetrical nanostructures and size effect, which appear as characteristics of the Cu catalyzed growth, absent in the Fe case. In addition, large sized symmetrical catalyst particle has never been seen in as-grown sample, revealing a poor evolution-ability of Fe catalyst. The discrepancies are possibly due to the difference on crystalline characteristic, if we notice that Cu has a fcc lattice but Fe features bcc at present growth temperature. Indeed, the geometry feature of catalyst particle, the morphology of as-grown nanostructure, the packing of atoms on catalyst free surface as well as the role of each low index crystalline faces of catalyst in the VFS process all tightly correlate to the intrinsic symmetry of catalyst metal. Therefore here we use another transition metal namely Ni to catalyze the low-temperature CVD growth. Because Ni has fcc lattice, similar to Cu, the result is a helpful supplement for a comprehensive understanding of the general VFS mechanism.

6.2.1 Bulky Ni catalyzed growth

For a quick insight into the catalytic activity of Ni at low temperature, bulky Ni Slug (Alfa Aesar, 99.98%) was used as catalyst precursor. To obtain a rough and clean surface, Ni slug ($\varnothing 6.35 \times 3$ mm) was polished by an abrasive paper (800 mesh) and then washed by distilled water and ethanol, respectively. Finally the slug was dried in warm air flow. The morphology of the Ni surface undergone abrasion is shown in Figure 6.8.

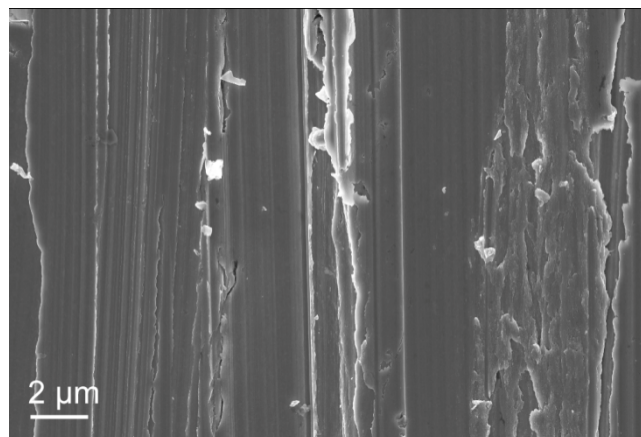


Figure 6.8. SEM image of the Ni surface after abrasion.

The pre-treated Ni slug was put into a ceramic boat and subsequently sealed in the quartz tube (reaction chamber) of the thermal CVD device. Then a standard growth progressed as the description in chapter 3.2. The process was carried out with an initial pressure of 500 mbar and lasted for 1h.

To determine the lower-limit of reaction temperature which allows for NFs growth, a series of experiments were carried out at 350, 300, 275 and 250°C, respectively. SEM images taken from the surface of as-grown Ni slug are shown in Figure 6.9. It shows that flower-like structure appears on the Ni slug which underwent a 350°C growth. Each petal of the flower actually consists of a bundle of NFs (Figure 6.9(a)). When the processes progressed at lower temperature of 300°C (Figure 6.9(b)) or 275°C (Figure 6.9(c)), similar structures still can be observed. However, for all above three samples, the flower-like structures only cover a small proportion of the Ni surface. The rest area shows a major topography agreeing with the original sanded Ni slug. But this area becomes smoother after growth because of uniformly covered reaction product. The deposition of reaction product was evaluated by EDS. Corresponding sampling points are marked by crosses in the SEM images. In principal, the intensity of received carbon signal in EDS decreases with the growth temperature decreasing, see Figure 6.9. It indicates that when a lower growth temperature was applied, less/thinner carbon-based reaction product deposited on the Ni surface. In particular, when the process was carried out at a temperature as low as 250°C, the surface of as-grown sample is quite clean (Figure 6.9(d)). EDS analysis only get very weak carbon signal. Meanwhile, this sample almost keeps the original morphology of the sanded Ni surface. Therefore, we can deduce that the growth of NFs requires about 275°C or a higher temperature. This kind of NF growth activation temperature is far below the typical ones reported for NF preparation processes,

which are associated with the VLS growth mechanism. Even to compare with those low-temperature growths reported in literature, present process temperature is 75°C lower¹⁵³.

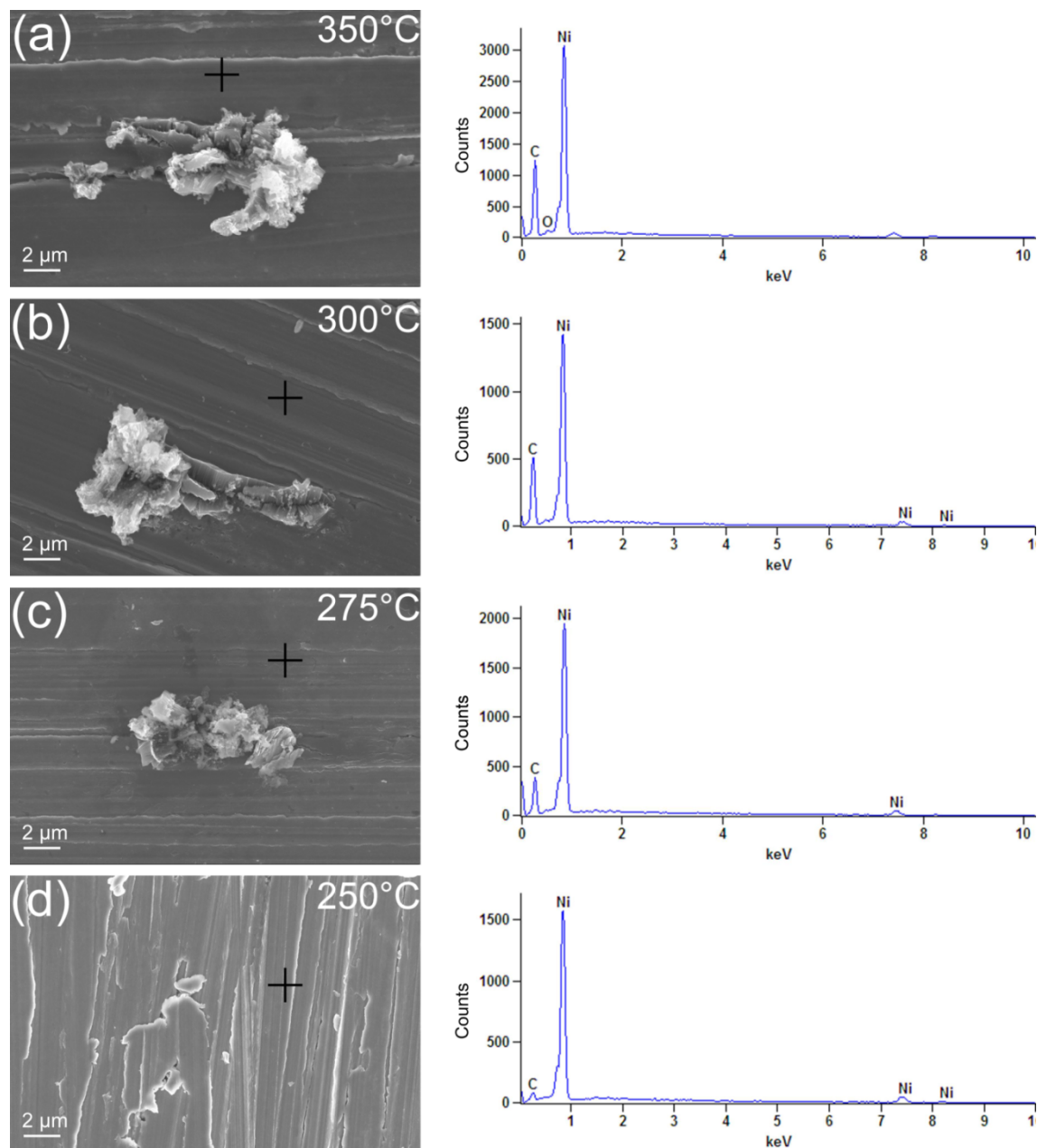


Figure 6.9. SEM images and EDS spectra taken from the surface of Ni slugs which underwent the growth at (a) 350°C, (b) 300°C, (c) 275°C, (d) 250°C .

Detailed features of the 350°C grown nanostructure are shown in Figure 6.10. Typically, the obtained structures can be described as featuring a root, a stem and a top region. Figure 6.10(b) shows the enlarged SEM image focusing on the root of nanostructure. It can be seen that the stems of the nanostructures are constructed by bundles of NFs. They spread to different directions from the root. To confirm the position of Ni catalyst in as-grown

nanostructure, energy selective back scattered (ESB) image is recorded simultaneously with SEM image. Ni particles emerge as bright spots in this image. They always appear at the locations where stems converge (Figure 6.10(c)).

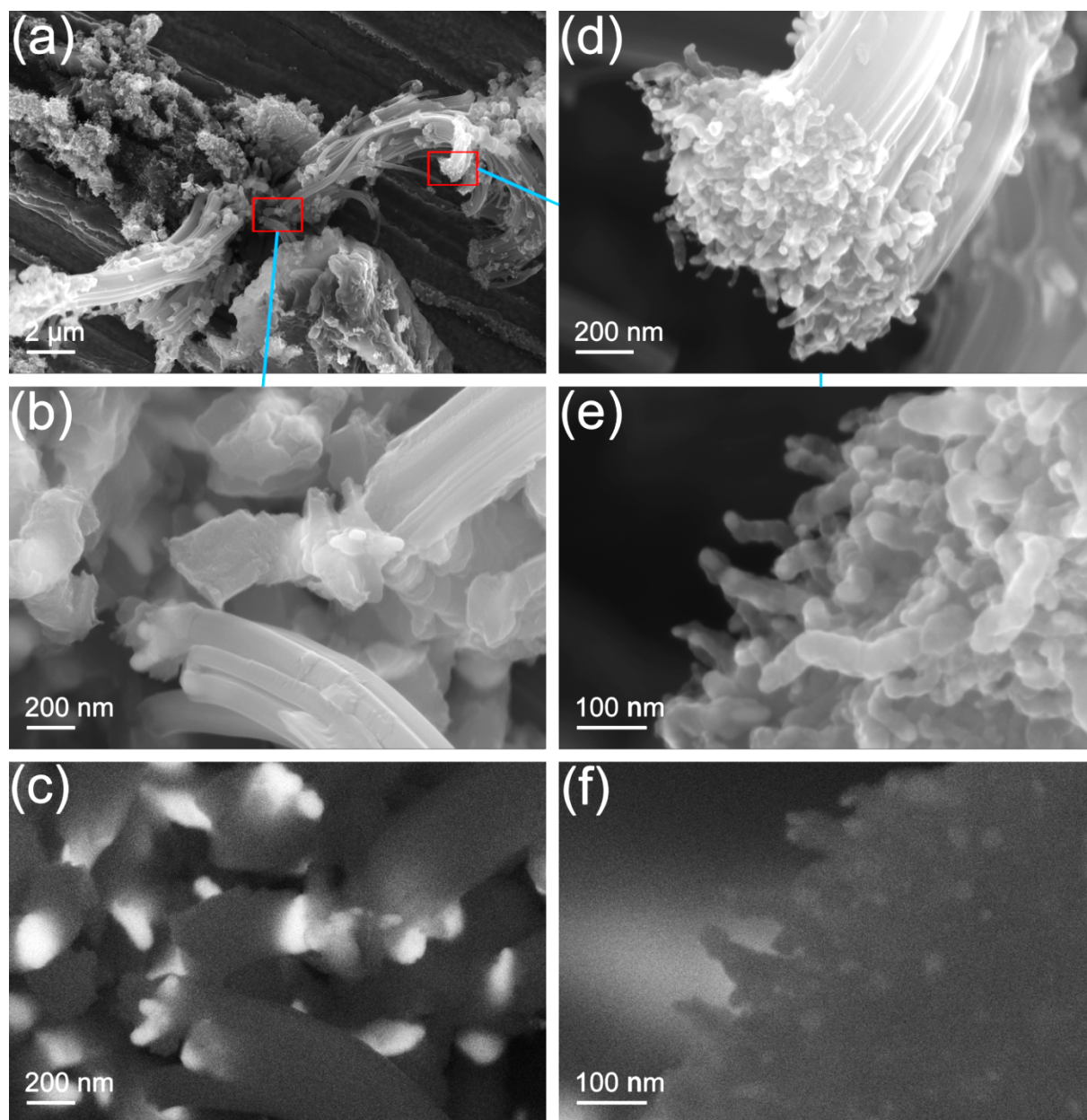


Figure 6.10. SEM images of the nanostructure prepared at 350°C: (a) integrated nanostructure; (b) enlarged image of the root section; (c) ESB image of the root section; (d) enlarged image of the top section; (e) further enlarged image of top section; (f) ESB image of the top section.

Meanwhile, the nanostructure features an absolutely different morphology at the top section. A mass of thin NFs alien to form a dense array on the top of flower-like structure, see Figure 6.10(d). Further enlarged SEM image (Figure 6.10(e)) clearly shows that these thin NFs have diameters less than 50 nm. A simultaneously recorded ESB image indicates that the Ni particles locate in the tips of the thin NFs, see the weak bright spots in Figure 10(f).

Therefore two different growth modes coexist in present experiment, i.e. tip-growth and base-growth (or symmetrical-growth, because usually two stems spread to opposite directions from the center located Ni catalyst particle). In addition, we can see a dependence of the growth mode on the size of Ni catalyst particle. Here tip-growth is only observed when Ni particle is smaller than 50nm, and Larger Ni particles always correspond to base-growth or symmetrical-growth. Such a size-dependence agrees very well with the size-effect, that we have observed in Cu catalyzed nanostructure growth process. For detailed described of this effect please see chapter 4.4.

Micro-Raman spectroscopy was applied to investigate the microstructure of the as-grown products. By carefully focusing the laser beam for sampling, spectra corresponding to the base, stem and top part of the flower-like nanostructure were recorded, respectively. The result is subsequently shown in Figure 6.11 in a normalized form. All spectra show similar

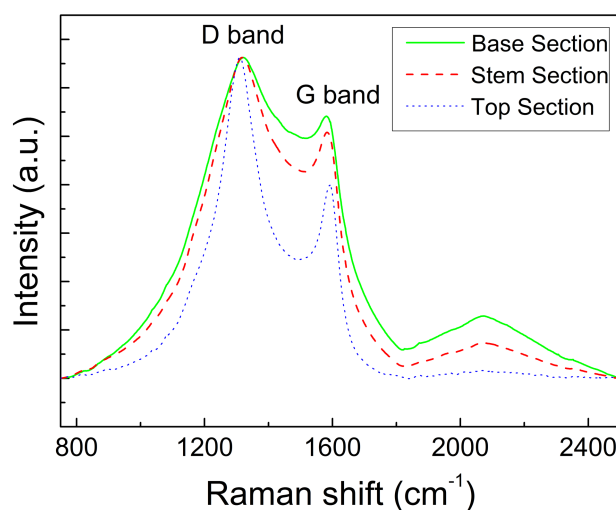


Figure 6.11. Raman spectra of the nanostructure which was prepared at 350°C.

characteristics in general, including a strong D peak at $\sim 1320\text{ cm}^{-1}$ and a relative weak G peak at $\sim 1580\text{ cm}^{-1}$. It indicates the as-grown nanostructure has an amorphous nature rather than crystalline graphite. However, spectra sampled at different locations also appear their respective characteristics. The one corresponding to the top part of the nanostructure shows lowest G peak. It thus results in a highest $I(D)/I(G)$ ratio. Meanwhile, in this spectrum the G peak has moved about 10 cm^{-1} to the right side (higher wavenumber direction) comparing with the other spectra. The higher $I(D)/I(G)$ ratio as well as moved G peak imply a smaller crystallite size of graphite, namely L_a (it also can be understood as the size of graphitic sheets in some cases)^{139, 140}. In addition, besides the D and G peaks another broad peak at $\sim 2100\text{ cm}^{-1}$ can be observed. It represents sp^1 chains in nanostructure. From the base to the stem, till the

top part, this peak weakens in turn, revealing a composition change. The Raman results imply that different parts of the as-grown flower-like nanostructure have inconsistent microstructure and composition. It is probably due to the distinct growth mode of each part (tip-growth or symmetrical-growth) and essentially correlated to the size of true catalyst particle as well as the size of the crystalline facets on catalyst.

The unique morphology of the flower-like nanostructure can be ascribed to a combined effect of the initial morphology of Ni catalyst precursor and its evolution during the growth. The abrasion in pre-treatment created a pretty rough surface on Ni slug. The surface was full of grooves, protuberances, even overhanging particles (Figure 6.12). This uneven topography

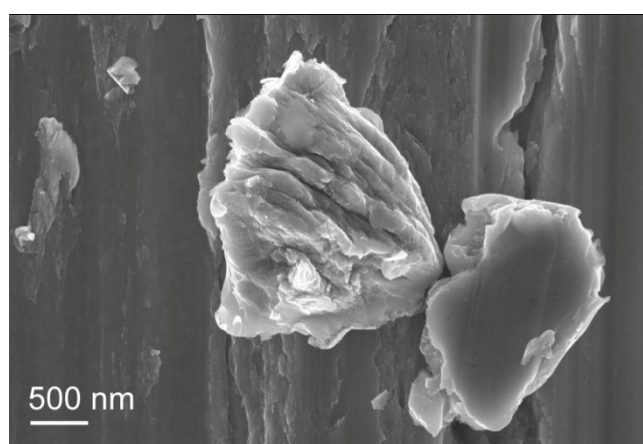


Figure 6.12. SEM image of overhanging particles on sanded Ni surface.

facilitated an evolution from bulky Ni towards individual Ni particles with certain size and shape, which finally catalyzed the growth. At 350°C, once introducing C_2H_2 into the reaction chamber, the deposition of hydrocarbon species started immediately. It was accompanied by the evolution of Ni catalyst. The small outshoots on Ni substrate have the highest curvature. They therefore evolved into individual Ni nanoparticles firstly (see the discussion about catalyst evolution in chapter 4.3). These small particles peeled from the Ni substrate because of the lift of growing nanofibers catalyzed by them. Later, the large protuberances (overhanging particles) on Ni substrate also evolved/split into individual particles. This evolution process finally created catalyst with a shape being fit for catalyzing fiber-growth. Notably, although the small outshoots evolved into separate Ni nanoparticles faster, the nanofibers catalyzed by them grew slowly. On the contrary, once a large protuberance or overhanging particle evolved into a property shape, the corresponding fiber grew rapidly. As a result, thin and short nanofibers composed dense clusters on the top of the flower-like nanostructure; thick and long fibers form a bundle (stem) to support the top section. Finally, a sketch of the different potential growth stages leading to the observed morphology of the

structures is given in Figure 6.13. In addition, the sanded Ni slug also featured relatively smooth surface for partial areas, beside/around the uneven part, see Figure 6.12. For that smooth area, the growth led to a homogeneous coverage of carbon-based reaction product instead of nanofiber, because without enough curvature, individual Ni catalyst particle had no chance to be generated there.

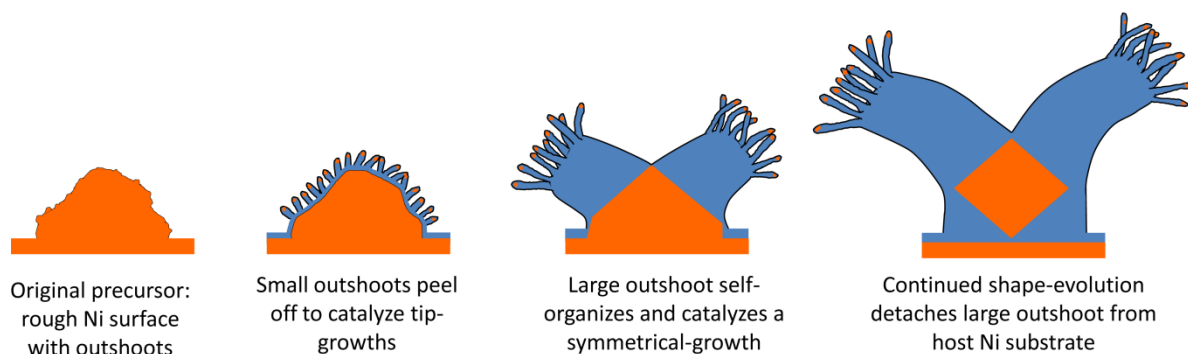


Figure 6.13. The sketch of the evolution of the nanostructure during growth.

In summary, using pure bulky metal Ni (slug) as a catalyst precursor, nanofibers were synthesized at the temperature as low as 275°C. This temperature is lower than the value in literature which reported a lower-limit of 350°C for nanofiber growth¹⁵³. In present process the true catalyst is individual Ni particles peeled from the Ni substrate. Interaction between C₂H₂ gas and Ni slug led to a surface reconstruction. Ni particles consequently peeled and evolved into certain size and shape. A pre-treatment to increase the surface roughness of Ni slug facilitated the catalyst-generation. Depending on the size of Ni catalyst particle, the fiber-growth followed two different modes. Tip-growth was observed only when Ni catalyst was smaller than 50 nm; but base-/symmetrical-growth corresponded to a broad size-range, even the Ni particle had a size up to hundreds nm. Comparing with base-/symmetrical-growth, tip-growth not only generated thinner nanofibers but also yielded finer microstructure (crystallite or graphitic sheets) in growth product.

6.2.2 Growth catalyzed by individual Ni nanoparticle (sol-gel route)

Now we have proved that with the aid of Ni catalyst, nanofiber can be synthesized in the low-temperature CVD process. At such a low temperature, carbon solubility as well as diffusion coefficient in Ni matrix are much lower than in those cases corresponding to high temperatures (VLS processes). Therefore, the VFS mechanism, which is based on hydrocarbon coupling and surface-diffusing, is a more reasonable path. However, to confirm this assumption, more information from the characterization of growth product is needed. Unfortunately, when use Ni slug as catalyst precursor, we always obtain bundles of

nanofibers which are hard to separate. From this sample we are unable to get detailed information, such as the geometry of catalyst particle in grown nanofiber and the role of catalyst faces. Therefore, we prepared individual Ni nanoparticles in Sol-Gel method. Using this method, monolayer Ni nanoparticles can be dispersed well on Si substrate. Then with the aid of this dispersed Ni particle catalyst, individual nanofibers were synthesized.

A piece of silicon wafer was dipped into the solution of water/ethanol (1:9 v/v) with 0.025M Nickel(II) chloride Hexahydrate, 0.40M citric acid and 0.80M polyethylene glycol (PEG, the concentration was calculated according to the mass of monomer), then lifted up in speed of 150mm/min to leave the solution. A homogenous film formed on the silicon wafer. After a drying at 200°C for 2 hours, this film evaporated and shrunk into a network (Figure 6.14(a)). This network subsequently transformed into individual Ni nanoparticles (Figure 6.14(b)) under the bombing of electron cyclotron resonance (ECR) nitrogen plasma.

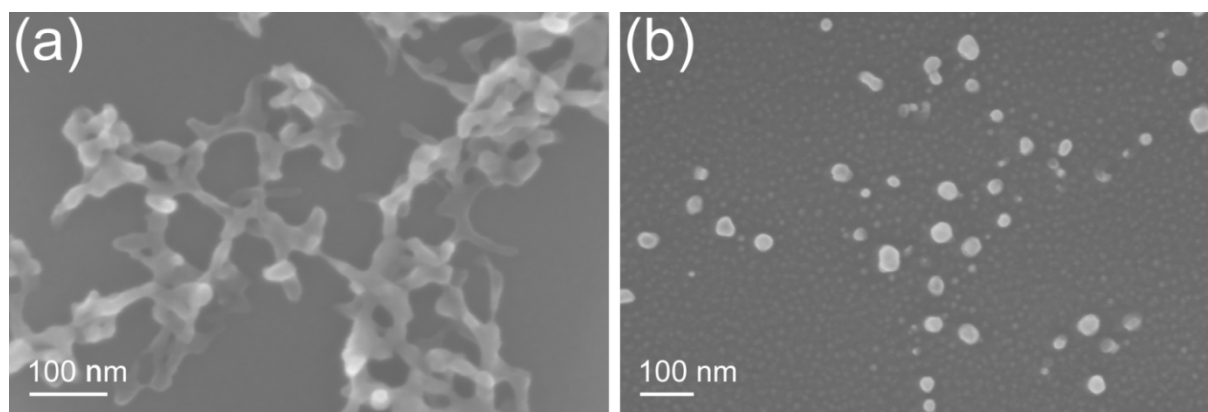


Figure 6.14. SEM images of: (a) Ni containing network; (b) individual Ni nanoparticles on silicon wafer.

The nanoparticles had an inhomogeneous size distribution between tens to hundreds nm. At last, the growth was achieved at 350°C for 2 hours; detailed operations are same as chapter 6.2.1.

Nanofibers were synthesized successfully. As-grown nanofibers laid on silicon wafer individually and they all appeared symmetrical-growth feature. In SEM image it can be seen that a bright particle locates in the middle of the nanofiber (Figure 6.15). EDS analysis confirmed this particle was Ni catalyst and the rest part of nanofiber was based on carbon. The synthesized nanofibers show various morphologies. In Figure 6.15(a), two symmetrical half-parts of a nanofiber stretch from the opposite sides of a Ni particle. The two half-parts connect each other smoothly. In Figure 6.15(b), two half-parts of a nanofiber are connected by catalyst particle to form a low-angle tuning. In Figure 6.15(c), the nanofiber appears helix features. All these morphologies were also observed in the CVD process using Cu catalyst,

see chapter 4. It reveals the Ni catalyzed growth possibly follows a same mechanism as the Cu case. Notably, not all the Ni nanoparticles are effective catalyst. After the CVD process most of the Ni particles were only covered by a layer of reaction product. Only a small number of Ni nanoparticles actually initiated fiber growth. They show regular quadrangle or triangle projections in SEM images (bright spots in the middle of nanofibers). This is apparently a result of catalyst evolution during the growth, because the original Ni particles have nearly spherical shape, see Figure 6.14(b). Actually, intensive catalyst-evolution is a hallmark of VFS process, since reactions occurring on certain low-index catalyst facets are crucial in this mechanism. These facets emerge along with the catalyst particle evolving into more regular shape. For example, for the Cu catalyzed process, the catalyst particles showed various projections after growth, including rectangular, triangle and irregular quadrangle or polygon. Based on the projections and geometrical relationship, we have deduced the three-dimensional shapes of Cu particles, which are mainly encapsulated by $\{111\}$ facets, see Figure 2.3.

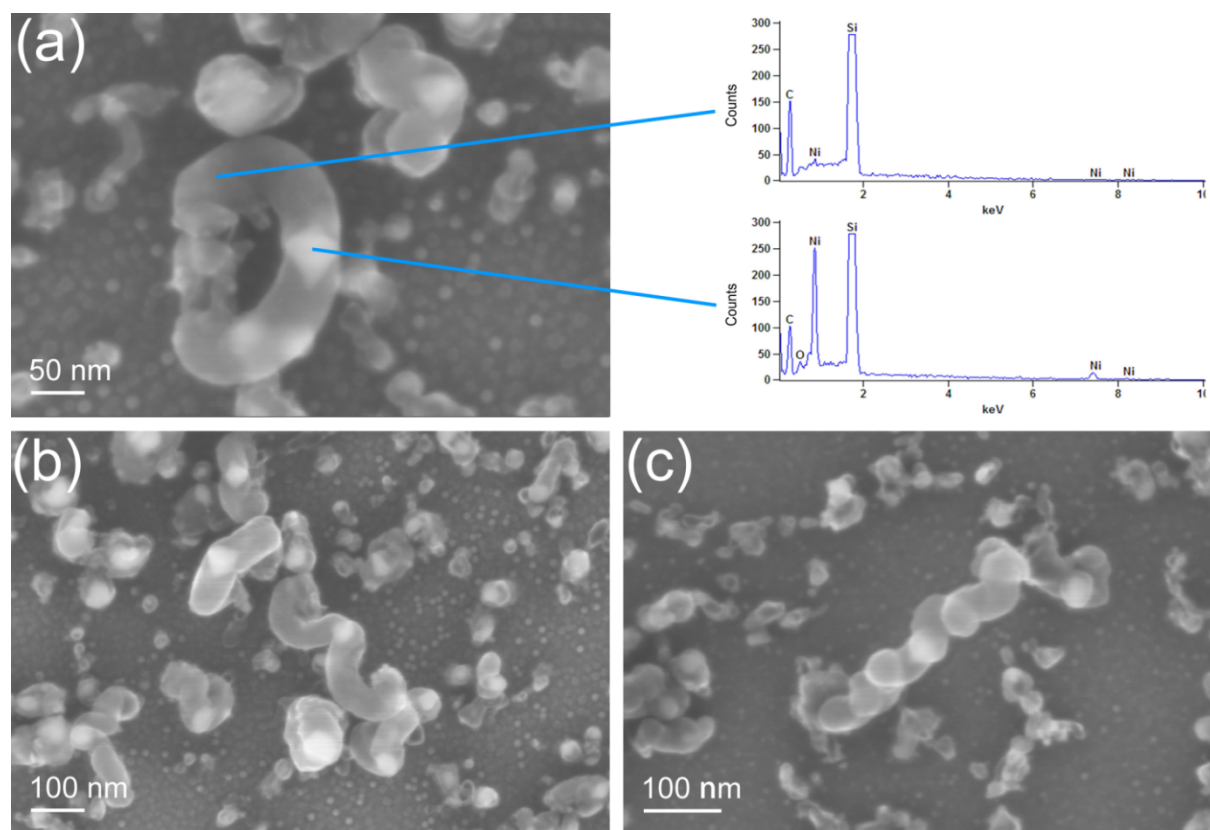


Figure 6.15. SEM images of various nanofibers. (a) A 'straight' nanofiber and corresponding EDS spectra. (b) A nanofiber with low-angle tuning. (c) Nanohelix.

Interestingly, in the context of the sol-gel route the ECR-plasma-treatment was essential to receive any fibers as growth product. This step in principle leads to a separation of the

catalyst nanoparticles. If Ni precursor with a network-shape was used directly in a CVD growth, at last irregular carbon layer covered this precursor, but there was no nanofiber formation (Figure 6.16). We also tried a calcination in air at 500°C to eliminate organic component in the sol-gelled Ni network precursor. It is unfortunately useless for producing effective catalyst. In contrast, the plasma-treatment was not necessary in the case of Cu catalyst based growth. In that case catalyst precursor with a random shape transformed spontaneously into regular particles during the growth. In addition, the nanofibers grown on Cu catalysts were much longer, even the same dip-coating and CVD growth were applied. It implies the evolution of Ni is much slower and more difficult. Therefore, a property catalyst preparation which endows the Ni catalyst with suitable size and shape is a critical step for the whole nanofiber preparation.

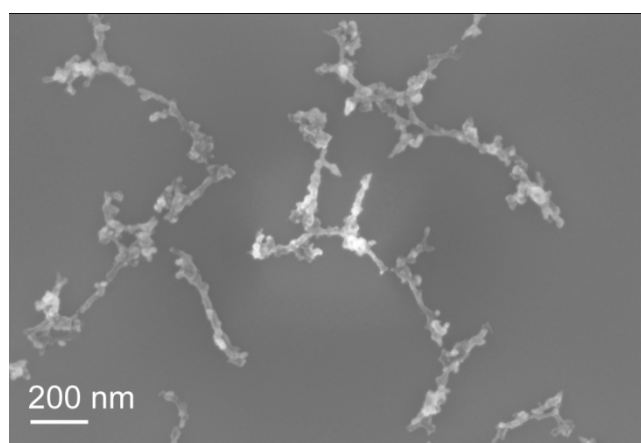


Figure 6.16. SEM image of the as-grown sample. Ni network precursor was used directly in the growth.

In summary, using a dip-coating and subsequent ECR-plasma-bombing process for catalyst preparation, individual Ni nanoparticles were dispersed on silicon wafer. Then in the following growth, fiber-like nanostructures with various morphologies were synthesized. During the growth Ni catalyst particles evolved to appear more regular shapes. However, such an evolution was slow and difficult. Therefore a property catalyst preparation is important. The observed phenomenon is coincident with the characteristics of VFS mechanism.

6.2.3 Growth catalyzed by individual Ni nanoparticle (nanopowder route)

As shown above Ni slug with rough surface is catalytically active down to temperatures about 275 °C. Sol-gel path was workable for synthesis of individual Ni nanoparticles as well as separate nanofibers. Unfortunately, the productivity of the aforementioned methods is not sufficient to facilitate a comprehensive study on the details of the growth mechanisms. For example, to evaluate the process with respect to kinetics, we need to monitor product increase

or reactant gas consumption. Large amount of high quality nanostructures has to be synthesized.

Consequently, we exploited Ni nanopowder as catalyst particles based on their ease of availability as well as the large size variety they conveniently offer. Ni nanopowder was prepared using an EEW technique. The powders have spherical shape and a size distribution between 10 to 100 nm. Few particles have anomalous size as large as 1 μm . For detailed information about nanopowder preparation please see chapter 3.1.4. The first growth experiment was carried out at 350°C for 5 hours. The operations were same as chapter 6.2.1.

6.2.3.1 Morphology diversity of as-grown nanostructures

The growth process had a high yield. It generated large amount of black powder. SEM image recorded in ‘in-lens’ mode shows the overall morphology of the powder-like growth product, see Figure 6.17(a). It shows the product was mainly composed of dense fibers, which feature lengths of several microns and diameters from 100 to 300 nm. To emphasize the Ni catalyst, a SEM image was also recorded in SE2 mode simultaneously, see Figure 6.17(b). In this mode Ni and Carbon show different contrasts; Ni particles emerge as bright spots. It can be seen the Ni catalyst particles locate in the middle of nanofibers, featuring a symmetrical-growth. Most of the Ni particles enwrapped by long fibers have polygon projection. To get detailed morphology information, a fiber is selected to show in the enlarged image of Figure 6.17(c).

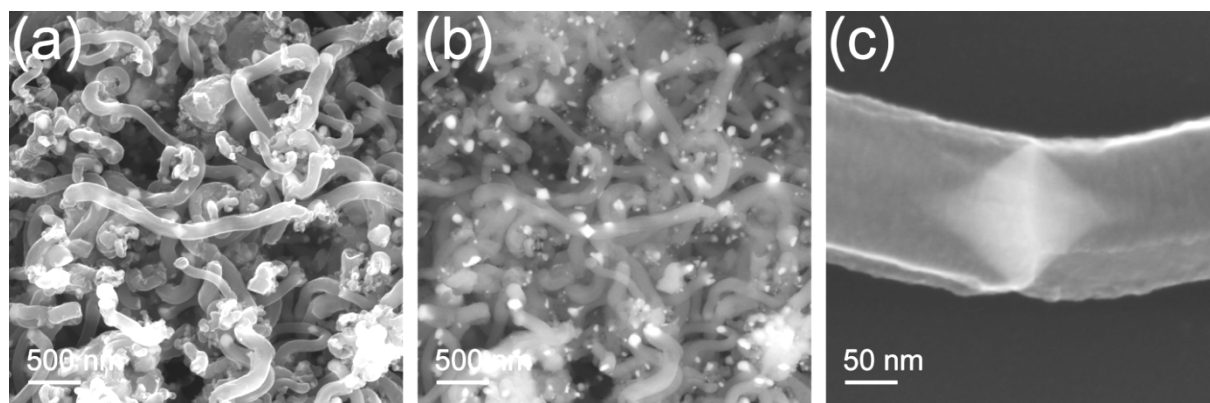


Figure 6.17. SEM images of as-grown product (a) In-lens mode. (b) SE2 mode. (c) Enlarged in-lens image of a nanofiber.

It clearly shows the nanofiber is not a smooth cylinder, because several edges along axial direction of the nanofiber can be seen. Normally the cross section of nanofiber is determined by the shape of corresponding catalyst. Therefore we can deduce here the Ni particle embedded in the nanofiber has a polygon-like projection not only in the axial but also in the

radial direction. Moreover, fine grains which are vertical to the axial direction exist on the surface of nanofiber. It implies that the nanofiber is possibly constructed by stacking lamellas.

The growth product was not limited to be ‘straight fiber’ as above description. Other nanostructures were also observed after a careful search in the as-grown sample, see Figure 6.18. But their yield is much lower than that of ‘straight fiber’. In Figure 6.18(a-1), a nanohelix is shown. It is thinner and shorter than normal ‘straight fiber’. The corresponding catalyst particle locates in the middle of nanohelix. It shows quadrilateral projection, similar

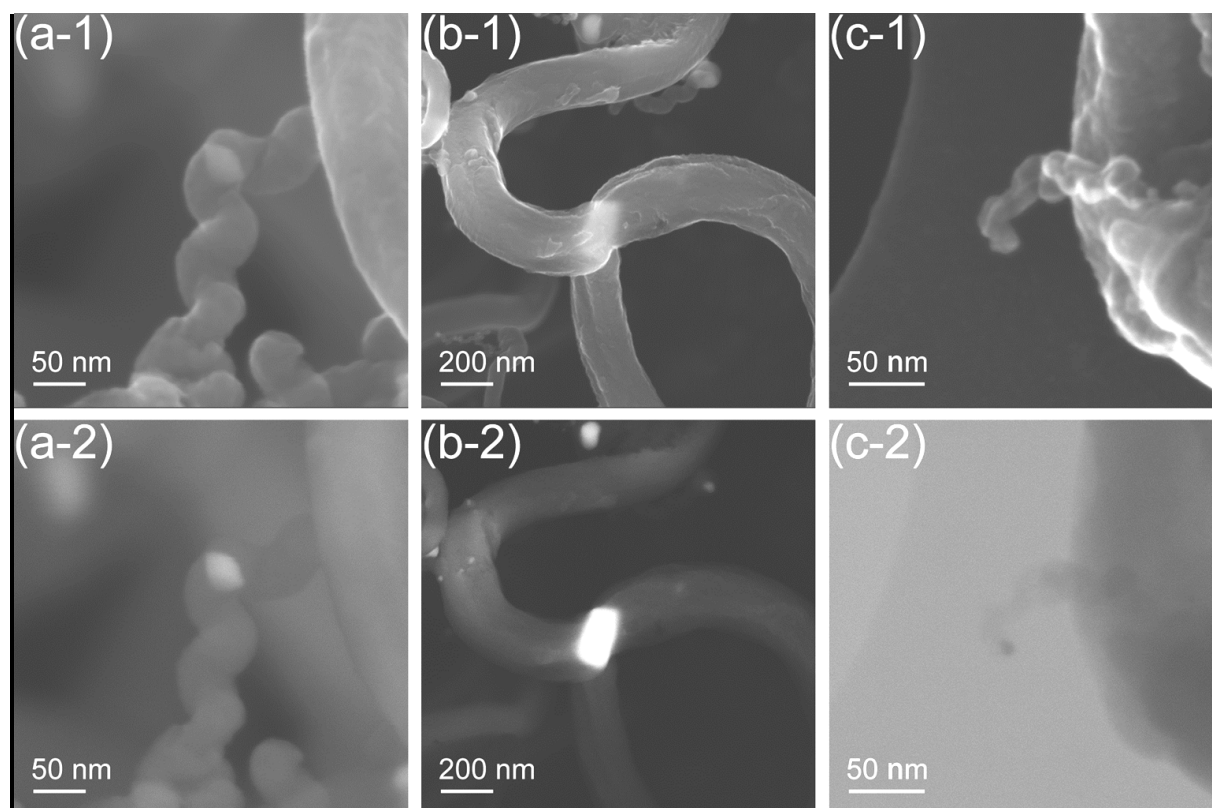


Figure 6.18. (a) Nanohelix: (1) in-lens mode; (2) SE2 mode. (b) Three branched nanostructure: (1) in-lens mode; (2) SE2 mode. (c) Thin nanofiber in tip-growth: (1) in-lens mode; (2) STEM mode.

to the one corresponding to ‘straight fiber’, but it is smaller, see the bright spot in the SEM image (SE2 mode, Figure 6.18(a-2)). Meanwhile, branched nanostructures appear in the as-grown sample. Figure 6.18(b-1) shows a SEM image (in-lens mode) of a three branched nanostructure. It can be seen three branches converge in a node. The node is occupied by a catalyst particle which has a bright trapezia projection in Figure 6.18(b-2). The three branches most likely grew from different faces of the polyhedron catalyst particle thus spread towards different directions. Uneven surface of the branches implies catalyst particle had unstable shape during the growth. We also observed nanofiber featuring very thin diameter, see Figure 6.18(c-1), STEM image indicates the catalyst particle locates in the tip of nanofiber, see the dark spot in Figure 6.18(c-2).

6.2.3.2 Size effect

In chapter 4.4 we have discussed the size effect in VFS process. It clarified that the morphology of nanostructure as well as growth mode (tip-/symmetrical-growth) depends on the size of corresponding catalyst particle. We also proposed several critical catalyst sizes in terms of Cu catalyzed low-temperature growth. Here we can review it briefly: Straight nanofiber or nanohelix tend to grow on Cu particles which are larger or smaller than 70nm, respectively, and they always show symmetrical-growth mode; when the Cu particle is smaller than 35nm, amorphous nanofiber tends to form in tip-growth mode.

The size effect is essentially a macroscopic-reflection of growth-rate-difference on different faces of catalyst particle. Therefore it is a signature feature of a process which relies on surface reaction and surface diffusion, e.g. VFS growth. In present investigation, the growth products based on the Ni nanopowder catalysts featured a predominantly symmetrical-growth mode. Only particles with diameters below 30 nm showed a tip-growth. Particles between 30 and 50 nm typically lead to a symmetric helical fiber configuration and particles larger than 50 nm to straight symmetric fiber morphology, respectively. The representative cases have been shown in Figure 6.17 and 6.18. Referring to the experimental fact observed in Cu catalyzed growth, here the identical size effect strongly suggests that the Ni based growth is also dominated by surface processes.

6.2.3.3 Catalyst evolution

Aside from the general morphology and growth modes observed, special attention was paid to the evolution of the catalyst particles during growth. A first glimpse at this evolution is gained by comparing the XRD spectra of the as-received nanopowder and the as-grown material, which is shown in Figure 6.19. While the original nanopowder features a pure fcc structure, after growth, a broad carbon (002) peak emerges at 2θ of 25.5° , corresponding to the as-grown nanofiber. Besides this peak, however, relative weak peaks representing hcp Ni appear at 2θ of 39.2° , 41.5° , 44.3° , 58.5° and 71.2° , respectively. This indicates a phase transformation of Ni catalysts particles during growth. Additionally, the mean Ni particle size was estimated by the well-known Scherrer relationship

$$D = \frac{k\lambda}{\beta \cos\theta} \quad (6.1)$$

where D is the mean grain size, k is shape factor which has a typical value of about 0.9, λ is the X-ray wavelength, β is the line broadening at half of the maximum intensity (FWHM) and θ is the Bragg angle. The calculation reveals the mean Ni particle size decreased from 44 to

14 nm for the original nanopowder and the as-grown material, respectively. Therefore we can deduce the original Ni powder split into smaller particles during the growth.

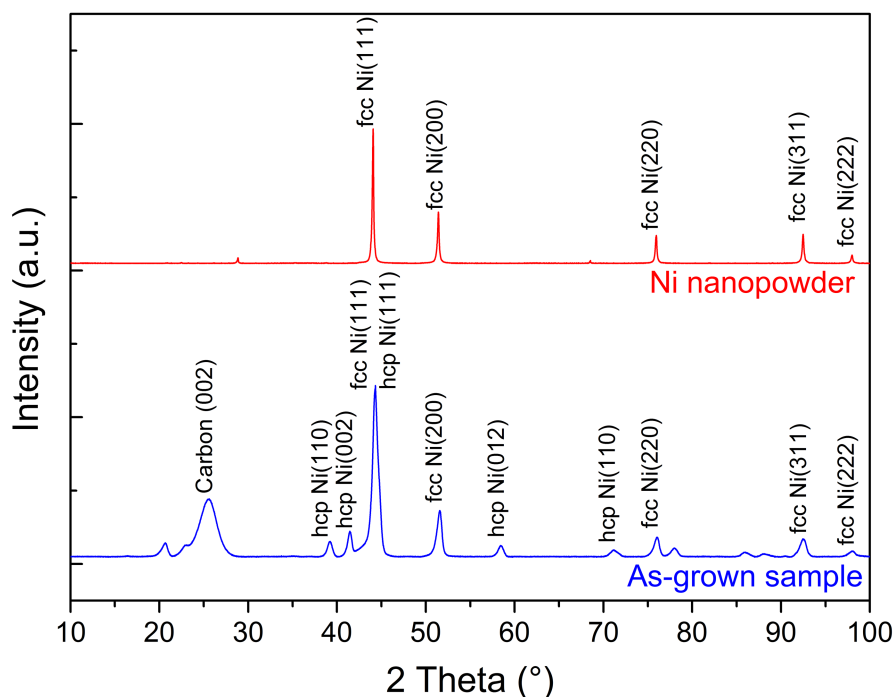


Figure 6.19. XRD spectra of original Ni nanopowder and as-grown sample.

The result of Ni catalyst evolution can be directly retraced in TEM studies. Figure 6.20(a) and (b) show a cluster of nanostructures combining together. Ni nanoparticles in these nanostructures are possibly a result of splitting of an original spherical Ni particle. The length of each nanofiber is proportional to the shape regularity of corresponding Ni catalyst particle enwrapped by the fiber. It implies that a stable growth only can be established after the Ni catalyst has evolved into a regular shape with certain facets exposing out. In Figure 6.20(c) and (d), a nanofiber close to reaching the stable growth stage is shown. It indicates Ni catalyst will finally have a projection close to quadrangle. The catalyst evolution process even left some traces in as-grown nanofiber, which can be observed in TEM image, see Figure 6.20(e). This image clearly shows a Ni catalyst particle in the middle of nanofiber. Interestingly, two small black spots can be seen below the lower vertex of the quadrangle Ni particle, aligning along the central axis of nanofiber. They are possibly peeling Ni fragments. Because the surface reconstruction occurred on Ni catalyst along with the growth, small Ni fragments peeled from the main body of Ni particle and then were enwrapped in the as-grown nanofiber. The nanofiber kept growing longer, so the peeled Ni was push forward. The peeled small Ni fragments contribute significantly to the decrease of mean Ni particle size. Therefore a low value of 14 nm is gotten in aforementioned calculation based on XRD spectrum.

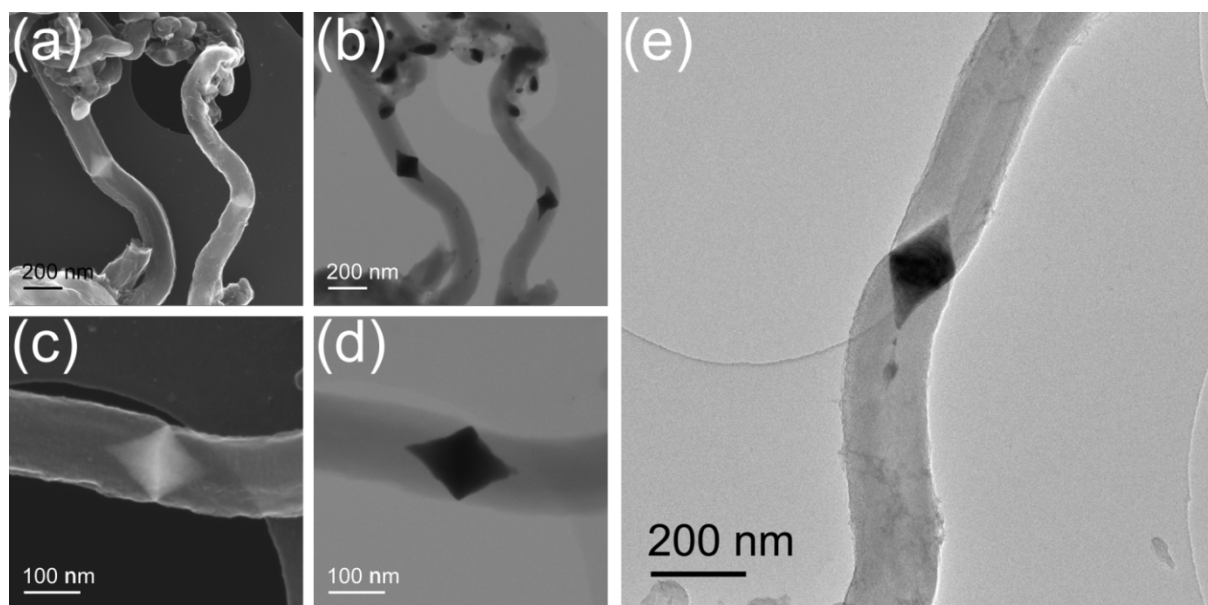


Figure 6.20. (a) in-lens SEM image and (b) STEM image of a cluster of nanostructures. (c) in-lens SEM image and (d) STEM image of a nanofiber with Ni catalyst evolved to stable stage. (e) TEM image of a nanofiber with Ni catalyst particle.

As we discussed in chapter 4.3, in a VFS process (typically with Cu catalyst), after growth the catalyst particle has normally a regular polyhedron shape. That is attributed to an evolution process. It reshapes the catalyst particles into appropriate size and shape to meet the requirement for hydrocarbon species absorption, surface reaction, and surface diffusion. Here the evolution-tendency we observed on Ni catalyst is a clear sign which points to the surface process controlled growth.

6.2.3.4 Microstructure

Although the low growth temperature, morphology diversity of synthesized nanostructure, size effect, and catalyst evolution all hint a possibility of VFS growth, to finally confirm the growth mechanism, systematic characterizations of the as-grown nanofibers is indispensable.

The microstructure of the as-grown fibers, studied by Raman spectroscopy, showed some degree of order, see Figure 6.21. It shows a strong D peak at $\sim 1305\text{ cm}^{-1}$ and weak G peak at $\sim 1587\text{ cm}^{-1}$. The shape of this spectrum is far away to match highly ordered graphite or carbon nanotube; but to compare with amorphous carbon material, the two peaks are sharper. However, the spectrum also features a high $I(D)/I(G)$ ratio of 2.6, indicating a small size of the graphitic clusters (or sheets) which build the nanofibers. Based on the T-K (Tuinstra and Koenig) relationship^{139, 140}, see equation (5.1), it is possible to calculate the size of the graphite clusters to 1.7 nm, which correlates very well with high resolution transmission microscope (HRTEM) observations, see Figure 6.22.

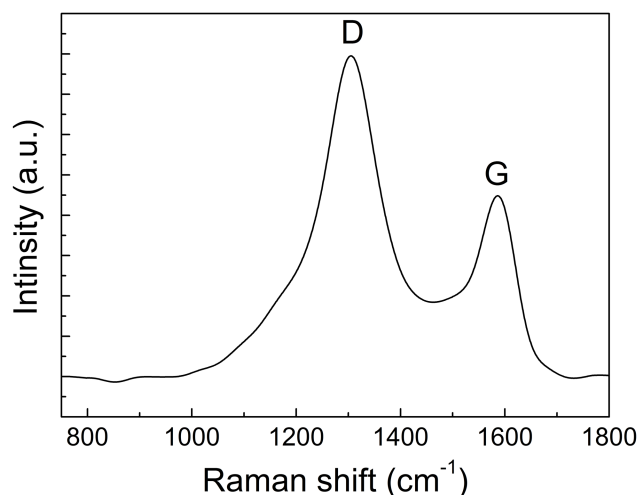


Figure 6.21. Raman spectrum of as-grown nanofiber.

In these HRTEM images it is possible to observe that the fibers actually consist of a multitude of small sheets or clusters, which are orientated parallel to the outer surface of the catalysts particle. Part (b) of the figure allows an estimation of cluster size on the order of 1 - 2 nm while featuring a layer thickness of 0.365 nm. The latter is slightly larger than the thickness of ordered graphite, which is 0.335 nm¹⁵⁴.

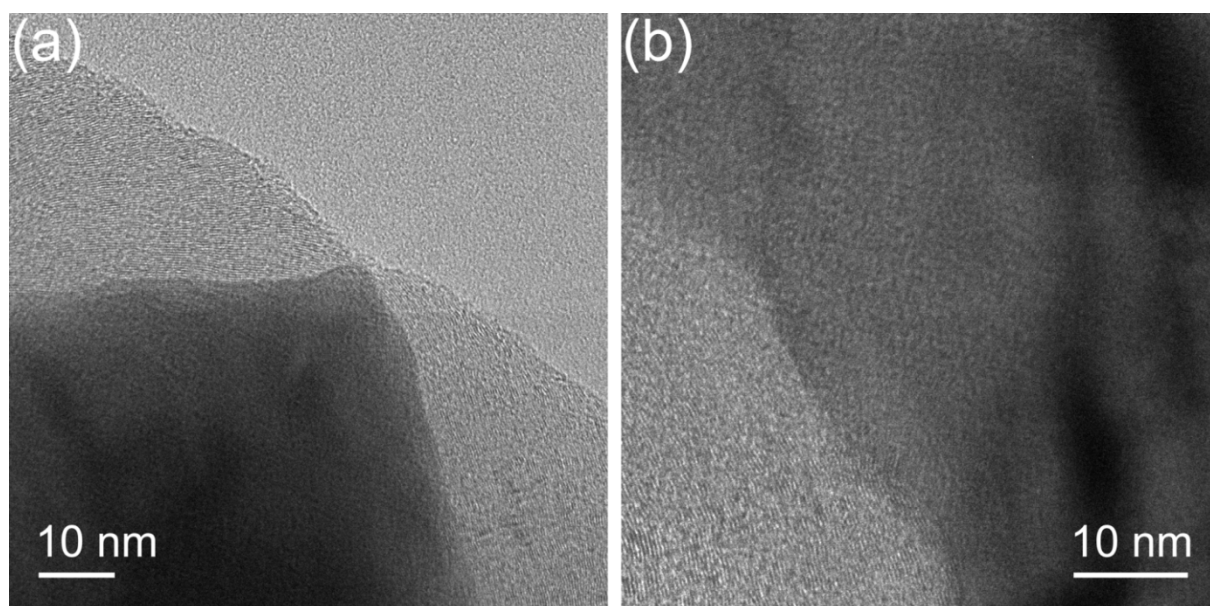


Figure 6.22. HRTEM images of as-grown nanofiber and Ni catalyst. (a) Small sheets in the nanofiber parallel to the catalyst surface. (b) The interface between Ni catalyst and nanofiber.

Selected area electron diffraction (SAED) pattern was recorded accompanying TEM image to identify the orientation relationship between as-grown nanofiber and corresponding Ni catalyst. TEM image in Figure 6.23(a) shows a Ni catalyst particle. Corresponding SAED pattern (c) confirms its single crystal nature. The incident electron beam is parallel to [011] direction of the Ni lattice. Notably, although this Ni particle exhibits regularity and symmetry

[illegible]

When the TEM images and SAED patterns were taken from other orientations, we observed identical relationship between Ni facets and growth product. In Figure 6.24(a)(b) and (c)(d), the incident electron beams are parallel to $[001]$ and $[1-1-2]$ directions, respectively. Although the Ni particles in these two images are still in evolution hence are far away from an equilibrium regular shape, we can see the low-index (002) and (111) facets are covered by a layer of as-grown carbon. Meanwhile, the other high index crystal facets attach to as-grown nanofibers directly.

When the TEM images and SAED patterns were taken from other orientations, we observed identical relationship between Ni facets and growth product. In Figure 6.24(a)(b) and (c)(d), the incident electron beams are parallel to $[001]$ and $[1-1-2]$ directions, respectively. Although the Ni particles in these two images are still in evolution hence are far away from an equilibrium regular shape, we can see the low-index (002) and (111) facets are covered by a layer of as-grown carbon. Meanwhile, the other high index crystal facets attach to as-grown nanofibers directly.

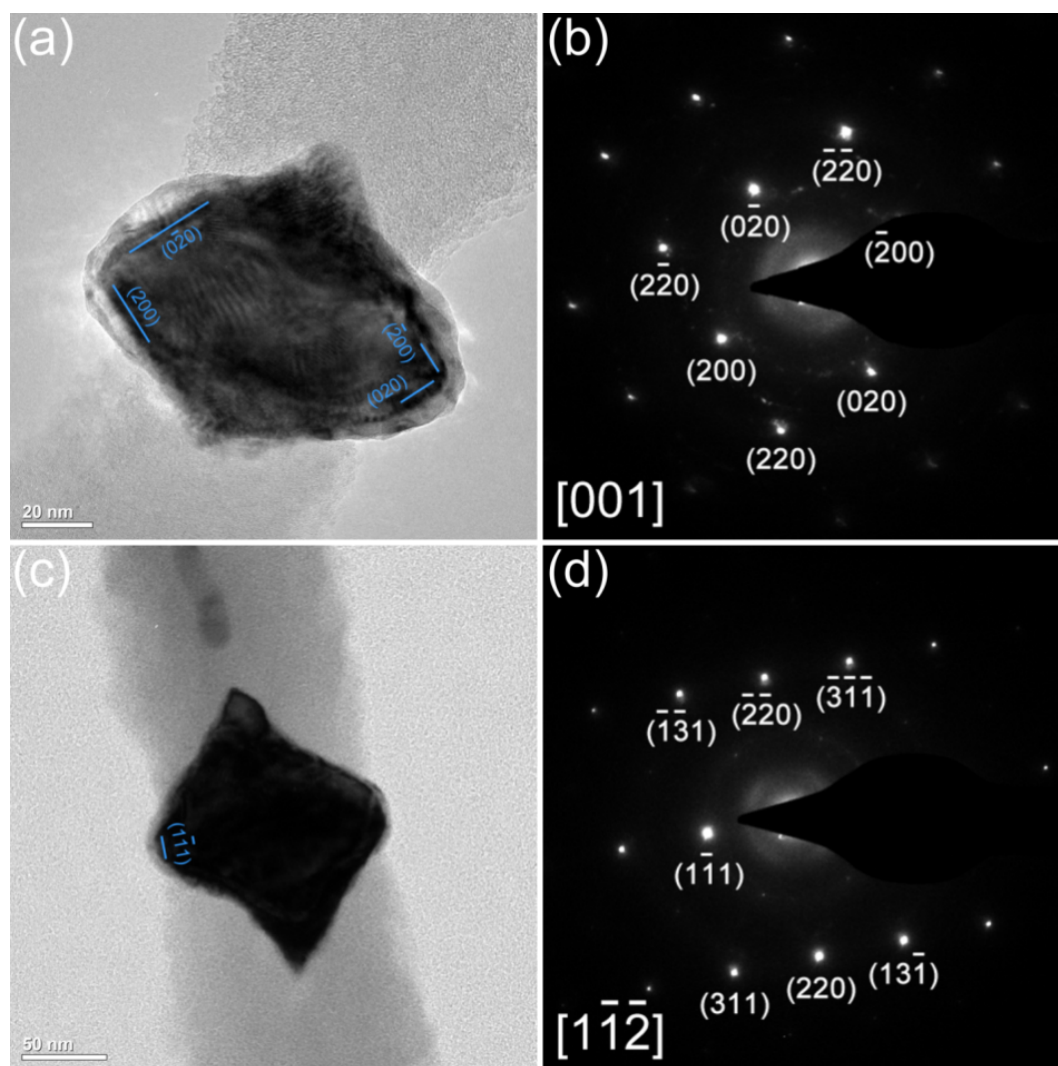


Figure 6.24. (a) TEM image and (b) SAED pattern of a Ni catalyst particle as well as nanofiber attaching on the Ni particle, recorded in $[001]$ direction. (c) TEM image and (d) SAED pattern a Ni catalyst particle as well as nanofiber attaching on the Ni particle, recorded in $[1-1-2]$ direction.

6.2.3.5 Chemical composition and structure

Elemental analysis was performed, for the method and instrument information please see chapter 3.3.2. The resultant composition is listed in Table 6.3. It shows the as-grown nanofiber is mainly composed of carbon and hydrogen, and oxygen takes a small proportion.

Table 6.3. The composition of as-grown sample

Element	C	H	O	Ni
wt. %	83.0	0.7	0.9	15.4
at. %	87.2	8.8	0.7	3.3

Infrared (IR) spectroscopy measurement did not receive any characteristic signal. It is possibly due to the black nanofiber strongly absorbing incident infrared light in the whole sampling wavelength and leaving no transmission signal. Fortunately, some binding information was still obtained from X-ray photoelectron spectroscopy (XPS). Three main peaks representing C, O, and Ni appear in the survey spectrum, see Figure 6.25(a). In a detail scan, besides the strong C 1s peak at 284.3 eV, another weak C 1s peak also can be observed at 289.6 eV (Figure 6.25(b)). The binding energy of this weak O peak as well as the O 1s peak at 531.7 eV agrees with the value of C-H-O polymer. TD-GC/MS detected a series of hydrocarbon fragments disassembling from the as-grown sample during heating up to 350°C, implying the nanofiber was constructed via hydrocarbon molecules coupling. These identified molecules have similar structure to those ones formed in Fe catalyzed growth (see Table 6.2, in chapter 6.1), but additional chain olefins was detected in present measurement. The complete list of the TD-GC/MS results can be found in Appendix B at the end of this thesis.

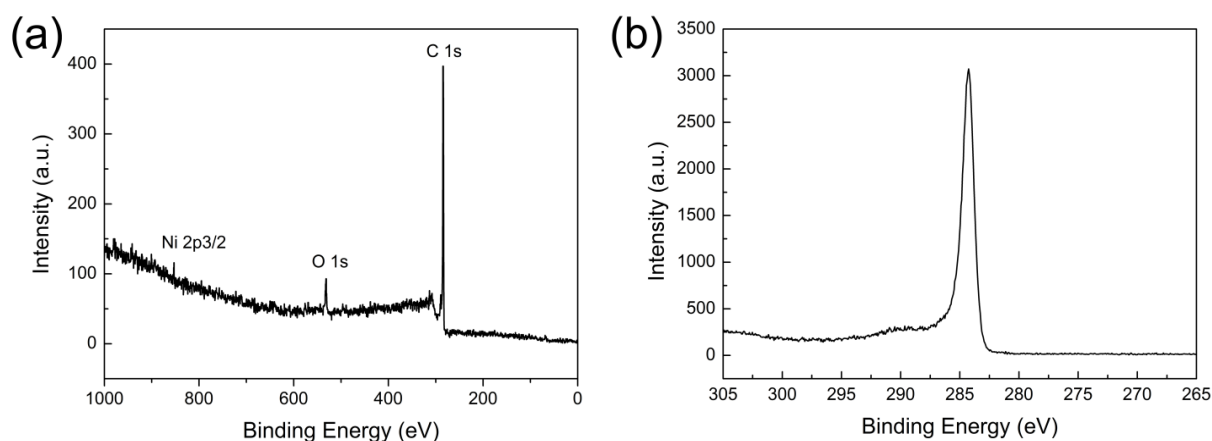


Figure 6.25. XPS spectra: (a) survey of as-grown nanofiber; (b) Detail scan of C peaks.

ESI-Mass spectrum (Figure 6.26) reflects the mass distribution of the building-blocks/molecules which construct the nanofibers. We conducted a calculation with an assumption that these molecules have graphene-like planar structure and mainly consist of carbon and hydrogen atoms. Then according to the values of high intensity peaks in the mass spectrum, we deduced these molecules have diameters of 1.0 - 1.5 nm. This dimensional feature agrees with the HRTEM observation.

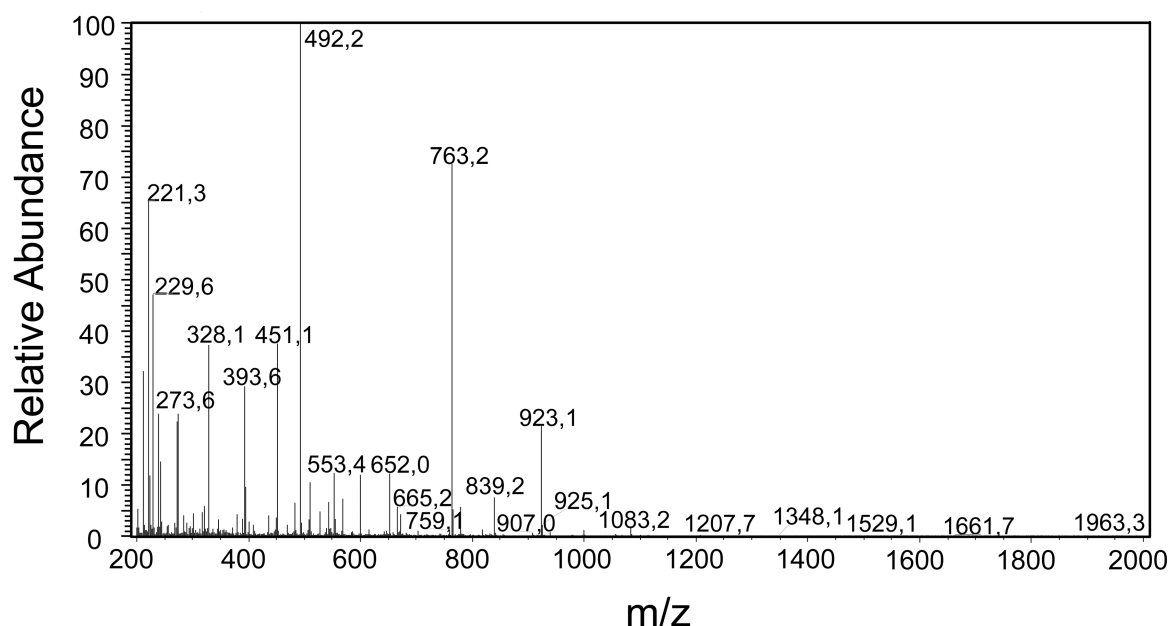


Figure 6.26. Mass spectrum of the as-grown sample.

Thermal analysis recorded thermogravimetric-differential scanning calorimeter (TG-DSC) curves as Figure 6.27. The sample was heated up with a speed of 5°C/min till 920°C. Weight loss, which began at 450°C, is shown on the TG curve. At the end of heating the sample lost about 35% weight in total, much higher than original hydrogen content of the nanofibers. Therefore aside from dehydrogenization, disintegration of nanofiber also progressed during the heating. No step appears on the TG curve and the DSC curve is also quite smooth. It indicates along with the temperature increase, the nanofiber disassembled via continuously releasing its structural unit, such as the small sheets observed in HRTEM image.

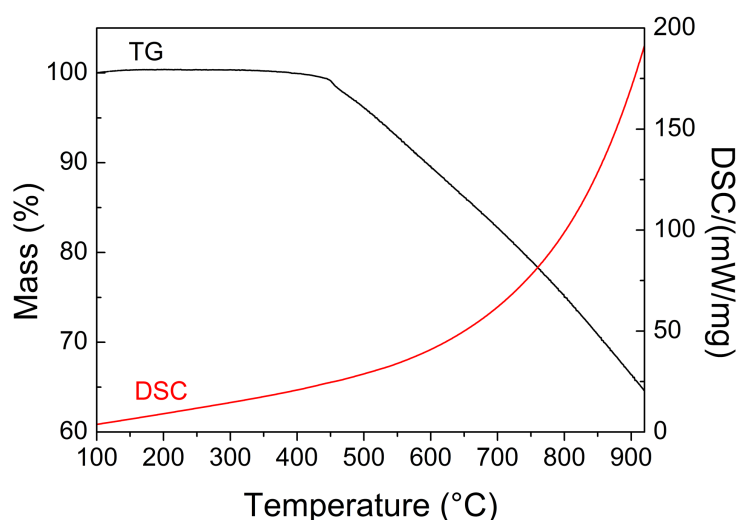


Figure 6.27. TG-DSC curve of the as-grown sample.

6.2.3.6 Kinetics research

Kinetic characteristics of a growth process (e.g. growth rate, the effect of temperature, pressure, and atmosphere) correlate essentially to the growth mechanism. Therefore a kinetics research is of importance for an in-depth understanding of the growth mechanism. In order to address this issue 50mg of Ni nanopowder catalyst particles were introduced to a CVD growth process at a temperature of 350 °C for 0.5, 1, 2, 5, 10, and 15 hours, respectively. After that the reaction chamber was evacuated rapidly to terminate the process. Detailed operation and parameters were same as the description in chapter 3.2. Consequently, the mass increase was taken as indicator of growth kinetics, see Figure 6.28. It is possible to observe different regimes of growth: After an initial nucleation time of about an hour that features hardly any mass increase, a fast increase of mass is detected.

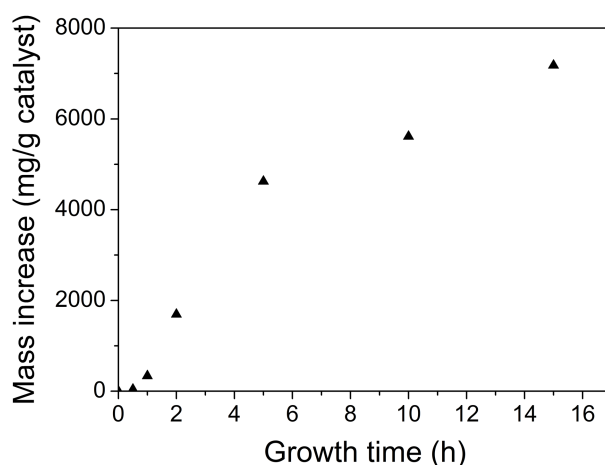


Figure 6.28. Mass increase after different time of growth.

The features of catalyst/nanofiber at different growth-stages can be observed by using SEM. In left column of Figure 6.29, SEM images (in-lens mode) show the morphology of nanostructures which underwent growths of 1, 2, 5 and 10 hours, respectively. Corresponding images in SE2 mode were recorded simultaneously. They are shown in the right column of Figure 6.29. In SE2 mode the contrast between carbon (grey) and Ni (bright) is intensified, so we can identify the position and shape of Ni catalyst particles. It reveals after 1 hour growth, the Ni particles are all covered by a layer of reaction product but no nanofiber can be seen. Partial of Ni particles still keep original spherical shape; the rest ones have evolved to exhibit edges and corners. After 2 hours growth short nanofiber emerge, and the Ni nanoparticles show more regular shapes. Long nanofiber can be observed in the sample which underwent 5 hours growth. For this sample, most of the Ni catalyst has polyhedron projection, indicating a stable growth. When the growth was further extended to 10 hours, the as-grown nanofibers are consequently longer and the density of Ni particles is lower in the field of view.

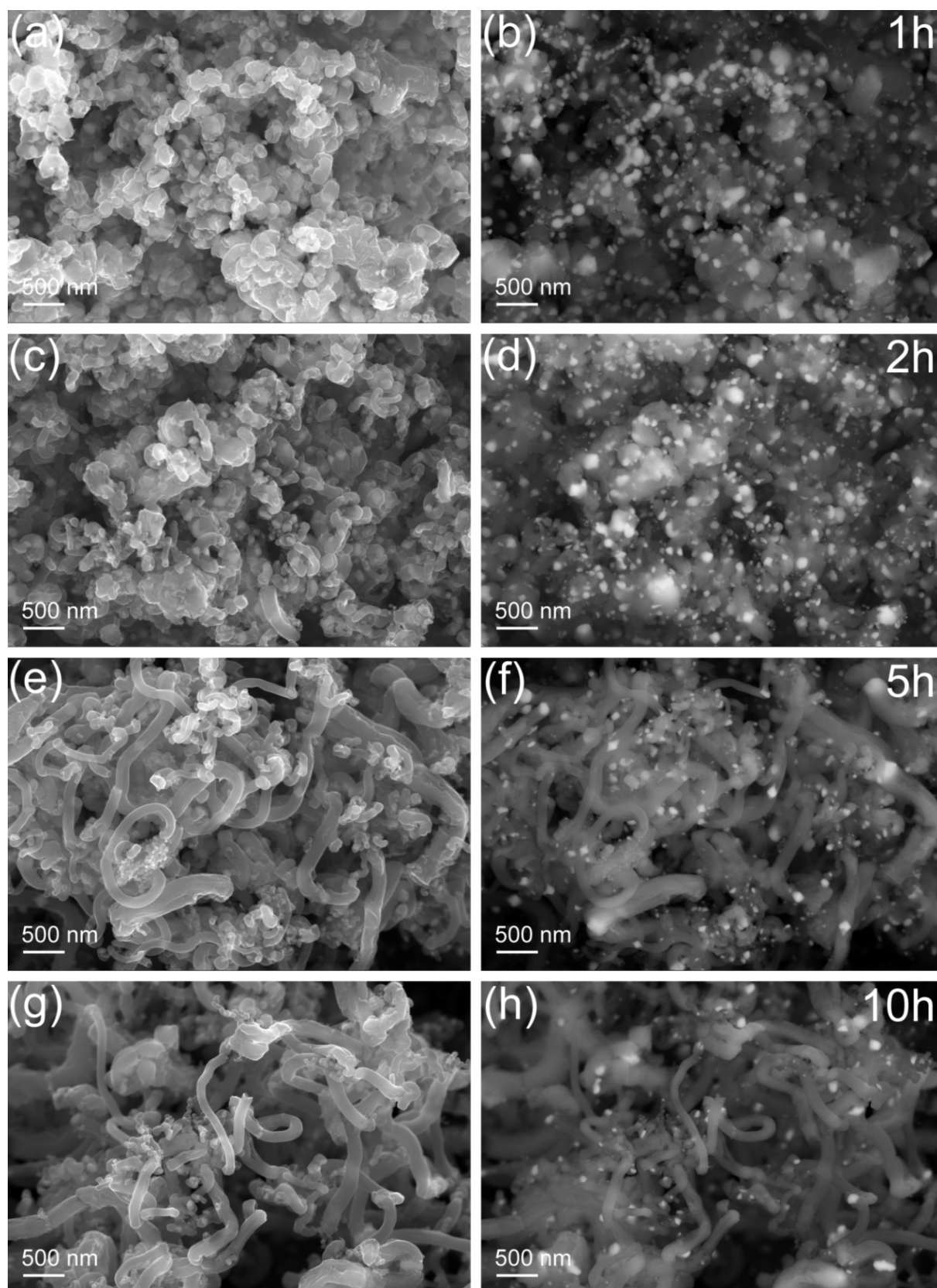


Figure 6.29. SEM images of samples which underwent growths of different time. (a) 1h, in-lens mode, (b) 1h, SE2 mode, (c) 2h, in-lens mode, (d) 2h, SE2 mode, (e) 5h, in-lens mode, (f) 5h, SE2 mode, (g) 10h, in-lens mode, (h) 10h, SE2 mode.

The results indicate catalyst pregnancy is a time-consuming but necessary step for nanofiber growth. Stable growth only can be achieved after this stage, wherein the Ni catalyst has evolved to show an appropriate shape, required facets has exposed out to support the surface reaction as well as to establish effective diffusion paths.

We can also evaluate the growth process based on reactant gas consuming. A growth was carried out in a sealed reaction chamber (5.4 liters) at 350°C. 50 mg Ni nanopowder was used in the process which started initially with 500 mbar C_2H_2 . Other detailed operations were same as the description in chapter 3.2. The pressure change during the process was recorded continuously and shown in Figure 6.30. The curve shows a little bit increase at beginning because of thermal expansion once C_2H_2 filled in the sealed hot chamber. Then the pressure features sustained decline, which is slow at the first 1 hour and accelerates since 1.5 hour. This result is coincident with the tendency of growth-product-accumulation shown in Figure 6.28.

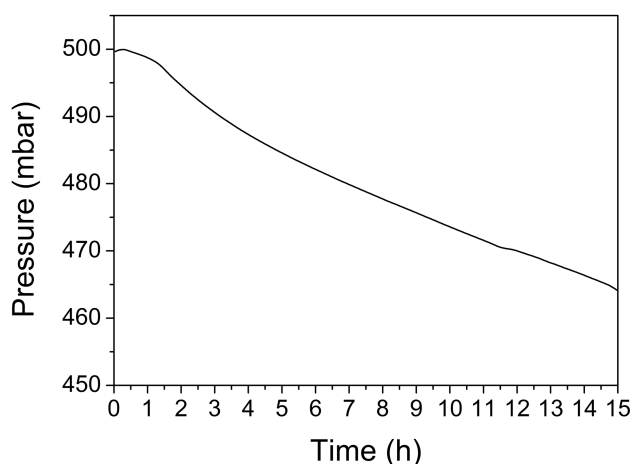


Figure 6.30. Pressure-drop during the growth.

In chapter 4.2 about the Cu catalyst based CVD process, we reported the acceleration-effect of oxygen containing molecule (e.g. H_2O) on the VFS growth. Here, in present study with Ni catalyst, similar effect was observed. In Figure 6.31, the red curve represents the experimental result which has already been shown in Figure 6.30 (50 mg Ni catalyst was used). Then another parallel experiment was carried out with the same reaction parameters. The only change is 500 mg Ni nanopowder was used for the latter. Since the amount of catalyst increased into 10 times than the former process, it is reasonable to predict the C_2H_2 consuming should be 10 times faster. As a result, in the sealed reaction chamber the pressure-drop-rate, i.e. the slope of Pressure-Time curve should be 10 times deeper. So in Figure 6.31 a predicted curve is plotted in blue dashed line. Surprisingly it contradicts real measured result

(green line) strongly. In practical, when a rapid C_2H_2 filling was finished, the pressure reduced immediately and the rate was much higher than prediction. It seems like the catalyst pregnancy stage was skipped and a fast growth started directly. An explanation of the unexpected rapid growth is the effect of oxygen, which is brought into the sealed reaction system with Ni nanopowder, because the surface of Ni nanopowder is oxidized inevitably. The more Ni nanopowder is used in a process, the more oxygen is introduced into the system. A higher oxygen concentration (in form of oxygen-containing-molecules) leads to rapider growth. Correspondingly, in the as-grown sample, oxygen was detected, see Table 6.3 and Figure 6.25.

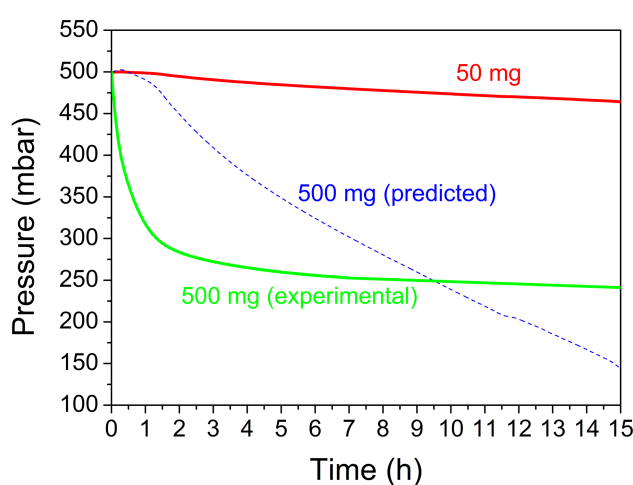


Figure 6.31. Pressure-drop during the growths which used different amount of Ni catalyst.

For above-mentioned process (500 mg catalyst), the pressure-time curve tends to be flat at the end, indicating termination of growth. A possible explanation is reactant exhaustion. Since the growth rate correlates tightly to the concentration of oxygen-containing-molecules in reaction system, once these molecules exhaust, the growth become very slow (if it does not stop). To verify if this assumption is true, a series of growth experiments were carried out with same operation and parameters, but different amount of initial C_2H_2 was introduced into the system for each process, namely 800, 500, and 200 mBar, respectively, see Figure 6.32. For all the growth processes, the resultant curve bends to be flat after a rapid drop at the early stage. So we should not ascribe the growth termination to oxygen exhaustion, because with the same amount of oxygen-containing-reactant, which was introduced into the system with 500 mg oxidized Ni catalyst, different amount of C_2H_2 reacted in each process at last. Notably, when a process achieves stagnant stage, the residual pressure in system is about half of the initial value, regardless of initial C_2H_2 pressure. Therefore the growth-termination is most likely a result of chemical equilibrium. During the growth, the reactions occurring on Ni

surface not only supply building-blocks for the nanofiber construction, but also release reaction products (e.g. hydrogen) into the surrounding atmosphere. Finally, equilibrium achieves and the reaction stops.

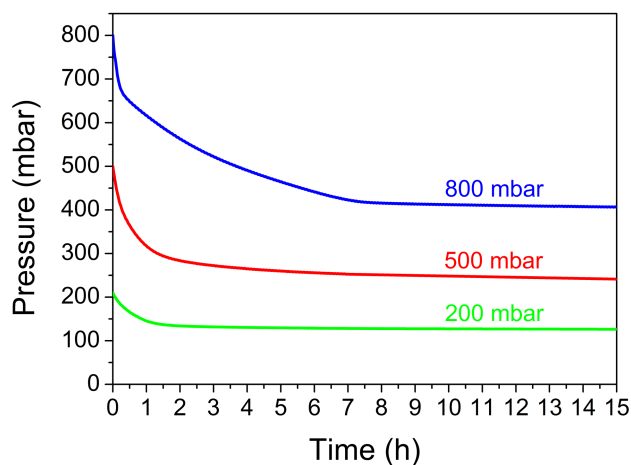


Figure 6.32. Pressure-drop during the growths which started with different amount of C_2H_2 .

Temperature is another crucial factor which influences the kinetic process. Therefore experiments were carried out at 275, 300, 325, and 350°C, respectively. All the processes started with 500 mbar C_2H_2 , under the catalysis of 50 mg Ni nanopowder. After growth the samples were weighed to calculate mass increase (product yield). The results are shown in Figure 6.33. In principle, the growth rate increases with the temperature increasing. The process at 275°C did not lead to any measurable yield. Higher process temperatures, e.g. 300 and 325°C, result in slow growth. A substantial increase in production appears when the process temperature increases to 350°C.

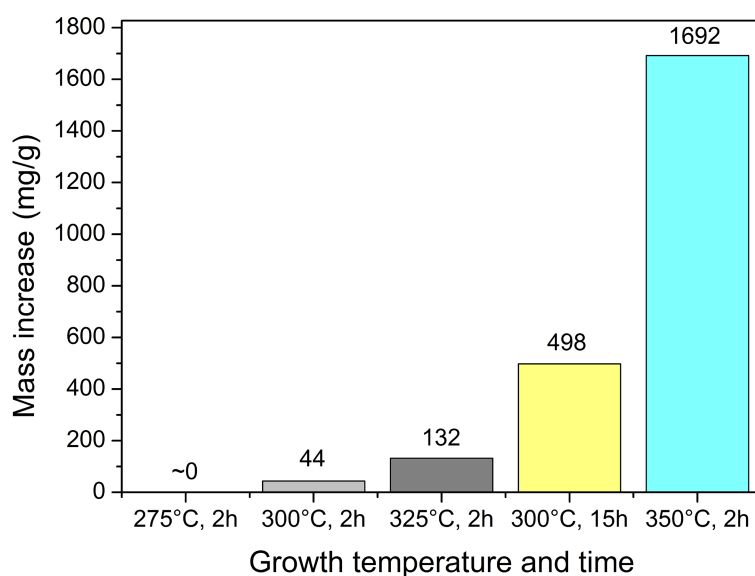


Figure 6.33. Mass increase after the growth at different temperature.

Accordingly, the effect of temperature on growth is demonstrated by the morphologies of as-grown products, see Figure 6.34. The growth at 275 and 300°C did not produce any nanofiber. After the process, Ni particles still keep their original spherical shape. However, EDS analysis indicates carbon based material covers the Ni particles. Such carbon layer is thicker for 300°C grown sample rather than 275°C one, because a stronger carbon peak in the

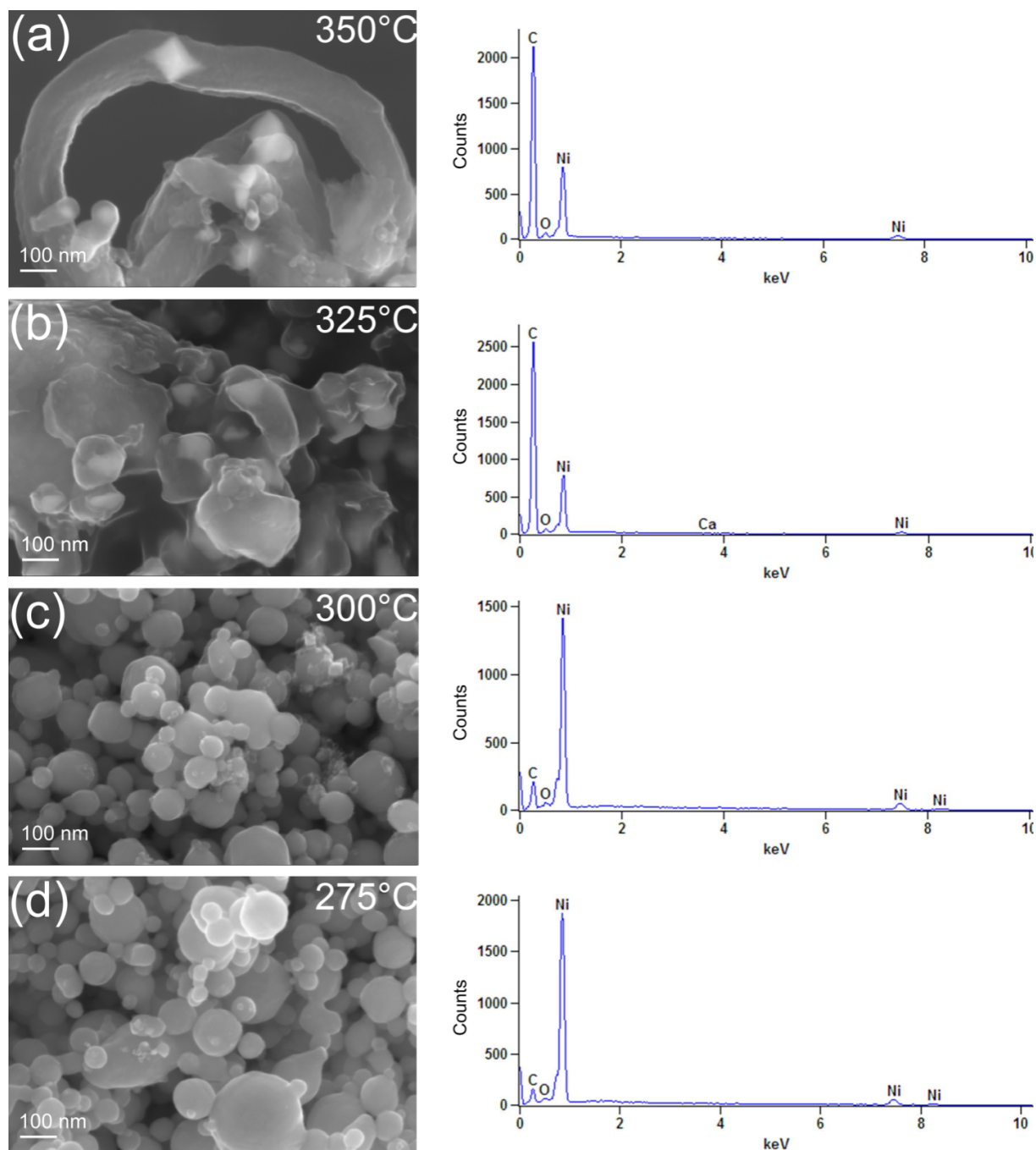


Figure 6.34. SEM images and EDS spectra of the samples grown at (a) 350°C (b) 325°C (c) 300°C (d) 275°C for 2h.

appears EDS spectrum corresponding to the former. When the growth temperature increased to 325°C, fiber-like structures emerge, but most of them combine together. The Ni catalyst particles (bright spots in SEM image) obviously deviate from their original spherical shape. For the sample prepared at 350°C, long and clear nanofiber grows on Ni catalyst particle which shows regular quadrangle projection. The results imply when Ni nanopowder is used as catalyst, temperature above 325°C is necessary for nanofiber growth. At lower temperature, although some carbon based solid substance deposits to cover the Ni catalyst particle, nanofiber cannot be synthesized.

Interestingly, we noticed the effect of catalyst-appearance on critical temperature of growth. In former experiments which used Ni slug as catalyst, the temperature to initiate nanofiber growth could be as low as 275°C, see Chapter 6.2.1. It was 50°C lower than present case based on Ni nanopowder catalyst. Therefore it looks like Ni slug has higher catalytic activity than Ni nanopowder. This experimental fact conflicts with common concept that catalyst in nanopowder appearance should be more active than bulky counterpart. This paradox is possibly ascribed to the initial surface-state of different catalysts. In former discussions we have pointed out the growth needs certain indexed crystal faces on catalyst. For sanded Ni slug, the exposing surface is composed by a lot of small facets which have random orientations, hence it more or less met the orientation requirement. At partial area a slight surface reconstruction is enough to create faces to initiate nanofiber growth (see Figure 6.9). In the case of nanopowder, because the Ni particle has spherical shape, the face which has both considerable area and appropriate orientation does not exist. Then to support a nanofiber growth, intense surface reconstruction must progress in advance, which reshapes the Ni particles but needs relatively high temperature. On the other hand, comparing with the oxidized surface of Ni nanopowder, the surface of Ni slug is cleaner and fresher because of the pretreatment (e.g. sanding). It also contributes to the low growth temperature.

Anyway, we suppose the higher critical temperature for Ni-nanopowder-based process is ascribed to catalyst pregnancy instead of growth. To prove this, three parallel experiments were carried out. Aside from two processes progressed at constant 300 and 350°C, respectively, the third one started and kept at 350°C for 30 min, after that the temperature reduced to 300 °C within 10 min and was maintained till the end. For all the processes, 500 mbar C₂H₂ was introduced into the sealed reaction chamber; 500mg Ni nanopowder was used as catalyst. Figure 6.35 shows the pressure-drop (reactant consuming) during processes. It can be seen when the temperature keeps at 300°C for the whole process, the pressure-drop is quite slow (blue line). If the process starts at 350°C, the pressure drops quickly (green and red line).

Notably, after the early stage (30 min) of a process which starts at 350°C, even reduce the temperature to 300°C (red line), the pressure-drop-rate is still higher than the process starting at 300°C, although the temperatures are same at this moment. This result indicates temperature is a key factor to control the catalyst pregnancy, but once the pregnancy finishes (in the first 30 min of the 350°C process), a stable growth can sustain at lower temperature with considerable rate.

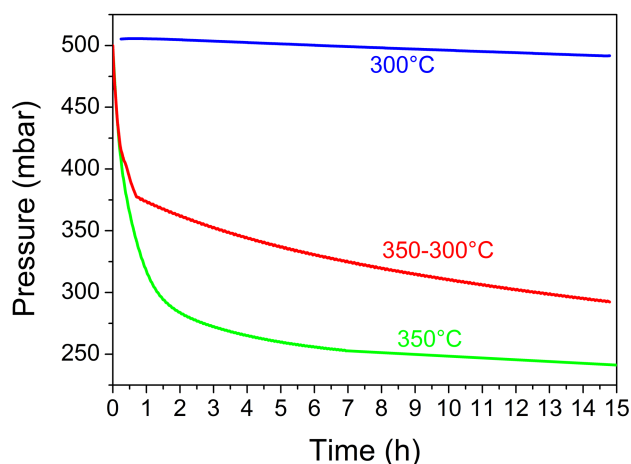


Figure 6.35. Pressure-drop during the growths at 350°C, 300°C and 350-300°C.

6.2.3.6 Growth mechanism

According to above experimental fact and discussion, the CVD growths based on Ni nanopowder catalyst had left clear tails which point to VFS mechanism, for example, the low process temperature, diversity of as-grown nanostructures, the size effect, the tendency of catalyst evolution as well as the important role of low-index catalyst face. These unique features are same as what we observed in Cu-catalyst-based process (the most typical VFS case). However, before to give a assured judgment of VFS growth, we have to exclude the possibility of VLS path in present case, because it is well known that C_2H_2 decomposes on Ni surface to form carbon atoms^{87, 155, 156} which can dissolve in Ni^{87, 157}, it finally leads to the VLS growth at high temperature.

In present low temperature condition, according to the dependence of carbon solubility on temperature⁴³

$$\ln S = 2.480 - 4880/T \quad (6.2)$$

here S is carbon solubility (weight percent) in Ni and T is temperature, it derives a considerable solubility of 0.0047% at the temperature as low as 350°C. But by extrapolating the experiments results in literature⁴³, the diffusion coefficient of carbon in Ni matrix is

estimated to be $\sim 10^{-18}$ m²/s at 350°C, five orders of magnitude lower than the value at 700°C. Therefore VLS growth based on bulk diffusion is difficult at low temperature. Instead, the surface of Ni catalyst is the only reasonable diffusion route. Specifically, the diffusion of reaction product is from low-index Ni facets to high-index ones. TEM images along with SAED patterns had confirmed this, see chapter 6.2.3.4.

For a surface-diffusion-based growth, surface reaction occurring on catalyst is crucial. Adsorbed C₂H₂ can dehydrogenize or couple on Ni surface to form a series of hydrocarbon molecules^{111, 148, 149, 158}. Among these surface reactions, oligomerization^{159, 160}, e.g. the cyclic trimerization of C₂H₂ on Ni(111) face to form benzene¹⁴⁹, and following polymerization which generate polymer-like products¹⁶¹ are notable. They can provide fundamental structural unit for the nanofiber construction thus make surface-diffusion-based growth be possible. On the other hand, kinetic investigation has clearly shown that the growth rate is sensitive to the oxygen-containing-molecules in reaction atmosphere (Figure 6.31). In correspondence it was reported carbon monoxide effects the oligomerization of acetylene on Ni¹⁶².

Integrating all the clues and referring the microstructure of growth product, here we are able to suppose a growth mechanism: Once C₂H₂ gas is introduced into the reaction chamber, C₂H₂ molecules are absorbed on Ni surface and then couple to form small hydrocarbon molecules (oligomers). Different catalytic activities of various exposing Ni facets lead to different yield and consequent concentration gradient of reaction product. It drives the diffusion along the surface of Ni catalyst, from low-index facets to high-index ones. Meanwhile, along with above coupling and diffusion, oligomers polymerize. As a result polymer sheets precipitate on high-index Ni facets to construct the nanofiber. Loose stacking growth product allows C₂H₂ gas keep filling in and contacting the Ni surface beneath to make the growth be sustainable.

The Ni facets, which the growth needs, do not exist at the beginning of process. But during the process interaction between C₂H₂ and Ni reforms the catalyst particle and enlarge the crystal faces until a stable diffusion as well as growth has been established. It appears as the catalyst pregnancy stage in above mentioned kinetic research.

Naturally, the as-grown nanofiber contains considerable hydrogen because of the growth mechanism based on coupling instead of decomposition of hydrocarbon species. However, to compare with the product of Cu-catalyst-based growth, hydrogen content in present Ni case is lower. It is ascribed partially to the relatively higher process temperature (350°C) than in the Cu based process (250°C), hence carbonization progresses accompanying the growth.

Actually even in Cu-C₂H₂ reaction system the hydrogen content of growth product also reduces with the reaction temperature increasing³⁸. Meanwhile, the dehydrogenation effect catalyzed by Ni also reduces the hydrogen content in final nanofiber.

6.3.2.7 Summary

Ni nanopowder is a high efficiency catalyst for nanostructures preparation via low-temperature CVD process. In this way various nanostructures can be synthesized, including straight nanofiber, nanohelix, branched nanostructure, etc. The size of catalyst particle not only influences the morphology of as-grown nanostructure but also determines the process to be symmetrical- or tip-growth mode. As-grown nanostructure, which contains considerable hydrogen, is constructed by stacking polymer sheets. These sheets are parallel to the surface of Ni catalyst. Reactions occurring on Ni surface not only supply building-blocks for the nanofiber construction, but also release reaction products into the surrounding atmosphere. In sealed reaction system it finally results in a chemical equilibrium state, and the reaction terminates consequently. Oxygen-containing-molecule in reaction atmosphere could accelerate the growth but does not influence above chemical equilibrium.

The growth could be described as adsorption (Vapor) - diffusion (Facet) - precipitation (Solid) process, i.e. VFS mechanism, see chapter 4.1 and 5.4. The basic growth steps are similar to that in Cu-C₂H₂ reaction system. However, in present Ni based process the diffusion route is different. It is from low-index Ni faces to high-index ones. The corresponding Ni facets emerge and enlarge in initial stage of growth, namely catalyst pregnancy. A temperature higher than 325°C is necessary in this stage.

6.3 The adoptability of VFS mechanism

The analysis of growth products obtained for Fe, Ni catalysts prepared by various paths showed that nanofiber production at relative low temperatures is in general possible. In direct analogy to the previous findings on Cu, depending on the size and morphology of the catalysts various nanostructures were observed. For all the as-grown nanostructures, the fundamental structural units are similar stacking nanosheets, which are identified to be planner molecules based on aromatic ring. Regardless of detailed surface reaction and diffusion route, the transportation and precipitation of hydrocarbon species on catalyst surface induced nanostructures growth. The surface processes can be generalized as a competition and cooperation between different catalyst crystalline faces. All these essential commons between the processes based on different catalysts illustrate an extensive adoptability of the proposed VFS mechanism.

However, distinct details need to be addressed as they demonstrate differences between Cu, Fe and Ni catalysts. Firstly, Cu, Fe, and Ni catalysts induce nanostructures featuring different hydrogen content. It is possibly ascribed to different molecular structures of growth products. General speaking, to form polymer nanosheet, when aromatic rings connect each other by short chain, it contains more hydrogen than the case in a form of fused six-membered rings. On the other hand, intense dehydrogenation occurring on Ni surface is also responsible for the low hydrogen content.

In terms of morphology of synthesized nanostructure, Cu and Ni catalysts have more commons. Similar multiform nanostructures, including straight nanofiber, nanohelix, 3-branched nanostructure were synthesized with the aid of both the two catalysts. Both symmetrical- and tip-growth can be observed. The size of catalyst particle determines the morphology as well as growth mode, i.e. size effect. Differently, for Fe catalyst only small sized particle shows catalytic activity. It is possibly due to the limited diffusion distance on Fe surface. So the large Fe particle only induces homogenous polymer deposition instead of fiber-like product, see Figure 6.1. However, we can still explain the sole tip-growth on small Fe catalyst, within framework of size effect.

Taking the kinetic feature into account, the growth rates of Cu and Ni based process are both sensitive to oxygen-containing-molecules. However, the Cu catalyzed growth can progress until oxygen exhaustion, while in Ni case the growth terminates with a chemical equilibrium. Hydrogen, which is generated in dehydrogenation occurring on Ni, contributes to the equilibrium. These hydrogen molecules compete against C_2H_2 for adsorption position on catalyst. On the other hand, according to the TD-GC/MS results (see chapter 6.2.3.5), the surface reactions on Ni not only generate aromatic molecules for nanofiber construction, but also produce chain olefins which accumulate and push the equilibrium reaction backward.

At last, the catalysts show different evolution-ability in CVD process, Cu is most shapeable while Fe is quite difficult to evolve into polyhedron shape. Accordingly, different temperatures are required for the catalyst-evolution before fiber-like nanostructure growth. A temperature higher than 250, 275, and 350°C is required for Cu, Ni, and Fe based process, respectively. This difference may be ascribed to the features of crystal lattice as well as bonding strength between metal atoms of catalysts, if we notice the high melt point of Ni, and the bcc lattice of Fe, which is different from Cu and Ni.

In summary, although different catalyst system exhibits distinct characteristics, this specificity can be explained within the framework of VFS mechanism.

7. Applications and prospects

All the researches in materials science, whatever focusing on preparation methods or fundamental scientific issues in background, will naturally point to an ultimate goal that serves and supports applications. In terms of one-dimensional (1D) carbon nanostructures (CNs), their special morphologies, unusual atomic architecture and novel properties grants them not only extensive applications in electronic transport, thermal conduct, fluorescence, field emission, hydrogen storage etc., but also an ability to work as template for preparing other types of 1D and 2D nanostructures.

In present study, no doubt the synthesized novel polymer nanostructures (PNs) as well as the CNs (via additional carbonization) can also be utilized in above applications, because they have the common features which endow all 1D nanomaterials with the excellent capabilities, for example, large specific surface area, high aspect ratio and sharp tip, and electrical conductivity (after carbonization). However, a simple repetitive work which replaces the materials in previous researches with our nanostructures will not necessarily bring significant improvement. Actually a valuable application must be correlated tightly to the distinctive characteristics of a material. Therefore, in present study the microstructure of the synthesized nanostructures deserves a special attention. To point out the uniqueness of our nanostructures, a brief review of conventional 1D CNs is necessary. According to structural characteristics, those CNs are usually sorted to following types:

- a) Highly ordered CNs. They feature large (with respect to the dimension of nanofiber) graphitic sheets stacking in particular orders. As an example, in a dramatic tubular nanostructure, graphene sheet(s) is/are rolled to form a single- or multi-layer coaxial cylinder, namely single-walled nanotubes (SWNTs) or multi-walled nanotubes (MWNTs), see Figure 7.1(a). Depending on the orientation of graphene sheets, a highly ordered CNs also can be constructed by stacking curved graphitic cones or cups. They are accordingly named as herringboned (Figure 7.1(b)) and bamboo (Figure 7.1(c)) type CNs, respectively.
- b) Amorphous carbon nanofiber. It does not have any crystalline structure or structural unit with considerable size and order.

In present study, the synthesized nanostructures are built with unique structural units, namely partially ordered discontinuous polymer/carbon sheets. These sheets are so small that are not comparable with the diameter of nanostructure, see Figure 7.1(d). Therefore, the

resultant nanostructures feature a structural characteristic between above two sorts of typical carbon nanomaterials.

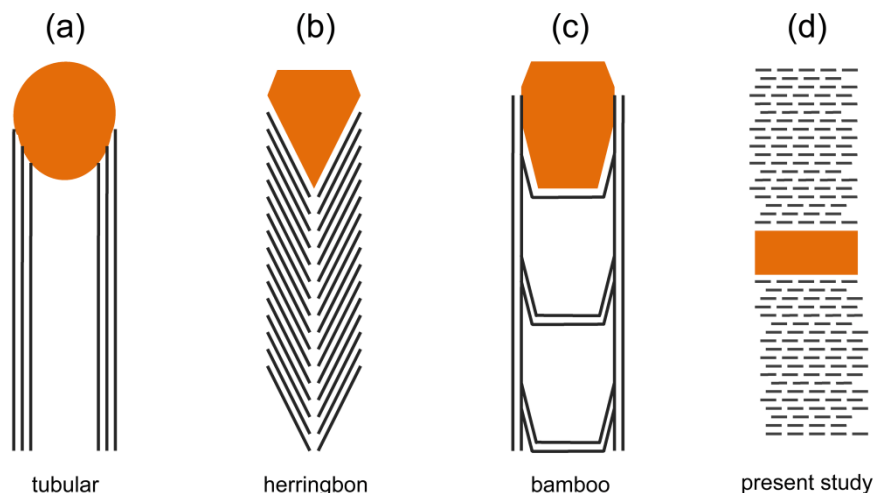


Figure 7.1. Sketch of different types of nanofibers. The orange part represent catalyst particle and the black part represent graphitic sheets.

Normally, structural defect such as edge of graphitic sheet is chemically active. Therefore our nanostructures with smaller sized structural unit may exhibit increased chemical activity under certain circumstance. It enables these nanostructures to be applied in a lot of chemical or electrochemical processes. Meanwhile, the small polymer/carbon sheets stack in an interlocking way hence present limited order. This order however cannot be compared with highly ordered CNs. In particular, when the nanofiber stretches longer during the growth, the extruding force leads to a further disorder of these small unit sheets. Such a unique microstructure reveals large distance between graphitic sheets and abundant diffusion channel. It thus facilitates functional ions, such as Si and Li, inserting and disengage in a chemical/electrochemical process.

In addition, the unique catalyst preparation and nanostructure synthesis process in present study also bring some advantages to application. Firstly, the nanostructure can be synthesized at a much lower temperature ($<250^{\circ}\text{C}$) comparing with conversional CVD synthesis processes ($>600^{\circ}\text{C}$). It avoids the risk arising from operating explosive or toxic gases (e.g. CH_4 , C_2H_2 , CO) at high temperature. Problems due to high temperature growth, for example carbon deposition on inner wall of instrument, also can be alleviated. Meanwhile, nanostructures can be synthesized in one step on conductive substrate, see chapter 3.1.3 and 4.3. A dense carbon nanofiber film can be obtained without complicated catalyst preparation. A special step to glue CNs on metal substrate is also unnecessary. At last, the morphology of nanostructure can be controlled via altering the surface roughness of substrate, the processing temperate and the

composition of reaction atmosphere. These operations are simple and easy to realize in practice.

Based on the evaluations of microstructure and synthesis process, the synthesized novel nanostructures are supposed to present advantage in many applications. They can be used as optical-adsorber, substrate of supercapacitor, electrode of lithium-ion polymer batteries, and counter electrode for dye sensitized solar cells, etc. Relative investigations are on the way and some preliminary results are shown here. Prospects as well as future investigations are also sketched and proposed here.

7.1 Applications as optical absorber

In previous investigations (both in theoretical^{163, 164} and experimental¹⁶⁵), the intense optical-adsorption of low-density CNT array/film was reported. Therefore extremely-dark material based on CNs is promising. However, to synthesize the CNT array/film, an elaborate catalyst preparation is often necessary. It thus complicates the whole process. In present study we developed a process to synthesize carbon nanofiber film on metal substrate in one step. The optical performance of prepared carbon nanofiber film was investigated for the potential application as optical absorber.

Cu plate (25×25×0.45mm) was firstly sanded (800 mesh sandpaper) to have a rough surface (Figure 7.2(a)), and then used as substrate as well as catalyst for the CVD growth. After a growth at 250°C for 1h, the surface of Cu plate was fully covered by a brown polymer-like coating, see Figure 7.2(b). This polymer-like coating was carbonized in a subsequent heat-treatment up to 800°C. The sample then shows an extremely dark appearance, see Figure 7.2(c). The carbonization can be carried out in a separate operation, or directly accomplished following the growth via evacuating reactive gas and elevating temperature. In the latter case the process is a ‘one-step-synthesis’. For detailed operations see chapter 3.1.3 and 3.2. SEM image reveals the brown coating on as-grown sample consists of tangled nanofibers (Figure 7.2(d)). These nanofibers construct a homogenous film in macroscopic view. Compare the SEM images in Figure 7.2(d) and (e), we know the heat-treatment (carbonization) at high temperature caused shrinkage of nanofibers but did not change the basic morphology of the nanofiber network, which agrees with the concept of low-density CNF array. Therefore at last the sample features a Cu plate substrate covered by homogeneous CNF film.

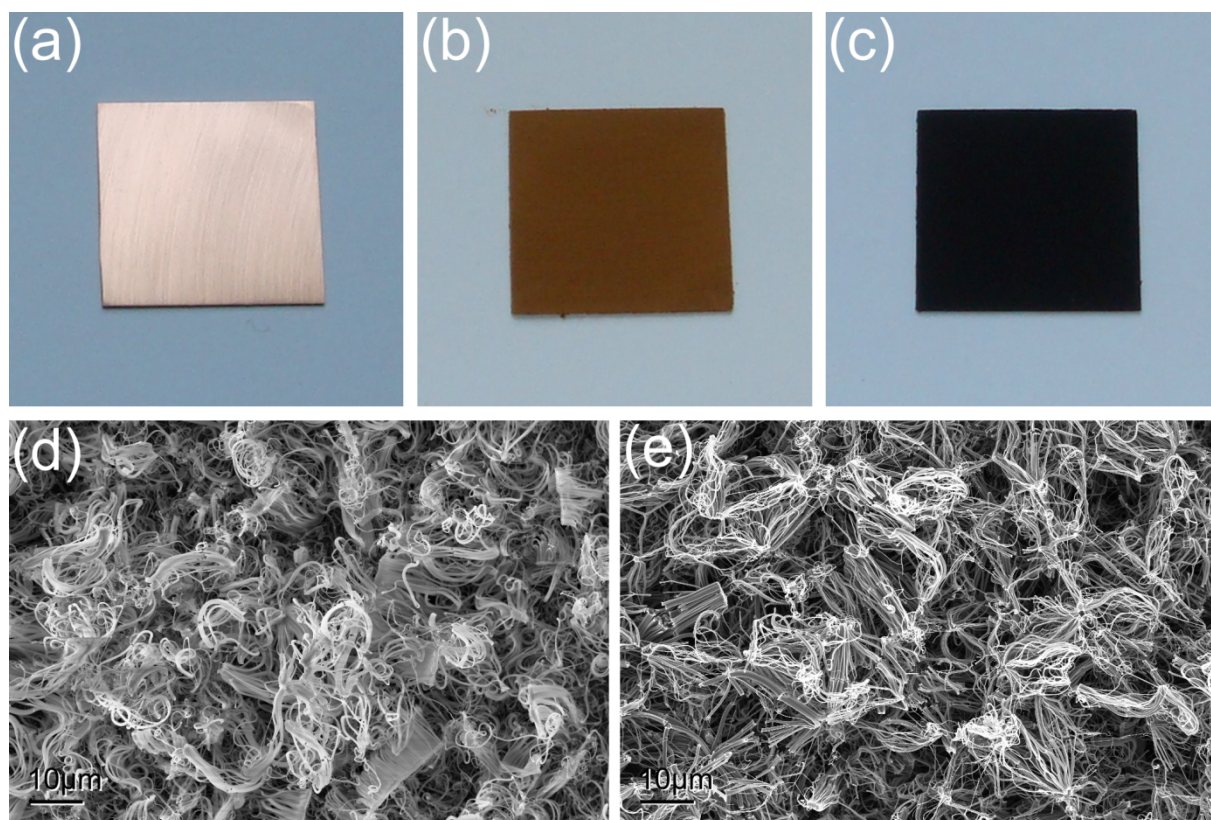


Figure 7.2. Optical images of a sample: (a) Cu substrate before growth; (b) after growth the Cu is covered by brown coating; (c) after carbonization the sample is black; (d) SEM image corresponding to (b); (e) SEM image corresponding to (c).

The total-reflectance of prepared CNF film was measured by using Hitachi U 3200 Spectrophotometer with 150 mm Dia. Integrating Sphere Accessory. The measurement was conducted in a wavelength range from 400 to 800 nm, corresponding to the visible light. The obtained spectrum reveals quite low reflectance at the whole sampling wavelength range, see Figure 7.3(a). Since the samples are nontransparent, low reflectance means high absorptance. In addition, because of the harmful effects of residual hydrogen on optical adsorption, the reflectance of sample depends significantly on the carbonization, which eliminates the hydrogen in the nanofiber. Higher temperature and longer time of heat-treatment show equivalent effect. They both promote the carbonization and consequently lead to a higher adsorptance. For example, when the sample is carbonized at 900°C for 1h, a reflectance comparable with the one treated at 800 °C for 10h can be achieved. No doubt, further increasing the carbonization temperature and time can result in lower reflectance. However, the carbonization process somehow damages the CNF film. It is partially due to the disintegration of the CNF during high temperature carbonization. Thermal expansion of metal substrate and consequent stress is also a possible reason, hence a thinner substrate like foil would be helpful. Therefore, to prepare high quality optical absorber, an optimized process is

necessary, which should take a series of parameters into account, including the growth time and corresponding length of CNF, the thickness of metal substrate, the combination of carbonization temperature and time, etc.

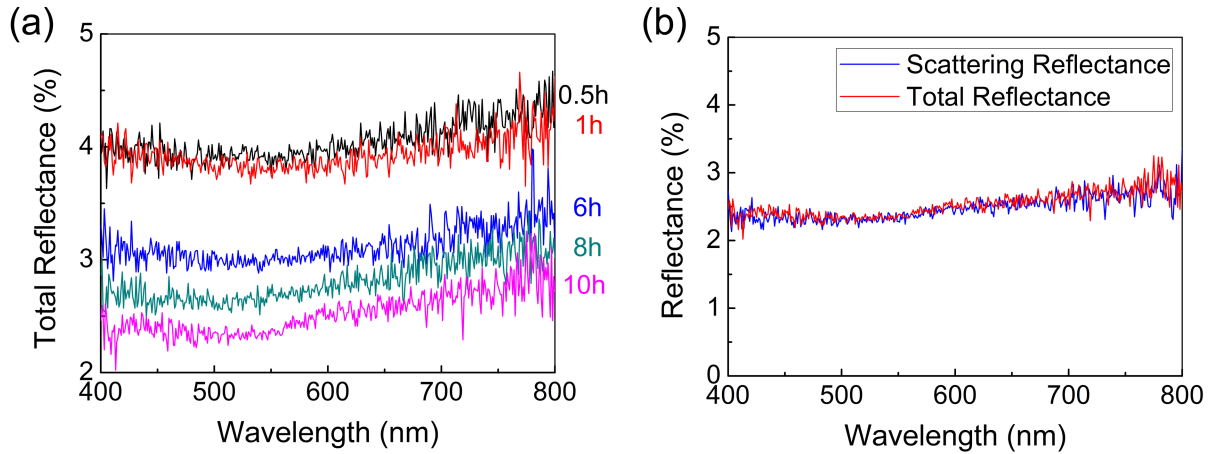


Figure 7.3. Total-reflectance of samples which underwent different time of carbonizations. (b) Total-reflectance and scattering reflectance of the sample which underwent 10h carbonization at 800°C.

For a comprehensive understanding of the optical property of the prepared samples, different modes of reflectance-measurements were performed. Besides the total-reflectance described above, the specular-reflectance was also measured using the same instrument but with a changed optical-path setting. The result is shown in Figure 7.3(b). It features a total-reflecting spectrum overlaps the scattering-reflecting one. Considering the total-reflectance includes two parts, namely specular-reflectance and scattering-reflectance, such a result reveals the specular-reflectance of the CNF film is ignorable, and all reflection comes from scattering part. The elimination of specular-reflection is ascribed to the special morphology that the nanofibers construct a rough surface in appropriate nanoscale. Actually for the CNF film shown here, it is difficult to define a normal plane and this morphology leads to a reflectance-independency upon incident direction. This feature is beneficial in applications of optical-adsorption. The other part, scattering-reflection, owns to the substantial characteristic of material. It can be reduced by intensifying the carbonization.

As references for present optical measurement and evaluation, some other usually used optical absorbers were also measured in the same method, see Figure 7.4. Compare to those absorbers coated with black paint or commercial N-Al based physical vapor deposition (PVD) multilayer film, our CNF film sample has lower reflectance almost in the whole sampling wavelength range. However, if take CNT array/film in previous report as a contrast, which can achieve an extremely high absorbance above 99%¹⁶⁵, the property of our CNF film is still

unsatisfactory. It is due to considerable hydrogen remaining in the carbonized sample, see Table 7.1. In other words, the carbonization is incomplete. The property of CNF film can be further optimized, just like we discussed above.

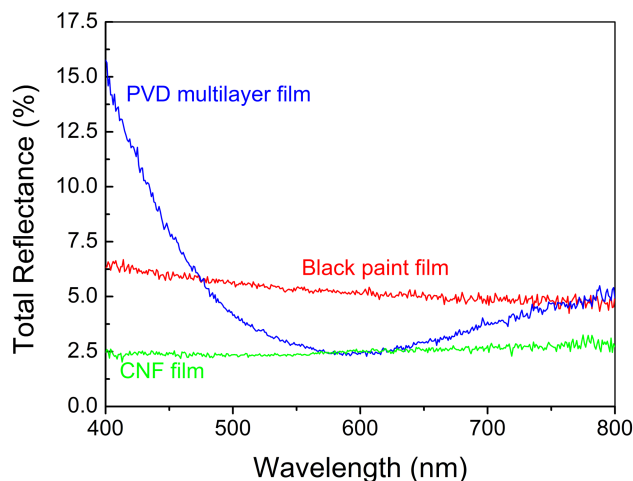


Figure 7.4. A compare between different optical absorbers.

Table 7.1. The composition of the CNF which is carbonized at 900°C for 1h.

	C	H	Cu
wt. %	84.5	0.4	15.1
at. %	91.7	5.2	3.1

In addition, the optical-absorb-ability of the CNF film is not confined within the range of visible light. When we tried to characterize the synthesized CNF using infrared spectroscopy, the CNF intensely absorbed incidence beam that we were unable to get any measurable single, whatever in transmittance mode or reflectance mode. It indicates a high absorbance in infrared range.

Besides the optical performance, the other properties of our CNF-film-based-optical-absorber also benefit the applications and make it be valuable. For example, the CNF film absorber is very stable at high temperature. In a high temperature application, diffusion of substrate material often deteriorates the optical property of absorber based on PVD multilayer film, but it does not influence the CNF film absorber. Meanwhile, the shape of CNF

film completely follows the metal substrate which can be machined to desired shape easily. Corner and groove on substrate do not influence the growth in CVD process. So the absorber has enough shape flexibility to satisfy different applications. Furthermore, in the one-step-CVD-synthesis process, high vacuum environment and high purity material are not necessary. Cheap raw material such as acetylene and simple substrate pretreatment method (e.g. sandblasting) are applicable to the synthesis. A normal chemical plant can offer the required production conditions. Therefore this material is suitable for a mass production in industry.

Practically, the CNF film based absorber can be assembled to construct a dark cell for fluorescence measurement, see Figure 7.5. The inner wall of the dark cell is completely covered by CNF; only two small holes are leaving for high power incident laser beam and detector. When incident laser shots on the sample placed in the center of the cell, fluorescence emits from the excited sample and then is received by the detector. Because the CNF film intensely absorbs any scattering beam, the detector can only receive the signal which emits directly from the testing sample. Fluorescence from other material (e.g. the inner wall of the cell, sample holder) is avoided. Such a dark cell can depress background noise during measurement, especially when short wavelength laser is used, in which case a lot of other optical-absorbers are incapable.

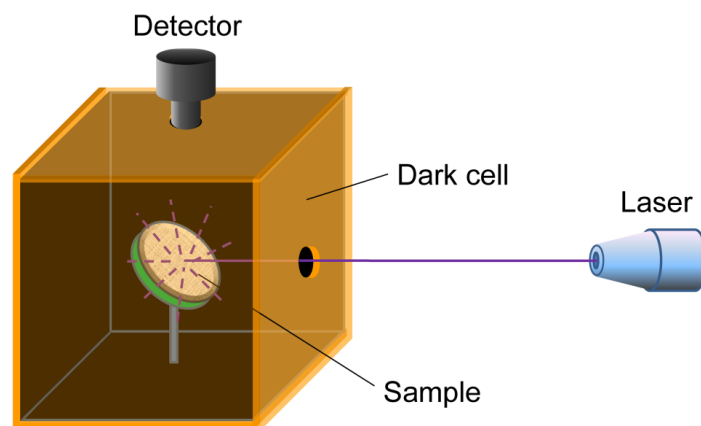


Figure 7.5. Configuration of a device for fluorescence measurement.

Besides the fluorescence measurement, the CNF film absorber also can be used in other optical devices. For example, it can be coated inside a telescope to depress scattering and thus increase the quality of image¹⁶⁶. Because the Cu substrate has ideal thermal conductivity, fabricability and affordable cost, when coat the CNF film on Cu pipes or large area Cu plates, photothermal conversion device can be produced. Both water and gaseous heat-carriers can be applied in these devices, see Figure 7.6.

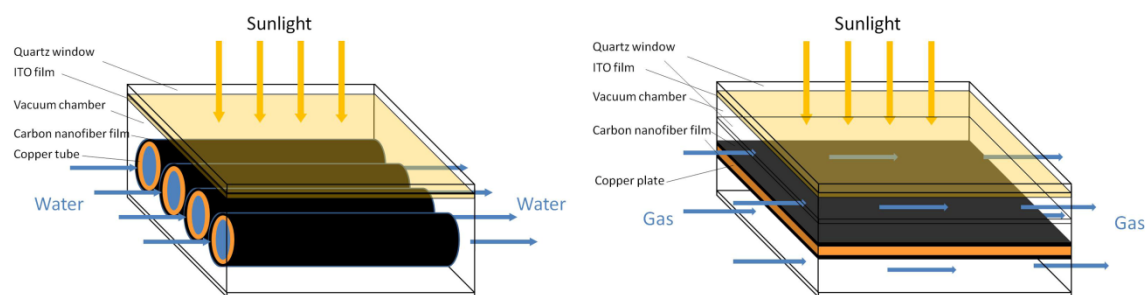


Figure 7.6. Configuration of photothermal conversion devices.

7.2 Applications as energy materials

Benefit from the intrinsic conductivity, unusual atomic architecture, abundant reserves and low costs, carbon nanomaterials are always the promising candidate for a lot of applications in energy area. For example, with more and more electronic equipments being involved in daily life, lithium-ion batteries with high capacity, long cycling life and high safety are urgently required. The function of lithium-ion batteries is based on lithium ions intercalation/deintercalation in matrix material on negative electrode during charge/discharge, respectively, while a reverse process progresses on positive electrode. Graphitized carbon can play the role of anode of the battery appropriately because the space between graphitic sheets allows lithium ions to insert in, see Figure 7.7(a), in an ideal case the lithium and carbon will form a LiC_6 structure with the maxim theoretical capacity of 372 mAh/g. However, the intercalation/deintercalation of lithium ions induces dramatic volume change and consequent fragmentation of the electrode material. It deteriorates the performance of battery significantly after cycling. To solve this problem people proposed a structure based on monolayer graphene, see Figure 7.7(b), in which both two sides of the graphene sheets can be attached by lithium ions and thus the theoretical capacity is doubled. The wrinkles generated by graphene zigzag stacking also contribute space for lithium ion storage. Up to date, such ideal graphene structured material has not been realized yet. In present study, the prepared nanofiber exactly has a structure close to the above description. The small graphene sheets stack in limited orderliness, generating large interlayer distance and abundant diffusion channels. Therefore, this material is supposed to have higher capacity than the traditional graphite-based materials. Moreover, confined by the dimension of the present CNFs, the length of diffusion route of Li^+/Li is limited to about several hundreds of nanometer within the small graphene sheets, which might allow a super-fast charge/discharge process, subsequently high power applications. In summary, the CNF in present work might have the

potential to become a novel anode material which provides high capacity together with high power property. Herein, preliminary evaluation work was carried out for this purpose.

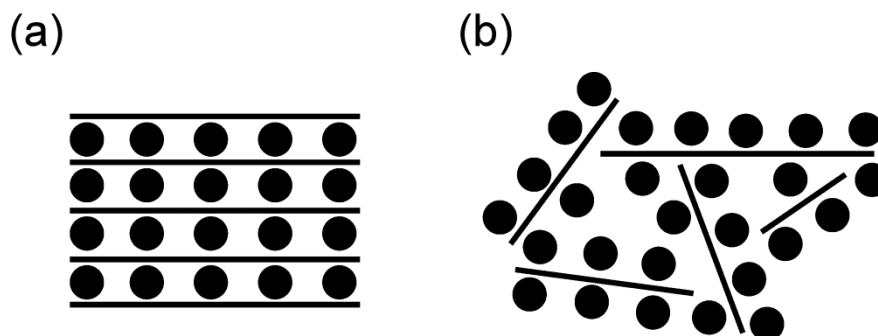


Figure 7.7. Illustration of lithium ions (a) intercalating in graphite and (b) attaching on graphene sheets.

CNF was prepared in a 5h growth at 250°C followed by 800°C carbonization for 1h. Copper nanoparticles prepared by thermal decomposition reaction were used as the catalyst. For detailed operation see chapter 3.1.2 and 3.2. A cell was assembled for the evaluation of electrochemical properties. The electrode was prepared by coating the mixture of CNF/binder/conductive agent with a ratio of 80/10/10 wt.%. Lithium foil was used both as counter electrode and reference electrode. Electrolyte was 1M LiPF₆ in a mixture of ethylene carbonate (EC) /diethyl carbonate (DEC) /ethyl methyl carbonate (EMC) solvent with volume ratio of EC/DEC/EMC=1:1:1. The cell was measured in discharge-charge cycles in the voltage of 0.01-2.0V vs. Li with 0.2mA current, and the discharge-charge rate of 0.2C. The result is shown in Figure 7.8.

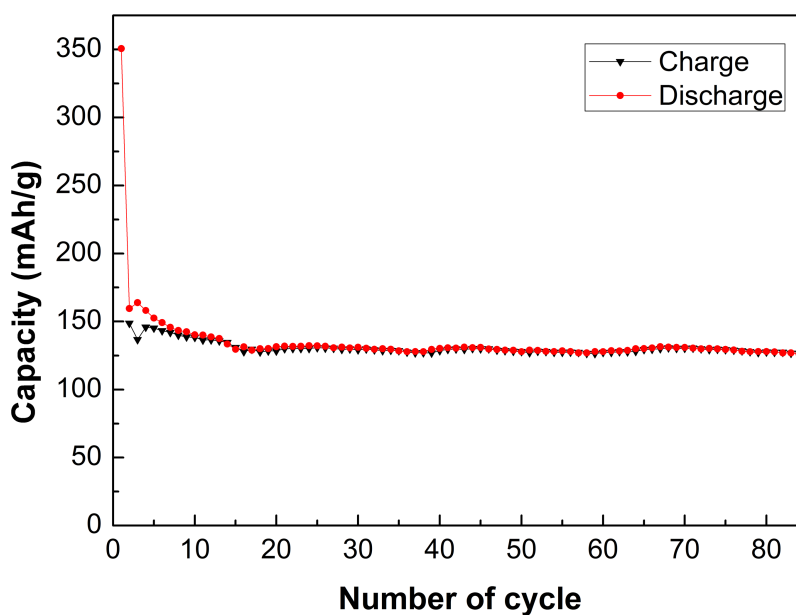


Figure 7.8. Cycling performances of CNF-based electrode.

It shows a high irreversible capacity (about 200 mAh/g) during the first cycle and a quite smooth and stable reversible capacity (about 130 mAh/g) after 15th cycle. The coulomb efficiency as high as 100% was obtained after 15th cycle since no apparent capacity fade was seen until the end of the measurement at 85 cycles and the charge values almost overlap the discharge ones. This could be attributed to the incomplete carbonization of CNFs. Since the as-grown CNFs sample contains high amount of hydrogen as well as other impurity like oxygen, it were heat-treated under 900 °C for an hour, which was still below than the requested temperature for fully carbonization. The residue hydrogen was detected as higher than 4 at.%, which might cause a lot of lattice defects and so that a large irreversible capacity. Moreover, about 15 wt.% residual of Cu catalyst was also included in the as-grown CNFs and could not be removed by heat-treatment. All these factors led to a high capacity loss (200 mAh/g) and a relatively low reversible capacity (130 mAh/g). This value is far away from satisfaction. But it could be assuaged by increasing heating temperature and prolonging time period.

Prospectively, the CNFs material is still a promising material in energy storage fields. For example, combining with Si or metal oxide to form composite, the CNF plays the role of skeleton to disperse Si nanoparticles. In this structure CNF buffers the volume change during charge/discharge as well as storages lithium ions by itself. Then the capacity of lithium storage can increase remarkably¹⁶⁷⁻¹⁶⁹. Meanwhile, in present study the size of carbon sheets in CNF is adjustable, it also makes influence on electrochemical performance hence can be optimized.

Besides the application in lithium-ion batteries, carbon nanomaterials are also used in dye-sensitized solar cells (DSSCs) as photoanode¹⁷⁰ or Pt free counter electrode^{171, 172}. For the latter application large specific surface area and high density of catalytic active sites are required, and then the I_3^- in electrolyte can be reduced in high efficiency. Normally, the active sites increase with the density of defect in carbon nanomaterials, such as the edges of graphene and dangling bonds on carbon nanotubes. Therefore people intentionally introduce defect into the structure during synthesis or in a post-treatment, e.g. acid functionalization^{173, 174}. Coincidentally the CNF prepared in present study naturally contain high density of defect, because of the unique structure, see Figure 7.1(d), and special preparation process. In addition, the CNF is converted from polymer nanofiber which contain large amount of hydrogen and considerable oxygen, see Table 4.1. By controlling the carbonization process, hydrogen and oxygen functional groups can be remained in the final CNF to increase the catalytic activity.

At last, because the CNF can be prepared in one step on conductive Cu plate or foil, it's very convenient for the application as electrode, whatever in lithium-ion batteries or dye-sensitized solar cells. The CNF film coated Cu plate or foil is also suitable for construction of supercapacitor which is a promising energy storage device. This device features high power density and extremely quick charge/discharge, therefore attracting more and more attention¹⁷⁵.

To accumulate fundamental data for the application such as supercapacitor, nitrogen adsorption-desorption isotherm analysis was carried out and the result curve is shown in Figure 7.9, based on the curve the specific surface area can be calculated. According to BET (Brunauer-Emmet-Teller) theory and Langmuir equation, the specific surface is 68.9 m²/g and 98.8 m²/g, respectively. These values are comparable with normal carbon nanotubes synthesized at high temperature.

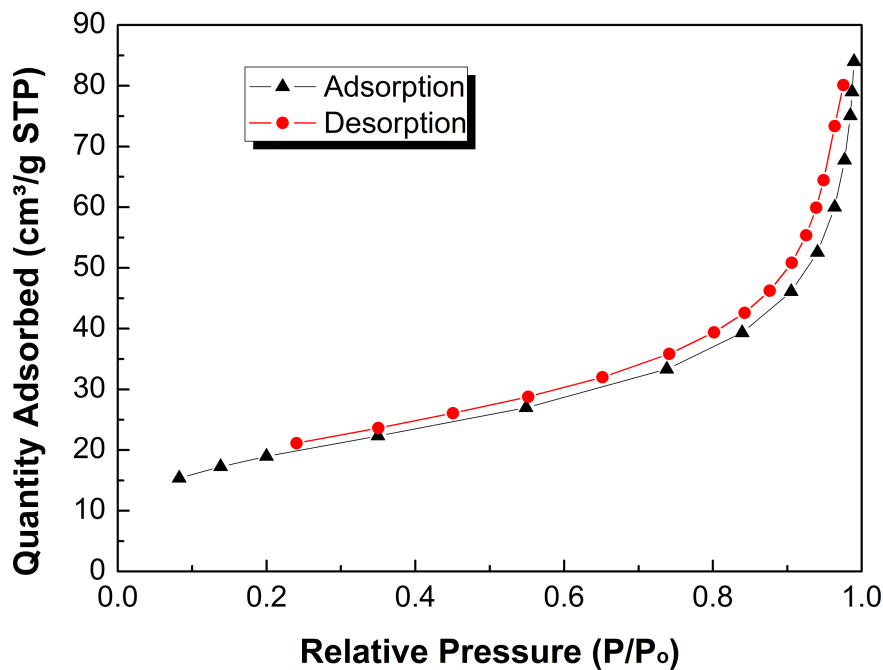


Figure 7.9. Nitrogen adsorption-desorption isotherm analysis.

7.3 In-situ doped CNs

We are not only interested in the microstructure of the synthesized carbon nanofibers, but also have willing to investigate their potential applications associated with the unique growth mechanism. Methodologically, the above-mentioned VFS mechanism provides us good chance to in-situ synthesize doped carbon nanostructures (CNs). The doped elements, such as nitrogen, silicon and boron change the morphology as well as the band structure of CNs, so that could probably improve their electrochemical properties. For instance, when the carbon anode in Li-ion battery is doped by Si, the capacity can be doubled, or even more. Doping

nitrogen into CNTs not only improves the performance in supercapacitors^{176, 177}, but also results in a new application, namely metal-free catalyst¹⁷⁸. It can be used in fuel cells to replace expensive Pt and Pd catalysts.

To realize an in-situ synthesis of CNs, a VFS growth is favored. For a conventional CVD process which follows the VLS mechanism, the growth is based on carbon atoms dissolving and diffusing in metallic catalyst particle. It's quite difficult to fuse other element besides carbon during this process. Therefore the doping is often achieved in an additional post-growth-treatment. To simplify the synthesis process and improve the property of the doped CNs, in-situ doping method is expected, which directly dopes functional element into the CNs during the growth. In present low-temperature VFS process, the basic reaction is that C_2H_2 molecular couple each other to form oligomers, such as benzene and its derivatives, and then these oligomers further couple to construct polymer nanosheets. Both the oligomer and polymer nanosheets contain plenty of hydrogen atoms and functional groups instead of a pure carbon lattice. They are able to connect other organic functional groups which contain desired elements. Meanwhile, the growth is a surface process, thus the doped atoms or groups do not need to dissolve or pass through the catalyst particle. Therefore we have chance to in-situ dope various elements into the growth product during the reaction. For example, if we introduce nitrogen containing reagent (such as ammonia or hydrazine) into the reaction atmosphere, probably the nitrogen will merge into the hydrocarbon molecules on metal catalyst and finally fuse into the polymer sheet along with the growth, see the schematic Figure 7.10. The new proposed VFS mechanism is expected to lead to a new route for doped CNs synthesis.

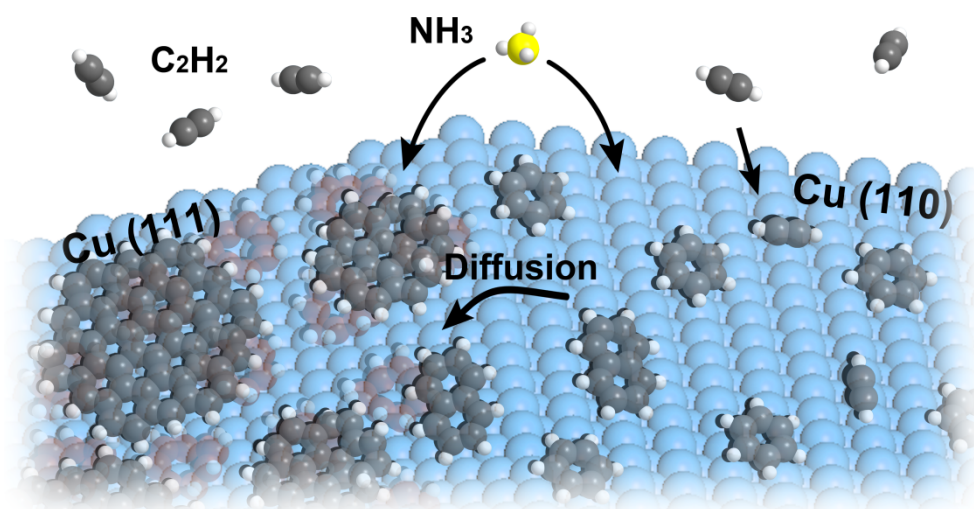


Figure 7.10. An idea for in-situ doping nitrogen into polymer nanofiber.

7.4 Two-dimensional (2D) nanostructures

In the investigations, besides various 1D nanostructures, some interesting two-dimensional nanostructures (nanoflakes) were found in the grown products as well. Most of them were synthesized coincidentally therefore in-depth investigation has not been performed yet. Relative work however is worth to push forward, because the unique morphology endows 2D nanostructures with distinct properties. For example, comparing with 1D nanostructures, the 2D ones feature a more stable connection with the substrate. Hence they are able to serve in situations with liquid or gas flows. Systematic investigation about the 2D nanostructures in the future will extend their applications.

Figure 7.11 shows 3 kinds of vertical aligned 2D nanostructures. They were all synthesized in standard growth processes at 250°C, see the description in chapter 3.2. Notably, this process temperature is much lower than that for conventional growth of 2D nanostructures, such as the typical CVD growth at 1000 °C for graphene synthesis^{179, 180}.

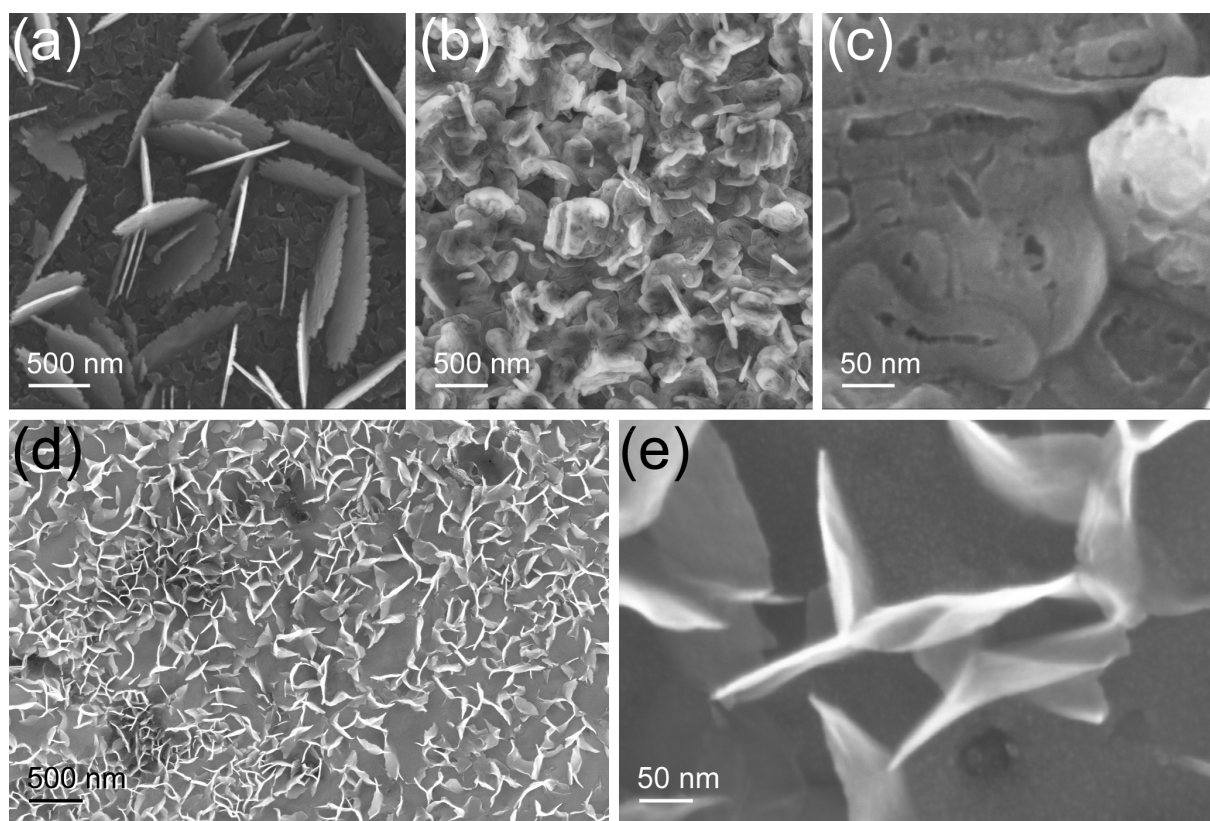


Figure 7.11. SEM images of various two-dimensional nanostructures prepared at 250°C: (a) vertical aligned 2D nanoflakes; (b) ear-like nanostructure; (c) enlarged image of (b); (d) graphene-like nanostructure; (e) enlarged image of (d).

The thin and flat flakes in Figure 7.11(a) were synthesized on well-polished Cu slug. In this process, besides the main carbon-source-gas namely C_2H_2 , a little amount of HCl was also

introduced into the reaction atmosphere. In another process, all operations are same except that the HCl was replaced by H_2O_2 . As a result dense ear-like nanostructure was obtained, see Figure 7.11(b). To enlarge the image, see Figure 7.11(c), it can be seen the ear-like nanostructure is constructed by twists and turns of nanofiber.

In chapter 4.3 we have pointed out that a large and smooth Cu surface cannot catalyze nanofiber growth. Normally, the growth of nanofiber requires catalyst in a particle appearance. Then the reaction product can accumulate on one or two sides of the particle to form a fiber. The accumulation/precipitation of reaction product on the catalyst must be inhomogeneous. In the case of large area smooth Cu surface, the growth product accumulates/precipitates almost in a homogenous way. It led to a coverage on the whole Cu substrate instead of fiber-like structure formation, see Figure 4.11. Here, although large and smooth Cu surface is used, we still obtain 2D nanostructures, because additional gases (HCl or H_2O_2) in the reaction atmosphere play a crucial role. These gases probably selectively adsorb on certain area of the Cu surface. Such a selective adsorption is due to the polycrystalline nature of Cu substrate. In other words, the polished smooth Cu surface actually features different orientations at different area. It leads to different interaction with those additional gases. The additional gas therefore adsorbs and blocks partial area of the Cu surface, but leaves the other area free to catalyze surface reaction. At last growth product accumulates on certain area of the Cu surface to construct 2D nanostructure. We can understand it in this way: the additional gas intensifies the difference between each parts of the Cu surface in terms of catalytic activity. It results in the inhomogeneous precipitation of growth product.

When using Fe slug instead of Cu as substrate, after a growth in pure C_2H_2 , very thin flakes vertically align on the slug, see Figure 7.11(d). In the enlarged SEM image (Figure 7.11(e)), the flakes show semitransparent feature. This morphology looks like graphene. To confirm the microstructure of these flakes, further characterizations are required. However, we can review the growth progressing on Fe nanoparticle catalyst (see chapter 6.1). It showed a unique reaction route on Fe surface that resulted in fused six-membered planar molecules. Therefore, here we should consider the possibility of graphene generation on Fe slug.

All above discoveries reveal 2D nanostructures also can be synthesized in low-temperature CVD processes. The catalysts and growth conditions are similar to the process for 1D nanostructures synthesis. It indicates our new proposed VFS growth mechanism possibly can be further extended to interpret the growth of 2D nanostructure. In-depth

investigation is worth to carry out in the future research. Such work will not only perfect and enrich the VFS mechanism, but also generate new types of material for various applications.

8. Conclusions

Multiform 1D nanostructures are synthesized by using thermal CVD as the growth technique in atmospheric pressure C_2H_2 . The process temperatures (250-350°C) are much lower than the usual CVD growth condition (>600°C). The synthesized nanostructures contain large amount of hydrogen and feature polymer-like nature. They are constructed by stacking polymer sheets based on aromatic structure. A post-growth heat-treatment at high-temperature can carbonize the polymer-like nanostructures into carbon nanostructure without shape change.

For present low-temperature growths, classical VLS mechanism is no longer applicable. Instead, the growth could be described as a Vapor (adsorption) - Facet (diffusion) – Solid (precipitation) process, we therefore name it ‘VFS mechanism’ to distinguish from the classical VLS and VSS (vapor-solid-solid) ones. In this new proposed mechanism, hydrocarbon molecule instead of carbon atom plays a role of structural-unit to build nanostructures. The VFS mechanism is composed by a series of surface processes. In detail, it corresponds to a 3-step growth model: 1) hydrocarbon source gas coupling on catalyst surface to form oligomers, 2) oligomers diffusion through the catalyst surface between different indexed facets, 3) oligomers further polymerization and nanofiber construction.

The diffusion of oligomers is driven by concentration gradient, because each crystalline face of catalyst particle exhibits different catalytic-activity (productivity) for producing free-moving oligomer. In particular, when immobilized reaction product forms and poisons certain facet of catalyst, above gradient is intensified significantly. For instance, immovable COT forms and sticks on Cu(111) face, carbon atoms accumulate on Fe(001) face and infiltrate inwards; these immovable products locally prevent further surface reaction as well as oligomer production. Then in terms of other movable oligomers, their concentration gradient is intensified between the poisoned and active catalyst facets.

Kinetics analysis reveals in the case of Cu catalyzed nanofiber growth, polymerization is the rate-determining-step. The polymerization as well as the whole growth can be accelerated by certain additional oxygen-containing-molecules in reaction atmosphere, such as H_2O in present study.

The extensive adoptability of the proposed VFS mechanism is proved by a series of experiments using different catalysts (Cu, Fe, and Ni). They were all carried out at low-temperature (250-350°C) and generate polymer-like nanofibers with similar microstructure.

Although each reaction system exhibits individual characteristics with respect to composition and morphology of product, growth mode, kinetics feature, and catalyst evolution, these specificities can be explained within the framework of VFS.

Nevertheless, common characteristics of the proposed VFS mechanism can be extracted from a variety of reaction systems. They feature: i) Competition and collaboration among different catalyst facets are the core elements of nanostructure growth. The facets on which adsorbed C_2H_2 molecules couple to form oligomers are defined as adsorbent facets, while the facets receiving coupling products and finally building up the polymer nanofibers are defined as growth facets. The diffusion progresses from adsorbent facets to growth facets. It is notable that the adsorbent facets and the growth facets may reverse in some cases, depending on surface energy of catalyst nanocrystal and reactions occurring on them, which are actually influenced by reaction temperature and gaseous environment. ii) The synthesized nanofibers consist of loosely stacking polymer sheets. It allows the new build-up units to insert themselves into gaps between existing nanofiber and the catalyst facets, and consequently to lift the old nanofiber up a bit to become a new part of it. It presents that the existing nanofiber do not act a barrier blocking further growth of themselves. iii) Catalyst nanocrystals have undergone a surface reconstruction process, and turn into regular appearances with certain low index facets exposing out.

The spontaneous shape-evolution of catalyst is ascribed to joint action of thermodynamic and kinetic elements. Certain ingredients such as H_2O in reaction atmosphere are absorbed on the catalyst and reduce the surface free energy of catalyst. Therefore catalyst splitting as well as surface reconstruction is possible in thermodynamics. Meanwhile, reactions progressing on catalyst surface (e.g. C_2H_2 coupling, oligomer diffusion and polymerization) accelerate the surface reconstruction. They make the catalyst evolution be realizable in kinetics. Therefore, although catalyst evolution allows a growth to initial on catalyst precursor featuring random size and shape, some preconditions must be met. A property reaction atmosphere to reduce surface free energy is required. Curved surface and well-ordered inner crystalline lattice of the catalyst precursor are also indispensable. They facilitate the evolution by reducing the number of atoms which need to be rearranged. Only then the evolution is able to progress under the acceleration of those kinetic processes.

Attribute to the catalyst evolution, nanostructures can be directly synthesized on a massive metal substrate without elaborate preparation of nanoparticle catalyst. Along with the growth, small metal particles peel from the substrate because of surface reconstruction. These

particles are true effective catalysts, and their size depends on the initial surface roughness of metal substrate (catalyst precursor). When alter the surface roughness of Cu substrate, various nanostructures are obtained. This experimental fact reveals a size effect. The morphology, growth mode and microstructure of the as-grown nanofiber all relate to the size of corresponding catalyst particles. Two critical sizes are extracted: Straight nanofiber or nanohelix tend to grow on the catalyst particles which are larger or smaller than 70nm, respectively, and they always show a symmetrical-growth mode; when the catalyst particle is smaller than 35nm, amorphous nanofiber tends to form in a tip-growth mode. The size effect is induced substantially by asymmetry of catalyst particle. Smaller catalyst particle shows lower symmetry. It leads to a high difference of growth velocity on two sides of catalyst particle, which consequently influences the morphology and microstructure of as-grown nanostructure.

Based on in-depth investigation of the intrinsic symmetry and corresponding geometry feature of the metal catalyst, a universal facet-selective catalytic CVD growth method is created to shape-controlled synthesize carbon nanostructures. Cu nanocrystal works as the node and carbon nanofibers (branches) grow selectively on the certain facets. The number of carbon nanobranches is designed by intentionally to expose specific facets of the nanocrystal via altering reaction temperature and atmosphere. In this way the stretching directions of carbon nanostructure follow the symmetry of nanocrystal. The length of carbon nanostructures can be tailored by growth duration. By means of patenting the catalyst, the precise control of the size and the location of carbon nanostructures are also possible. 2-, 3-, 6-, and 8-branched carbon nanostructures are finally synthesized.

The unique microstructure and synthesis process endow the synthesized nanostructures with broad applications. Homogeneous CNF film is prepared on Cu substrate via a one-step CVD process. It features optical-absorptance as high as 97% at the wavelength from 400 to 800 nm. The specular reflection is eliminated almost completely. The optical performance, thermal stability, shape flexibility and the simple synthesis process enable the CNF film coated Cu plate to work as optical-absorber. On the other hand, the synthesized carbon nanostructure consists of discontinuously stacking small carbon sheets. It provides large interlayer distance and abundant diffusion channel for Li ion intercalation. It is therefore a potential anode material for lithium-ion polymer batteries. Preliminary evaluation work indicates quite stable capacity and high efficiency of the material, but the capacity is still waiting to be improved in future work. The synthesized nanostructures also show potentials for the applications in supercapacitor and dye-sensitized solar cells. Methodologically, the

VFS mechanism provides us good chance to in-situ synthesize doped carbon nanostructures (CNs).

General speaking, novel 1D nanostructures are synthesized via low-temperature catalytic CVD processes. A unique VFS mechanism is proposed to interpret the growth. The synthesized materials show various morphologies and distinct microstructure therefore have broad application prospects. In-depth investigation is worth to carry out in the future research.

9. References

1. Liu, T. X.; Phang, I. Y.; Shen, L.; Chow, S. Y.; Zhang, W. D., Morphology and Mechanical Properties of Multiwalled Carbon Nanotubes Reinforced Nylon-6 Composites. *Macromolecules* 2004, 37, 7214-7222.
2. Zhan, G. D.; Kuntz, J. D.; Garay, J. E.; Mukherjee, A. K., Electrical Properties of Nanoceramics Reinforced with Ropes of Single-walled Carbon Nanotubes. *Appl. Phys. Lett.* 2003, 83, 1228-1230.
3. Thostenson, E. T.; Chou, T. W., Aligned Multi-walled Carbon Nanotube-reinforced Composites: Processing and Mechanical Characterization. *J. Phys. D-Appl. Phys.* 2002, 35, L77-L80.
4. Goh, C. S.; Wei, J.; Lee, L. C.; Gupta, M., Development of Novel Carbon Nanotube Reinforced Magnesium Nanocomposites Using the Powder Metallurgy Technique. *Nanotechnology* 2006, 17, 7-12.
5. Han, Z. J.; Ostrikov, K., Controlled Electronic Transport in Single-walled Carbon Nanotube Networks: Selecting Electron Hopping and Chemical Doping Mechanisms. *Appl. Phys. Lett.* 2010, 96.
6. Shi, S. L.; Liang, J., Electronic Transport Properties of Multiwall Carbon Nanotubes/Yttria-stabilized Zirconia Composites. *J. Appl. Phys.* 2007, 101.
7. Cahill, D. G.; Ford, W. K.; Goodson, K. E.; Mahan, G. D.; Majumdar, A.; Maris, H. J.; Merlin, R.; Phillpot, Sr., Nanoscale Thermal Transport. *J. Appl. Phys.* 2003, 93, 793-818.
8. Wang, J. A.; Wang, J. S., Carbon Nanotube Thermal Transport: Ballistic to Diffusive. *Appl. Phys. Lett.* 2006, 88.
9. Satishkumar, B. C.; Brown, L. O.; Gao, Y.; Wang, C. C.; Wang, H. L.; Doorn, S. K., Reversible Fluorescence Quenching in Carbon Nanotubes for Biomolecular Sensing. *Nat. Nanotechnol.* 2007, 2, 560-564.
10. Nakayama-Ratchford, N.; Bangsaruntip, S.; Sun, X. M.; Welsher, K.; Dai, H. J., Noncovalent Functionalization of Carbon Nanotubes by Fluorescein-polyethylene Glycol: Supramolecular Conjugates with Ph-dependent Absorbance and Fluorescence. *J. Am. Chem. Soc.* 2007, 129, 2448-+.
11. Bonard, J. M.; Salvetat, J. P.; Stockli, T.; de Heer, W. A.; Forro, L.; Chatelain, A., Field Emission from Single-wall Carbon Nanotube Films. *Appl. Phys. Lett.* 1998, 73, 918-920.
12. Deheer, W. A.; Chatelain, A.; Ugarte, D., A Carbon Nanotube Field-emission Electron Source. *Science* 1995, 270, 1179-1180.

13. Ma, S. B.; Nam, K. W.; Yoon, W. S.; Bak, S. M.; Yang, X. Q.; Cho, B. W.; Kim, K. B., Nano-sized Lithium Manganese Oxide Dispersed on Carbon Nanotubes for Energy Storage Applications. *Electrochem. Commun.* 2009, 11, 1575-1578.
14. Sathiya, M.; Prakash, A. S.; Ramesha, K.; Tarascon, J. M.; Shukla, A. K., V2O5-Anchored Carbon Nanotubes for Enhanced Electrochemical Energy Storage. *J. Am. Chem. Soc.* 2011, 133, 16291-16299.
15. Xu, D. D.; Xu, Q.; Wang, K. X.; Chen, J.; Chen, Z. M., Fabrication of Free-Standing Hierarchical Carbon Nanofiber/Graphene Oxide/Polyaniline Films for Supercapacitors. *ACS Appl. Mater. Interfaces* 2014, 6, 200-209.
16. Liu, J. W.; Kuo, Y. T.; Klabunde, K. J.; Rochford, C.; Wu, J.; Li, J., Novel Dye-Sensitized Solar Cell Architecture Using TiO₂-Coated Vertically Aligned Carbon Nanofiber Arrays. *ACS Appl. Mater. Interfaces* 2009, 1, 1645-1649.
17. Vander Wal, R. L.; Ticich, T. M.; Curtis, V. E., Substrate-support Interactions in Metal-catalyzed Carbon Nanofiber Growth. *Carbon* 2001, 39, 2277-2289.
18. Qin, L. C., CVD Synthesis of Carbon Nanotubes. *J. Mater. Sci. Lett.* 1997, 16, 457-459.
19. Zhang, G. Y.; Jiang, X.; Wang, E. G., Tubular Graphite Cones. *Science* 2003, 300, 472-474.
20. Qi, X. S.; Zhong, W.; Deng, Y.; Au, C. T.; Du, Y. W., Characterization and Magnetic Properties of Helical Carbon Nanotubes and Carbon Nanobelts Synthesized in Acetylene Decomposition over Fe-Cu Nanoparticles at 450 degrees C. *J. Phys. Chem. C* 2009, 113, 15934-15940.
21. Li, D. W.; Pan, L. J.; Wu, Y. K.; Peng, W., The effect of changes in synthesis temperature and acetylene supply on the morphology of carbon nanocoils. *Carbon* 2012, 50, 2571-2580.
22. Xia, J. H.; Jiang, X.; Jia, C. L.; Dong, C., Hexahedral Nanocementites Catalyzing the Growth of Carbon Nanohelices. *Appl. Phys. Lett.* 2008, 92.
23. Tavares, M. T.; Bernardo, C. A.; Alstrup, I.; Rostrupnielsen, J. R., Reactivity of Carbon Deposited on Nickel Copper Alloy Catalysts from the Decomposition of Methane. *J. Catal.* 1986, 100, 545-548.
24. Bernardo, C. A.; Alstrup, I.; Rostrupnielsen, J. R., Carbon Deposition and Methane Steam Reforming on Silica-supported Ni-Cu Catalysts. *J. Catal.* 1985, 96, 517-534.
25. Charlier, J. C.; DeVita, A.; Blase, X.; Car, R., Microscopic Growth Mechanisms for Carbon Nanotubes. *Science* 1997, 275, 646-649.

26. Shibuta, Y.; Maruyama, S., Molecular Dynamics Simulation of Formation Process of Single-walled Carbon Nanotubes by CCVD Method. *Chem. Phys. Lett.* 2003, 382, 381-386.
27. Gavillet, J.; Loiseau, A.; Journet, C.; Willaime, F.; Ducastelle, F.; Charlier, J. C., Root-growth Mechanism for Single-wall Carbon Nanotubes. *Phys. Rev. Lett.* 2001, 87.
28. Kukovitsky, E. F.; L'Vov, S. G.; Sainov, N. A., VLS-Growth of Carbon Nanotubes from the Vapor. *Chem. Phys. Lett.* 2000, 317, 65-70.
29. Huang, S. M.; Woodson, M.; Smalley, R.; Liu, J., Growth Mechanism of Oriented Long Single Walled Carbon Nanotubes Using "Fast-heating" Chemical Vapor Deposition Process. *Nano Letters* 2004, 4, 1025-1028.
30. Helveg, S.; Lopez-Cartes, C.; Sehested, J.; Hansen, P. L.; Clausen, B. S.; Rostrup-Nielsen, J. R.; Abild-Pedersen, F.; Norskov, J. K., Atomic-scale Imaging of Carbon Nanofibre Growth. *Nature* 2004, 427, 426-429.
31. Wagner, R. S.; Ellis, W. C., Vapor-liquid-solid Mechanism of Single Crystal Growth (New Method Growth Catalysis from Impurity Whisker Epitaxial + Large Crystals Si E). *Appl. Phys. Lett.* 1964, 4, 89-&.
32. Kanzow, H.; Ding, A., Formation Mechanism of Single-wall Carbon Nanotubes on Liquid-metal Particles. *Physical Review B* 1999, 60, 11180-11186.
33. Kumar, M.; Ando, Y., Chemical Vapor Deposition of Carbon Nanotubes: A Review on Growth Mechanism and Mass Production. *J. Nanosci. Nanotechnol.* 2010, 10, 3739-3758.
34. Alstrup, I., A New Model Explaining Carbon-filament Growth on Nickel, Iron, and Ni-Cu Alloy Catalysts. *J. Catal.* 1988, 109, 241-251.
35. Kock, A.; Debokx, P. K.; Boellaard, E.; Klop, W.; Geus, J. W., The Formation of Filamentous Carbon on Iron and Nickel-catalysts .2. Mechanism. *J. Catal.* 1985, 96, 468-480.
36. Snoeck, J. W.; Froment, G. F.; Fowles, M., Filamentous Carbon Formation and Gasification: Thermodynamics, Driving Force, Nucleation, and Steady-state Growth. *J. Catal.* 1997, 169, 240-249.
37. Qin, Y.; Eggers, M.; Staedler, T.; Jiang, X., Symmetric Growth of Carbon Nanosheets on Cu Nanowires by a Surface Diffusion Mechanism. *Nanotechnology* 2007, 18.
38. Qin, Y.; Jiang, X.; Cui, Z. L., Low-temperature Synthesis of Amorphous Carbon Nanocoils via Acetylene Coupling on Copper Nanocrystal Surfaces at 468 K: a Reaction Mechanism Analysis. *J. Phys. Chem. B* 2005, 109, 21749-21754.
39. Qin, Y.; Zhang, Q.; Cui, Z. L., Effect of synthesis method of nanocopper catalysts on the morphologies of carbon nanofibers prepared by catalytic decomposition of acetylene. *J. Catal.* 2004, 223, 389-394.

40. Qin, Y.; Zhang, Z. K.; Cui, Z. L., Helical Carbon Nanofibers with a Symmetric Growth Mode. *Carbon* 2004, 42, 1917-1922.
41. Xia, J. H.; Jiang, X.; Jia, C. L., The Size Effect of Catalyst on the Growth of Helical Carbon Nanofibers. *Appl. Phys. Lett.* 2009, 95.
42. Deck, C. P.; Vecchio, K., Prediction of Carbon Nanotube Growth Success by the Analysis of Carbon-Catalyst Binary Phase Diagrams. *Carbon* 2006, 44, 267-275.
43. Lander, J. J.; Kern, H. E.; Beach, A. L., Solubility and Diffusion Coefficient of Carbon in Nickel-Reaction Rates of Nickel-Carbon Alloys with Barium Oxide. *J. Appl. Phys.* 1952, 23, 1305-1309.
44. Lobo, J. A.; Geiger, G. H., Thermodynamics and Solubility of Carbon in Ferrite and Ferritic Fe-Mo Alloys. *Metallurgical Transactions a-Physical Metallurgy and Materials Science* 1976, 7, 1347-1357.
45. Wert, C. A., Diffusion Coefficient of C in α -iron. *Physical Review* 1950, 79, 601-605.
46. Alter, W.; Borgmann, D.; Stadelmann, M.; Worn, M.; Wedler, G., Interaction of Acetylene with Films of the Transition-Metals Iron, Nickel, And Palladium. *J. Am. Chem. Soc.* 1994, 116, 10041-10049.
47. Iijima, S., Helical Microtubules of Graphitic Carbon. *Nature* 1991, 354, 56-58.
48. Hone, J.; Llaguno, M. C.; Nemes, N. M.; Johnson, A. T.; Fischer, J. E.; Walters, D. A.; Casavant, M. J.; Schmidt, J.; Smalley, R. E., Electrical and Thermal Transport Properties of Magnetically Aligned Single Wall Carbon Nanotube Films. *Appl. Phys. Lett.* 2000, 77, 666-668.
49. Yu, M. F.; Files, B. S.; Arepalli, S.; Ruoff, R. S., Tensile Loading of Ropes of Single Wall Carbon Nanotubes and Their Mechanical Properties. *Phys. Rev. Lett.* 2000, 84, 5552-5555.
50. Kataura, H.; Kumazawa, Y.; Maniwa, Y.; Umez, I.; Suzuki, S.; Ohtsuka, Y.; Achiba, Y., Optical Properties of Single-wall Carbon Nanotubes. *Synth. Met.* 1999, 103, 2555-2558.
51. Hutchison, J. L.; Kiselev, N. A.; Krinichnaya, E. P.; Krestinin, A. V.; Loutfy, R. O.; Morawsky, A. P.; Muradyan, V. E.; Obratzsova, E. D.; Sloan, J.; Terekhov, S. V.; Zakharov, D. N., Double-walled Carbon Nanotubes Fabricated by a Hydrogen Arc Discharge Method. *Carbon* 2001, 39, 761-770.
52. Gamaly, E. G.; Ebbesen, T. W., Mechanism of Carbon Nanotube Formation in The Arc-discharge. *Physical Review B* 1995, 52, 2083-2089.

-
53. Scott, C. D.; Arepalli, S.; Nikolaev, P.; Smalley, R. E., Growth Mechanisms for Single-wall Carbon Nanotubes in a Laser-ablation Process. *Appl. Phys. A-Mater. Sci. Process.* 2001, 72, 573-580.
54. Zhang, Y.; Iijima, S., Formation of Single-wall Carbon Nanotubes by Laser Ablation of Fullerenes at Low Temperature. *Appl. Phys. Lett.* 1999, 75, 3087-3089.
55. Tanaka, A.; Yoon, S. H.; Mochida, I., Formation of Fine Fe-Ni Particles for the Non-supported Catalytic Synthesis of Uniform Carbon Nanofibers. *Carbon* 2004, 42, 1291-1298.
56. Motojima, S.; Chen, Q. Q., Three-dimensional Growth Mechanism of Cosmo-mimetic Carbon Microcoils Obtained by Chemical Vapor Deposition. *J. Appl. Phys.* 1999, 85, 3919-3921.
57. Cassell, A. M.; Raymakers, J. A.; Kong, J.; Dai, H. J., Large Scale CVD Synthesis of Single-walled Carbon Nanotubes. *J. Phys. Chem. B* 1999, 103, 6484-6492.
58. Couteau, E.; Hernadi, K.; Seo, J. W.; Thien-Nga, L.; Miko, C.; Gaal, R.; Forro, L., CVD Synthesis of High-purity Multiwalled Carbon Nanotubes Using CaCO₃ Catalyst Support for Large-scale Production. *Chem. Phys. Lett.* 2003, 378, 9-17.
59. Kim, Y. A.; Hayashi, T.; Naokawa, S.; Yanaisawa, T.; Endo, M., Comparative Study of Herringbone and Stacked-cup Carbon Nanofibers. *Carbon* 2005, 43, 3005-3008.
60. Zhu, Y. A.; Sui, Z. J.; Zhao, T. J.; Dai, Y. C.; Cheng, Z. M.; Yuan, W. K., Modeling of Fishbone-type Carbon Nanofibers: A Theoretical Study. *Carbon* 2005, 43, 1694-1699.
61. de Lucas, A.; Garcia, P. B.; Garrido, A.; Romero, A.; Valverde, J. L., Catalytic Synthesis of Carbon Nanofibers with Different Graphene Plane Slignments Using Ni Deposited on Iron Pillared Clays. *Appl. Catal. A-Gen.* 2006, 301, 123-132.
62. Cui, H.; Zhou, O.; Stoner, B. R., Deposition of Aligned Bamboo-like Carbon Nanotubes Via Microwave Plasma Enhanced Chemical Vapor Deposition. *J. Appl. Phys.* 2000, 88, 6072-6074.
63. Lee, C. J.; Park, J., Growth Model of Bamboo-shaped Carbon Nanotubes by Thermal Chemical Vapor Deposition. *Appl. Phys. Lett.* 2000, 77, 3397-3399.
64. Lee, C. J.; Park, J. H.; Park, J., Synthesis of Bamboo-shaped Multiwalled Carbon Nanotubes Using Thermal Chemical Vapor Deposition. *Chem. Phys. Lett.* 2000, 323, 560-565.
65. Lin, M.; Tan, J. P. Y.; Boothroyd, C.; Loh, K. P.; Tok, E. S.; Foo, Y. L., Dynamical Observation of Bamboo-like Carbon Nanotube Growth. *Nano Letters* 2007, 7, 2234-2238.
66. Tu, J. P.; Zhu, L. P.; Hou, K.; Guo, S. Y., Synthesis and Frictional Properties of Array Film of Amorphous Carbon Nanofibers on Anodic Aluminum Oxide. *Carbon* 2003, 41, 1257-1263.

67. Pan, Z. W.; Xie, S. S.; Chang, B. H.; Sun, L. F.; Zhou, W. Y.; Wang, G., Direct Growth of Aligned Open Carbon Nanotubes by Chemical Vapor Deposition. *Chem. Phys. Lett.* 1999, 299, 97-102.
68. de Andrede, M. J.; Lima, M. D.; Bergmann, C. P.; Ramminger, G. D.; Balzaretto, N. M.; Costa, T. M. H.; Gallas, M. R., Carbon Nanotube/Silica Composites Obtained by Sol-gel and High-pressure Techniques. *Nanotechnology* 2008, 19.
69. Bacsa, R. R.; Laurent, C.; Peigney, A.; Bacsa, W. S.; Vaugien, T.; Rousset, A., High Specific Surface Area Carbon Nanotubes from Catalytic Chemical Vapor Deposition Process. *Chem. Phys. Lett.* 2000, 323, 566-571.
70. Pinheiro, J. P.; Schouler, M. C.; Gadelle, P., Nanotubes and Nanofilaments from Carbon Monoxide Disproportionation over Co/MgO Catalysts I. Growth Versus Catalyst State. *Carbon* 2003, 41, 2949-2959.
71. Li, Y. M.; Kim, W.; Zhang, Y. G.; Rolandi, M.; Wang, D. W.; Dai, H. J., Growth of Single-walled Carbon Nanotubes from Discrete Catalytic Nanoparticles of Various Sizes. *J. Phys. Chem. B* 2001, 105, 11424-11431.
72. Venegoni, D.; Serp, P.; Feurer, R.; Kihn, Y.; Vahlas, C.; Kalck, P., Parametric Study for the Growth of Carbon Nanotubes by Catalytic Chemical Vapor Deposition in a Fluidized Bed Reactor. *Carbon* 2002, 40, 1799-1807.
73. Hernadi, K.; Fonseca, A.; Nagy, J. B.; Bernaerts, D.; Fudala, A.; Lucas, A. A., Catalytic Synthesis of Carbon Nanotubes Using Zeolite Support. *Zeolites* 1996, 17, 416-423.
74. Ago, H.; Komatsu, T.; Ohshima, S.; Kuriki, Y.; Yumura, M., Dispersion of Metal Nanoparticles for Aligned Carbon Nanotube Arrays. *Appl. Phys. Lett.* 2000, 77, 79-81.
75. Li, Y.; Liu, J.; Wang, Y. Q.; Wang, Z. L., Preparation of Monodispersed Fe-Mo Nanoparticles as the Catalyst for CVD Synthesis of Carbon Nanotubes. *Chem. Mat.* 2001, 13, 1008-1014.
76. Cheung, C. L.; Kurtz, A.; Park, H.; Lieber, C. M., Diameter-controlled Synthesis of Carbon Nanotubes. *J. Phys. Chem. B* 2002, 106, 2429-2433.
77. Shang, N. G.; Jiang, X., Large-sized Tubular Graphite Cones with Nanotube Tips. *Appl. Phys. Lett.* 2005, 87.
78. Shang, N. G.; Milne, W. I.; Jiang, X., Tubular Graphite Cones with Single-crystal Nanotips and Their Antioxygenic Properties. *J. Am. Chem. Soc.* 2007, 129, 8907-8911.
79. Zhang, G. Y.; Ma, X. C.; Zhong, D. Y.; Wang, E. G., Polymerized Carbon Nitride Nanobells. *J. Appl. Phys.* 2002, 91, 9324-9332.

80. Zhang, Y. G.; Chang, A. L.; Cao, J.; Wang, Q.; Kim, W.; Li, Y. M.; Morris, N.; Yenilmez, E.; Kong, J.; Dai, H. J., Electric-field-directed Growth of Aligned Single-walled Carbon Nanotubes. *Appl. Phys. Lett.* 2001, 79, 3155-3157.
81. Ural, A.; Li, Y. M.; Dai, H. J., Electric-field-aligned Growth of Single-walled Carbon Nanotubes on Surfaces. *Appl. Phys. Lett.* 2002, 81, 3464-3466.
82. Ermakova, M. A.; Ermakov, D. Y.; Chuvilin, A. L.; Kuvshinov, G. G., Decomposition of Methane over Iron Catalysts at the Range of Moderate Temperatures: the Influence of Structure of the Catalytic Systems and the Reaction Conditions on the Yield of Carbon and Morphology of Carbon Filaments. *J. Catal.* 2001, 201, 183-197.
83. Tsunekawa, S.; Ito, S.; Kawazoe, Y.; Wang, J. T., Critical Size of the Phase Transition from Cubic to Tetragonal in Pure Zirconia Nanoparticles. *Nano Letters* 2003, 3, 871-875.
84. Fan, S. S.; Liang, W. J.; Dang, H. Y.; Franklin, N.; Tombler, T.; Chapline, M.; Dai, H. J., Carbon Nanotube Arrays on Silicon Substrates and Their Possible Application. *Physica E* 2000, 8, 179-183.
85. Baker, R. T. K., Catalytic Growth Of Carbon Filaments. *Carbon* 1989, 27, 315-323.
86. Rodriguez, N. M.; Chambers, A.; Baker, R. T. K., Catalytic Engineering Of Carbon Nanostructures. *Langmuir* 1995, 11, 3862-3866.
87. Yang, R. T.; Chen, J. P., Mechanism Of Carbon-filament Growth On Metal-catalysts. *J. Catal.* 1989, 115, 52-64.
88. Juang, Z. Y.; Lai, J. F.; Weng, C. H.; Lee, J. H.; Lai, H. J.; Lai, T. S.; Tsai, C. H., On the Kinetics of Carbon Nanotube Growth by Thermal CVD Method. *Diam. Relat. Mat.* 2004, 13, 2140-2146.
89. Louchev, O. A.; Sato, Y.; Kanda, H., Multiwall Carbon Nanotubes: Self-organization and Inhibition of Step-flow Growth Kinetics. *J. Appl. Phys.* 2001, 89, 3438-3446.
90. Hofmann, S.; Kleinsorge, B.; Ducati, C.; Ferrari, A. C.; Robertson, J., Low-temperature Plasma Enhanced Chemical Vapour Deposition of Carbon Nanotubes. *Diam. Relat. Mat.* 2004, 13, 1171-1176.
91. Louchev, O. A.; Laude, T.; Sato, Y.; Kanda, H., Diffusion-controlled kinetics of carbon nanotube forest growth by chemical vapor deposition. *J. Chem. Phys.* 2003, 118, 7622-7634.
92. Louchev, O. A., Formation Mechanism of Pentagonal Defects and Bamboo-like Structures in Carbon Nanotube Growth Mediated by Surface Diffusion. *Phys. Status Solidi A-Appl. Res.* 2002, 193, 585-596.
93. Louchev, O. A.; Sato, Y.; Kanda, H., Growth Mechanism of Carbon Nanotube Forests by Chemical Vapor Deposition. *Appl. Phys. Lett.* 2002, 80, 2752-2754.

-
94. Li, D. C.; Dai, L. M.; Huang, S. M.; Mau, A. W. H.; Wang, Z. L., Structure and Growth of Aligned Carbon Nanotube Films by Pyrolysis. *Chem. Phys. Lett.* 2000, 316, 349-355.
95. Hofmann, S.; Csanyi, G.; Ferrari, A. C.; Payne, M. C.; Robertson, J., Surface diffusion: The low activation energy path for nanotube growth. *Phys. Rev. Lett.* 2005, 95.
96. Gan, X. C.; Zhou, H. B.; Zhu, B. J.; Yu, X. Y.; Jia, Y.; Sun, B.; Zhang, M. Y.; Huang, X. J.; Liu, J. H.; Luo, T., A Simple Method to Synthesize Graphene at 633 K by Dechlorination of Hexachlorobenzene on Cu Foils. *Carbon* 2012, 50, 306-310.
97. Xia, J. H., *Growth of Carbon Nanofibers Studied by Using Transmission Electron Microscopy*. Shaker Verlag: D-52018 Aachen, 2010.
98. Stipe, B. C.; Rezaei, M. A.; Ho, W., Single-molecule Vibrational Spectroscopy and Microscopy. *Science* 1998, 280, 1732-1735.
99. Stipe, B. C.; Rezaei, M. A.; Ho, W., Coupling of Vibrational Excitation to the Rotational Motion of a Single Adsorbed Molecule. *Phys. Rev. Lett.* 1998, 81, 1263-1266.
100. Szanyi, J.; Paffett, M. T., Dimerization and Trimerization of Acetylene over a Model Sn/Pt Catalyst. *J. Am. Chem. Soc.* 1995, 117, 1034-1042.
101. Fischer, T. E.; Kelemen, S. R., Influence of the Substrate Structure on the Bonding of Chemisorbed Acetylene to Transition Metal Surfaces. *Surf. Sci.* 1978, 74.
102. Kotov, Y. A., Electric Explosion of Wires as a Method for Preparation of Nanopowders. *J. Nanopart. Res.* 2003, 5, 539-550.
103. Tsai, Y. M.; Boerio, F. J., Molecular structure of interfaces between plasma-polymerized acetylene films and steel substrates. *Journal of Applied Polymer Science* 1998, 70, 1283-1298.
104. Dvorak, J.; Hrbek, J., Adsorbate ordering effects in the trimerization reaction of acetylene on Cu(100). *J. Phys. Chem. B* 1998, 102, 9443-9450.
105. Lomas, J. R.; Baddeley, C. J.; Tikhov, M. S.; Lambert, R. M., Ethyne Cyclization To Benzene Over Cu(110). *Langmuir* 1995, 11, 3048-3053.
106. Kyriakou, G.; Kim, J.; Tikhov, M. S.; Macleod, N.; Lambert, R. M., Acetylene coupling on Cu(111): Formation of butadiene, benzene, and cyclooctatetraene. *J. Phys. Chem. B* 2005, 109, 10952-10956.
107. Chen, P.; Zhang, H. B.; Lin, G. D.; Hong, Q.; Tsai, K. R., Growth of Carbon Nanotubes by Catalytic Decomposition of CH₄ or CO on a Ni-MgO Catalyst. *Carbon* 1997, 35, 1495-1501.

108. Ni, L.; Kuroda, K.; Zhou, L. P.; Kizuka, T.; Ohta, K.; Matsuishi, K.; Nakamura, J., Kinetic Study of Carbon Nanotube Synthesis over Mo/Co/MgO Catalysts. *Carbon* 2006, 44, 2265-2272.
109. Einarsson, E.; Murakami, Y.; Kadowaki, M.; Maruyama, S., Growth Dynamics of Vertically Aligned Single-walled Carbon Nanotubes From in Situ Measurements. *Carbon* 2008, 46, 923-930.
110. Liao, X. Z.; Serquis, A.; Jia, Q. X.; Peterson, D. E.; Zhu, Y. T.; Xu, H. F., Effect of Catalyst Composition on Carbon Nanotube Growth. *Appl. Phys. Lett.* 2003, 82, 2694-2696.
111. Zaera, F.; Hall, R. B., High-Resolution Electron Energy Loss Spectroscopy and Thermal Programmed Desorption Studies of the Chemisorption and Thermal Decomposition of Ethylene and Acetylene on Ni(100) Single-Crystal Surfaces. *J. Phys. Chem.* 1987, 91, 4318-4323.
112. Patterson, C. H.; Lambert, R. M., Molecular Mechanisms in the Cyclotrimerization of Acetylene to Benzene on Palladium(111). *J. Phys. Chem.* 1988, 92, 1266-1270.
113. Ramirezcuesta, A.; Zgrablich, G.; Tysoe, W. T., Simulation of Benzene Formation from Acetylene on Palladium and Oxygen-covered Palladium Surfaces. *Surf. Sci.* 1995, 340, 109-118.
114. Ormerod, R. M.; Lambert, R. M., Critical Ensemble Required for Acetylene Cyclization on Pd(111) - A Study of Steric Inhibition by Coadsorbed Oxygen. *J. Phys. Chem.* 1992, 96, 8111-8116.
115. Mori, K.; Oishi, Y.; Miyashita, T.; Matsuda, M., Polymerization of Monomer Films of Triazine Dithiols on a Copper Surface. *Polym. Int.* 1992, 28, 193-199.
116. Hirai, H.; Toshima, N.; Kanaka, K.; Koshirai, A., Polymerization of Benzene Catalyzed by Aluminum Chloride-Copper(i) Chloride Under Oxygen. *Chem. Lett.* 1987, 1461-1464.
117. Patra, B. N.; Bhattacharjee, M., Cp₂VCl₂-catalyzed Aqueous Polymerization Using Oxygen as a Cocatalyst: The Remarkable Effect of Oxygen on the Molecular Weights and Yields of the Polymers. *J. Polym. Sci. Pol. Chem.* 2006, 44, 2749-2753.
118. Hansen, P. L.; Wagner, J. B.; Helveg, S.; Rostrup-Nielsen, J. R.; Clausen, B. S.; Topsøe, H., Atom-resolved imaging of dynamic shape changes in supported copper nanocrystals. *Science* 2002, 295, 2053-2055.
119. Hu, J. T.; Li, L. S.; Yang, W. D.; Manna, L.; Wang, L. W.; Alivisatos, A. P., Linearly polarized emission from colloidal semiconductor quantum rods. *Science* 2001, 292, 2060-2063.
120. Yin, A. X.; Min, X. Q.; Zhang, Y. W.; Yan, C. H., Shape-Selective Synthesis and Facet-Dependent Enhanced Electrocatalytic Activity and Durability of Monodisperse Sub-10 nm Pt-Pd Tetrahedrons and Cubes. *J. Am. Chem. Soc.* 2011, 133, 3816-3819.

121. Mostafa, S.; Behafarid, F.; Croy, J. R.; Ono, L. K.; Li, L.; Yang, J. C.; Frenkel, A. I.; Cuenya, B. R., Shape-Dependent Catalytic Properties of Pt Nanoparticles. *J. Am. Chem. Soc.* 2010, 132, 15714-15719.
122. Zhang, H.; Jin, M. S.; Xiong, Y. J.; Lim, B.; Xia, Y. N., Shape-Controlled Synthesis of Pd Nanocrystals and Their Catalytic Applications. *Accounts Chem. Res.* 2013, 46, 1783-1794.
123. Narayanan, R.; El-Sayed, M. A., Catalysis with transition metal nanoparticles in colloidal solution: Nanoparticle shape dependence and stability. *J. Phys. Chem. B* 2005, 109, 12663-12676.
124. Leng, Y. H.; Zhang, Y. H.; Liu, T.; Suzuki, M.; Li, X. G., Synthesis of single crystalline triangular and hexagonal Ni nanosheets with enhanced magnetic properties. *Nanotechnology* 2006, 17, 1797-1800.
125. Jun, Y. W.; Choi, J. S.; Cheon, J., Shape control of semiconductor and metal oxide nanocrystals through nonhydrolytic colloidal routes. *Angew. Chem.-Int. Edit.* 2006, 45, 3414-3439.
126. Xia, Y. N.; Xiong, Y. J.; Lim, B.; Skrabalak, S. E., Shape-Controlled Synthesis of Metal Nanocrystals: Simple Chemistry Meets Complex Physics? *Angew. Chem.-Int. Edit.* 2009, 48, 60-103.
127. Tao, A. R.; Habas, S.; Yang, P. D., Shape control of colloidal metal nanocrystals. *Small* 2008, 4, 310-325.
128. Inomata, K.; Aoki, N.; Koinuma, H., PRODUCTION OF FULLERENES BY LOW-TEMPERATURE PLASMA CHEMICAL-VAPOR-DEPOSITION UNDER ATMOSPHERIC-PRESSURE. *Jpn. J. Appl. Phys. Part 2 - Lett.* 1994, 33, L197-L199.
129. Satishkumar, B. C.; Thomas, P. J.; Govindaraj, A.; Rao, C. N. R., Y-junction carbon nanotubes. *Appl. Phys. Lett.* 2000, 77, 2530-2532.
130. Li, J.; Papadopoulos, C.; Xu, J., Nanoelectronics - Growing Y-junction carbon nanotubes. *Nature* 1999, 402, 253-254.
131. Murphy, C. J.; Jana, N. R., Controlling the aspect ratio of inorganic nanorods and nanowires. *Adv. Mater.* 2002, 14, 80-82.
132. Ha, T. H.; Koo, H. J.; Chung, B. H., Shape-controlled syntheses of gold nanoprisms and nanorods influenced by specific adsorption of halide ions. *J. Phys. Chem. C* 2007, 111, 1123-1130.
133. Habas, S. E.; Lee, H.; Radmilovic, V.; Somorjai, G. A.; Yang, P., Shaping binary metal nanocrystals through epitaxial seeded growth. *Nat. Mater.* 2007, 6, 692-697.

134. Xiong, Y. J.; McLellan, J. M.; Yin, Y. D.; Xia, Y. N., Synthesis of palladium icosahedra with twinned structure by blocking oxidative etching with citric acid or citrate ions. *Angew. Chem.-Int. Edit.* 2007, 46, 790-794.
135. Chen, G. Z.; Zhang, J. M.; Gupta, A.; Rosei, F.; Ma, D. L., Shape-controlled synthesis of ruthenium nanocrystals and their catalytic applications. *New J. Chem.* 2014, 38, 1827-1833.
136. Lee, S. M.; Jun, Y. W.; Cho, S. N.; Cheon, J., Single-crystalline star-shaped nanocrystals and their evolution: Programming the geometry of nano-building blocks. *J. Am. Chem. Soc.* 2002, 124, 11244-11245.
137. Hernadi, K.; Fonseca, A.; Nagy, J. B.; Bernaerts, D.; Lucas, A. A., Fe-catalyzed carbon nanotube formation. *Carbon* 1996, 34, 1249-1257.
138. Chen, D.; Christensen, K. O.; Ochoa-Fernandez, E.; Yu, Z. X.; Totdal, B.; Latorre, N.; Monzon, A.; Holmen, A., Synthesis of carbon nanofibers: effects of Ni crystal size during methane decomposition. *J. Catal.* 2005, 229, 82-96.
139. Tuinstra, F.; Koenig, J. L., Raman Spectrum of Graphite. *J. Chem. Phys.* 1970, 53, 1126-&.
140. Ferrari, A. C.; Robertson, J., Interpretation of Raman Spectra of Disordered and Amorphous Carbon. *Physical Review B* 2000, 61, 14095-14107.
141. Carley, A. F.; Davies, P. R.; Harikumar, K. R.; Jones, R. V.; Roberts, M. W., Oxygen states at magnesium and copper surfaces revealed by scanning tunneling microscopy and surface reactivity. *Top. Catal.* 2003, 24, 51-59.
142. Davies, P. R.; Edwards, D.; Richards, D., Possible Role for Cu(II) Compounds in the Oxidation of Malonyl Dichloride and HCl at Cu(110) Surfaces. *J. Phys. Chem. C* 2009, 113, 10333-10336.
143. Dayeh, S. A.; Yu, E. T.; Wang, D., III-V nanowire growth mechanism: V/III ratio and temperature effects. *Nano Letters* 2007, 7, 2486-2490.
144. Rhodin, T. N.; Brucker, C. F.; Anderson, A. B., Structure and Bonding of Acetylene and Ethylene on Alpha-iron Surfaces at Low-temperatures. *J. Phys. Chem.* 1978, 82, 894-898.
145. Anderson, A. B.; Mehandru, S. P., Acetylene Adsorption to Fe(100), Fe(110), and Fe(111) Surfaces - Structures and Reactions. *Surf. Sci.* 1984, 136, 398-418.
146. Hung, W. H.; Bernasek, S. L., Adsorption and Decomposition of Ethylene and Acetylene on Fe(100). *Surf. Sci.* 1995, 339, 272-290.
147. Erley, W.; Baro, A. M.; Ibach, H., Vibrational-spectra of Acetylene and Ethylene Adsorbed on Fe(110). *Surf. Sci.* 1982, 120, 273-290.

148. Stroschio, J. A.; Bare, S. R.; Ho, W., The Chemisorption and Decomposition of Ethylene and Acetylene on Ni(110). *Surf. Sci.* 1984, 148, 499-525.
149. Bertolini, J. C.; Massardier, J.; Dalmatimelik, G., Evolution of Adsorbed Species During C₂H₂ Adsorption on Ni(111) in Relation to their Vibrational Spectra. *Journal of the Chemical Society-Faraday Transactions I* 1978, 74, 1720-1725.
150. Seip, U.; Tsai, M. C.; Kupperts, J.; Ertl, G., Interaction of Acetylene and Ethylene with an Fe(111) Surface. *Surf. Sci.* 1984, 147, 65-88.
151. Yoshida, K.; Somorjai, G. A., Chemisorption of CO, CO₂, C₂H₂, C₂H₄, H₂ and NH₃ on Clean Fe(100) and (111) Crystal-surfaces. *Surf. Sci.* 1978, 75, 46-60.
152. Mason, R.; Textor, M., Chemisorption of Simple-substituted and Halogeno-substituted Unsaturated-hydrocarbons on Alpha-Fe(111) Single-crystal Surface - Photoelectron Spectroscopic Studies. *Proc. R. Soc. London Ser. A-Math. Phys. Eng. Sci.* 1977, 356, 47-60.
153. Motojima, S.; Kawaguchi, M.; Nozaki, K.; Iwanaga, H., Growth of Regularly Coiled Carbon Filaments by Ni Catalyzed Pyrolysis of Acetylene, and Their Morphology and Extension Characteristics. *Appl. Phys. Lett.* 1990, 56, 321-323.
154. Zhifeng Ren, Y. L., Yang Wang, *Aligned Carbon Nanotubes*. Springer-Verlag Berlin: Heidelberg, 2013.
155. Baker, R. T. K.; Barber, M. A.; Waite, R. J.; Harris, P. S.; Feates, F. S., Nucleation And Growth Of Carbon Deposits From Nickel Catalyzed Decomposition Of Acetylene. *J. Catal.* 1972, 26, 51-&.
156. Chen, Y.; Liu, C.; Du, J. H.; Cheng, H. M., Preparation of Carbon Microcoils by Catalytic Decomposition of Acetylene Using Nickel Foam as Both Catalyst and Substrate. *Carbon* 2005, 43, 1874-1878.
157. Singh, M. K.; Singh, P. P.; Titus, E.; Misra, D. S.; LeNormand, F., High Density of Multiwalled Carbon Nanotubes Observed on Nickel Electroplated Copper Substrates by Microwave Plasma Chemical Vapor Deposition. *Chem. Phys. Lett.* 2002, 354, 331-336.
158. Benninghoven, A.; Beckmann, P.; Greifendorf, D.; Schemmer, M., Investigation of Surface-reactions by SIMS And TDMS - Interaction of Ethylene and Acetylene with Hydrogen on Polycrystalline Nickel. *Appl. Surf. Sci.* 1980, 6, 288-296.
159. Mattlis, P. M., The Oligomerization of Acetylenes Induced by Metals of the Nickel Triad. *Pure Appl. Chem.* 1972, 30, 427-448.
160. Trimm, D. L.; Liu, I. O. Y.; Cant, N. W., The oligomerization of acetylene in hydrogen over Ni/SiO₂ catalysts: Product distribution and pathways. *J. Mol. Catal. A-Chem.* 2008, 288, 63-74.

161. Lesiak, B.; Jablonski, A.; Palczewska, W.; Kulszewiczbajer, I.; Zagorska, M., Identification of the Carbonaceous Residues at Nickel and Platinum Surfaces on the Basis of the Carbon KII Spectra. *Surf. Interface Anal.* 1992, 18, 430-438.
162. Trimm, D. L.; Liu, I. O. Y.; Cant, N. W., The effect of carbon monoxide on the oligomerization of acetylene in hydrogen over a Ni/SiO₂ catalyst. *J. Mol. Catal. A-Chem.* 2009, 307, 13-20.
163. Garcia-Vidal, F. J.; Pitarke, J. M.; Pendry, J. B., Effective Medium Theory of the Optical Properties of Aligned Carbon Nanotubes. *Phys. Rev. Lett.* 1997, 78, 4289-4292.
164. Shirley, L. G.; George, N., Diffuser Radiation-patterns over a Large Dynamic-range .1. Strong Diffusers. *Appl. Optics* 1988, 27, 1850-1861.
165. Yang, Z. P.; Ci, L. J.; Bur, J. A.; Lin, S. Y.; Ajayan, P. M., Experimental Observation of an Extremely Dark Material Made by a Low-density Nanotube Array. *Nano Letters* 2008, 8, 446-451.
166. Harvey, J. E.; Choi, N.; Krywonos, A.; Peterson, G.; Bruner, M., Image Degradation due to Scattering Effects in Two-mirror Telescopes. *Opt. Eng.* 2010, 49.
167. Kong, J. H.; Yee, W. A.; Wei, Y. F.; Yang, L. P.; Ang, J. M.; Phua, S. L.; Wong, S. Y.; Zhou, R.; Dong, Y. L.; Li, X.; Lu, X. H., Silicon Nanoparticles Encapsulated in Hollow Graphitized Carbon Nanofibers for Lithium Ion Battery Anodes. *Nanoscale* 2013, 5, 2967-2973.
168. Eom, J. Y.; Kwon, H. S., Preparation of Single-Walled Carbon Nanotube/Silicon Composites and Their Lithium Storage Properties. *ACS Appl. Mater. Interfaces* 2011, 3, 1015-1021.
169. Yang, Z. C.; Shen, J. G.; Archer, L. A., An in Situ Method of Creating Metal Oxide-Carbon Composites and Their Application as Anode Materials for Lithium-ion Batteries. *J. Mater. Chem.* 2011, 21, 11092-11097.
170. Yen, M. Y.; Hsiao, M. C.; Liao, S. H.; Liu, P. I.; Tsai, H. M.; Ma, C. C. M.; Pu, N. W.; Ger, M. D., Preparation of Graphene/multi-walled Carbon Nanotube Hybrid and Its Use as Photoanodes of Dye-sensitized Solar cells. *Carbon* 2011, 49, 3597-3606.
171. Lee, B.; Buchholz, D. B.; Chang, R. P. H., An all Carbon Counter Electrode for Dye Sensitized Solar cells. *Energy Environ. Sci.* 2012, 5, 6941-6952.
172. Hsieh, C. T.; Yang, B. H.; Lin, J. Y., One- and Two-dimensional Carbon Nanomaterials as Counter Electrodes for Dye-sensitized Solar Cells. *Carbon* 2011, 49, 3092-3097.
173. Banerjee, S.; Hemraj-Benny, T.; Wong, S. S., Covalent Surface Chemistry of Single-walled Carbon Nanotubes. *Adv. Mater.* 2005, 17, 17-29.

174. Bahr, J. L.; Tour, J. M., Covalent Chemistry of Single-wall Carbon Nanotubes. *J. Mater. Chem.* 2002, 12, 1952-1958.
175. Zhang, L. L.; Zhao, X. S., Carbon-based materials as supercapacitor electrodes. *Chem. Soc. Rev.* 2009, 38, 2520-2531.
176. Long, C. L.; Qi, D. P.; Wei, T.; Yan, J.; Jiang, L. L.; Fan, Z. J., Nitrogen-Doped Carbon Networks for High Energy Density Supercapacitors Derived from Polyaniline Coated Bacterial Cellulose. *Advanced Functional Materials* 2014, 24, 3953-3961.
177. Wickramaratne, N. P.; Xu, J. T.; Wang, M.; Zhu, L.; Dai, L. M.; Jaroniec, M., Nitrogen Enriched Porous Carbon Spheres: Attractive Materials for Supercapacitor Electrodes and CO₂ Adsorption. *Chem. Mat.* 2014, 26, 2820-2828.
178. Wei, W.; Liang, H. W.; Parvez, K.; Zhuang, X. D.; Feng, X. L.; Mullen, K., Nitrogen-Doped Carbon Nanosheets with Size-Defined Mesopores as Highly Efficient Metal-Free Catalyst for the Oxygen Reduction Reaction. *Angew. Chem.-Int. Edit.* 2014, 53, 1570-1574.
179. Li, X. S.; Cai, W. W.; An, J. H.; Kim, S.; Nah, J.; Yang, D. X.; Piner, R.; Velamakanni, A.; Jung, I.; Tutuc, E.; Banerjee, S. K.; Colombo, L.; Ruoff, R. S., Large-Area Synthesis of High-Quality and Uniform Graphene Films on Copper Foils. *Science* 2009, 324, 1312-1314.
180. Reina, A.; Jia, X. T.; Ho, J.; Nezich, D.; Son, H. B.; Bulovic, V.; Dresselhaus, M. S.; Kong, J., Large Area, Few-Layer Graphene Films on Arbitrary Substrates by Chemical Vapor Deposition. *Nano Letters* 2009, 9, 30-35.

Appendix A

The complete list of TD-GC/MS results of Fe catalyzed polymer nanofiber

PK	RT	Area	Area Pct	mg/kg Toluol- equivalent	Library/ID	CAS	Qual
1	20.65	3409628	0.58	554	Indene	000095-13-6	93
2	22.57	2501145	0.43	406	2-Methylindene	002177-47-1	94
3	22.88	2011928	0.34	327	Naphthalene, 1,2-dihydro-	000447-53-0	93
4	23.24	1645267	2.81	2672	Naphthalene	000091-20-3	94
5	24.81	3587832	0.61	583	17-Epi-trenbolone, trimethylsilyl ether	1000293-11- 0	35
6	24.95	3313388	0.56	538	Naphthalene, 2-methyl-	000091-57-6	94
7	25.22	2083210	0.36	338	Naphthalene, 2-methyl-	000091-57-6	87
8	26.10	1275631	2.18	2072	Biphenyl	000092-52-4	91
9	26.34	4109547	0.70	667	Naphthalene, 2-ethyl-	000939-27-5	94
10	26.48	3112672	0.53	505	Naphthalene, 2,6-dimethyl-	000581-42-0	64
11	26.61	1979385	0.34	321	.beta.-(1-Naphthyl)acrylic acid	013026-12-5	59
12	26.78	9255934	1.58	1503	Diphenylmethane	000101-81-5	86
13	26.83	7816099	1.33	1269	Naphthalene, 2-ethenyl-	000827-54-3	93
14	27.09	1496286	0.26	243	1,4-Ethenonaphthalene, 1,4- dihydro-	007322-47-6	62
15	27.48	5041063	0.86	819	1,1'-Biphenyl, 4-methyl-	000644-08-6	94
16	27.61	2806502	0.48	456	1,1'-Biphenyl, 4-methyl-	000644-08-6	90
17	27.66	3145456	0.54	511	Acenaphthene	000083-32-9	93
18	27.97	4181800	0.71	679	2,2'-Dimethylbiphenyl	000605-39-0	96
19	28.29	6379134	1.09	1036	1,1'-Biphenyl, 2-ethyl-	001812-51-7	90
20	28.59	2438720	0.42	396	2,2'-Dimethylbiphenyl	000605-39-0	58

21	28.71	4019452	0.69	653	1,1'-Biphenyl, 2-methyl-	000643-58-3	93
22	28.90	5425325	9.25	8811	Fluorene	000086-73-7	94
23	29.01	6586030	1.12	1070	1,1'-Biphenyl, 4-ethenyl-	002350-89-2	91
24	29.12	4936914	0.84	802	9H-Fluorene, 9-methyl-	002523-37-7	91
25	29.18	2120654	0.36	344	Fluorene	000086-73-7	70
26	29.22	4392537	0.75	713	1,1'-Biphenyl, 2-methyl-	000643-58-3	53
27	29.31	6363332	1.08	1033	1,1'-Biphenyl, 4-ethenyl-	002350-89-2	89
28	29.43	4286719	0.73	696	Fluorene	000086-73-7	94
29	29.71	4556387	0.78	740	Bicyclo[4.2.1]nona-2,4,7-triene, 7-phenyl-	1000164-41-0	94
30	29.84	6486048	1.11	1053	Propyne, 1,3-diphenyl-	004980-70-5	90
31	29.92	2178206	0.37	354	1,1'-Biphenyl, 2-ethyl-	001812-51-7	81
32	29.99	1129141	1.93	1834	4a,9a-Methano-9H-fluorene	019540-84-2	89
33	30.21	3432191	5.85	5574	9H-Fluorene, 2-methyl-	001430-97-3	95
34	30.25	1752489	2.99	2846	9H-Fluorene, 2-methyl-	001430-97-3	97
35	30.34	1184297	2.02	1923	9H-Fluorene, 2-methyl-	001430-97-3	96
36	30.42	1110377	1.89	1803	1,2-Diphenylcyclopropane	029881-14-9	94
37	30.48	6607295	1.13	1073	9H-Fluorene, 3-methyl-	002523-39-9	91
38	30.64	3603384	0.61	585	1H-Cyclopropa[1]phenanthrene, 1a,9b-dihydro-	000949-41-7	45
39	30.66	4188138	0.71	680	Naphthalene, 2-(1-cyclopenten-1-yl)-	074793-18-3	64
40	30.74	9691148	1.65	1574	9H-Fluorene-9-one	000486-25-9	80
41	30.87	3002073	0.51	488	Benzene, 1,1'-(2-butene-1,4-diyl)bis-	013657-49-3	42
42	30.94	7288073	1.24	1184	1H-Indene, 2-phenyl-	004505-48-0	93
43	31.01	1104210	1.88	1793	Phenanthrene, 1,2-dihydro-	056179-83-0	95

44	31.22	1825115	0.31	296	Phenanthrene, 9,10-dihydro-1-methyl-	095676-48-5	90
45	31.27	2064282	3.52	3352	Phenanthrene	000085-01-8	94
46	31.37	1655298	2.82	2688	Phenanthrene	000085-01-8	94
47	31.41	7200853	1.23	1169	Propyne, 1,3-diphenyl-	004980-70-5	76
48	31.46	5244133	0.89	852	1H-Indene, 1-phenyl-	001961-96-2	81
49	31.51	4572098	0.78	742	Benzene, 1-methyl-2-(2-phenylethenyl)-	074685-42-0	86
50	31.68	4832455	0.82	785	5H-Dibenzo[a,d]cycloheptene	000256-81-5	55
51	31.73	3025222	0.52	491	Propyne, 1,3-diphenyl-	004980-70-5	64
52	31.86	5032530	0.86	817	Benzene, 1,1'-(2-cyclopropen-1-ylidene)bis-	022825-21-4	83
53	31.96	4284995	0.73	696	Anthracene, 9-ethenyl-	002444-68-0	90
54	32.03	1302724	2.22	2116	1H-Indene, 2-phenyl-	004505-48-0	96
55	32.20	1317033	2.25	2139	9-Ethylfluorene	002294-82-8	40
56	32.31	6898016	1.18	1120	9,10-Dimethylanthracene	000781-43-1	64
57	32.36	1788309	0.30	290	9,10-Dimethylanthracene	000781-43-1	86
58	32.44	5856380	1.00	951	Phenanthrene, 2-methyl-	002531-84-2	96
59	32.52	5524985	0.94	897	Anthracene, 2-methyl-	000613-12-7	95
60	32.62	1464620	2.50	2378	1a,9b-Dihydro-1H-cyclopropa[a]anthracene	006109-24-6	90
61	32.74	1821513	3.11	2958	Phenanthrene, 2-methyl-	002531-84-2	94
62	32.79	4797085	0.82	779	Anthracene, 9-methyl-	000779-02-2	80
63	32.87	4300013	0.73	698	9,10-Dimethylanthracene	000781-43-1	81
64	32.95	5333292	0.91	866	di-p-Tolylacetylene	002789-88-0	92
65	33.12	3137881	0.54	510	[14]Annulene, 1,6:8,13-bis(methano)-, syn	085385-68-8	60
66	33.15	1763532	3.01	2864	Naphthalene, 2-phenyl-	000612-94-2	95

67	33.26	5662090	0.97	920	Naphthalene, 1,2-dihydro-4-phenyl-	007469-40-1	70
68	33.51	4759600	0.81	773	1H-Cyclopenta[1]phenanthrene, 2,3-dihydro-	000723-98-8	70
69	33.54	5198719	0.89	844	1H-Indene, 2-methyl-3-phenyl-	035099-60-6	87
70	33.77	5781117	0.99	939	9,10-Dimethylanthracene	000781-43-1	95
71	33.83	4788550	0.82	778	Naphthalene, 1,2-dihydro-4-phenyl-	007469-40-1	92
72	33.91	5425282	0.93	881	Indeno[2,1-a]indene, 5,10-dihydro-	006543-29-9	91
73	34.06	6827960	1.16	1109	3-Bromo-5-ethoxy-4-hydroxybenzaldehyde	003111-37-3	59
74	34.21	9832545	1.68	1597	Fluoranthene	000206-44-0	95
75	34.77	1041710 1	1.78	1692	Pyrene	000129-00-0	90
76	35.07	3257832	0.56	529	Naphthalene, 2-(phenylmethyl)-	000613-59-2	64
77	35.59	3844130	0.66	624	11H-Benzo[b]fluorene	000243-17-4	94
78	36.16	3583507	0.61	582	Pyrene, 1-methyl-	002381-21-7	96
	Summe	5864872 78	100	95243			

Appendix B

The complete list of TD-GC/MS results of Ni catalyzed polymer nanofiber

	RT	Area	Area Pct	mg/kg Toluol-equivalent	Library/ID	CAS	Qual
1	20.29	834208	0.2	88	Acetophenone	000098-86-2	49
2	21.33	1383673	0.3	146	Benzene, (2-methyl-1-propenyl)-	000768-49-0	95
3	21.47	1141746	0.3	121	2,4-Dimethylstyrene	002234-20-0	96
4	21.85	2259104	0.5	238	2-Methylindene	002177-47-1	94
5	21.95	2152640	0.5	227	2-Methylindene	002177-47-1	94
6	22.29	1690921	0.4	178	1-Dodecene	000112-41-4	95
7	22.41	1476270	0.3	156	Nonadecane	000629-92-5	80
8	22.51	5347288	1.2	564	Azulene	000275-51-4	91
9	23.39	2075989	0.5	219	2-Ethyl-1-H-indene	017059-50-6	89
10	23.61	5614038	1.3	593	1H-Indene, 1,3-dimethyl-	002177-48-2	87
11	23.72	4269012	1.0	451	(1-Methylbuta-1,3-dienyl)benzene	054758-36-0	94
12	23.80	2330299	0.5	246	1H-Indene, 4,7-dimethyl-	006974-97-6	90
13	23.91	2344007	0.5	247	Tridecane	000629-50-5	30
14	24.23	15574154	3.6	1644	Naphthalene, 1-methyl-	000090-12-0	95
15	24.34	1638914	0.4	173	Benzene, 4-(2-butenyl)-1,2-dimethyl-, (E)-	054340-86-2	60
16	24.50	8617535	2.0	910	Naphthalene, 1-methyl-	000090-12-0	91
17	24.64	2048713	0.5	216	1-Naphthalenemethanol, 1,2,3,4-tetrahydro-8-methyl-	036052-28-5	42
18	24.78	3690569	0.9	390	1H-Indene, 1,1,3-trimethyl-	002177-45-9	55
19	24.98	9035283	2.1	954	(1-Methylpenta-2,4-dienyl)benzene	1000210-01-1	91
20	25.20	6465429	1.5	682	1-Tetradecene	001120-36-1	93

21	25.30	5646020	1.3	596	1,2,3-Trimethylindene	004773-83-5	91
22	25.39	13100851	3.0	1383	Biphenyl	000092-52-4	94
23	25.62	10188313	2.4	1075	Naphthalene, 1-ethyl-	001127-76-0	93
24	25.68	5088237	1.2	537	Naphthalene, 2-ethyl-	000939-27-5	91
25	25.78	8707183	2.0	919	Naphthalene, 2,6-dimethyl-	000581-42-0	96
26	25.89	2907697	0.7	307	1,4-Ethenonaphthalene, 1,4-dihydro-	007322-47-6	53
27	25.99	20311334	4.7	2144	Naphthalene, 1,7-dimethyl-	000575-37-1	97
28	26.27	13781043	3.2	1455	Naphthalene, 1,3-dimethyl-	000575-41-7	94
29	26.49	15815506	3.7	1669	Naphthalene, 2,3-dimethyl-	000581-40-8	86
30	26.77	9159343	2.1	967	1,1'-Biphenyl, 4-methyl-	000644-08-6	95
31	26.92	15340098	3.5	1619	Acenaphthene	000083-32-9	86
32	27.06	8634825	2.0	911	Naphthalene, 1,4,6-trimethyl-	002131-42-2	94
33	27.13	5218975	1.2	551	Naphthalene, 2,3,6-trimethyl-	000829-26-5	93
34	27.22	7908577	1.8	835	Naphthalene, 1,6,7-trimethyl-	002245-38-7	90
35	27.35	8852479	2.0	934	Naphthalene, 2,3,6-trimethyl-	000829-26-5	97
36	27.42	7855248	1.8	829	Naphthalene, 1,4,6-trimethyl-	002131-42-2	95
37	27.63	14221049	3.3	1501	Naphthalene, 2,3,6-trimethyl-	000829-26-5	98
38	27.89	15326542	3.5	1618	2,2'-Dimethylbiphenyl	000605-39-0	91
39	28.18	32981883	7.6	3481	Fluorene	000086-73-7	94
40	28.32	9122909	2.1	963	1-Isopropenyl-naphthalene	001855-47-6	95
41	28.40	11838813	2.7	1250	9H-Fluorene, 9-methyl-	002523-37-7	53
42	28.49	18591730	4.3	1962	1-Isopropenyl-naphthalene	001855-47-6	83
43	28.73	7845774	1.8	828	Benzene, 1,1'-ethylidenebis-	000612-00-0	64
44	28.90	5764939	1.3	609	Benzene, 1,1'-cyclopropylidenebis-	003282-18-6	83

45	29.03	3241222	0.7	342	Benzene, 1-methyl-3-(phenylmethyl)-	000620-47-3	90
46	29.10	4837490	1.1	511	9H-Fluorene, 9-methyl-	002523-37-7	64
47	29.21	2443360	0.6	258	1,1'-Biphenyl, 4-(1-methylethyl)-	007116-95-2	55
48	29.31	4870360	1.1	514	9H-Fluorene, 1-methyl-	001730-37-6	84
49	29.51	18009374	4.2	1901	9H-Fluorene, 1-methyl-	001730-37-6	96
50	29.63	11988687	2.8	1265	9H-Fluorene, 9-methyl-	002523-37-7	94
51	29.77	9525996	2.2	1006	9H-Fluorene, 3-methyl-	002523-39-9	94
52	29.92	4915501	1.1	519	4,4'-Dimethylbiphenyl	000613-33-2	60
53	30.03	3262683	0.8	344	9H-Fluoren-9-one	000486-25-9	64
54	30.20	5662870	1.3	598	Benzhydryl isothiocyanate	003550-21-8	91
55	30.56	5241256	1.2	553	Phenanthrene	000085-01-8	95
56	30.67	3944890	0.9	416	Phenanthrene	000085-01-8	49
57	31.32	514593	0.1	54	Anthracene, 9-ethenyl-	002444-68-0	89
	Summe	432657442	100	45670			

Curriculum Vitae

Yao Ma

Institute of Materials Engineering

University of Siegen

57076 Siegen, Germany

Phone: 0271 740 2298

Email: yaoma0309@gmail.com



Personal data

Date of birth: 9th March 1982

Place of birth: Shaanxi, China

Nationality: Chinese

Gender: Male

Marital status: Married

Education and career

2000-2004 **B. Eng.**, School of Materials Science and Engineering, University of Science and Technology Beijing

2004-2006 **Research Assistant**, Shaanxi University of Technology

2006-2009 **M. Sc.**, School of Materials Science and Engineering, University of Science and Technology Beijing

2009-till date Institute of Materials Engineering, University of Siegen, Germany.
Supervisor: Prof. Dr. rer. nat. habil. Xin Jiang